Combustion Behaviour of Biomass in Air and Oxy-fuel Environments and Techno-economic Analysis of Biomass Energy with Carbon Capture

By

Khalidah A. J. Al-Qayim

A thesis submitted in the fulfilment of the requirements for the degree of

Doctor of Philosophy

The University of Sheffield
Faculty of Engineering
Department of Mechanical Engineering

May, 2017

The candidate confirms that the work submitted is her own, except where work which has formed part of jointly-authored publications has been included. The contribution of the candidate and the other authors to this work has been explicitly indicated below. The candidate confirms that appropriate credit has been given to within the thesis where reference has been made to the work of others.

Some of the work presented in Chapter 5 of this thesis forms part of the following publication:

- Al-Qayim, K., Nimmo, W., Hughes, K. and Pourkashanian, M. “Kinetic parameters of the intrinsic reactivity of woody biomass and coal chars via thermogravimetric analysis” Fuel. 2017 (under review).

Some of the work presented in Chapter 6 of this thesis forms part of the following presentation

- Finney K, Szuhanszki J, Al-Qayim K, Nimmo W & Pourkashanian M (2016) Comparison of Metal Aerosol Emissions from Air-Firing of Coal and Biomass for Carbon Capture Applications. *ECCRIA Conference*, 2-7 September **2016**, Sheffield, UK.

Some of the work presented in Chapter 6 of this thesis forms part of the following publications:

- K. Al-Qayim, W. Nimmo*, K. Hughes, M. Pourkashanian. 2017. Experimental and theoretical investigation on the influence of oxy-fuel combustion on ash deposition of pulverized wood pellets and El Cerrejon coal. (under preparation)

Some of the work presented in Chapter 7 of this thesis forms part of the following publications:

- Al-Qayim, K., Nimmo, W., and Pourkashanian, M. *Comparative techno-economic assessment of biomass and coal with CCS technologies in a pulverized combustion power plant in the United Kingdom.* International Journal of Greenhouse Gas Control, 2015. **43**: p. 82-92.
- Al-Qayim, K., Nimmo, W., and Pourkashanian, M. *Comparative techno-economic assessment of biomass and coal with CCS technologies in a pulverized combustion power plant in the United Kingdom.* Poster presentation in the 23rd Europian Biomass Conference & Exhibition (ECBCE 2015). June **2015,** Vienna, Austria.

Acknowledgment

First, I am indebted to God for giving me the enthusiasm, and strength all the way through this journey to accomplish my dream. I would like to thank my prime supervisor Prof Mohammed Pourkashanian for his guidance, and advisory support throughout my research. I highly appreciate the financial support he offered me during the hardship times in my study. My Deep gratitude is extended to my co-supervisor Dr William Nimmo for his time, guidance and immense support and understanding to achieve this work. I learned a lot from both of them. Special thanks go to Dr Kevin Hughes for his support to complete my experimental work. A deep gratitude is paid to Prof Derek Ingham for his time to review the language of this thesis for many times during my study. My thanks are extended to Dr Janos Szuhanszki, and Mr. Paul Crosby for their technical support to perform my experimental work. I am also grateful to Dr Zandi and the technical staff at the Chemical Engineering Department Mr. James Grinham, Mr. Keith Penny, and Mr. Duncan Schofield for the opportunity and the support to facilitate my analytical work.

In carrying out my research I have been fortunate to learn from Dr Alan Dunbar, and Dr Nik Reeves the highly advanced analytical equipment. I am thankful to both of them for providing me the training and knowledge that I needed to perform an important part of my research. Also, I would like to thank the University of Leeds for giving me the opportunity to do my PhD study in the UK in the first place.

I would like to express my gratitude to my family, my husband and daughters Ghada and Sara for their support, patience, and understanding to my passion for continuous scientific achievements.

I have been lucky to meet my colleagues in the Energy 2050 group. We had memorable times that we shared our joy, concerns, and laughter. I learned about their diverse cultures as well as I shared my culture and knowledge with them.

Abstract

This thesis explores biomass performance in pulverized fuel combustion in terms of ash behaviour, investigates the biomass chemical reactivity on a bench scale, and assesses the techno-economic viability of biomass energy with carbon capture in comparison to coal. White wood pellets and the EL-Cerrejon coal were selected for these investigations.

The kinetic study aimed to identify the kinetic reactivity of the biomass in the two principal combustion steps; devolatilization and char combustion. Thermogravimetric analysis technique was employed for this purpose. In comparison to coal, the biomass released 90% of its volatile matter in a temperature about 773 K, whereas the coal released less than 38-66% of its volatile matter at this temperature. The pyrolysis temperature had a disparate effect on the biomass and the coal. The biomass char produced and burned at temperatures higher than 973 K possesses higher reactivity than the corresponding coal chars. The intrinsic activation energy of the biomass was found to be 180 kJ mol^{-1}, and the corresponding value for coal was found in the range 153-167 kJ mol^{-1}.

Oxy-fuel combustion tests were performed on a 250 kW pilot scale combustion rig. The results of those tests have shown that the effect of oxy-fuel on the ash behaviour is less significant on coal than its effect on biomass. For wood pellets, the oxy-fuel combustion can inhibit the slagging tendencies and reduce the furnace deposition, but increases, the fouling tendencies on the convective passes. Furthermore, the effect of oxy-fuel conditions on the combustion efficiency was trivial for both fuels.

Finally, the biomass with oxy-fuel technology has more economic potential to compete with the Oxy-coal plants than the post-combustion carbon capture and storage (CCS) technology. Annually, biomass can eliminate the release of 3M tonnes of CO_2 from a 650 MW power plant. However, the cost of electricity needs more incentives to boost the biomass energy with carbon capture. Also, the feedstock supply chain and land use remain as major concerns in the bioenergy.

A summary of the outcomes of this study is that biomass can compete coal in the power industry due to its higher reactivity, and lower ash deposition problems than coal, and the negative carbon emissions that can be resulted from the bioenergy with carbon capture technology. However, economically, it needs more incentives from the government to become sustainable.

Table of Contents

List of Tables

List of Figures

Chapter 1 Introduction

1.1 Background

Biomass is a natural or processed complex of organic and inorganic compounds [1]. Plant photosynthesis collects solar energy to store as latent energy inside the green parts of the plant, and released as food energy inside the human and animal bodies via metabolism. The enormous solar energy available at the earths' surface as continuous radiant power is estimated to be in excess of 10^{17} W. Annually, plants utilize 0.02% of this power to produce a total 10^{21} J energy storage [2]. Also, photosynthesis preserves the atmospheric oxygen at a constant level for living respiration as well as for other combustion processes necessary for human society.

Natural biomass is considered an advantageous combustion fuel due to the high volatility, and high reactivity of both the fuel and the resulting char [3, 4]. Plant wood was historically fired for cooking and heat. However, in comparison to solid fossil fuels, biomass has lower carbon content and heating value [4].

1.2 Challenges to Biofuels

As biofuels gain a larger market share and international trading of biomass, raw materials and biofuels expand, the need to ensure environmental and socio-economic sustainability along the entire supply chain becomes more pressing. This includes aspects such as land use, agricultural practices, competition with food, energy efficiency, greenhouse gases emissions, and lifecycle analysis, etc [5, 6]. The challenge of biomass supply chain will be discussed in detail in section 7.5.

1.3 Current Biomass Energy Technologies

At the end of the last century, biomass contributed about 6% of the global energy consumption [2], mainly in primitive low efficiency highly polluting combustion for cooking and heating fires. However, new technologies of biomass conversion have been developed during the last three decades as well as many research studies conducted to adapt fuel properties for the technology of choice.

Today, bioenergy is the third largest renewable energy source after hydro power and solar energy providing heat, electricity, as well as transportation fuels [7, 8]. Moreover, bioenergy will be one of the main renewable energy resources in the future due to its large potential, and its contribution to face the environmental challenges [4]. In 2012, the International Energy Agency (IEA) estimated that bioenergy could provide 7.5% of the total world electricity generation by 2050. In addition heat from bioenergy could provide 15% of the total energy consumption in industry and 20% (of the total) in the buildings sector in 2050. The IEA projects that the primary bioenergy share of the global total primary energy supply (TPES) will increase to ~160 EJ by 2050, providing ~24% of TPES compared to 10% today. About 62.5% of this will be required to provide electricity and heat for the residential sector, industry and other sectors [6].

The four major technologies of biomass conversion into synthetic fuel are: (a) Combustion; (b) Pyrolysis; (c) Gasification; and (d) Bioconversion [4, 9]. The limitations of biomass fuel conversions in the first three processes are as follows:

- High moisture content that reduces the efficiency of combustion process.
- Low melting-point of ash metals (more alkali metals) causes fouling and slagging then ultimately corrosion problems.
- High-temp corrosion induced by chlorine on boiler tubes.
- Low heating value.

1.3.1 Combustion

The oldest way known of using biomass as a fuel is combustion, it is the most important and mature technology available for biomass utilization [3]. Combustion is responsible for over 97% of the world's bio-energy production [4], and biomass can be directly fired in dedicated boilers, or co-fired with coal. It can be applied to either whole biomass or to the remaining organic parts of other treatment such as fermentation [2]. In general, combustion can be described as the thermal degradation of the organic compounds in the solid fuel followed by the oxidation of the remaining inorganic carbon. Thermal degradation products of the biomass consist of moisture, volatile matter, and char that consists mainly of carbon and ash-forming minerals [2-4, 10]. The volatile matter consists of gases such as light hydrocarbons, CO, CO_2, H_2, CH_4, and tars and H_2O. The yield components depend on the fuel composition, temperature, and heating rate of the combustion process. Due to its nature of occurrence, char oxidation mainly occurs on the carbon particle surfaces, thus its reaction rate is lower than the

devolatilization rate. Therefore, the overall combustion rate depends on the burning rate of the char as the limiting step in the combustion reactions.

1.3.2 Pyrolysis

Pyrolysis is defined as the thermal destruction of organic materials in the absence of oxygen [11]. The products of carbonaceous materials devolatilization are divided into hydrogen-rich volatile fraction consisting of gases, vapour and tar components, and a carbon-rich solid residue. The process converts biomass into liquid (bio-oil), charcoal, non-condensable gases, acetic acid, acetone, and methanol, by heating the biomass to 750 K in the absence of air. The process can be in favour of the bio-oil, however, the oil produced has low thermal stability and highly corrosive. Lowering the oxygen content and removing alkali by means of catalytic cracking can improve the oil quality [12].

The pyrolysis process consists of a very complex set of reactions involving the formation of radicals. The radicals are very unstable and can undergo secondary reactions like cracking and carbon deposition. The process occurs in five stages:

i. Moisture and some volatile loss.
ii. Breakdown of hemicellulose; emission of CO and CO_2.
iii. Exothermic reaction rises the biomass temperature; emission of methane, hydrogen and ethane.
iv. External heating to the biomass.
v. Complete decomposition occur; bio-oil and charcoal formation.

1.3.3 Gasification

Gasification is a form of pyrolysis (partial oxidation with air or oxygen) carried out at elevated temperatures in order to optimize the gas production. The resulting gas, known as producer gas, is a mixture of CO, H_2, CH_4, CO_2 and N_2 [13]. Biomass gasification is the latest technology used to improve the efficiency and reduce the investment costs of electricity generation by using combined-cycle gas turbine systems. The hot waste gas is recovered to produce steam used in a steam turbine.

To increase the gasification efficiency, steam at high temperatures is used to convert biomass into a clean burning synthesis gas (called as syngas, H_2 and CO in a ratio of 2:1) [14]. In addition to syngas combustion to produce heat or electricity, biomass gasification can be used to produce other organic compounds, such as methanol and ammonia by catalytic conversion of the syngas.

1.3.4 Bioconversion

Plants comprising of high levels of free sugars, such as sugar cane and sweet sorghum, are used as feedstock for biological processes, such as bio-ethanol fermentation, similar to starch crops such as corn and other grains [2, 15]. Fermentation technologies provide additional CCS opportunities. Figure 1.1 illustrates the major routes to biomass-CCS. CO_2 is a byproduct of fermentation in bio-ethanol production, implying that CO_2 available for capture scales with ethanol production and that fuel carbon capture rates scale with conversion efficiency. The retrofit potential of this strategy implies nearly 9MtC yr^{-1} is available at very low capture cost given global bio-ethanol production of approximately 40M m^3 in 2003 [6]. Also, bio-ethanol production generally includes combustion or gasification and combustion of waste biomass, providing further carbon capture opportunities, with additional cost [5].

1.4 Research Interest

In recent years, there has been an increasing interest in the biomass conversion technologies; yet, biomass combustion is with special interest to the researcher as it is a well-established technology that can be applied on a wide range of biomass species. The reason for this interest is the abundance of palm trees in Iraq; the origin country of the researcher. Currently, there are more than 16M palm trees dispersed in the middle and southern parts of Iraq. Annually, 450,000 tons of dry palm leaves are expelled from these trees. The potential of using this enormous amount of biomass in producing energy is evident and needs recognition first from the academic society in the country, and second from the government authorities. Therefore, this study is concerned mainly, about the biomass combustion technology.

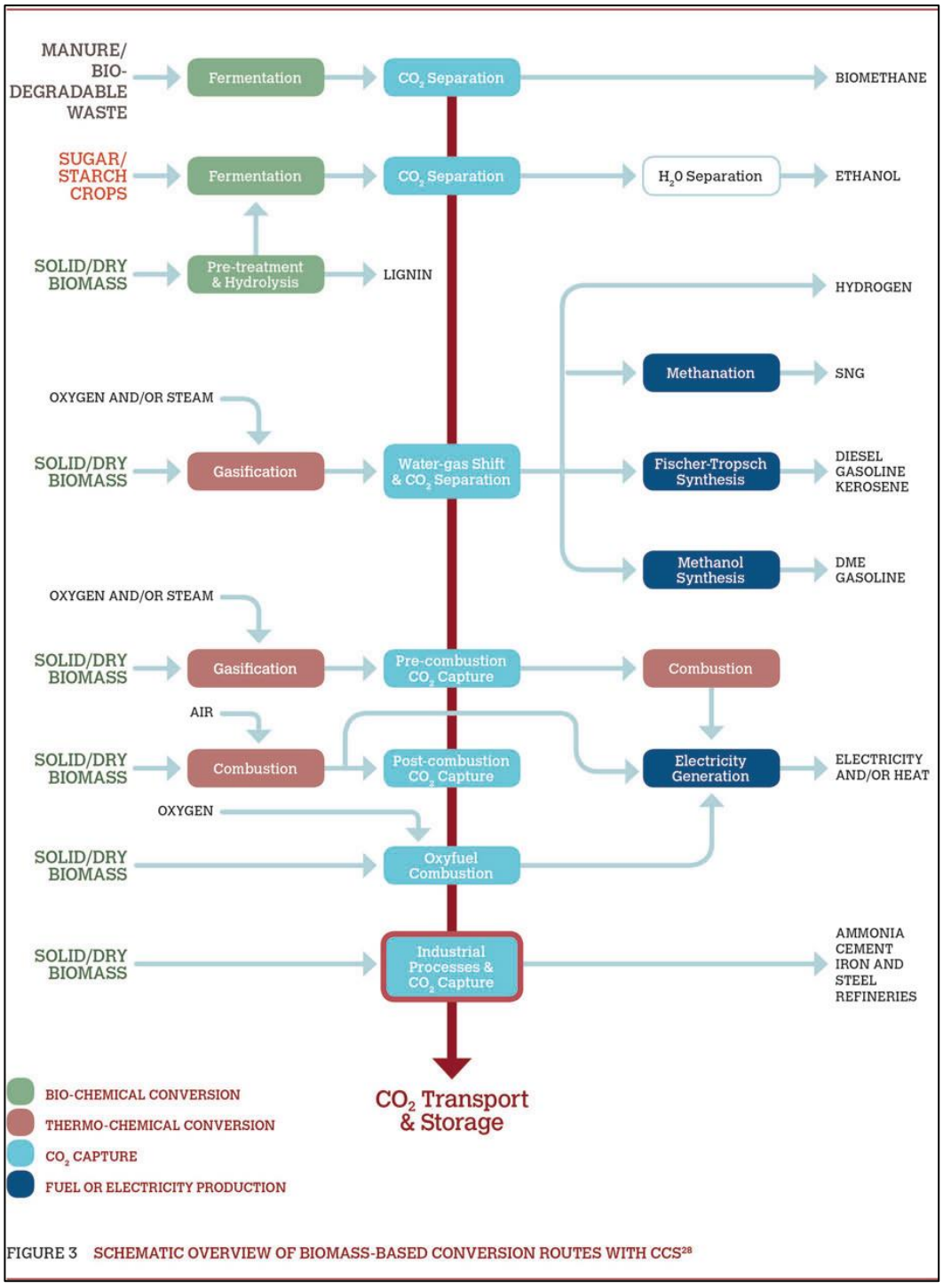

Figure 1.1 Schematic of possible bioenergy with carbon capture routes [6].

1.5 Fuel Selection for this Study

In this research work, the biomass fuel selected for the combustion plant is the white wood pellets. The reasons for this selection are as follows: (i) Wood pellets have a high heat and carbon content and low moisture content compared to other wood forms and biomass species, (ii) Wood pellets are utilized by the large heat and power generation companies in the UK. By far the largest proportion of imported wood pellets to the UK power stations came from Canada (1.72 million tonnes of pellets) in 2012 [16]. This was followed by just over 376,000 tonnes of pellets from the US and much smaller quantities from Portugal, New Zealand, South Africa and Latvia. The Colombian El-Cerrejon coal is widely used in power generation in the UK. Therefore, for the pilot scale experimental combustion work, US white wood pellets (USWWP) and El-Cerrejon coal (ELC) will be used in combustion runs, because these two fuels have the most interest of the power companies. Accordingly, these two fuels are fully characterized in this study.

For comparison, two more fuels are used in the fundamental kinetic study. The Vietnamese coal (VC), a fuel that is rarely studied in the literature, and the Canadian white wood pellets (CAWWP). Due to the highly expensive experiments of the pilot scale combustion, the latter fuels are not tested in the pilot scale. The CAWWP is also used in the techno-economic study, in comparison to three coal types; the US coal, the ELC and the Russian coal.

1.6 Aims & Objectives of the Research Study

There have been many research works on pulverized combustion on a laboratory scale and modelling schemes [17-19]. Other research work was conducted on cofiring biomass with coal on a pilot scale [20-22]. A recent work on the combustion of pelletized energy crops investigated the NO_x emissions in comparison to the EU standards [23]. Other research on wood pellets at $20kW_{th}$ thermoelectric cogeneration system studied the heat transfer and electrical efficiencies [24, 25]. Very few studies compared the wood performance with that of coal [26, 27].

However, to the best knowledge of the author, the study of white wood pellets combustion on a pilot scale and the investigation of ash behaviour and combustion efficiency in the air-fuel and oxy-fuel technologies has not been investigated in the

literature. Correspondingly, the aims of this research work are to explore these topics of research and fill the gap in a useful data to the scientific and industrial interest. The objectives are to answer the following questions:

1. What are the characteristics that distinguish wood pellets from coal in terms of thermal properties, kinetic reactivity, and combustion rate? And, what are the effects of these properties on the wood pellets combustion?
2. What are the differences between wood pellets and coal behaviours during the combustion process on a pilot scale pulverized combustion, in terms of ash behaviour, deposition tendencies, and combustion efficiency?
3. What is the effect of oxy-fuel combustion on the combustion efficiency and burnout of the wood pellets in comparison to the air-fuel case? And, how does this effect vary with the coal?
4. What is the potential future for bioenergy as an alternative to the coal in the power generation industry?

Chapter 2 Literature Review

2.1 Chapter Overview

A considerable amount of literature has been published on biomass characterization and elemental analysis. In addition, a relatively small body of the literature is concerned with the combustion technologies that can be applied to the biomass.

In this chapter, the necessary knowledge on the biomass combustion is established, and the methodologies used for biomass characteristics evaluation are reviewed. Utilizing the published data, a comparison between wood pellets and coal compositions is made to increase the understanding of the wood pellets characteristics as an alternative fuel to coal. In addition, the combustion technologies available for biomass and the operational parameters that affect the process efficiency are identified.

In addition to the comparison with the results of this study for validation, parts of the data collected in this literature review are employed to serve in a novel way two purposes; First, the prediction of the missing data of the biomass under study that is difficult to obtain experimentally, by generating a mathematical model as shown in Chapter 4, Section 4.4. Secondly, to examine the results of the model used to calculate the intrinsic reactivity parameters as shown in Chapter 5, Section 5.5.8.

2.2 Biomass Structure

The study of thermal behaviour of biomass is important to predict the quality of devolatilization products in the pyrolysis and combustion processes. Natural biomass structure is consistent of three major compounds cellulose, hemicellulose, and lignin with small portion of extractive oils and proteins and mineral matter [11]. Cellulose is the main component of the cell wall of the plants. It comprises about 40-50% of wood and about 90% of the cotton fibres, a polysaccharide consisting of a linear chain of 7000-15,000 anhydrous β(1→4) linked D-glucose units with a formula of $(C_6H_{10}O_5)_n$ [28]. Wood cellulose has a degree of polymerization of up to 10,000 units. The multiple hydroxyl groups of a chain form hydrogen bonds with oxygen atoms on the same or on a neighbouring chain, holding the chains together and forming *micro*

fibrils with high ductile property [29]. The degree of polymerization (DP) and the location of hydrogen bonds determines the properties of cellulosic species.

Hemicellulose is also a chain of glucose units, however it is branched by hetropolymers of D-pentose sugars mainly xylose, galactose, mannose and arabinose. Unlike cellulose, hemicelluloses have lower DP (only 50-300) and are basically amorphous [30]. Hemicellulose comprises 28-32% wt. of wood.

Whereas lignin is an aromatic complex of cross-linked phenolic polymers supporting the cell wall and varies from one species to another according to the various polymer constituents in it. Lignin constitutes 20-35% of the dry mass of wood and responsible for the aroma of smoke during pyrolysis of wood.

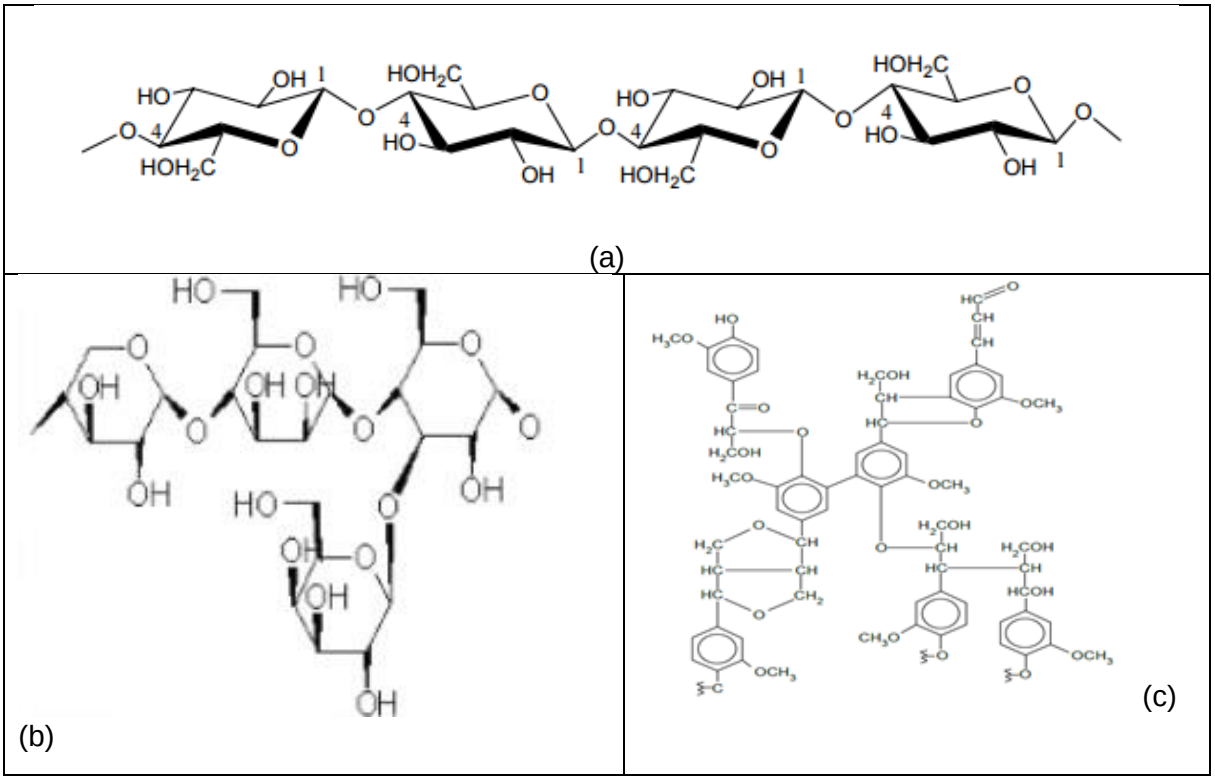

Figure 2.1 Structure of biomass constituents: (a) cellulose, (b) hemicellulose, and (c) lignin [31].

2.3 Biomass Fuel Properties for Combustion

Biomass combustion is a complex chemical reaction coupled with heat and mass transfer, and fluid flow mechanisms [2]. For the design purpose and control of the combustion process, fuel properties must be identified, and the manner that these

properties impact the outcomes of the combustion process. Moisture content in the biomass affects the ignition temperature of fuel. Heavy metals could cause ash deposition. Whilst light gases in the combustion chamber can impact the radiative property of the atmosphere. The prediction of environmental pollutant gases, such as NO_x and SO_x, requires N and S measurement. Also, ash composition is imperative in the prediction of fouling and slagging occurrence during the combustion process.

Historically, alkali, chlorides, sulphates, carbonates and silicates content define the ash quality for deposition prediction. All these properties in addition to the thermal properties of the fuel assist in the design and scale up calculations. Jenkins et al. [2] have listed the standard methods to measure these properties. However, the British Standards Institute (BSI) has recently approved the final standard methods for solid biofuel characterization (BS EN ISO 17225) [32] and those will be followed in this study.

A wide range of biomass varieties have been investigated for fuel properties [2-4, 33-37] such as wood, wood waste, herbaceous species, bagasse, grass, industrial residues, sawdust, waste paper, municipal solid waste, food waste, algae and animal waste [4]. These research data are used for comparison with the results of this study whenever it is possible. Fuel combustion properties of biomass can be grouped into physical, thermal, and chemical properties [3]. Table 2.1 presents a list of the conventional properties of biomass fuels required for the combustion applicability evaluation.

Table 2.1 Conventional fuel properties for combustion process design.

Property	**Description**
Physical properties	Density, bulk density, particle size, char surface area per unit volume, char porosity, and color
Chemical Properties	Ultimate analysis (C, H, O, N, S), Proximate analysis (analysis of pyrolysis products) Higher heating value (calorific value)
Ash composition analysis	Mineral and trace elements content
Thermal Properties	Specific heat of wood and char, Thermal conductivity of wood and char, Ash fusion temperature

2.4 Fuel Properties of Wood

Wood and wood waste have gained the most interest among other varieties in the biomass combustion industry for their low ash, nitrogen and sulphur content and for their global renewable abundance [2, 3, 34]. Therefore, the fuel properties of wood are particularly reviewed.

2.4.1 Physical Properties

In general, wood biomass differs from coal in many physical, thermal and chemical properties. Physically, wood has a lower density than coal (oven dry basis 300-550 kg m^{-3} for wood and 1300 kg m^{-3} for coal) [3]. Also, fresh, green wood has a moisture content of 35-60%, whereas dried wood typically has 2.5-20% moisture content [3, 4]. The bulk density, particle size, and shape distribution of the pulverized wood is related to the preparation technology of that fuel. These physical properties in addition to the porosity and the internal surface area of wood char, are required for modelling of pulverized wood combustion. The particle size of biomass fuel is critical to understand the reactivity of the fuel during the combustion process and the flowability inside the feeder and the furnace.

The bulk density of the solid biomass fuels with the net calorific value (NCV) identify the energy density of the fuel, that is defined as the energy produced by one normal cubic meter of the biomass fuel (MJ m^{-3}). The energy density influences the fuel-feeding rate and the process control on the feeding system. The higher is the bulk density of the fuel, the lower is the flowability and more blockage possibly occur in the feeding hopper [38].

The porosity and internal surface area of the wood char are required for detailed modelling of pulverized wood combustion. These two characteristics are essential parameters to calculate the char oxidation reactivity. The reactivity of the charcoal obtained from the wood pyrolysis is affected by the pyrolysis conditions of the biomass particles, such as the heating rate and the residence time [39]. Although many researchers have studied the reactivity of the biomass, few of them have reported the wood and char porosity and surface area measurement. Ragland et al. [3] have investigated the physical and thermal properties of the dry wood and bark, and they have recorded the internal surface area of wood char to be the order of 10^6 m^2 kg^{-1}, and its porosity as 0.8-0.9. Mermoud et al. [39] studied the reactivity of beech wood char

particles and found the porosity to be 0.73 for 10 mm long wood particles. Another study on entrained-flow biomass particle combustion that has been performed by Hong Lu et al. [40], investigated poplar particles char reactivity via a spherical-equivalent particle diameter model to measure the thermal properties of the particle combustion. They reported the specific surface area of the biomass and the char as $9.04x10^4$ and $1.0\ x10^6\ m^2\ m^{-3}$, respectively, and the sawdust porosity to be 0.4. Also, Teixeira et al. [13] measured the wood pellets char bed properties in a fixed bed gasifier, and they found the porosity to be 0.51. The common ranges of the physical properties of wood and coal are listed in Table 2.2.

Table 2.2 Physical properties of wood and coal fuels [3, 4, 33, 41, 42].

Property	Wood	Coal
Density (kg m^{-3})	300 – 500	~1300
Bulk density (kg m^{-3})	157-227	640-930
Moisture content (wt%)	35-60	2- 10
Particle size	~ 3 mm	~ 100 µm
Char porosity	0.8-0.9	0.54
Internal surface area, $m^2\ kg^{-1}$	10^6	$1.8\ -3.1*10^5$
Color	variable	Black

2.4.2 Chemical Composition

A reasonable amount of data on the wood chemical properties is available in the literature. For comparison, many researchers have listed equivalent coal data to wood composition analysis [1, 2, 4, 33, 34]. The comparison of wood properties with coal has assisted the investigators in evaluating the energy value of wood as an alternative feedstock in power generation plants. Other researchers have analysed wood feedstock in various forms such as chips, barks, pellets and pulverized to provide data for the design and modelling of the combustion units [3, 13, 19, 23, 24, 36, 43-46].

Jenkins et al. [2] studied the chemical composition of wood and the impact of certain composition elements on fouling, corrosion, pollutant emissions, and on the prediction of the rate of reaction for the design purposes. Their work on wood fuel blends for power plants, willow wood, hybrid poplar, and 16 other biomass species in comparison

with two types of coal, showed that wood is highly oxygenated with respect to coal; 40-50% oxygen of dry weight basis. Further, carbon is the substantial constituent of wood, comprising 47-51% of dry matter. The third organic component of wood is hydrogen with 5-6% dry matter.

Vassilev et al. [1] have extensively investigated the chemical composition of 86 varieties of biomass to determine the fuel properties compared to coal. They found a high variation in chemical composition of different biomass varieties. In general, the abundance of elements in biomass in decreasing order was found to be: C, O, H, N, Ca, K, Si, Mg, Al, S, Fe, P, Cl, Na, Mn, and Ti. Whereas, coal is abundant with C, Si, and Al in addition to higher ash content. Similar conclusions have been presented by Jenkins et al. [2] and Demirbas [4].

The chemical composition data of certain wood and coal varieties are given in Table 2.3. It can be seen from the table that the proximate analysis of wood on dry basis samples exhibits a range of 54-85% volatile matter, 0.4-3.2% ash and 12-40% fixed carbon. In general., the soft wood species (pine, cypress, fir, larch, and spruce) have higher volatile matter than hard wood (aspen, beech, birch, oak, olive, poplar, and willow) [3]. The ultimate analysis dry ash-free weight basis shows that wood has a carbon content of 47-55%, 40-47% oxygen, and 6% hydrogen, while coal has 60-83% dry weight carbon, less than 20% oxygen content, and about 6% H. Further, the nitrogen content in wood is much lower compared to coal. Coal has 1-5% dry ash-free nitrogen, while wood nitrogen content is less than 1%. Sulphur and chlorine, were found in wood biomass with less than 0.1%.

In summary, relative to coal, wood and woody biomass have higher moisture, volatile and oxygen content while the ultimate analysis shows lower carbon, nitrogen, sulphur, and much lower ash content (<3% in biomass and up to 30% in coal). However, both biomass and coal have about the same hydrogen content of 5-6% dry-ash free content.

2.4.2.1 Ash Composition

From the data in Table 2.3, wood produces about 2% ash after combustion. Despite this low percentage, the ash deposition on the heat transfer surfaces in the boilers and inside the furnaces still occur. Therefore, there is a need to investigate the wood ash composition to predict the effects of the deposition problem. The wood ash is typically used in agricultural applications due to its high alkaline and earth alkali contents [47]. However, the interest of wood ash comprehensive characterization started when the

environmental regulations of the soil pollutants were becoming more compulsory and more interest in the use of wood combustion in the industrial boilers of the thermal power plants. Many researchers have investigated the wood ash composition since then [47-52].

Campbell, [47] studied the temperature dependence of ash yield and composition. He found that the ash yield decreased by 45% when the combustion temperature increased from 823 to 1366 K, with a decrease of K, Na, Zn and carbonate content in the ash.

An extensive overview of the phase-mineral and origin of constituents of 86 biomass varieties ash was published by Vassilev et al. [52]. Interestingly, they classified three phases of ash composition according to the origin and occurrence of mineral compounds. The three groups of mineral compounds were; (i) Si-Al-Fe-Na-Ti as glass, silicates and hydroxides, (ii) Ca-Mg-Mn mainly carbonates, silicates and some phosphate and sulphates, and (iii) K-P-S-Cl normally phosphates, sulphates, and chlorides.

General ash composition of biomass and coal varieties is listed in Table 2.4. The data in Table 2.4 clearly shows that the enrichment of biomass in alkali and earth alkaline metals, such as calcium, potassium, magnesium and phosphorus in comparison to coal. Most wood species are depleted in silica compared to coal, except oak wood in which the silica content was 49% of the ash, analogous to 54-56% of coal ash. Furthermore, wood is mostly depleted in sulphate, aluminate, and titanium dioxide.

2.4.3 Calorific Value

The energy content of combustion fuels is usually measured by the heating value or calorific value [2] of the fuel. The heating value can be expressed in two measures, the gross or higher calorific value (GCV) in which the enthalpy change of combustion at constant pressure is calculated with water condensed at the reference temperature. And, the lower or net calorific value (NCV) represents the enthalpy change of combustion at constant pressure with water in the vapour phase [2-4]. The BS EN14918-2009 standard method is used to measure the GCV using a bomb calorimeter. When the combustion is carried out in a combustion bomb at a constant volume, the higher heating value is the specific energy of combustion, in joules, per unit mass of the biomass burned with water condensed. The amount of energy produced from the sample combustion increases the temperature of the calorimeter

and a certain amount of water. Therefore, the corrected temperature increase is the total observed temperature increase considering the heat exchange with the equipment.

In the literature, there are few mathematical expressions employed to calculate the GCV. Demirbas [53] developed a formula to calculate the higher heating value of biomass (lignocellulosic materials) that is dependent on the ultimate analysis of biomass summing the oxidation heat of C, H, the reduction heat of O, and the negative of N oxidation values:

$$GCV_{\mathrm{daf}}=\left(33.5[\mathrm{C}]+142.3[\mathrm{H}]-15.4[\mathrm{O}]-14.5[\mathrm{N}]\right)\times 10^{-2} \quad (2.1)$$

where,

GCV_{daf}: gross calorific value in MJ kg^{-1} fuel in dry ash-free basis

Another empirical formula that was developed by Channiwala & Parikh [54], recommended elsewhere [55], and used by Musinguzi et al. [56] accounts for the ash content in addition to the essential elements as follows:

$$GCV_{\mathrm{db}}=0.3491.X_{\mathrm{C}}+1.1783.X_{\mathrm{H}}+0.1005.X_{\mathrm{S}}-0.0151.X_{\mathrm{N}}-0.1034X_{\mathrm{O}}-0.0211X_{\mathrm{ash}} \quad (2.2)$$

where,

GCV_{db}: gross calorific value in MJ kg^{-1} fuel in dry basis

X_i : is the fraction of C, H, S, N, O, and ash in wt% (db).

As it can be seen from Eq. (2.2), the C, H and S contents contribute positively to the value of GCV, while the contents of O, N, and ash contribute negatively to the GCV.

The average GCV of soft wood is 20-22 MJ kg^{-1}, and the hard wood 19-21 MJ kg^{-1} [53, 55]. The lower heating value NCV for 30% moisture wood chips is 12.5 MJ kg^{-1}, while oven dried solid wood has 19 MJ kg^{-1} NCV [57].

2.4.4 Burning Profile

The burning profile of biomass fuels is important in the study of the fuel reactivity in terms of flame characteristics and stability in the combustion process [4, 46]. These characteristics are essential in the modelling of the combustion boilers. The burning profile can be obtained from thermogravimetric analysis (TGA) of a sample of that fuel. A plot of the rate of weight loss against temperature while burning a sample up to 1073 K is referred, to as the burning profile. The first peak on the burning profile is related to the moisture release. The most important characteristic temperature of a burning profile is the Ignition Temperature and Peak Temperature [58]. The *ignition temperature*

corresponds to the temperature at which a sudden rise in weight loss occurs. The temperature at which the maximum weight loss occurs is the *peak temperature*, and this is a measure of the fuel reactivity. The peak temperature of wood varies from 560 to 575 K [4]. The rate of weight loss at the peak temperature is called the maximum weight loss rate. Figure 2.2 illustrates the rate of weight loss of white wood pellets with temperature K. The derivative of thermogravimetric profile (DTG) shows the peak at which the maximum reaction rate occurs.

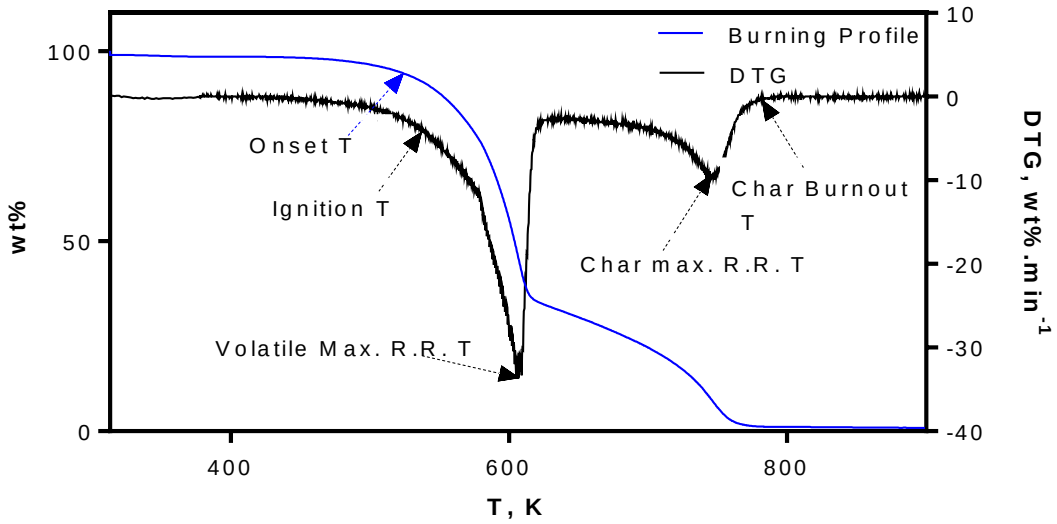

Figure 2.2 Characteristic Burning profile of a biomass substance (example from this work).

Table 2.3 Chemical composition of wood biomass and coal fuels given in the literature.

Type of Fuel	HHV, MJ/kg	Moist. Wt.%	Proximate Analysis[a], wt.%			Ultimate Analysis[b] wt.%						Ref.
Soft Wood			**Ash**	**VM**	**FC**	**C**	**H**	**O**	**N**	**S**	**Cl**	
Pine wood	20.56	5.00	0.90	81.90	17.20	52.77	5.85	41.27	0.20	0.00	-	[59]
Pine wood chips		2.5				50.0	5.57	44.2	0.1	0.10	0.04	[33]
Spruce wood		-	1.7	80.2	18.1	52.8	6.2	41.6	0.3		-	[3]
Swedish Wood		7.8	0.2	84.1	15.7	49.6	6.1	44.0	0.1	0.06	0.01	[60]
Fir wood	21.05		0.80	81.50	17.70	52.72	6.35	40.83	0.10	0.02	-	[61, 62]
Fir wood pellets	17.79	6.50	0.30	85.10	14.60					0.30		[63]
Spruce pellets	18-19	5.0-9.0	0.2-0.45						0.00-0.22	0.00-0.01	0.0- 50 ppm	[63]
White w. pellets	19-20	7.0-8.5	0.1-0.64	81-82	17.0-18.39	47-50	6- 7	43-46	0.08-0.15	0.01	30- 250 ppm	[63]
Hard Wood												
Oak wood		6.5	0.5	77.6	21.9	50.3	6.0	42.6	0.3		0.004	[4]
White Oak		-	1.5	81.3	17.2	50.2	5.5	43.8	0.4	-		[34]
Beech wood		-	0.5	82.5	17.0	49.8	6.3	41.4	0.5			[4]
Beech w. chips		-	0.8	82.0	17.2	47.2	6.1	46.6	0.1	0.01	0.01	[52]
Poplar Hybrid	19.02	-	2.7	84.81	12.49	50.2	6.06	40.4	0.6	0.02	0.01	[2]
Wood chips		15.3	2.0	83.89	14.04	50	6.0	42.0	0.6	0.1	-	[36]
Olive wood[c]		-	3.2	79.6	17.2	48.9	5.4	44.8	0.7	0.03	-	[35, 51]
Willow wood	19.59		1.71	82.22	16.07	49.90	5.90	41.80	0.61	0.07	<0.01	[2]
Coal												
UK Bitt. Coal		3.06	9.97								0.003	[64]
Russian Coal	27.29	10.65	15.67	33.42	50.90	60.36	4.50	8.35	1.84	0.30	0.0005	[36]
US Appl. Low Sulphur Coal	30.42	5.630	9.79	34.23	56.16	71.74	4.62	6.09	1.42	0.6400	7.000e-2	[65, 66]
Colombian Coal	32.0	3.09	1.39	36.79	58.73	78.72	5.18	9.71	1.52	0.39	0.000226	[64]
Bituminous coal			15.70	30.00	54.30	83.1	5.00	9.50	1.30	1.10	0.04	[1]
a: Dry basis. b: Dry, ash-free basis. c: value is average of two ref.												

Table 2.4 Ash composition of various wood and coal types.

Type of Fuel	Ash Composition, wt.%											Ref.
Wood	SiO_2	CaO	K_2O	P_2O_5	Al_2O_3	MgO	Fe_2O_3	SO_3	Na_2O	TiO_2	MnO	
Oak wood	49.0	17.50	9.50	1.80	9.5	1.10	8.50	2.60	0.50	-		[4]
Beech wood	12.33	67.80	2.95	2.29	0.12	11.43	1.09	0.80	0.89	0.10		[4]
Beech w. chips	12.33	67.80	2.50	2.29	0.12	11.43	1.09	0.80	0.89	0.10	0.40	[52]
Willow wood	2.35	41.20	15.00	7.40	1.41	2.47	0.73	1.83	0.94	0.05		[2]
Poplar Hybrid	5.90	49.92	9.64	1.34	0.84	18.40	1.40	2.04	0.13	0.30		[2]
Wood chips	25.00	44.70	6.70	3.60	4.60	4.80	2.30	1.90	0.60	-		[67]
Olive wood	8.1	32.8	19.9	8.5	1.6	2.4	0.70	2.1	2.9	0.1	0.10	[35]
Swedish Wood	23.15	30.49	9.46	2.37	4.69	5.93	2.67	4.04	2.10	0.98	4.61	[60]
Coal												
UK Bitt. Coal	37.81	3.37	1.98	0.243	23.55	1.657	19.67	4.433	2.094	0.800		[64]
Colombian Coal	47.8	1.20	0.060	0.110	41.40	1.20	8.70	2.60	0.580	0.610		[64]
Russian Coal	63.35	1.5	2.18	0.444	23.07	1.386	5.75	0.058	0.35	0.995		[36]
US Appl. Coal	46.20	3.40	1.500	0.600	27.70	0.800	17.20	1.10	0.500	1.000		[65]

a: ppm. b: wt.%

2.5 Fundamentals of the Solid Particle Combustion

The combustion of solid fuel particles is a complex series of sequential and simultaneous reactions that can be classified in two major steps. The first step is the devolatilization of hydrocarbons and oxygen radicals (pyrolysis), supplemented by a large change in the particle structure. The second step is the combustion of the solid porous residue (char) generated in the first step [68, 69]. In the literature, the kinetics of these two steps have been expressed by different mathematical models that were based on the suggested reaction mechanisms.

2.5.1 Devolatilization Mechanism

Researchers have examined the biomass devolatilization products and many have developed reactivity models to calculate the kinetic parameters based on the three components classification (cellulose, hemicellulose and lignin). Ghetti et al. [70] compared the thermal behaviour of various biomass species with standard cellulose and lignin substances to distinguish the DTG peaks that appear in the pyrolysis profile. They found that devolatilization of biomass starts at 473 K and 90% of volatile matter is released before 723 K. Also, they found that pure cellulose decomposes between 533-700 K with a peak rate at 623 K, and pure lignin started to decompose at 473 K and ended at 823 K with a peak rate at 793 K. Similar results were found by Conesa et al. [71]. Bennadji et al. [72] observed a narrower range of devolatilization temperatures for pine and poplar wood at a temperature between 473 K to 673 K.

Biomass pyrolysis was described to a certain acceptable extent by a global irreversible first-order reaction, and the devolatilization rate is only a function of the temperature [73-75]. In general, the kinetics of solid fuel thermal decomposition (pyrolysis) is traditionally expressed by an n-power reaction rate law with a rate constant of the Arrhenius form [76]. Nevertheless, the assumption of a single reaction rate has been questioned by many researchers [77-80] as pyrolysis is a complex reaction that depends on the devolatilization conditions, amount of sample and the heating rates. Hence, the reaction can be demonstrated by more than one step and combines various species reactions. Agrawal [81] and Conesa et al. [71] found that the model proposed by Kilzer and Broido [82] (KBM) of wood pyrolysis had the best fitting with the TGA experimental data. The KBM assumes a sequence of reaction steps starting with the

formation of anhydrocellulose (Ce*) and tar then the intermediate Ce* decomposes into volatiles and char as follows:

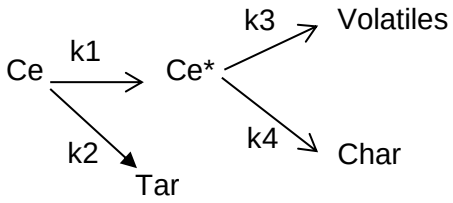

Diebold [83] suggested a more complex reaction pattern in which two reactions compete in the first step to produce a condensed phase of active cellulose and char plus water. Then the intermediate active cellulose can be cracked by three possible reactions; (a) to produce secondary gases, (b) primary vapours that form gases or tars in a further step, or (c) to char. However, this model failed to reproduce the peaks in the DTG curves and the variance of the char peaks among the diverse types of wood.

Mania et al. [84], Branca et al. [85], and Martin-Lara et al. [86] assumed three parallel non-interactive decomposition reactions of the three components (cellulose, hemicellulose and lignin) in sugarcane bagasse and waste wood with a first-order model for hemicellulose and cellulose, and a third-order model for lignin as follows:

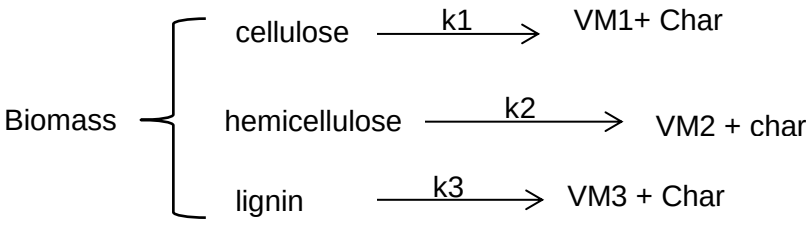

However, lignin decomposes at a wide range of temperatures that overlap with the other components [87].

Similar to biomass, the kinetics of the coal thermal decomposition (pyrolysis) is traditionally expressed by an n-power reaction rate law with a rate constant of the Arrhenius form [76].

2.5.2 Char Combustion Reactivity

In the combustion and gasification processes of coal and biomass fuels, the char reactivity is an imperative parameter in the simulation and process design due to the major contribution of the char oxidation to the heat value of the fuel. Lignocellulosic chars are produced after a rapid release of volatiles at relatively low temperatures (473 – 773 K) [11]. On further heating of the char, two discrete exothermic combustion steps occur, the aliphatic and aromatic compounds combustion.

The carbon content is usually a measure of the coal rank. The rank increases with an increase in the carbon percent and a decrease in the volatile matter, hydrogen, oxygen and moisture content. Researchers have noticed that there is an inverse correlation between the coal rank and the char reactivity, the higher rank (higher carbon content) has less reactivity [88, 89]. Higher coal rank contains more polynuclear aromatic structures than aliphatic and hydroaromatic forms [90]. The coal structure tends to approach the pure graphite structure, and therefore the higher carbon content in the coal elucidates more graphitization which results into reduced porosity and lower reactivity. Lower rank coals have higher porosity, concentration of carbon edges, mineral matter, and oxygen. Hence, char reactivity increases as the rank of the parent coal decreases [91].

The reactivity of a char depends on three elements; Concentration of edge carbon atoms and dislocations, 2-mineral matter and trace elements, 3- oxygen and hydrogen content. The overall reactivity depends on the three chemical properties in addition to the porosity [90, 92].

2.5.2.1 Effect of the Mineral Content on Char Reactivity

Minerals and trace elements in coal transform to ash during pyrolysis or combustion, in the form of metal oxides or silica, or carbonates. The mineral impurities promote permanent dislocations even at elevated temperature. During heating, the inorganic impurities, diffuse and concentrate on the crystallite edges and dislocations. Mineral matter and trace elements can provide direct catalytic activity to the surface. It was found that mineral oxides, particularly Fe_2O_3 , CaO, and MgO that are present in the char enhances the char reactivity by two orders of magnitude [90]. Also, surface impurities can be catalyst to the secondary homogeneous reactions such as the gas-water shift $CO + H_2O \rightarrow CO_2 + H_2$.

The effect of inorganic constituents on char reactivity varies with coal rank. The reactivity of lignite is highly influenced by the presence of cat-ions, whereas bituminous coals char's reactivity is not significantly influenced by inherent minerals in the char.

Catalytic reactivity of minerals increases with burn off, and certain forms of minerals such as Fe, have more effect than Fe_3O_4, small inclusions than large inclusions, and distribution of mineral atoms on the carbon surface. Therefore, trace elements have a significant effect on the char reactivity.

2.5.2.2 Hydrogen and oxygen effect on char reactivity

The char varies in its hydrogen and oxygen content. During pyrolysis, the carbon concentration increases and the hydrogen decreases with the treatment temperature [93]. Oxygen and hydrogen increase carbon reactivity, as chemisorption of non-aromatic sites is favoured more than the aromatic sites [90]. The oxygen groups particularly the carbonyl and heterocyclic aromatics increase the reactivity via electron exchange, whereas hydrogen promotes carbon reactivity by preferential oxidation of hydrogen rich sites producing more promising carbon sites of high reactivity.

2.5.2.3 Effect of Pyrolysis Conditions on the Char Reactivity

In addition to the fuel composition, char reactivity also depends on the preparation conditions i.e. heating rate, final pyrolysis temperature, and the residence time of the pyrolysis step [89, 94]. High heating rates during pyrolysis corresponds to rapid volatile escape and less tar re-polymerization on the char surface. Fuels with higher porosity develop mainly micro and mesoporous chars. In addition, higher concentration of active sites and higher hydrogen and oxygen content are found in favour of less re-polymerization. In contrast, reduced heating rates decrease the reactivity due to; (a) favourable thermal annealing conditions, and (b) slow devolatilization results into less porosity and more tar deposition [90].

Pyrolysis at low temperatures increases the macropores size and decreases the micro and mesoporous due to re-polymerization, particularly for plasticizing bituminous coals (high volatile matter content), and therefore increases the porosity of the char. The surface area increases in the pyrolysis due to chemisorption reaching smaller pores and then increases the diffusivity. While at higher pyrolysis temperatures the structural carbon crystallization increases, thus resulting in a lower concentration of the active

sites and internal surface area [92, 94]. Such conclusions were reached for anthracite coal due to graphitization [95], and for sub-bituminous coal [96] due to microporous blockage. Also, the char density increases with the increase of the heat-treatment temperature [93].

2.5.3 Thermal Analysis of the Solid Particles

The scientific research on characterization, chemical and thermal analysis of coal has been widely investigated in the literature. When biomass was used as an alternative fuel, scientists applied the same techniques and methodologies of characterization and kinetic mechanisms of coal on biomass with some variations in the reactivity modelling and compositional classification.

In TGA, a few milligrams of solid substance are placed in a furnace to be heated under an inert or oxidizing atmosphere with the weight monitored by an electronic balance as a function of the temperature and time. The first derivative of the weight loss curve is called the derivative thermogravimetric (DTG), and it is used to determine the maximum reaction rate [11].

The main advantage of the TGA experiments is the controlled conditions (temperature and pressure), repeatability and the study of a suite of samples under the same conditions in comparative studies. In addition, the small sample size gives the best heat transfer and thus reliable weight loss data for the calculations of the kinetic parameters. In terms of the kinetics parameters, the TGA technique is a direct method to measure the reaction order from the data of the weight loss against temperature and time, and this eliminates the uncertainty in extracting parameters from the transport models [97].

On the other hand, the disadvantage is the risk of extrapolating the kinetic parameters of low heating rates at moderate temperatures to higher temperature kinetics with enormously fast heating rates.

Traditionally, kinetic data of solid-state reactions were obtained from isothermal conditions where experiments were performed under constant temperature and repeated at different temperatures. However, this method cannot predict reactivity before or after the selected temperature of experiment. On the contrary, the non-isothermal techniques have been proven to be more efficient to examine the whole region of the temperatures under investigation [11]. Even though, the high sensitivity to

the noise in experimental data and inconsistency with the kinetic theory principle of homogeneous reactions made the non-isothermal methods also questionable. In order to improve the results of non-isothermal data, multiple sets of data under different heating rates were suggested [98].

TGA data of biomass and coal has been extensively used to study the solid-phase reactivity [76, 99-105]. Still, the intrinsic reactivity of biomass char combustion in comparison to coal has not gained enough interest and investigations in the literature. The intrinsic reaction rate is the reaction rate per unit surface area of the internal or external pore surface area where there is no heat or mass transfer limitations [106]. Also, the effect of the ash content on the pore surface area is not intensively highlighted in the research work [107]. Thus, part of the experimental work in this study aims to evaluate the thermal behaviour of biomass devolatilization, reactivity of the char combustion in comparison to coal and to describe the intrinsic kinetic parameters based on the specific surface area of the char pores. In addition, the effect of char preparation conditions, parent fuel composition, and ash content on the kinetic parameters will be investigated.

2.6 Pulverized Fuel Combustion Technology

Biomass fuels can be used in three well established combustion technologies, mainly spreader stoker (pulverized combustion), mass burn grate and fluidized bed combustion (FBC) [108]. This study puts emphasis on the pulverized biomass combustion technology. The reasons for this consideration are, first there is a considerable interest in reducing the carbon footprint of pulverized coal power plants through the replacement by or cofiring with biomass as it is considered a neutral carbon emission fuel. Secondly, the pulverized combustion method provides the highest heat transfer rate among other combustion technologies (0.1 – 1 MW m^{-2}) [55]. In addition, there is not sufficient experimental data on pulverized biomass combustion for modelling validation, and, moreover, the experimental work of this study will be applied on a pilot scale pulverised fuel combustion rig.

In pulverized fuel (PF) combustion, the fuel particles are small enough to be transported with the primary combustion air (diameter smaller than 2 mm) [45] to the furnace. The start-up of the furnace is achieved by an auxiliary burner using natural gas. When the furnace temperature reaches a certain value then the biomass is

injected and the gas burner is turned off. Due to the dust-explosion nature of the fine fuel particles, feeding the fuel into the furnace requires a highly-controlled system. Fuel/air mixtures are usually injected tangentially into the cylindrical furnace to establish a rotational flow (usually a vortex flow). The furnace is shielded with water-cooled jacket to control the elevated temperature of the furnace walls. The fuel gasification and char oxidation occur simultaneously because of the small particle size. Thus, a continuous fuel load can be easily controlled.

2.7 Limiting Factors of Biomass Combustion

2.7.1 Fuel Composition Impact on the Heating Value

The standard measure of the energy content of a fuel is its heating value. The GCV of biomass fuels usually varies between 18 and 22 MJ kg^{-1} (db) [55] and the lower values refers to herbaceous fuels, and the higher ones to the fresh wood and bark. The fuel characteristics such as moisture, carbon content, oxygen and hydrocarbons contents are limiting factors to the wood heating value [2, 34].

2.7.1.1 Moisture Content

The moisture content impacts the combustion behaviour, the adiabatic temperature of combustion and the yield of flue gas per unit energy of the fuel. The moisture content reduces the heating value in comparison to dry weight basis, and this is due to the endothermic evaporation of water molecules from the fuel particles. Every 10% increase in the moisture content reduces the fuel heating value by about 2 MJ kg^{-1} [34]. The maximum limit for the moisture content in wood combustion is 60%, after that self-supporting combustion will not occur and supplemental fuel, such as natural gas, is added [2]. At a moisture content of 50-55%, incomplete combustion products, such as CO, may be emitted in greater amounts. Therefore, a longer residence time and a larger furnace chamber are required [55]. However, if combustion takes place at high pressures, the dew point increases and the latent heat recovered at useful temperatures for more efficient power generation [34]. Ultimately, the combustion efficiency decreases with the increase of the moisture content of the fuel. These parameters are taken into consideration in the optimization of the temperature control system. In general., the moisture content of woody biomass ranges from 2-25% [3] that requires more energy for the drying stage of the fuel combustion. To avoid this

negative impact, pelletized wood fuel is now commonly used for domestic heating stoves and the power generation companies after milling the pellets to 1 mm maximum diameter. The moisture content of the wood pellets is not higher than 10% of the pressed pellet weight.

2.7.1.2 Relevance of Atomic O, C, H and Volatiles

From Table 2.3, it is observed that C, O, and H are the main components of the biomass fuels. The organically bound O is released during the thermal decomposition of the biomass fuel partially contributing to the oxidation reactions of other fuel components. Carbon and hydrogen are oxidized during the combustion process by exothermic reactions. Therefore, the heating value is correlated to the carbon and hydrogen contents in the fuel. Compared to coal, the lower carbon content of wood reduces the higher heating value by 30-40% from that of coal. Jenkins et al. [2] measured a 0.39 MJ kg^{-1} increase for each 1% increase in carbon content of wood and wood pyrolysis products. In addition, the degree of oxidation of the HC in the biomass affects the heating value. Part of the fuel carbon is present in highly oxidized forms (cellulose, hemicellulose) that moderate the oxidation reactions and ultimately decrease the GCV of the biomass compared to the coal [55]. On the other hand, the lignin content of the biomass fuel has a lower degree of oxidation than cellulose and therefore requires more oxygen for combustion and this results in a higher heating value than for cellulose [2]. The higher hydrogen to carbon ratio, the higher is the weight loss of the fuel during pyrolysis (formation of CH_4). This explains the difference between coal and biomass burning profiles. For example, anthracite can lose 10% and bituminous coal loses 5-65% of their weight during pyrolysis, while biomass can lose 90% of its weight during this first stage of combustion [2].

The volatile components in the woody biomass usually vary between 70-85% dry basis (see Table 2.3). Due to this high volatile matter content, the major part of the fuel is vaporized before the homogeneous gas phase oxidation reaction takes place, then the remaining char undergoes a heterogeneous oxidation. Therefore, the volatile content heavily affects the combustion behaviour of the biomass.

2.7.2 Pollutant Emissions

Wood contains nitrogen, sulphur, and chlorine with low concentrations in comparison to fossil fuels. Still, considerable pollutant emissions are derived from those three

elements, in addition to the hydrocarbons produced from incomplete combustion. The pollutants known for wood/biomass combustion are produced from either complete or incomplete combustion and they are mainly the following:

2.7.2.1 Carbon Oxides (CO_x)

The carbon content in the fuel is the major source of the CO_2 gas in the complete combustion of biomass. However, biomass fuels are considered carbon-neutral in respect to the GHG emissions [6, 15, 55]. While carbon monoxide (CO), is an intermediate product that can be oxidized to CO_2 if oxygen is available, or released with the flue gases. The rate at which CO is oxidized to CO_2 depends primarily on temperature. In the industrial biomass combustion, the presence of CO in the flue gas is an indication of the combustion efficiency, and optimization of the combustion process can be achieved through the excess air ratio. Nussbaumer [109], studied the CO emissions of different biomass furnaces as a function of the excess air ratio, and he found that the minimum CO emission in ppm is obtained at excess air ratios between 1.1 and 1.8. Higher excess air ratios will result in a decreased combustion temperature, and lower excess air ratios will result in insufficient air-fuel mixing [55].

2.7.2.2 Nitrogen Oxides (NO_x & N_2O)

NO_x emissions can be generated from three sources during the biomass combustion. These sources are as follows:

Fuel nitrogen, is 90% converted to NO and 10% to NO_2 through a series of intermediate reactions with primary N-containing compounds NH_3 and HCN in the pyrolysis gas phase with some NO and N_2 [110]. When oxygen is available, the NH_3 and HCN are converted to NO. The released NO with the flue gases is converted to NO_2 in the atmosphere. However, in fuel-rich conditions, it is possible to have the NH_3 and HCN react with the NO to form N_2. This is considered as a primary NO_x reduction measure [55]. The fuel nitrogen can also be retained in the char and mainly oxidized to NO in the char combustion,

Thermal nitrogen oxides can be formed when the air nitrogen reacts with oxygen radicals at higher temperatures than 1300 °C. In coal combustion the temperature often reaches higher than this degree, while in biomass combustion, the adiabatic combustion temperature is generally lower than 1573 K [62]. Thermal NO_x occurs in the post-flame zone as it depends on the oxygen availability and residence time.

Prompt nitrogen oxides are formed when the air nitrogen reacts with the hydrocarbons to form HCN, then the same mechanism of the fuel NO_x occurs to form the NO_x. The prompt NO_x mechanism is only significant when the concentration of CH is high and the combustion is under fuel-rich conditions.

NO_x in combination with HC form ozone which is an irritant to lungs and eyes, and also damaging plants. Also, sulphur dioxides are irritant and both nitrogen and sulphur oxides can be part of acid rains. When the air-fuel ratio is less than 1, the oxygen tends to burn HC to form CO_x rather than NO_x, thus leading to less oxygen available for nitrogen oxides formation.

Nitrous oxide (N_2O) is also a result of the complete biomass combustion. Although the N_2O emissions from biomass combustion are very low, they contribute to the GHG impact on the global warming and the ozone depletion [111].

2.7.2.3 Particulate Matter (PM)

The complete combustion of biomass produces fly-ash particles and aerosols. The fly-ash consists of coarse particles entrained in the flue gas that have a diameter larger than 1 µm. The aerosols are particles with a diameter less than 1 µm, that are formed from the reaction of alkali metals with Cl and S to form compounds such as KCl, NaCl, and K_2SO_4. Due to the low melting point of these compounds, subsequently, aerosols can form deposits on the boiler walls and cause severe corrosion [55].

2.7.2.4 Hydrocarbons (HC)

Hydrocarbons including CH_4, volatile organic compounds (VOC) mainly carbon, and polycyclic aromatic hydrocarbons (PAH) called tar, are the main products of incomplete combustion, and they are all intermediates to the CO_2 and H_2O formation [2, 55]. Char particles can be entrained in the high flow rate flue gas as well, due to their low density. These compounds are formed because of too low combustion temperature, too short residence time, or lack of available oxygen. Incomplete combustion can be controlled by stoichiometry and moisture removal from the fuel as primary reduction measures.

Particles such as soot, ash, VOC and PAH, have less than 1 µm particle diameter [2]. Particles of 10 µm diameter (PM10) or smaller are considered respiratory hazards [2]. Therefore, combustion aerosols should be carefully controlled to avoid health hazards. Now a days, the large-scale biomass combustion power plants utilize the cold-side

electrostatic precipitators (CESPs) as a secondary particle emissions measure [55]. However, all these pollutants were found in a lower rate in wood combustion than the rate of coal combustion [33].

2.7.2.5 Ammonia (NH_3)

Ammonia is the intermediate compound in the conversion of fuel nitrogen to the NO. If the conversion is not complete, some of the ammonia will slip to the flue gases. In addition, the ammonia injection as a secondary measure for NO_x emission reduction, may contribute to the emission of ammonia gas with the flue gases as well. Optimizing the injection is a secondary emission reduction measure of NH_3.

2.7.2.6 Sulphur Oxides (SO_x)

Sulphur oxides are formed from the complete oxidation of the fuel sulphur, mainly SO_2 in more than 95% and SO_3 in less than 5%. Not all of the fuel sulphur is converted to SO_x, at lower temperatures, a significant fraction of the fuel sulphur remains in the ash and a minor fraction is emitted as K_2SO_4, or as H_2S [55]. The primary measures for SO_x emission reduction is by lime or limestone injection [111, 112].

2.7.2.7 Hydrogen Chloride (HCl)

Wood has a very low content of chlorine. The main fraction of the Cl content is retained in the fly ash as KCl and NaCl. Wei et al. [60] found that a small fraction of the Cl content is released as HCl at combustion temperatures higher than 1473 K and the minimum HCl content is at 1373 K [60]. Also, the increase in the excess air (λ) increases the conversion of K vapour, KCl and NaCl aerosols into HCl gas. The release of HCl acid in the flue gas causes a severe corrosion on the boiler walls. To reduce the HCl emissions, washing fuels of high Cl content is a considerable primary reduction measure [111].

2.7.3 Ash Deposition

Ash deposition is a classic problem in the solid fuel combustion power plants. Coal and biomass ash depositions can cause heat transfer deficiency and corrosion problems to the boiler tubes. The inorganic elements of wood biomass are inherently atomically dispersed throughout the fuel [2]. The release of these elements from a fuel particle during combustion is driven by their volatility and the chemical reactions of organic

components in the fuel. At the combustion temperature, the most notably volatile materials are compounds of alkali, chlorine, Sulphur, and phosphorous [51, 113, 114]. Elements such as silicon, alkali, and earth alkaline metals react to form elemental or poly-silicates that melt at a temperature lower than 1373 K and form alkali sulphates that can condense on the heat transfer surfaces in the combustor leading to unavoidable depositions on the furnace walls or boiler tubes surfaces namely slagging and fouling, and less troublesome soot [50].

Slagging is the fused glassy deposits on the fireside walls of the furnace (radiation zone) that are formed from the reaction of the fuel ash silica with alkali oxides, hydroxides, and aluminium oxide to form low-melting temperature silicates (less than 1073 K). Other ash compounds, such as heavy metal oxides and silicates, bind to form agglomerates that can be seen at the bottom of the furnace. In high silica content ashes, these deposits are highly viscous melt that causes mainly slagging problems in pulverised fuel fired boilers, but may occur also in fluidised bed boilers when quartz is used as the bed material. Viscous flow sintering of glassy silicate particles may cause extensive deposition problems.

Fouling is the condensation of the volatile alkali sulphates, chlorides, and carbonates either on the ash particles forming sticky ash agglomerates on the convection walls and boiler tubes that are parallel to the gas flow (convective passes), or condense directly on the tube walls.

Soot is formed on the furnace walls and on the super heater tubes, by thermophoresis and impaction phenomena. The small particles of hydrocarbons are impacted by the larger particles of the fly ash to the furnace walls and on the boiler tubes that are perpendicular to the flue gas flow. At temperatures, lower than about 1033 K, these particles build up on the walls or condense on the super heater tubes to form soot. At higher temperatures than about 1073 K, the particles will be sticky and attract more particles to build up a wedge-shaped deposition on the super heater tubes.

On the other hand, the release of the fuel sulphur and chlorine can cause severe corrosion problems on the boiler tube surfaces in the presence of water vapour and alkali hydroxides in the flue gas (FG). Historically, corrosion was found under the fouling layers on the heat exchanger tubes of the power station boilers. Miles et al. [50] found that with the higher alkali, silica, chlorine or sulphur content in the biomass fuel, the high exit flue gas temperature promotes slagging and deposition on the boiler surfaces. The presence of chlorine, also assists in the transfer of the alkali metals from

the fuel to the furnace surfaces as chlorides. Gruber et al. [115] measured the high temperature corrosion rate of various types of wood combustion in a 50 kW grate furnace, and correlated this rate exponentially with the FG temperature and linearly with FG velocity and the boiler steel pipes temperature. However, with the pulverized fuel combustion, caution must be applied due to the difference in the fuel particle size, fuel transport with the primary air, and the full process design.

So far, there is little published data on the ash deposition behaviour of the wood pellets. One of the few studies on wood pellets combustion is presented by Wiinikka et al. [116]. They used an 8 kW fixed bed reactor to burn three types of wood pellets and examined the high temperature emissions in the flue gases. Their results have shown a high dependency of the aerosol formation in the flue gases on the fuel ash composition and the combustion temperature. The wood pellets that consist of low Si had the lowest slag formation and highest potassium release in the fly ash as $K_3Na(SO_4)_2$ and KCl.

Although an extensive research on a laboratory scale has been carried out on the ash deposition, the actual problem on the industrial scale remains enormous due to the complexity of the chemical reactions that occur post-combustion, the number of parameters that assist in creating the slagging and fouling problems, and its multiphase occurrence. For example, a comparative study on various types of wood by Misra et al. [48] have shown that the ash lost between 30- 47% of its weight, and the alkali compounds were transformed from carbonates at 873 K to oxides at 1573 K. However, at 1123 K temperature, pine ash showed sintering and at higher temperatures showed slagging due to K_2CO_3 melting. The potassium and sulphur contents play an important role in the deposition process and the same conclusion was reached by Ragland et al. [49]. Therefore, researchers suggest to maintain the fuel ash test temperature at 823 K [2, 50], or use the wet chemical analysis on the fuel itself instead of fuel ash samples to avoid the mineral losses during the preparation step.

To solve the ash deposition problem, data from several studies suggest that leaching of alkali metals and chlorine from biomass fuels is one of the methods used to increase the fusion temperature of the ash and reduce the deposition problem. Jones et al. [117] have reviewed the published data on water washing and acid washing of various species of biomass. They found that up to 90% of the alkali content of waste wood can be removed by hot washing, and 35% of Ca, 60% of Mg, 95% S, 80% P, and 30% Fe can be reduced from the original ash composition. This technique improves the fuel

properties in terms of corrosion and acid gas emissions, as well as reducing the chlorine impact on the ash deposition.

Further investigation on the mineral slagging/fouling of biomass ashes was conducted by Vamvuka et al. [51]. They tried different mitigation methods to control the mineral content of the fly ash to decrease the deposition problem. Their results showed a significant reduction of K, Na, S, and Cl content in the fly ash by leaching the fuel with water or using clay additives to the fuel.

2.8 Ash Deposition Indices

Historically, the fuel ash slagging and fouling tendencies were predicted through empirical indices of the mineral composition of the fuel ash. Those indices were developed based on industrial coal ash deposition problems and experimental biomass ash behaviour during combustion.

The base-to-acid $R_{B/A}$ ratio is commonly used as indicator of slagging propensity in the combustion furnace, expressed by the basic and acidic mineral oxides on mass basis as follows [50] :

$$R_{\mathrm{B/A}}=\frac{\mathrm{Fe_2O_3+CaO+MgO+Na_2O+K_2O}}{\mathrm{SiO_2+Al_2O_3+TiO_2}} \tag{2.3}$$

where,
$R_{\mathrm{B/A}}$:base to acid ratio.

Pronobis [114] described the severity of slagging as low at $R_{\mathrm{B}/\mathrm{A}} < 0.15$, medium at $0.15 < R_{\mathrm{B}/\mathrm{A}} < 0.75$, and high at $R_{\mathrm{B}/\mathrm{A}} \geq 0.75$. He also proposed another slagging index referred to as the slag viscosity index (R_{SL}) as follows:

$$R_{\mathrm{SL}}=\frac{\mathrm{SiO_2}}{\mathrm{SiO_2+Fe_2O_3+CaO+MgO}} \tag{2.4}$$

where,
R_{SL}:Slag viscosity index.

The higher R_{SL} value, the higher is the viscosity and therefore indicates low slagging propensity. Wiinikka et al. [116] suggested another slagging index that is the potassium slagging index (molar ratio) as follows:

$$R_{KS} = \frac{K+Na}{Si} \quad (2.5)$$

where,
R_{KS}: Potassium slagging index (molar ratio).

If this ratio is high, then there is not enough Si to bind the alkali metals to form silicates and increase the slagging predilection. Instead, K and Na vaporise to be released with the flue gases. On the contrary, if this ratio is low, higher amounts of alkali can bind with Si and the slagging tendency is higher. The opposite of this ratio was used to predict the release of K in the flue gases [113].

The alkali index (*AI*) is one simple method used to predict the fouling tendency of a solid fuel. It expresses the quantity of alkali oxides in the fuel per unit of fuel energy (kg GJ^{-1}) [2, 35, 50, 51, 118] as follows:

$$AI = \frac{kg(Na_2O+K_2O)}{GJ} \quad (2.6)$$

where,
AI: Alkali index (kg GJ^{-1}).

Miles et al. [50] suggested *AI* at a value of 0.17 kg alkali GJ^{-1} fouling is probable, and above 0.34 kg GJ^{-1} fouling is certain to occur. Jenkins et al. [2] used the molar ratio (Cl+ 2S)/(K + Na) as a better indicator for fouling tendency due to the condensation of alkali sulphates and chlorides on the boiler tubes surfaces. However, this index had no statistical significance when it was applied on the biomass fuels [113, 119]. Therefore, this index is not applied in this study.

Recently, Sommersacher et al. [113, 120] used new approaches for biomass slagging and fouling indices. They evaluated the ash melting behaviour by the molar ratio (R_{AM}) as follows:

$$R_{AM} = \frac{Si+P+K}{Ca+Mg+Al} \quad (2.7)$$

where,
R_{AM}: Ash melting index (molar ratio).

The Si, P, and K metals reduce the ash melting point by forming K_2SiO_3 and K_2HPO_4 depositions, both have low melting points. On the other hand, the earth alkaline metals increase the ash melting point, then, as this ratio decreases, the ash sintering temperature increases resulting in a lower slagging tendency.

Also, they used the molar ratio of 2S/Cl as an indicator for the high-temperature chlorine corrosion risk (R_{CC}) on the boiler tubes due to the formation of alkali chlorides in the combustion depositions as follows:

$$R_{CC}=\frac{2S}{Cl} \quad (2.8)$$

where,

R_{CC}:Chlorine corrosion risk index (molar ratio).

They set a minimum value of 8 for this index to have insignificant high-temperature corrosion. These indices were used later by Obernberger [119] on straw, and De Fusco et al. [121] on various species of wood.

Although they are the simplest methods to the primary predictions of the deposition problems in the combustion power plants, the main drawback associated with the use of ash deposition indices is that they are qualitative not quantitative. In this study, the list of deposition indices used to evaluate the biomass performance compared to coal is presented in Table 2.5. These indices were selected for their widespread use in the industrial scale and their statistical significance.

Table 2.5 Slagging and fouling indices. [50, 113, 114, 116].

Index	Formula	Slagging and Fouling Tendency		
		Low	Medium	High
$R_{B/A}$	$\frac{Fe_2O_3+CaO+MgO+Na_2O+K_2O}{SiO_2+Al_2O_3+TiO_2}$	< 0.15	0.15 – 0.75	> 0.75
R_{SL}	$\frac{SiO_2}{SiO_2+Fe_2O_3+CaO+MgO}$	>0.72	0.65 – 0.72	≤ 0.65
AI	$\frac{kg(Na_2O+K_2O)}{GJ}$	< 0.17	0.17-0.34	≥ 0.34
R_{AM} (molar)	$\frac{S+P+K}{Ca+Mg+Al}$	<1	1 - 4	>4
R_{CC} (molar)	$\frac{2S}{Cl}$	≥ 8	4 - 8	< 4
R_{KS} (molar)	$\frac{K+Na}{Si}$	>1.0	0.5 -1.0	<0.5

2.9 Design Parameters of the Industrial Scale Combustion

In the design of the combustion systems, the rate of combustion is major element as the energy produced by the process. The thermodynamics of the gas phase equilibrium

is important to calculate the adiabatic temperature and the thermal efficiency of the combustion process. The two major factors affecting the rate of combustion are the rate of heat transfer, and the kinetic rates of reactions [2]. The heat transfer is influenced by the particle size of the fuel. Thin particles heat rapidly, and thick, coarse particles heat more slowly. The rate of combustion is determined by the rate of pyrolysis and the rate of char combustion. The char combustion is a heterogeneous reaction and is slower than the gas combustion as it occurs in the solid phase where the oxygen is adsorbed on the char surface, reacted with the carbon and then the CO or CO_2 formed is desorbed and carried out from the particles by diffusion/convection. The char oxidation rate depends on the porosity and the surface area of the char as well as on the preparation temperature [2, 55].

2.9.1 Combustion Reaction Parameters

The amount of emissions from the combustion process is the most important optimization measure of the combustion operational variables. The high emission ratio in the combustion flue gases is a result of the incomplete combustion of the fuel and that is attributed to one of the following reasons:

- Inadequate air-fuel mixing in the combustion chamber,
- Lack of available oxygen,
- The combustion temperatures are too low, or
- The residence times are too short.

The oxidation rate of the biomass increases with an increase in the temperature, and oxygen concentration. The residence time is also imperative for satisfactory char combustion that undergoes a slow heterogeneous reaction. Therefore, the particle size of the fuel should be small enough to overcome the short residence time in the furnace.

2.9.2 Heat Transfer Mechanisms

The conjugated heat with the exothermic fuel combustion reactions can be transferred by conduction, convection, or radiation [55, 122]. The heat losses from the combustion chamber are controlled through the optimization of these three heat transfer mechanisms to achieve the maximum heat exchange and hence maximum thermal efficiency of the combustion process. The heat exchange usually occurs between the hot flue gases and the surroundings or with water tubes as in the boilers. The radiation

fraction of the total heat transfer occurs in the flame zone and the combustion gases in the surrounding space of the combustion chamber. Radiation heat transfer then plays a dominant role in most industrial furnaces and it can be predicted from the radiation properties and temperature distribution in the combustion media. The convective heat transfer occurs at the wall surfaces at which heat flows from the hot gases to the walls. The radiative heat flux is measured by the heat flux probes inserted axially at different distances from the flame center, and the convective heat flux probes are inserted tangentially along the height of the combustion furnace.

At the start up ignition of the combustion process, a significant fraction of the heat produced in the combustion chamber is reserved inside the walls by conduction and transferred to the outer surroundings with a time delay. Therefore, the combustion furnace is usually surrounded with sufficient insulation thickness to minimize the heat loss.

2.9.3 Air Preheating

In the industrial combustion process, the inlet air is preheated to maintain the combustion temperature with the minimum heat required [55, 123]. The inlet air passes through a heat exchanger with the flue gases after the flue gases have left the combustion chamber and passed the main heat exchangers of the steam generation boiler.

2.9.4 Excess Air Ratio

The complete combustion of biomass requires sufficient amounts of oxygen to cover the stoichiometric ratios required for the oxidation reactions. In practice, it was found that excess air was necessary to achieve sufficient mixing of the reactant gases and the fuel. The typical excess ratio for small scale biomass combustion is between 1.1-1.5 [55]. On the other hand, the high excess air ratios reduces the boiler efficiency and increases the NO_x emissions due to the O_2 availability for NO formation [108]. At the same time, the CO formation increases with less O_2 availability although it depends on other parameters, such as fuel moisture and combustion conditions.

2.10 Oxy- Fuel Combustion

Air combustion produces high NO_x polluted flue gas. In the last decade, the notion of Oxygen Enhanced Combustion (OEC) has been presented, discussed and examined as a primary reduction measure of the air combustion pollutants and enhancement of the combustion efficiency. In the oxy-fuel combustion, oxygen is mixed with CO_2 to achieve a moderate combustion temperature and reduce the melting and slagging of the ash mineral oxides. Carbon dioxide has a molar specific heat that is 1.7 times higher than that of the molecular nitrogen. Therefore, the flame temperature in the oxy-fuel combustion is lower than that of the air-fuel combustion for the same stoichiometric ratios to fuel [10]. Also, the absence of N_2 in the combustion gases eliminates the formation of thermal NO_x. Although, some of the produced gases including the NO_x are recycled in the case of flue gas recycling (FGR) and increasing the ratio of NO_x emissions, the oxy-fuel combustion reduces the NO_x emissions by a factor not less than three.

For biomass combustion plants, the OEC is applied to achieve negative carbon emissions when the pure CO_2 produced in the flue gas is directly captured and stored. However, the actual biomass combustion plants are still few and many researchers have studied the OEC as a retrofit on the coal-biomass cofiring processes [17, 18, 20, 21, 36]. The OEC includes maintaining the O_2 percentage in the oxidant gas at higher than 21% by volume. Oxygen can be used to enhance the combustion process in four mechanisms [124]:

i. Air enrichment (adding O_2 into the incoming combustion air stream),
ii. O_2 lancing (Injecting O_2 into an air/fuel flame),
iii. Replacing the combustion air with high purity O_2, and
iv. Oxy-fuel & Flue Gas Recycle.

2.10.1 Air Enrichment

This method can be applied to the conventional air-fuel burners as an inexpensive retrofit to enhance the combustion process. O_2 is premixed with the air stream before entering the burner. This process shortens the flame and increases its intensity. However, the addition of O_2 should be to a certain extent after which, the short flame will have an elevated temperature that may damage the burner, and the NO_x emissions increase. The industrial experiments on unmodified burners have shown that an

excellent performance can be obtained at 26% volume O_2. Higher than this value, the process failed to operate properly [124]. Nimmo et al. [20] studied the O_2 enrichment of the coal-shea meal cofiring at different enrichment levels. They found that at higher levels of enrichment (up to 40% O_2) there was an increase in the NO_x emissions, while at 100% O_2 in the secondary air, reduced the level of the NO_x emissions. They recommended a modification of the flame dynamics by altering the mixing rates. Figure 2.3-(a) illustrates a scheme of the air enrichment method.

2.10.2 O_2 Lancing

O_2 lancing is another retrofit method to enhance the combustion by the addition of oxygen to the furnace from a different point than the burner. It is considered as a staging technique to the oxidant that helps protecting the burner and the furnace sides from the elevated temperature flame as well as reducing the NO_x emissions. As it can be seen from Figure 2.3-(b), O_2 is injected to below the burner towards the flame and this helps to lengthen the flame and distribute the heat transfer inside the furnace. The oxygen lancing is also at low ratios like the enrichment method. One potential cost factor in this process is the addition of oxygen inlet joints and pipes to the furnace. Another disadvantage is the poor mixing of the oxygen with the air/fuel stream. However, this defect is outweighed by the more effective heat transfer efficiency.

2.10.3 Oxy-Fuel

When the oxidant is mainly pure oxygen, the process is referred to as the oxy-fuel combustion. In the oxy-fuel case, the oxygen is completely separated from the fuel in the burner until they both reach the outlet of the burner that is called a nozzle-mix burner. Prevention of premixing the oxygen with the fuel is for safety reasons to avoid a highly potential explosion. The oxy-fuel has the highest cost due to the cost of oxygen generation. Figure 2.3-(c) shows the oxy-fuel injection into the furnace. The disadvantage of this process is the reduction of flame emissivity and heat transfer.

2.10.4 Oxy-Fuel & Flue Gas Recycle

This is the latest technology for OEC, where a pure oxygen is mixed with recycled flue gas to form the oxidant in an O_2 ratio higher than the oxygen ratio in the air. The flue gas is mainly CO_2 and H_2O, both have higher heat capacity than N_2, therefore mixing the flue gas with the oxidant reduces the flame stability that requires a larger oxygen

ratio to maintain a similar performance of the air combustion. For the same reason, the pure oxygen ratio can be higher than 21% and still have a safe combustion environment, and the same heat transfer properties. The flue gases recirculation (FGR) requires an additional fan and ductwork that can withstand elevated temperatures to recycle the flue gases to the burner. The presence of hot water vapour in the FG enhances the thermal radiation in the furnace. On the other hand, the high concentration of CO_2 reduces the combustion rate of the volatiles and respectively the char combustion due to the decrease in the oxygen diffusivity.

Figure 2.3-(d) shows the FGR method. Smart et al., 2010 [21] studied oxy-fuel with FGR cofiring Russian coal with 20% shea meal and sawdust in a 0.5 MW_{th} combustion test facility. The recycle ratios (RR) they applied were 65% and 75% and the furnace exit O_2 was maintained at 3%. Their results showed that the highest radiative heat flux and highest flame intensity corresponded to the lower RR. Conversely, the lower RR resulted in a lower convective heat flux. The oxy-FGR process also increased the burnout of biomass cofiring case rather than the air combustion. The same conclusions were reached by a recent experimental study on oxy-FGR biomass combustion conducted by Alvarez et al. [19].

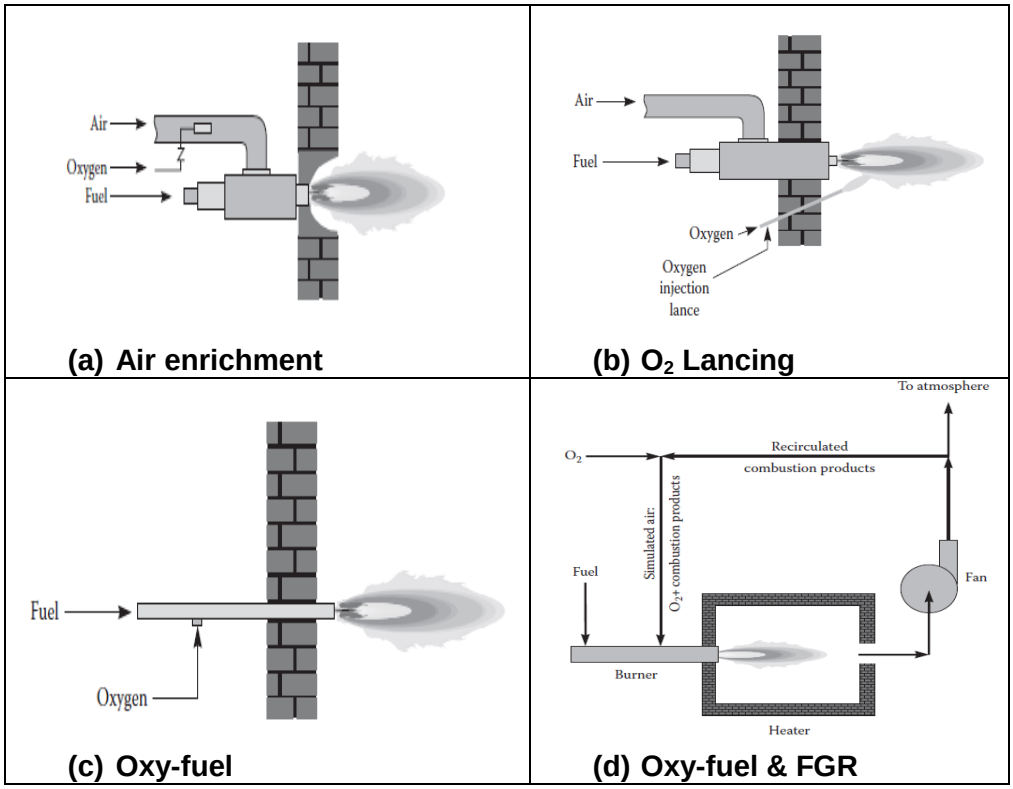

Figure 2.3 Oxygen enhanced combustion methods (OEC). [124]

The research studies on dedicated oxy-biomass combustion are very few in the literature. In 2014, Wang et al. [125] experimentally investigated the combustion kinetics of bio-char in an O_2/CO_2 atmosphere using the TGA method. They found that the O_2/CO_2 atmosphere has delayed the bio-char ignition and reduced the activation energy. Trabadela et al. [126] studied the oxy-biomass maximum pressure produced using a recycled mixture of oxygen and carbon dioxide. They found that with 25% oxygen the ignition and combustion performance are like air-biomass combustion. A recent study conducted by Farrow et al. [127], used a drop tube furnace to study the sawdust and pinewood powder pyrolysis under N_2 and CO_2 atmospheres. Their results showed that the volatile yield under CO_2 conditions is higher than the volatile yield under N_2 conditions, as well as the char burnout is faster. These results are in agreement with Wang et al findings [125].

2.11 Biomass Feeders

Several types of biomass feeders are used in combustion chambers of power plants, such as the lock-hoppers, rotary-valve feeders, piston feeders, and the screw feeder, all depending on the air pressure to move the fuel particles into the furnace [128]. The most common type of feeder used with biomass is the hopper-screw feeder [38]. Dai and Grace [38] examined the impact of particle size, size distribution, density, moisture content, and the compressibility of the fuel particles on the feeding process. The larger particle sizes and the lower bulk density need a higher hopper level up to 0.6 m, depending on the particle size and size distribution, to increase the mass flow rate. Conversely, fuels with higher bulk density require a lower hopper level than 0.2 m to avoid blockage or bridging over the screw, but also, they need a lower screw speed to achieve the same mass flow rate. The bridging of the biomass occurs due to the increase in the cohesion forces among the fuel particles and the adhesion with screw and casing surfaces [38]. Further, rough particle surfaces and irregular particle shapes, increase the friction between the particles and the feeder walls for which a higher power and torque is needed to push the particles forward.

Higher moisture content in fuel particles increases the required torque of the screw rotation and needs a higher screw speed (>30 rpm) to reduce the tendency to blockage [38].

2.12 Hazards in the Use of Wood Pellets

White wood pellets consist primarily of pine and spruce with a small percentage of mixed hardwoods chipped, dried, ground and compressed without binder additives. According to the European Pellet Council, the maximum moisture content of the wood pellets should not exceed 10% [129]. In pulverized fuel combustion, wood pellets are milled to 0.1 - 3 mm dia and usually stored in large silos or 1 m^3 bulk bags. As a natural combustible material, wood pellets can cause fire for many reasons, such as self-heating, overheating, sparks, and vehicle fires. Moreover, milled wood pellets can cause dust explosion. Therefore, extreme caution should be taken during the transportation, handling, storage and usage of milled wood pellets.

2.12.1 Hazards During storage

With all fire control precautions during wood pellets storage, fire hazard is still existing as a result of self-heating. Self-heating is the rise of the species temperature due to exothermal reactions inside the bulk of species pile. In wood pellets case, it occurs by one or more of the following three means [130]:

1. Microbiological activities by micro-organisms metabolism,
2. Oxidation reactions of unsaturated fatty acids in the biomass, and
3. Moisture absorption and condensation.

Although wood pellets are made of dried wood chips and saw dust (*MC* is $\leq$10%), piling the pellets for heights over 6 m in closed silos or A-shaped open storages can cause self-heating. During pellet processing and milling, the cell structure opens up and the cellulose, hemicellulose, and the protein extractives are oxidized at temperatures as low as 278 K. These oxidation reactions generate heat to increase the temperature, and produce gases such as CO, CO_2, and CH_4. In the same manner, micro-organisms growth increases in the presence of moisture and for fresh-harvested wood. When the wood chips are dried, the process stops. However, bacteria growth can accelerate the fatty acid oxidation up to 343 K. After this temperature the chemical oxidation controls the

self-heating leading to further higher temperatures. In addition to the oxidation and biochemical activity, the humidity can cause self-heating by increasing the temperature through the heat of adsorption/condensation. Thus, forced ventilation with humid air can increase the moisture content of the pellets and ultimately increases the temperature [131]. If the generated heat is not transferred away and the material under goes a temperature increase, spontaneous ignition occurs starting with pyrolysis and when it reaches the surface, flame occur due to oxidation. Figure 2.4 shows photographs of (a) pile of wood pellets, (b) off-gases on the top of wood pellets pile, and (c) actual spontaneous fire inside wood pellets pile. The larger the size of the pile, the greater is the risk of central spontaneous ignition.

Figure 2.4 Photographs of wood pellets; (a) wood pellets pile in A-shaped storage, (b) off-gases from pellets pile, and (c) spontaneous central ignition [130].

It was found that for wood pellets, the main source of self-ignition is the low-temperature oxidation of the wood constituents, and the temperature increases after few days of storage to reach 338 K [130]. For large scale piles and silos, the temperature can be higher than 363 K, at which the risk of spontaneous ignition increases.

The best practice to reduce the fire hazard due to self-heating, is by distributing the pile to the minimum layer possible thickness to enhance the cooling process, and for smaller scale storage, the 1 m^3 bulk bags are used to protect the milled pellets from moisture, sparks, and spillage.

2.12.2 Hazards Inside the combustion Unit

During the combustion process, the dust explosion and spontaneous ignition of the fuel particles is also a possible hazard that should be avoided. For the spontaneous combustion to take place, it requires three elements; ignition source, oxygen, and combustible dust, whereas the elements of dust explosion occurrence are as follows: dispersion of dust in the air, oxygen, combustible dust, ignition source, and containment of dust cloud [132]. These elements are shown in Fig. 2.5.

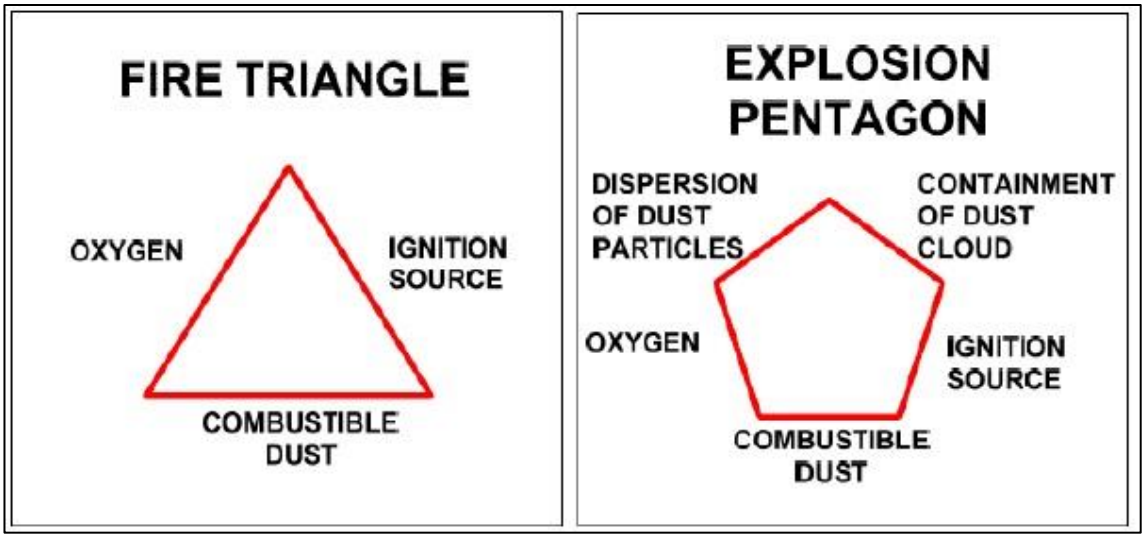

Figure 2.5 Elements of fire triangle and explosion pentagon hazards of biomass combustion.

Wilen and Rautalin [128] studied the self-ignition and dust combustion of forest residue and wood bark during the combustion process, and they reached the conclusion that

raising the temperature from room temperature to 423-473 K reduced the minimum oxygen content required for dust explosion by 3-5%. Furthermore, any heat brought up to the fuel inside the lock hopper, or screw hopper because of convection, radiation, or friction inside the screw part, would cause self-ignition of the fuel particles in the feeding system. The reason is due to the lower self-ignition temperature than the smouldering temperature of the dried wood.

To mitigate this hazard, for large silos an appropriate oxygen-free atmosphere using nitrogen as an inert agent is imperative. Hence, maintaining the oxygen level of the ambient atmosphere, below 2% will avoid spontaneous ignition of the fuel as it will result in an increase in the ignition temperature. For few tons storage of wood pellets, sealed bulk bags are used and stored in a separate fuel storage area, dust clouds should be avoided during loading the fuel to the biomass feeder, and immediate clean-up of any spillages is necessary. This should be carefully considered in handling biomass fuels in hot weather locations or in sizzling summer.

2.13 Co-firing of Wood in Combustion Plants

Cofiring refers to the combustion of biomass with coal for power generation [4]. Fitzpatric et al. [33], studied the influence of cofiring pine sawdust briquettes with coal on the boiler performance in a fixed bed furnace. They observed a reduction in the average temperatures of the bed and flue gases, and the volatile release rate was higher for cofired coal than for pure coal-fired fuel.

Cofiring wood with coal assists to reduce the total emissions per unit energy produced by reducing the NO_x and SO_x levels from the existing coal power plants [4], also supressing HC pyrolysis products such as PAH and phenols [33]. Recent studies have shown that cofiring of biomass with fossil fuels has a positive impact both on the environment and the economics of power generation [4]. The global warming concern due to greenhouse gases can also be mitigated by replacing fossil fuels with biomass in the power plants knowing that the CO_2 produced from biomass combustion comes originally from the atmosphere during the photosynthesis process [33].

The elemental composition differences between wood and coal are important parameters in cofiring plants. Wood has more oxygen-containing compounds such as phenol, whereas coal has alkyl-aromatics and less phenol. As shown in Table 2.3, the ultimate analysis indicates substantially higher oxygen and lower carbon content in

wood than in coal. Also, wood has less nitrogen, sulphur, chlorine, and ash. On the other hand, wood has more potassium, magnesium, and calcium than coal. All these distinct differences contribute positively or negatively to the NO_x, SO_x emissions, corrosion, and ash slagging and fouling issues in the combustion process.

Chapter 3 Experimental Methodology

3.1 Chapter Overview

This chapter describes the design and implementation of the research plan throughout three stages; the solid fuel characterization, fundamental thermal treatment analysis, and the description of experiments performed in the pilot plant of the 250-kW combustion rig, at Beighton, UK. The objectives of these stages are to collect the necessary data that establishes the understanding of pulverised wood pellets combustion via both small and pilot scale empirical research approaches. The fundamental study explores the chemical and thermal fuel properties, such as elemental composition, proximate composition, heat value, thermal treatment behaviour and the kinetic reactivity of the particle char combustion. The other main part of this study is the experimental work in the pilot plant; the combustion efficiency and the ash formation during the combustion of wood pellets in comparison to coal are investigated. In addition, the oxy-fuel combustion is compared to the air-fuel combustion for both fuels. The combustion rig is designed to enable the sampling of the fly ash and bottom ash for compositional analysis to investigate the ash partitioning and estimate the carbon burn out and combustion efficiency.

3.2 Fuel Characterization

The knowledge of accurate biomass fuel properties is essential to the detailed combustion modelling in furnaces and boilers [3]. Of course, the data required for all biomass fuels are not available in one reference. Moreover, the white wood pellets properties are completely dependent on the properties of the original wood used to produce them, and in general they are made of different white wood species, such as pine trees or spruce trees. In addition, the same wood species can vary in properties from one country to another depending on the soil and climate that they grow in. For all above-mentioned reasons, it is imperative to perform full characterization for the specific biomass fuel that will be used in a specific project.

In this chapter, the compositional analysis of the USWWP, CAWWP, ELC, and VC is performed. The USWWP and ELC samples used in the characterization are collected from the bulk quantities used in the pilot scale combustion experiments.

3.3 Methods of Characterization

The characterization methods used in this study are based on the European and British Standard for Solid Biofuel Specifications and Classes – Graded Wood Pellets BS EN 17225-2 that was approved in April 2014. However, some of the properties, such as the burning profile, and major elements of ash composition, are not described by a BS method, and thus methods used by previous published work in the literature are applied to the sample. The properties and testing methods applied in this study are listed in Table 3.1.

Table 3.1 Methods of fuel compositional analysis.

Parameter	Testing Method
Particle size	BS EN 16126-2012
Proximate Analysis	
Total Moisture	BS ISO DIS 18134-1: Reference Method
Volatile Matter	BS ISO DIS 18123
Ash Content	BS ISO DIS 18122
Fixed Carbon	By difference
Gross Calorific Value	BS EN 14918-2009 Combustion Bomb
Ultimate Analysis	
Total C, H, N and S	BS ISO DIS 16948 – Elemental Analyser
O is determined by difference	

3.3.1 Particle Size Distribution

Usually, for the power generation plants, the pulverized coal is milled to particle size <500 μm, and the biomass is less than 1 mm. In this research study, the biomass was milled to ensure a particle size (PS) less than 1 mm. However, the building block structure of the two fuel types are completely different, hence the resulting particle size distribution (PSD) during the milling process is expected to be different.

The British Standard method BS EN 16126:2012 for measuring particle size distribution of wood pellets performed on the milled wood pellets as received from the supplier. A Retsch AS 200 sieve shaker at 30 rpm speed was utilized to sieve the sample for 15 minutes. To have a representative sample, the sample was prepared by subdividing 150 g sample by the riffle divider into two subsamples. The sieve size fractions used, were sequentially 1.00 mm, 500 μm, 250 μm, 200 μm, 125 μm, 60 μm, and 25 μm.

3.3.2 Proximate Analysis

Researchers have followed various methods for the proximate analysis of biomass fuels. The gradual thermal degradation of biomass samples was investigated to identify the moisture, volatile matter and ash content based on the burning profile behaviour and the rate of weight loss [73, 133]. The other method of proximate analysis is to measure each constituent separately using the loss in weight of the samples that result from the heating to a given temperature under certain conditions. This method is adopted by the ASTM and BSI for the solid biofuel analysis. The British Standard methods of measuring the moisture content, volatile matter and ash contents are applied for the characterization analysis in this study.

3.3.2.1 Total Moisture Content

The moisture content of the biomass fuel is a very important parameter in the combustion process, as it affects the thermal properties of the fuel such as specific heat, thermal conductivity, and emissivity. In addition, the moisture content reduces the NCV of the fuel. As the fuel is heated in the combustion chamber, the moisture evaporates and takes the energy from the combustion process, and this lowers the maximum combustion temperature (adiabatic temperature) and increases the necessary residence time for complete combustion [134]. Consequently, the thermal efficiency of the combustion process decreases. The fuel moisture content also affects

the fuel feeding process, the higher is the moisture content in the fuel, the higher is the probability of the fuel bridging inside the hopper and the non-constant fuel flow would cause an unstable flame in the burner. Therefore, a fuel with lower moisture is a more efficient fuel. The BS EN ISO 17225-2:2014 for industrial wood pellets grade A1, and the EU Standards for wood pellets EN 14961-2 A1 pellets specify the maximum moisture content of the wood pellets at 10% (mass) [32, 129].

A GenLab oven was used to perform the total moisture content test according to the BS ISO DIS 18134-1 Reference method. Four Petri dishes are cleaned, weighed empty for three duplicates of the sample and one is the reference empty dish. Samples of about 3 g were added, spread, and put immediately in the drying oven at 378 K to stay overnight and then left to cool down in the desiccator for the total moisture measurement. The dried samples were saved in a sealed container for further property testing.

3.3.2.2 Volatile Matter

The volatile matter of the four fuel types were tested according to the BS ISO DIS-18123 [135]. The principle is to heat the sample without the presence of air at a temperature 1173 K± 10 K for 7 minutes to achieve an inert environment for the sample enabling the volatile components to evaporate without exposure to the air. Usually a metal stand that holds 4 crucibles is placed in a furnace set at a constant temperature of 1173 K. One of the crucibles is empty for calibration. The sample weight before testing is 1 g ± 0.1 g. After cooling in a desiccator, the sample is weighed again for residual char content. Depending on whether it is a wet or dry sample, the difference in weight is the volatile matter with or without the moisture content. Therefore, the moisture content should be measured for the same sample simultaneously with the volatile matter. For a dry sample, the volatile matter is given by:

$$VM_{\mathrm{db}} = \left[\frac{100\times(m_2 - m_3)}{m_2 - m_1} - MC\right] \times \left(\frac{100}{100 - MC}\right) \tag{3.1}$$

where,
VM_{db}:volatile matter on dry basis, (wt%)
m_1:mass of empty crucible with lid, (g)
m_2:mass of the crucible with lid and sample before heating, (g)
m_3:mass of the crucible with lid and sample after heating, (g)
MC:moisture content in the original sample, (wt%)

3.3.2.3 Ash Content

Determination of the ash content was performed according to the BS ISO DIS 18122 (14775) [136]. A Carbolite LHT6/30 forced-air convection oven is employed to perform the ash content tests. The testing porcelain crucibles are dried empty at 823 K for at least 60 min then left to cool in the desiccator and the weight of the empty cool crucible is recorded. A test sample of a nominal top size of 1 mm or less, is placed in a 10 mL glassed silica crucible and heated to 823 $\pm$ 10 K, at a heating rate of 4.5-7.5 K min^{-1}, holding the temperature for 30 min at 523 K and for 180 minutes at the end of heating ramp at 823 K. The weight of the remaining sample is the primary ash content in the biomass fuel. Some researchers do the ash content analysis at 1088 K to simulate the actual combustion temperature in the power plants. However, at this temperature the ash content is different from that at 823 K due to the volatilization of metal carbonates and higher oxidation of the oxides. Some of these compounds are recovered in the fly ash.

3.3.3 Calorific Value

In this study, the actual measurement of the *GCV* is performed rather than using the empirical equations those were reviewed in Section 2.4.4, Eqs. (2.1) and (2.2) to obtain the best specific values for the fuels under study. The British Standard method EN 14918:2009 for *GCV* determination of solid biofuel was followed in this test. A wet sample from each of the USWWP, and ELC fuels is sieved to less than 500 µm before testing to ensure a stable oxidation rate. From that sample, about 1 g subsample is placed in a Parr 6200 Calorimeter bomb under pure oxygen pressure at 30 bars, using a 100 mm ignition nickel-chromium wire, 0.16 mm in diameter and in a closed 300 mL bomb surrounded by a water jacket and connected to the computer based program to measure the temperature increase. Three millilitres of distilled water are added to the combustion bomb initially to give a saturated vapour phase prior to combustion, thereby allowing all the water formed to be in the liquid phase. The heat produced from the combustion process increases the temperature of the 2000 g water jacket.

The gross calorific value is calculated from the corrected temperature rise of the water. The temperature record is set to be 1 min intervals and the experiment lasts for 10 min. The equipment remains closed until the temperature reduced to room temperature. For accurate calculations, the heat produced by burning the air-nitrogen to NO_2 then HNO_3 in the presence of high pressure of oxygen and H_2O and burning the sample sulphur to

SO_2 then H_2SO_4 both are deducted from the total heat produced. In addition, the heat consumed by the nickel wire is deducted from the total heat, however the exact length of the wire is determined by measuring the part remained in the bomb electrodes after combustion. The *GCV* is calculated as follows:

$$GCV = \frac{\Delta T.EF_B - \Delta H_{\text{acid}} - L_{\text{w}}.EF_{\text{w}}}{m_{\text{s}}} \quad (3.2)$$

where,
GCV :gross calorific value of the fuel, (J g^{-1})
ΔT :total temperature increase, (°C)
EF_{B} :bomb calorimeter energy factor, (J $°C^{-1}$)
ΔH_{acid} :total heat produced from acid formation, (J)
L_{w} :wire length, (mm)
EF_{w} :wire combustion energy factor, (J mm^{-1})
m_{s} :sample mass, (g)

In order to calculate the exact calorimeter energy factor, the equipment was standardized with a standard benzoic acid pellet that has a combustion heat value of 26,454 kJ kg^{-1}. The calorimeter energy factor is calculated as follows:

$$EF_{\text{B}} = \frac{CV_{\text{BA}}.m_{\text{BA}} + L_{\text{w}}.EF_{\text{w}} + \Delta \boldsymbol{H}_{\textbf{acid}}}{\Delta \boldsymbol{T}} + CP_{\text{cr}}.m_{\text{cr}} \quad (3.3)$$

where,
CV_{BA} :Benzoic acid heat value, (J g^{-1})
m_{BA} :mass of benzoic acid, (g)
CP_{cr} :heat capacity of crucible, (J g^{-1} $°C^{-1}$)
m_{cr} :mass of crucible, (g)

The GCV of a dry sample is calculated after simultaneous determination of the moisture content of the fuel as follows:

$$GCV_{\text{db}} = GCV \times \frac{100}{(100\text{-}MC)} \quad (3.4)$$

where,
GCV_{db} :gross calorific value of the fuel on dry basis, (J g^{-1})
MC :moisture content of the sample , (%)

In the industrial practice, the net calorific value NCV at constant pressure for the fuel with specified moisture content is used rather than the GCV. This value is derived from GCV_{db}, and the H, N, and O content in the fuel. The NCV_{db} at constant pressure for a dry sample is calculated as follows [137]:

$$NCV_{\mathrm{db}}=GCV_{\mathrm{db}}\ -212.2\times \mathrm{H}\%_{\mathrm{db}}-\ 0.8\times(\mathrm{O}\%_{\mathrm{db}}+\mathrm{N}\%_{\mathrm{db}}) \quad (3.5)$$

where,
NCV_{db}: net calorific value on dry basis, (J g^{-1})

For a fuel received with certain moisture content, the NCV can be calculated as follows:

$$NCV_{\mathrm{ar}} = NCV_{\mathrm{db}}\left(1-\frac{MC}{100}\right) - 24.43\times MC \quad (3.6)$$

where,
NCV_{ar}: net calorific value as received, (J g^{-1})
24.43 = enthalpy difference between gaseous and liquid water at 25 °C, (J g^{-1})

3.3.4 Ultimate Analysis

The C, H, N, S and O contents in the solid fuel determine the energy content of the fuel and identify the ultimate operation conditions of the combustion process, such as the combustion temperature, air-fuel ratio and flow rate, and the flue gas flow rate and composition. Therefore, the ultimate analysis is an essential part of the biomass fuel characterization.

Usually the ultimate analysis is recorded for the dry-ash-free samples, as the C, H, N, S, and O are the major elements of the volatile matter and do not contribute to the ash content. The BS ISO/DIS 16948-2012 was followed in this test. 1.5-2.0 mg of dried sample is burned in the oxygen in such conditions to be converted to ash and gaseous compounds that are analysed for C, H, N and S elements. The combustion process conditions should ensure that the hydrogen associated with the sulphur and halides is all converted to water, and the nitrogen oxides are reduced to nitrogen. A Thermo Flash 2000 Element Analyser was used to test the C, H, N and S content of the four fuel samples. The equipment is fitted with a flame photometric detector, which offers ppm level determinations of S as well as C, H and N. The O content is determined by difference. Each run of samples starts with three weighed samples of the standard reference (Cysteine in this case) and three empty capsules to calibrate the data results. The computer software compares the sample peaks with the mean of the last three standard readings saved in the program. The calibration method is based on the K-factor method. To ensure the calibration is correct, samples of the standard reference were tested as unknowns. The standard error of triplicate samples is recorded.

3.4 Fundamental Kinetic Study

Wood pellets and coal particles are thermally treated with TGA to determine the combustion kinetics parameters. The TGA experimental matrix is designed to approach the industrial interest conditions, as most of the published literature on coal combustion treats the fuel in two separate steps; first devolatilization under an inert gas and then cool the produced char, reheat it under oxidizing conditions with different temperatures and gas pressures. In this work though, the fuel samples are treated in one continuous process in two stages. The first stage is to run the samples under an inert gas and then immediately switch the purging gas into an oxidizing gas or air at the same temperature for char combustion.

3.4.1 Sample Preparation for TGA

Two types of wood pellets and two coal samples are used in this comparison. The biomass samples are the milled US white wood pellets (USWWP) and the Canadian milled wood pellets (CAWWP) and the coal samples are the ELC and the VC.

Samples of 10 g were oven dried up to 378 K for 4 hours, then cooled in a desiccator and crushed in a mortar and pestle to homogenise for sieving to less than 80 μm particles, and stored in sealed containers for further analysis. The published studies have shown that in TGA experiments, pulverized coal or biomass is within the particle size 63-100 μm [69, 93, 138-140]. The small particle size is necessary for the TGA testing to ensure uniform heat distribution and gas diffusion within the sample particles, and to eliminate the effect of particle size on the rate of pyrolysis [141].

3.4.2 Thermogravimetric Analysis

A two-step procedure of the TGA experiments was performed with the Perkin-Elmer Pyris 1 TGA analyser for each sample. First, is the pyrolysis with inert gas (nitrogen) to a certain temperature, and then the temperature is held constant until a steady weight is achieved, then the sample is subjected to the air for the char combustion until a constant weight is obtained. 5 mg $\pm$ 5% of each fuel type were used in the TGA tests to achieve consistency and uniform heat transfer throughout the sample particles. The weight calibration with a 100 mg standard weight was performed every day before starting the first run. Also, the temperature calibration was performed using Curie point reference materials copper and iron, both materials are provided by Perkin Elmer.

3.4.2.1 Devolatilization Step

Pure oxygen-free nitrogen gas was used as the inert gas with a total flow rate of 40 cm^3 min^{-1} flow rate. The gas flowrate is controlled by a gas station control valve. Samples of 5 mg ±5% were placed in a platinum pan of 5 mm diameter and 1 mm height in a 10-mm diameter furnace, hanged by a quartz rod linked to an electronic balance. A thermocouple is placed 3 mm under the pan to monitor the temperature.

The nitrogen continued purging the furnace for 20 minutes before the heating step to eliminate any air in the furnace tube and stabilize the balance reading. Then, the sample was heated to 383 K and held for 20 min to remove any moisture, then heating to 773, 873, 973, 1073, 1173 or 1273 K, with a constant heating rate at 100 K min^{-1}. Iso-thermal conditions at the final temperature were continued until a constant weight was achieved. The final temperatures were selected to cover both combustion regimes, namely Zone I, where the reaction is under chemical control, and Zone II, where the reaction is affected by both diffusion limitation through the particle pores and chemical kinetics.

3.4.2.2 Char Combustion Step

An immediate change in the char combustion step was achieved by switching the purging gas to air at the same flowrate. The test was ended when the final mass was constant. Those tests were repeated twice for each operating condition, and the baseline weight loss was subtracted from the sample weight in each test.

This method of devolatilization followed by immediate char combustion without cooling and reheating to the combustion temperature, is analogues to the proximate analysis of solid fuels used by Ottaway [133] to calculate the volatiles and char components of the coal. Also, it is a resemblance of the conditions demonstrated in the industrial scale of pulverized combustion where the devolatilization and combustion occur simultaneously. In addition, the consistency of the devolatilization and the char combustion temperatures produces better prediction of the char structure alteration with the temperature increase, and the cooling step effects on the char structure, is avoided.

3.5 Pilot-Scale Experimental Work

3.5.1 Unit Description

The combustion rig is in Beighton, Sheffield, UK and it is part of the UKCCSRC Pilot-Scale Advanced Capture Technology (PACT). The combustion testing rig consists of a 250 kW down fired cylindrical furnace using a burner that is designed particularly to fire pulverised biomass under either air or O_2/CO_2 mixtures namely oxy-fuel firing. The furnace is pre-heated by Natural Gas (NG) and cooled by a water jacket system with temperature/flow monitoring. The unit has a dedicated biomass feeder with a maximum capacity 80 kg h^{-1}, interchangeable with a coal feeder, supplied with a dedicated air and O_2/CO_2 metering skid. The flue gas pipe leaves the bottom of the furnace to a cyclone to remove the large particulates of the fly ash. The flue gas is then cooled to a temperature of about 873 K, then it passes through an elevated temperature candle filter to remove the remaining fly ash. After the filter, an exhaust fan is attached to the flue gas pipe to keep the furnace pressure below atmospheric for safety measures, and the cooled flue gas passes through an amine plant for carbon capture before the stack. A schematic diagram and a CAD drawing of the combustion rig are illustrated in Fig. 3.1.

3.5.2 Furnace

The furnace is 4 m long, made of eight 500 mm long sections, with 900/1100 mm inner/outer diameters. The refractory is made of 100 mm thick, lightweight alumina silicate that provides more rapidly heated furnace than a furnace lined with refractory bricks. The top section and the burner are cast with high density concrete to maintain the flame stability. There are three viewing ports in the top three sections, and many other ports for various measurement probe insertions. Figure 3.2 illustrates the furnace CAD drawing and photographs of the relative parts of the furnace. At the bottom of the furnace there is a circular opening of a diameter of about 500 mm, and the bottom of the furnace is immersed in a water tray to prevent the escape of the flue gases and to collect any slagging deposits or the bottom char particles.

3.5.3 Burner

The biomass burner is designed to simulate the commercial scale low-NO_x burners. The NG passes through the inner pipe, and then sequentially, the primary, secondary and tertiary annulus pipes are mounted to introduce the primary oxidant with the pulverized biomass, secondary oxidant, and the tertiary oxidant, respectively. The secondary and tertiary oxidants are internally split from a single supply by a movable damper slide. Furthermore, the secondary and tertiary are fitted with movable swirl vanes which allow independent adjustment of the respective swirl intensities. The optimized conditions of these three variables were setup by a previous project. Hence, the actual flowrates of the oxidant that can be measured are the primary and the tertiary only, and the split between the secondary and tertiary internal to the burner is determined by subsequent CFD modelling. However, the split position between the secondary and tertiary flowrates is used to indicate the burner condition during the burner optimization process. Another burner that was designed for the pulverized coal combustion is used for the coal runs. The difference in the design of the two burners is out of the scope of this study.

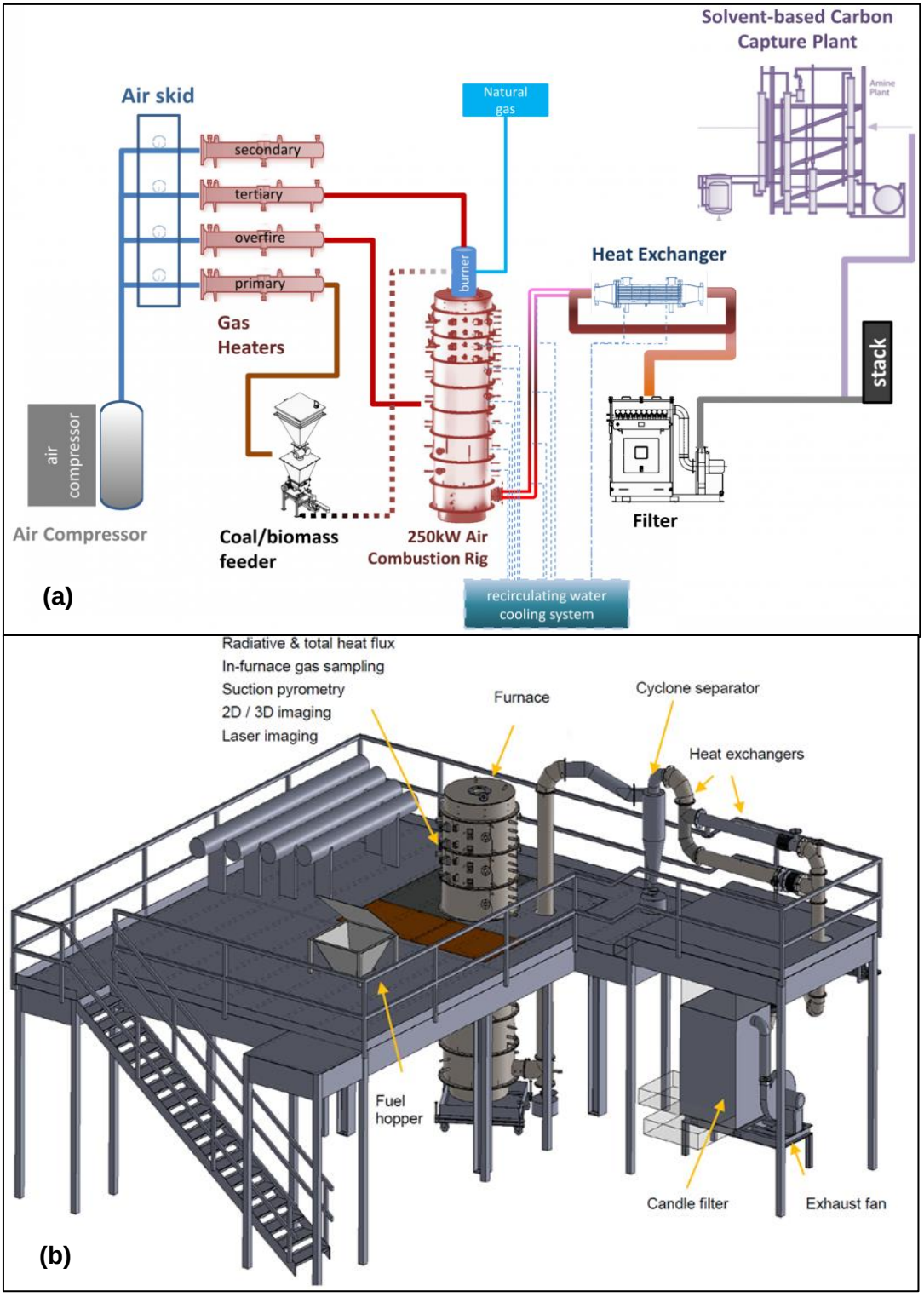

Figure 3.1 The pilot scale combustion testing rig: (a) flowchart of the rig with the air supply unit and carbon capture plant, and (b) a CAD drawing of the actual set up.

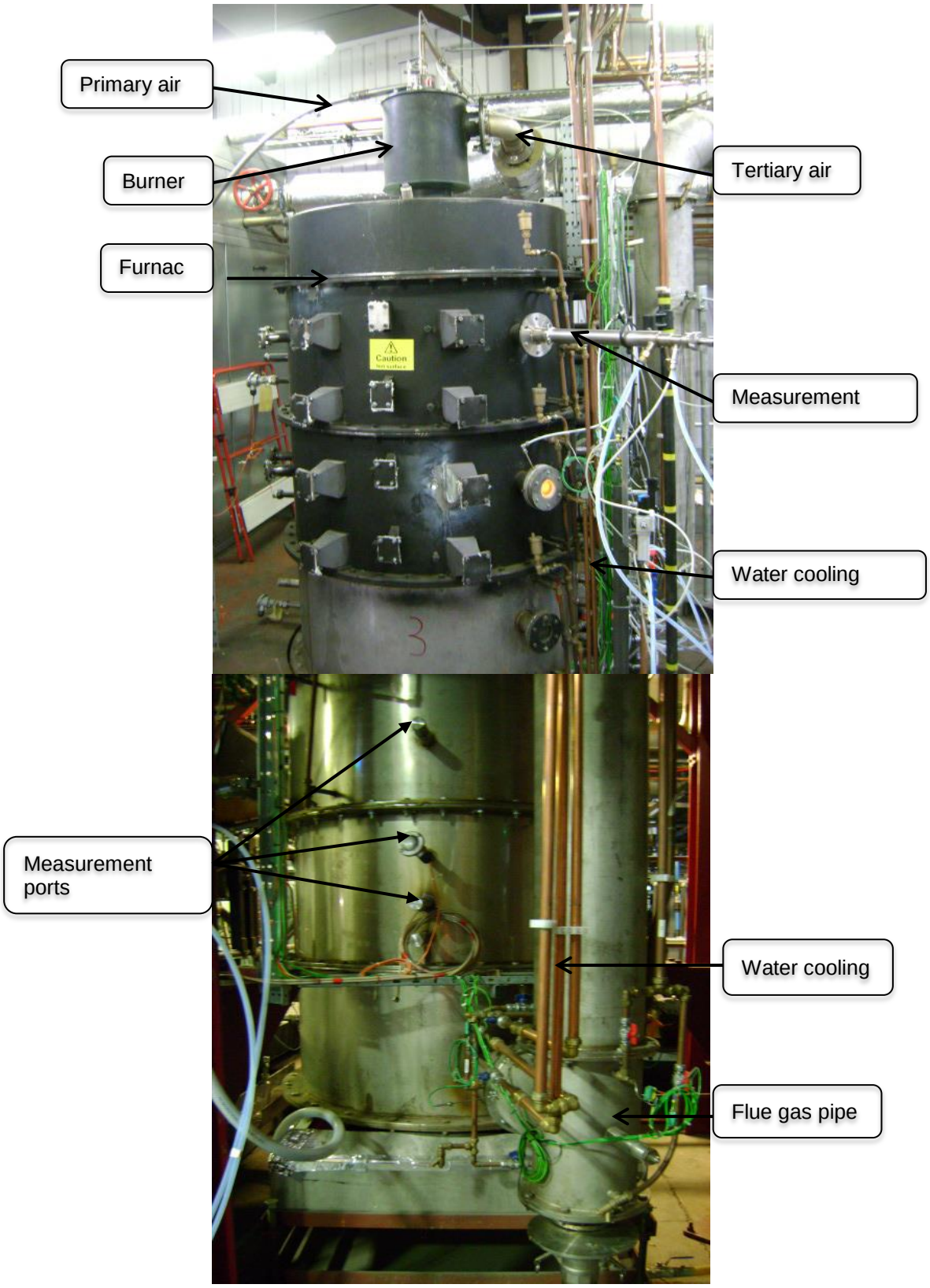

Figure 3.2 Photograph of the combustion furnace of the pilot scale testing rig, (upper) mezzanine section, and (lower) ground floor section, of the furnace.

3.5.4 Air Supply

The combustion air is supplied to the furnace at a pressure of 6-7 bars. The possible oil and moisture contaminations are removed from the supply line by two filters. The primary and tertiary air flowrates are measured by Bronkhorst thermal mass flow meters with a high precision. The mass flow rate is controlled by flow control valves, and connected to a programmable logic controller (PLC) that allows the setting of the flowrates and records the readings on the Siemens system.

The primary air is connected to the biomass feeder to carry the fuel particles to the burner. Therefore, the primary air is usually maintained at ambient temperature due to the safety concerns of fire hazards. The secondary and tertiary airlines are provided in a single line and split inside the burner by a slide gate to optimize the combustion performance. The ratio of the primary to tertiary and secondary air flows is set to provide enough primary air to transfer the biomass particles, however, not less than a minimum of 18% volumetric primary flowrate of the total required air.

The tertiary air is preheated by electrical heaters to maintain the burner inlet temperature at 523 K. This set temperature is based on the information resulting from the TGA analysis of the biomass performed in this study. It was found that the wood pellets ignition temperature is about 533-543 K, therefore the inlet temperature of the biomass to the burner should be below this temperature range, otherwise, a possible ignition could occur inside the burner and that is a major safety concern. The pre-heating temperature is controlled by sheathed Type-K thermocouples.

3.5.5 Fuel Feeding System

The biomass feeder is a K-TRON Loss-in-Weight Feeder type K2-ML-D5-T35 manufactured by Coperion K-TRON specifically for biomass with a feeding capacity of 80 kg h^{-1}. A 250 L asymmetrical hopper containing the biomass to be fed is placed on a suspension scale weighing system. This hopper discharges the biomass by gravity through a horizontal power sphere agitator to another 50 L weighing hopper that is connected to a twin-screw feeder. The agitator helps to prevent the fuel bridging and the biomass is discharged from the screw feeder to a receiving cone through a closed outlet tube. The cone is linked to the primary airline through a venturi system to carry the biomass particles along with the primary air to the burner.

The weight of the feeding device and hopper is electronically tared, and the resultant weight loss per unit of time is determined by a high resolution (4 parts per million), zero deflection, vibration and temperature immune weighing system. The actual weight loss per unit of time is compared to a desired weight loss per unit of time based upon a desired continuous feed rate set point. Any difference between the actual and desired weight loss per unit of time results in a correction to the speed of the feeding device. When the hopper content reaches a predetermined minimum weight level, the control by weight loss is briefly interrupted and the hopper is refilled.

The feeding device is controlled by a control Module that combines the feeder control function together with the motor drive and it is mounted directly on the feeder frame. A photograph and schematic diagram of the biomass feeder are illustrated in Fig. 3.3.

During the feeding process, air must enter and leave the hopper as the process material is being discharged or refilled. A vent to the atmosphere through an attached fabric filter is mounted on the lower cone. There has been a necessary modification to the vent system in order to provide enough air ingress for the biomass to be transferred through the venturi, and this is made by a bypass air line from the main primary line to the top of the cone, as shown in Fig. 3.4-(a). The negative pressure on the suction side of the venturi is monitored by a differential pressure cell. Ultimately the total primary air inlet is not changed. The biomass is loaded to the feeder by large bulk bags held by a cross frame hook as shown in Fig. 3.4-(b).

An alternative Rospen coal feeder used for coal feeding experiments that is a screw feeder transfers the coal particles to a vibrating tray, and the latter evenly drops the coal particles into the venturi and the coal particles are carried with the primary air to the burner.

3.5.6 Fuel Supply

The white wood pellets are filled in 1 m^3 closed bags and stored in a well-ventilated location to prevent decomposition or dust explosion. At first, the pellets were milled so that 88% of the total fuel weight had a particle size greater than 250 microns, and 36% was greater than 1 mm. The first attempts of firing the biomass have failed to produce a stable or a symmetrical flame. One of the reasons for these results is the relatively high particle size compared to the industrial practice with the coal combustion in the power plants. Therefore, a decision was made to further mill the wood pellets to a

particle size less than 1 mm. Usually the coal is milled to an average size 75-250 micron in the power generation industry. The small size range provides better heat transfer and distribution between the particles, increases the surface area of the contact with the oxidizer, enhances the oxidizer diffusion to the porous structure, and therefore improves the combustion flame.

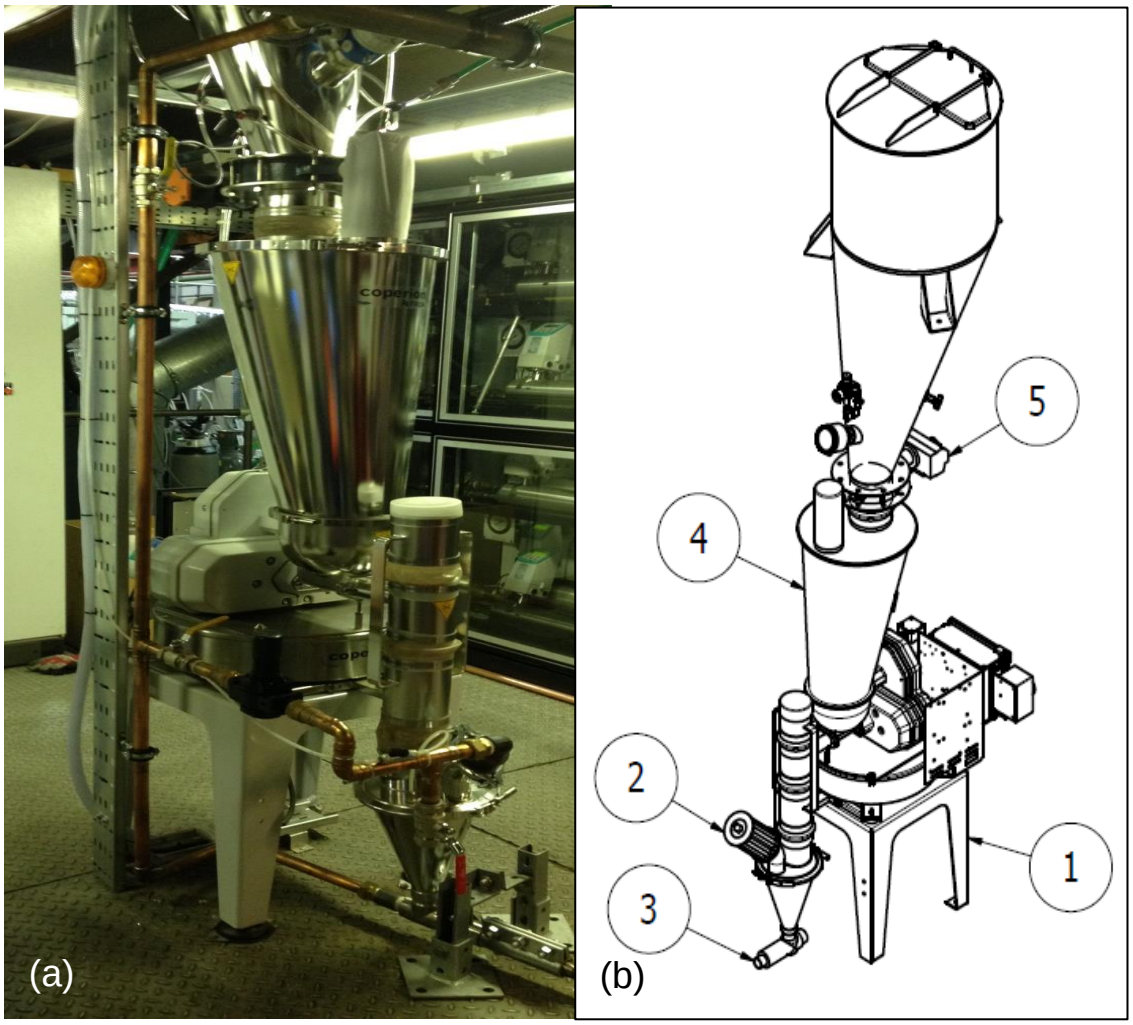

Figure 3.3 Biomass feeder (a) Photograph of the biomass feeder, and (b) Schematic diagram of the feeder: (1) Steel base and electronic panel, (2) Air vent filter, (3) Vent pipe of biomass with primary air, (4) Loss on weight hopper, and (5) Refill controller.

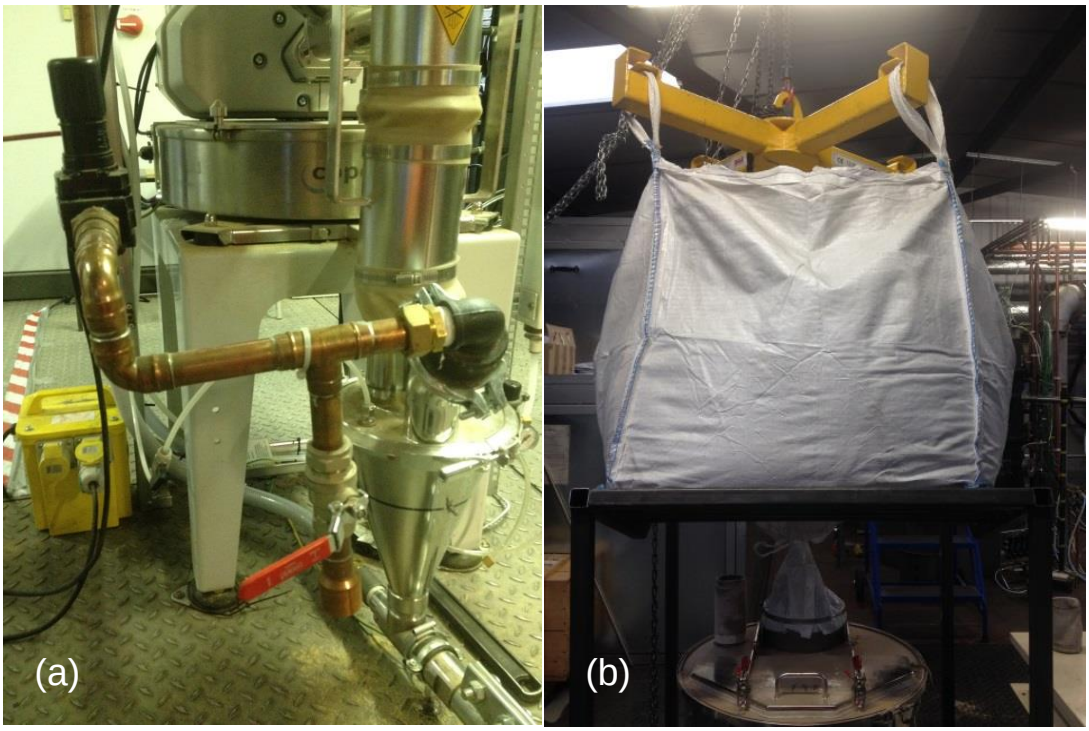

Figure 3.4 Photographs of (a) the biomass feeder indicating its ingress air to the biomass discharge cone to control the negative pressure at the venturi, and (b) the biomass loading to the feeder.

3.5.7 Flue Gas Sampling

The flue gas samples are collected from two points in the furnace body using water-cooled gas extraction probes. The first probe is permanently installed in the eighth bottom section at the exhaust level, and the second one is inserted temporarily whenever it is needed in any section of the furnace body. Each sampling probe is connected to a drainage glass bottle to remove the water droplets condensed during the cooling process, and any large particles in the fly ash. The sample is filtered with a heated filter at a temperature 453 K to prevent any vapour condensation and to remove fine particulates. While maintained at 464 K through a heated line, the sample is pumped to a Signal MAXSYS 900 Series gas analyser. The gas sample is introduced to a cooling unit inside the analyser where the temperature is 278 K to remove the remaining moisture content and reduce the gas temperature to a maximum temperature 313 K.

Another sample of the flue gas is collected from the exhaust pipe after the cyclone to measure the wet oxygen content.

3.5.8 Parameter Measurements

The combustion testing rig is provided with a set of online measurements. All the furnace section temperatures and pressure, water cooling temperatures, flow rates, and flue gas composition are monitored via a Human-Machine Interface (HMI) panel that is connected to a SCADA logging system located in a separate control room. In addition, a full control on the natural gas (NG) ON/OFF, switching to the biomass, fuel and air flowrates is maintained through the HMI panel. The panel screen displays these parameters as shown in Fig. 3.5, and in addition the online analyser measurements are recorded in 5 second intervals.

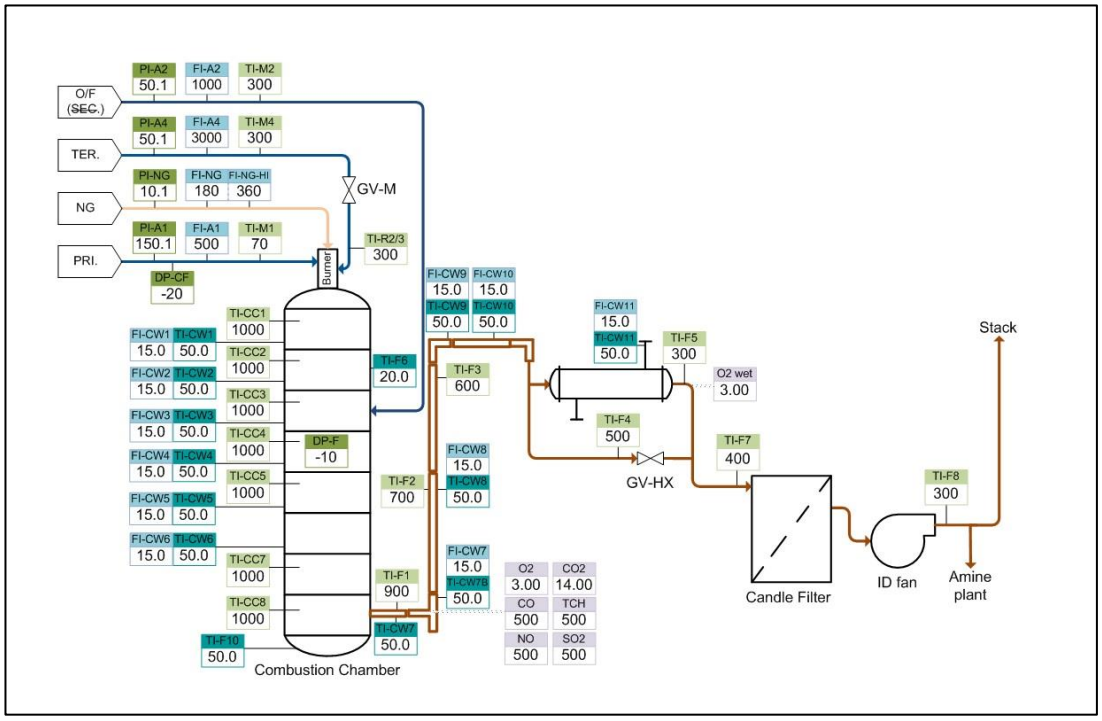

Figure 3.5 Process flow diagram of the pilot scale combustion rig (parameter values are for illustrative purposes only).

3.5.8.1 Temperatures

Ceramic sheathed Type R thermocouples are installed in each section of the furnace to measure the temperature at a distance 200 mm from the furnace wall. Type K thermocouples are installed in the flue gas and the cooling water pipes. The temperature readings of the thermocouples inside the furnace are used as indicators of the overall furnace temperature. However, they do not represent the in-flame or the real gas temperatures due to the radiation losses from the central line of the furnace to

the thermocouple positions and the convection effects near them. Therefore, these readings are not reliable for accurate radiation and convection heat transfer calculations. Instead, a suction pyrometer is used to measure the actual in-flame temperature and this can be located at different points in the top section, downwards of the location of the flame centre and it is moved horizontally for the radial measurements.

However, for the purposes of this study, of which the main concern is the burn out and the combustion efficiency, the thermocouple temperature readings are considered satisfactory.

3.5.8.2 Gaseous Emissions Analysis

The flue gas composition is determined for the dry O_2 content in wt%, dry CO_2 content in wt%, CO, NO, SO_2, and total hydrocarbons (HC) contents in ppm. A 7208MGA multi gas analyser, supplied by Signal Group Limited, is used for this purpose, see Fig. 3.6. The gas analyser combines six analysers, each one detects the emissions of one of these gases and the gas sample is introduced to the analyser at a flow rate 0-2 L min^{-1}.

The dry oxygen concentration is detected by a dumb-bell paramagnetic sensor analyser. The principle of the analysis is to detect a current generated from a displacement of a magnetic field that occurs due to the oxygen atoms and the current intensity is proportional to the oxygen concentration.

A Gas Filter Correlation (GFC) Non-dispersive Infrared (NDIR) analyser is fitted in the 7208MG analyser rack to measure the CO_2, CO, and SO_2 concentrations. An infrared (IR) light at a specific wavelength is used to measure the concentration of different gases by measuring the intensity of the radiation light that passes through a sample cell. The difference in the light intensity depends on the individual gas absorbance. The repeatability of the analyser is $\pm$1% of the total range, or $\pm$5 ppm, and the response time is less than 15 s (5% to 95%) at 1 L min^{-1} flow, with 2.0 s time constants.

All the analysers are regularly calibrated before starting the tests and during the testing day. Each analyser is connected to nitrogen for zero calibration and to the standard nitrogen-diluted gas bottle for span calibration. Further details on the gas analyser can be found in the literature [142].

Figure 3.6 Photograph of the online gas analyzer for O_2, CO_2, NO, CO, SO_2, and THC.

3.5.9 Ash Sampling and Collection Points

A combination of quantitative and qualitative approaches was used in the data collection of all the ash samples. During the testing day, samples of the fly and bottom ashes are collected after reaching a steady state condition in the biomass feeding rate, air flowrate and gaseous emission values. Normally a steady state is achieved after 30-

40 minutes of continuous running and stable data readings are deemed to occur for at least 10 minutes. As shown in Fig. 3.7 and Fig. 3.8 the fly ash is collected from three different points; the cyclone ash (CLA) that is collected in a portable catching pot connected to the bottom of the cyclone, and the bottom ash (BOA) that is collected at the flue gas exit pipe from the bottom section of the furnace. Sample collection takes place for periods of 1-hour period with a sample weight of 70-150 g of the cyclone ash and 20 g of the bottom ash.

The third fly ash sample is collected from the candle filter (FTA) at the end of the testing day which represents the aerosol particulates in the fly ash. Due to the difficulty to open the filter during the test run, the FTA sample represents the total ash accumulated during the testing day, and an average hourly flowrate is taken for the mass balance calculations.

Also, the biomass has another source of ash during combustion that is the large particles of unburned fuel, and char residue, dropped from the flue gas to the water tray combined with the ash depositions that are formed on the furnace walls and base (BCD). At the end of the testing day, after the furnace is cooled down, the water tray is drained and the bottom residue is collected. The next day, the wet sample is dried according to the standard methods and saved in a sealed container for further analysis.

Ash samples are preserved in sealed containers and flushed with nitrogen for further analysis to determine the carbon-in-ash, ash mineral composition, and loss on ignition, for the calculation of the carbon burnout and the combustion efficiency. Each analysis test was repeated three times to ensure measurement accuracy and repeatability.

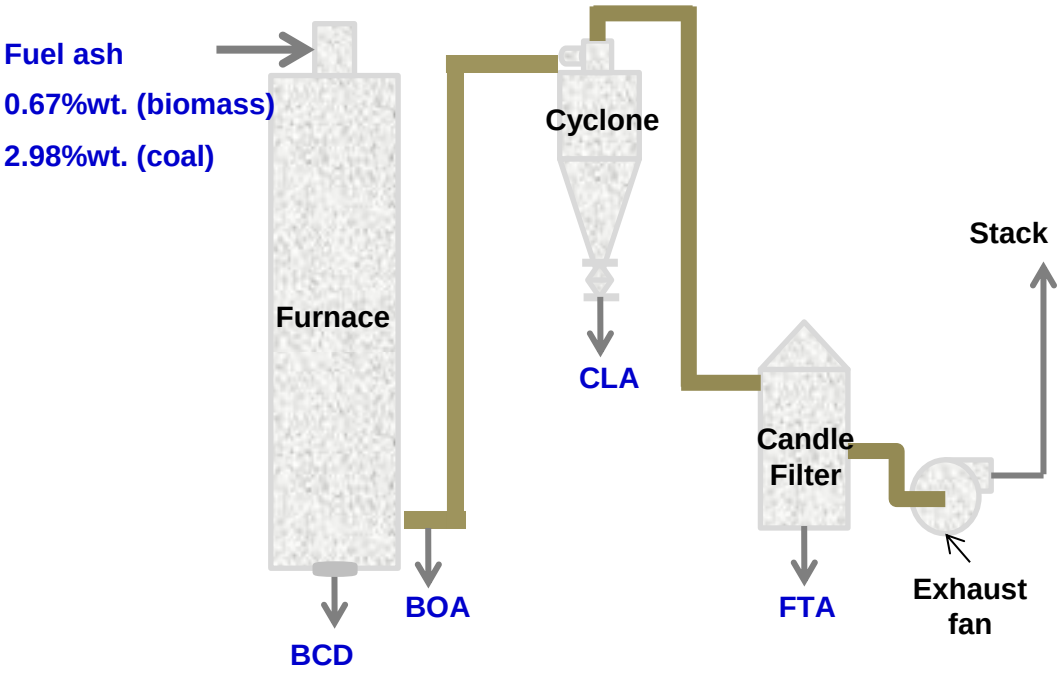

Figure 3.7 Illustration of the ash collection points in the 250 kW combustion rig.

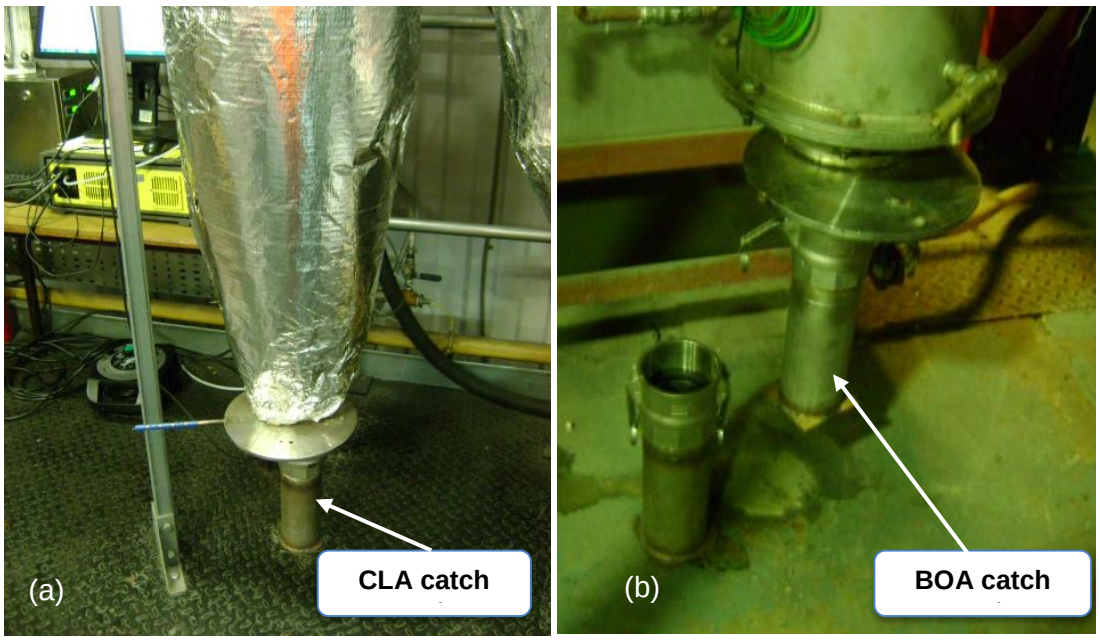

Figure 3.8 Photograph of the ash samples collection during the combustion process, (a) the fly ash at the bottom of the cyclone, and (b) the bottom ash at the furnace exit.

3.5.10 X-Ray Fluorescence Analysis

Further to the burn-out analysis, compositional analysis of the USWWP and ELC ashes that were produced at a temperature 823 K, and the collected ash samples of CLA, FTA, BOA, and BCD were carried out to characterize the ash mineral partitioning in comparison to the initial fuel ash composition. The analysis is performed by the X-ray fluorescence (XRF) method, and the PANalytical Zetium (XRF) was employed for this purpose. The machine uses a rhodium anode to produce the electron beam, and the energy dispersive system (EDS) is applied to detect the elements Na – U where the fluorescent X-rays come from the sample onto a diffraction crystal that uses Bragg's law to diffract X-rays of different wavelengths, or energies, in different directions. The gas filled detector system scans through an angular range to measure the diffraction peaks at their different angles. In case of powder samples as in this study, helium is used to fill the sample chamber, however, it absorbs the radiation from light elements such as O_2 and Cl up to F, and therefore these elements are not correctly detected. In order to achieve high quality measurements, the equipment is calibrated weekly by running two standard references; the EDS gain control, and the Drift Omnian standards. The corrections are applied automatically. The calibration results of the expected major elements in the ash samples of this study have shown ±1-5% corrections. Ash samples were placed in 37 mm open cups that are sealed in the bottom with a levelled Mylar film, making sure that the sample amount is enough to fully cover the base. Each sample test was repeated twice to ensure measurement accuracy and repeatability.

3.5.11 SEM Analysis

Furthermore, scanning-electron-microscope analysis (SEM) for the char produced at the bottom of the furnace (BCD) were carried out to investigate the particle morphology in comparison to the initial fuel chars that were produced from the TGA tests of the fuel. JEOL JSM-IT100 scanning electron microscope (SEM) was used. Char samples were prepared by coating the sample with gold layer at a thickness 20 nm, deposited at 40 mA current and 0.04 mbar vacuum of helium for 10 seconds. Various magnifications were applied to clearly illustrate the pore structure of the particles.

3.5.12 Baseline Conditions

The optimization process of the baseline cases on both the biomass and coal are beyond the scope of this study. It is based on a constant thermal input and a target exit oxygen ratio, and a target primary/tertiary oxidant split that are desired by the power generation industry to characterize the combustion process. In this study, the selected baseline thermal input is 200 kW, the exit oxygen is 3.5-3.8% by volume, and the primary oxidant is 18-20% of the total oxidant.

Accordingly, the baseline case parameters such as the fuel flowrate, oxidant flowrates, tertiary oxidant temperature, air/fuel ratio (λ), and primary/tertiary oxidant split, were determined prior to the current study experiments. Four baseline case studies; (a) USWWP-air, (b) USWWP-oxy, (c) ELC-air, and (d) ELC-oxy comprise the full set of experiments in this study. The experimental matrix of the operational parameters is shown in Table 3.2.

Table 3.2 Experimental matrix of the pilot scale biomass combustion tests.

Parameter	Unit	USWWP-air	USWWP-oxy	ELC-Air	ELC-oxy
Thermal input	kW	200	200	200	200
Fuel flowrate	$kg.h^{-1}$	41.86	41.86	25.14	25.14
Total oxidant : fuel ratio, λ	ratio	1.22	1.18	1.22	1.18
Total Oxidant flowrate	$L.min^{-1}$	3898	2460	4084	2816
Total Oxygen in Oxy case	$kg.h^{-1}$		61		63
Primary% of total air	% vol	18.0		20.2	20.2
Oxygen ratio in oxy-fuel	% vol		27		27
Exit $O_{2\ (dry)}$	% vol	3.57	3.6	3.8	3.78
T_{PA}	K	294.8	291.8	296.4	300.5
$T_{TA\ at\ burner\ inlet}$	K	250	250	250	250

3.5.13 Estimation of Errors

Data were gathered from multiple sources at various time points during the experimental work in this study, leading to several sources of error. The main error sources identified in this study are discussed in this section.

3.5.13.1 Instrumental Errors

The main equipment used for the measurements in the experimental work are as follows:

- Gas analyser
- Thermocouples
- Biomass feeder
- Air rotameters
- Analytical equipment used for fuel and ash compositional analysis, and fuel burnout (furnaces, TGA, balance, elemental analyser, Bomb calorimeter, and XRF).

Error values are collected from the analyser and equipment manuals, or factory calibration certificates. The gas analyser accuracy and repeatability is ±1% O_2, NO, CO_2, CO, and SO_2. The output is directly proportional to the absolute barometric pressure (measured at EXHAUST port). However, due to the relatively constant pressure during the day, this effect is neglected. On the other hand, the ambient temperature influences the analyser unit readings. For the temperature range 278-313 K ±0.03% is added to the zero and ±0.1% to the span per K of highest range. The zero/span drift is less than 1% of the range in 1 hour at constant temperature and pressure. The temperature errors associated with the thermocouple measurements are determined by the manufacturer as ±3%. Similarly, the air rotameters have a ±2% error. The actual biomass feeding rate was fluctuating around the set point by less than 1% due to the vibration of the platform or due to the change in the ingress pressure.

The laboratory analytical equipment used in the characterization of the fuel, ash composition and burnout analysis have different instrumental errors, some of them are determined by the manufacturers and the others are observed during the testing procedures. For example, the Carbolite muffle furnace has a ± 5 K deviation from the

set temperature. The list of instrumental errors in the flowrates, gas composition and fuel analysis is shown in Table 3.3.

Table 3.3 Instrumental errors during data measurement.

Instrument		Error value
250 kW rig experiments		
Thermocouples	Measurement accuracy	±3%
Biomass Feeder	screw drive variation	≤±1%
Drift - Biomass feeder	Feeder adjustment	5 sec
Air rotameters	Measurement accuracy	±2%
Gas analyzer	Measurement accuracy	±1%
T: Zero- Gas analyzer	Measurement accuracy	±0.03%
T: Span- Gas analyzer	Measurement accuracy	±0.1%
Drift -Gas analyzer	Measurement accuracy	1% per 1 h
Analytical equipment		
Carbolite Oven	Temp measurement variance	±4 K
Carbolite muffle furnace	Temp measurement variance	±5 K
CHN/S analyzer	Measurement accuracy	±0.1%
Bomb Calorimeter	Mass measurement, acid heat factor	±0.1%
Analytical balance	Balance measurement accuracy	±0.1 mg
TGA	Sample and Program Temperature difference	±5 K

3.5.13.2 Experimental & Human Errors

The main experimental sources of error are during the ash sample collection. The quantitative analysis of the ash partitioning and the fuel burnout requires an accurate measurement of the produced ash from all sources. Although it was possible to collect the CLA and the BOA samples accurately with the time, the FTA sample represents the average of the total testing day operation. Knowing that there are fluctuations in the

fuel and oxidant flowrates during the testing day, and ultimately the temperature and the gaseous emissions change, this could produce some errors in the composition and the amount of the collected ash. Another source of error is the ingress in the primary air that is sometimes hard to control and maintain constant. Its vacuum pressure usually fluctuates between – 9 psi to +5 psi, and that could influence the biomass feeding rate. In addition, the biomass and biomass chars are sensitive to humidity, thus the moisture content can change with direct contact with the atmosphere, especially after the drying steps and for sample mass in the range of 2-3 mg.

The compositional analysis procedures depend on the human eyes and performance accuracy. Therefore, there is a possibility of error in the measurements.

3.5.13.3 Control Measures for Errors

The gaseous emissions are measured directly as volume fractions, either ppm or % of the flue gas, and therefore, the volumetric changes due to the pressure and temperature are avoided. Furthermore, the gas analyser calibration data of the zero and span conditions are used to correct the gaseous data for instrumental uncertainties. For the external temperature effect on the gas measurements, the actual data are normalised to the temperature of the coal baseline results.

For the ingress in the primary line, the biomass feeder is self-controlled for variations in the pressure inside the balance chamber and drop tube. Also, a continuous monitoring of the ingress pressure not to exceed $\pm$1 bar is sustained.

All the compositional analysis results are the mean value of triplicates to ensure repeatability. The TGA and CHN/S analysers are calibrated daily before the testing runs. The standard deviation (STDEV) values are calculated and when there is a high deviation in the mean value, the analysis is repeated more times. The STDEV values are presented with the data results.

3.5.14 Combustion Test Calculations

The basic calculations of the combustion process aim to evaluate the overall fuel conversion reactions and the thermal performance. Essential parameters, such as air flow rate, excess air ratio, biomass calorific value, combustion temperature, and flue gas flow rate and composition are required to calculate the combustion efficiency and the thermal efficiency of the process.

3.5.14.1 Fuel Flowrate

The combustion rig is designed to operate at 250 kW maximum thermal inputs. For safety issues, the maximum thermal input selected for this research work is 200 kW for both biomass and coal. In each testing day, after reaching a steady temperature with firing natural gas (NG) for about 2 hours, switching to biomass starts at about 160 kW thermal input then the biomass feed rate is increased until the 200 kW is achieved.

For coal, the baseline conditions are set by the rig operator from previous experiments. All other operational parameters were calculated based on this value. The biomass mass flowrate is calculated based on the NCV(ar) value that is calculated from the GCV measured by the bomb calorimeter. As soon as the desired feeding rate is set in the feeder control panel, the actual feeder screw speed is set to maintain the required loss in weight of the biomass, and takes few seconds to reach the set point.

3.5.14.2 Air Flowrates

For each experiment setup, the predicted primary air (PA) and tertiary air (TA) flowrates are calculated based on the material balance with the fuel feeding rate to achieve the required access air or the exit O_2 designed for that experiment. A spreadsheet that is prepared for this purpose is shown in Appendix A as an example for all combustion cases. Biomass contains the five main fuel elements C, H, S, N, and O, and the oxygen contributes in the oxidation reactions of the other four elements, hence the total required amount of oxygen is reduced.

Upon determination of the fuel feeding rate, the elemental mass flowrates (C, H, N, O, S) are calculated based on the ultimate analysis of the fuel, then converted to the molar flowrates.

If the C and H are completely oxidized during the combustion process, the fuel-N is converted to NO, and the S is converted to SO_2 the required stoichiometric moles of oxygen are calculated according to the following chemical reaction equations:

$$C + O_2 \rightarrow CO_2 \quad (3.7)$$

$$2H + 1/2O_2 \rightarrow H_2O \quad (3.8)$$

$$N + 1/2O_2 \rightarrow NO \quad (3.9)$$

$$S + O_2 \rightarrow SO_2 \quad (3.10)$$

However, the fuel nitrogen might only be converted by 25% to 50% depending on conditions. There are competing reactions in rich/lean combustion for fuel-N to find a pathway through HCN or NH_3 intermediates to N2 rather than NO or NO_2. Taking into consideration the fuel oxygen content, the total theoretical oxygen is calculated as follows:

$$\sum \bar{m}_{O_2,\text{air}} \left[\text{kg } O_2 \text{ kg}_{\text{fuel}}^{-1}\right] = \left(X_{C,f}\frac{M_{O_2}}{M_C} + \frac{X_{H,f}}{2}\frac{M_{O_2}}{M_{H_2}} + X_{S,f}\frac{M_{O_2}}{M_S} + X_{N,f}\frac{M_{O_2}}{M_N} - X_{O,f}\right) \quad (3.11)$$

where,
$\bar{m}_{O2,\text{air}}$: Theoretical stoichiometric oxygen , (kg kg^{-1} fuel)
M_i: molecular mass of element, (kg kmol^{-1})
$M_C = 12.01115, \quad M_H = 1.00797, M_S = 32.064, M_{O_2} = 31.9988$
$X_{i,f}$: mass fraction of element i in the fuel

Then the actual oxygen molar flowrate is calculated based on the access ratio (λ) as follows:

$$n_{O_2,\text{air}} = \sum \frac{\bar{m}_{O_2\ \text{air}}}{M_{O_2}} . \lambda \quad (3.12)$$

Based on the theoretical oxygen molar flowrate and the access ratio (λ), the actual air flowrates are calculated taking the O_2 molar ratio in the air as 20.95% at standard conditions (0 °C and 1 atm).

$$n_{N_2,\text{air}} = \left(n_{O_2\ \text{air}}\frac{Y_{N_2\ \text{air}}}{Y_{O_2\ \text{air}}}\frac{M_{N_2}}{M_{O_2}}\right) \quad (3.13)$$

where,
$Y_{O_2\ \text{air}}$: volume fraction of O_2 in air ($= 0.2095$)
$Y_{N_2\ \text{air}} = 1 - Y_{O_2\ \text{air}}$

$$n_{\text{air}} = n_{\text{O}_2\text{air}} + n_{\text{N}_2\ \text{air}} \tag{3.14}$$

Regularly, the air flowrate meters measure the volumetric flowrate in the pipelines; hence the air molar flowrate is converted to the volumetric flowrate by the ideal gas low at STP (273 K, 1 atm). In addition, the room temperature at the rig facility is also measured, hence, the actual volumetric flowrate is corrected accordingly.

The air density (ρ_{air}):

$$\rho_{\text{air}}\ [\text{kg.Nm}^{-3}] = \frac{P_o}{\frac{R}{M_{\text{air}}}T_o} \tag{3.15}$$

where,
ρ_{air}: density of air, (kg m^{-3})
M_{air}[kg kmol^{-1}] : air molecular mass $= Y_{\text{O}_2\ \text{air}}M_{\text{O}_2} + Y_{\text{N}_2\ \text{air}}M_{\text{N}_2}$

The air mass flowrate $\dot{m}_{\text{air}}$:

$$\dot{m}_{\text{air}}[\text{kg h}^{-1}] = \dot{m}_{\text{F}} \times \overline{m}_{\text{air}} \tag{3.16}$$

The air volumetric flowrate $\dot{V}_{\text{air}}$:

$$\dot{V}_{\text{air}}\ [\text{Nm}^3.\text{h}^{-1}] = \frac{\dot{m}_{\text{air}}}{\rho_{air}} \tag{3.17}$$

3.5.14.3 Primary Air Entrainment

The biomass feeding system is designed to convey the solid particles by the primary air flow through a venturi system at the bottom of the feeder drop tube. This procedure leads to a vacuum inside the drop tube when the feeding system is completely sealed. If this vacuum is higher than -1 bar the electronic balance reading of the biomass feeder is disturbed and the screw drive changes the speed to overcome this disturbance. Due to this issue, there was a problem of biomass blockage in the start-up attempts at the primary flow neck. Accordingly, a side ingress flow pipe that is partitioned from the primary air is connected to the bottom drop tube cone to control the vacuum pressure in the feeder and maintain a smooth flow of the biomass particles. The flowrate of this ingress is measured by a control valve and rotameter fitted in the pipe.

3.5.14.4 Flue Gas Flow & Composition

The flue gas flow is a result of the fuel combustion with the air (O_2) and can be calculated from the mass balance over the furnace. According to Eq. (3.7- 3.10), the main constituents of the flue gas are CO_2, H_2O, SO_2, NO, N_2, and O_2. The wet *FG* flow can be calculated by the summation of the gas species mass flowrates:

$$\bar{m}_{\mathrm{CO_2}}[\mathrm{kg\ CO_2\ kg_{fuel}^{-1}}] = X_{\mathrm{C,f}}\frac{M_{\mathrm{CO_2}}}{M_{\mathrm{C}}} \tag{3.18}$$

$$\bar{m}_{\mathrm{SO_2}}[\mathrm{kg\ SO_2\ kg_{fuel}^{-1}}] = X_{\mathrm{S,f}}\frac{M_{\mathrm{SO_2}}}{M_{\mathrm{S}}} \tag{3.19}$$

$$\bar{m}_{\mathrm{H_2O}}[\mathrm{kg\ H_2O\ kg_{fuel}^{-1}}] = \frac{X_{\mathrm{H,f}}}{2}\frac{M_{\mathrm{H_2O}}}{M_{\mathrm{H_2}}} + X_{\mathrm{H_2O,f}} \tag{3.20}$$

$$\bar{m}_{\mathrm{N_2}}[\mathrm{kg\ N_2\ kg_{fuel}^{-1}}] = n_{\mathrm{N_2,air}}M_{\mathrm{N_2}} \tag{3.21}$$

$$\bar{m}_{\mathrm{NO}}[\mathrm{kg\ NO\ kg_{fuel}^{-1}}] = X_{\mathrm{N,f}}\frac{M_{\mathrm{NO}}}{M_{\mathrm{N}}} \tag{3.22}$$

$$\bar{m}_{\mathrm{O_2}}[\mathrm{kg\ O_2\ kg_{fuel}^{-1}}] = \frac{\bar{m}_{\mathrm{O_2\ air}}}{\lambda_{\mathrm{T}}}(\lambda_{\mathrm{T}} - 1) \tag{3.23}$$

$$\sum FG\ [\mathrm{kg\ FG\ kg_{fuel}^{-1}}] = \bar{m}_{\mathrm{CO_2}} + \bar{m}_{\mathrm{SO_2}} + \bar{m}_{\mathrm{H_2O}} + \bar{m}_{\mathrm{N_2}} + \bar{m}_{\mathrm{NO}} + \bar{m}_{\mathrm{O_2}} \tag{3.24}$$

The flue gas mass fractions X_{CO2}, X_{H2O}, X_{SO2}, X_{N2}, X_{NO}, and X_{O2} are found by normalizing the flue gas mass.

3.5.14.5 Fuel Burnout & Combustion Efficiency

When biomass is burned then the mineral content forms the ash particles with a portion of unburned volatiles and carbon. The unburned carbon ratio represents a loss in the thermal energy produced and the combustion efficiency. The energy loss due to incomplete combustion can be calculated from the carbon monoxide (CO) concentration ($\bar{E}_{\mathrm{CO}}$) in the flue gas and the unburned carbon ($\bar{E}_{\mathrm{uc}}$) found in the ash as follows:

$$\bar{E}_{\mathrm{CO}}[\mathrm{kJ\ kg_{fuel}^{-1}}] = CV_{\mathrm{CO}}.\bar{m}_{\mathrm{CO}} \tag{3.25}$$

where,
$\bar{E}_{\mathrm{CO}}$: Energy loss of incomplete combustion to CO, ($\mathrm{kJ\ kg_{fuel}^{-1}}$)
CV_{CO}: calorific value of $\mathrm{CO} = 10088\ \mathrm{kJ\ kg_{CO}^{-1}}$ at 298 K
$\bar{m}_{\mathrm{CO}}$: mass of CO produced per kg fuel, ($\mathrm{kg_{CO}\ kg_{fuel}^{-1}}$)

$$\bar{E}_{\mathrm{uc}}[\mathrm{kJ\ kg_{fuel}^{-1}}] = 34080\ \bar{m}_{\mathrm{uc}} \tag{3.26}$$

where,
$\bar{E}_{\mathrm{uc}}$: Energy loss of unburned carbon, ($\mathrm{kJ\ kg_{fuel}^{-1}}$)
$\bar{m}_{\mathrm{uc}}$: mass of unburned carbon per kg fuel, ($\mathrm{kg_C\ kg_{fuel}^{-1}}$)
34080 : calorific value of C, ($\mathrm{kJ\ kg_C^{-1}}$)

The combustion efficiency (η_{Comb}) is a process design parameter related to the incomplete combustion of the fuel and fuel char. The heat losses in the CO and C enthalpies calculated in Eqs. (3.25) and (3.26) are combined to calculate the combustion efficiency as follows:

$$\eta_{\mathrm{Comb}} = 1 - \frac{(CV_{\mathrm{uc}}.\bar{m}_{\mathrm{uc}} + CV_{\mathrm{CO}}.\bar{m}_{\mathrm{CO}})}{NCV_{\mathrm{fuel}}} \tag{3.27}$$

In the power generation industry, engineers collect the fly ash and measure the combustible species by burning the fly ash at 1023 K and measure the loss in weight due to ignition (named Loss-on-Ignition) as an indication of the combustion efficiency of the process [143]. This procedure follows the ATSM standard method D7348 [144]. The Loss-on-Ignition (LOI) is calculated as follows:

$$LOI = \frac{m_{\mathrm{uc}}}{m_{\mathrm{FA}}} \tag{3.28}$$

where,
LOI: Loss − on − Ignition in the fly ash
m_{uc}: mass of unburned combustibles in the fly ash sample, (g)
m_{FA}: mass of dry fly ash sample, (g)

The carbon burnout is calculated as follows:

$$C_{\mathrm{BO}} = 1 - \frac{\bar{m}_{\mathrm{uc}}}{\bar{m}_{\mathrm{tc}}} \tag{3.29}$$

where,
C_{BO}: Carbon burnout fraction
$\bar{m}_{\mathrm{tc}}$: total combustibles in the fuel, (kg kg^{-1}fuel)

Substituting Eq. (3.28) in Eq. (3.29), the final carbon burnout can be written as follows:

$$C_{\mathrm{BO}} = 1 - \frac{LOI}{(1 - A_{\mathrm{fuel}})} \tag{3.30}$$

However, Eq. (3.30) can be questioned as a reliable evaluation of the carbon burnout and combustion efficiency for two reasons;

i. In pulverized biomass combustion, there is a reasonable amount of char accumulated at the bottom of the furnace due to the large particle size of the biomass, and this char normally contains a large fraction of unburned carbon. Therefore, the unburned carbon fraction should be calculated for all ash streams in the process.
ii. The LOI testing method overestimates the carbon content in the fly ash sample due to the presence of volatile organic compounds (VOC) in the fly ash. Fan and Brown [145] measured the LOI of 70 combustion boiler ash samples, and compared the results with a TGA combustion of the unburned carbon after removal of the VOC under inert gas conditions. They found that the LOI overestimated the unburned carbon by a minimum 20% that resulted from the VOC contribution to the fly ash. Also, Burris et al. [146] found that the LOI testing in a temperature 1223 K gives higher values of unburned carbon than a combustion at 973 K. This difference in the combustion yield is due to the decomposition of metal carbonates at temperatures higher than 973 K.

For the above-mentioned reasons, the author suggests distinguishing between two process parameters; the combustion efficiency, and the fuel burnout. The first is related only to the incomplete combustion of carbon to CO and the unburned carbon in the char residue, while the latter is the total burnout of the fuel. Any burning process by a furnace or a TGA will result in a total weight loss, including the carbon, VOC and non-organic volatiles decomposition. Therefore, the carbon contents in the cyclone ash (CLA), filter ash (FTA), bottom ash (BOA), and the char residues that are collected in the water tray ash (BCD), are determined by the CHN/S analyzer to calculate the total actual unburned carbon $\overline{m}_{uc}$ in kg carbon per kg fuel as follows:

$$\overline{m}_{\mathrm{uc}} = (X_{\mathrm{uc}})_{\mathrm{CLA}}.\dot{m}_{\mathrm{CLA}} + (X_{\mathrm{uc}})_{\mathrm{BOA}}.\dot{m}_{\mathrm{BOA}} + (X_{\mathrm{uc}})_{\mathrm{FTA}}.\dot{m}_{\mathrm{FTA}} + (X_{\mathrm{uc}})_{\mathrm{BCD}}.\dot{m}_{\mathrm{BCD}} \quad (3.31)$$

where,
$(X_{\mathrm{uc}})_{\mathrm{CLA}}, (X_{\mathrm{uc}})_{\mathrm{BOA}}, (X_{\mathrm{uc}})_{\mathrm{FTA}}, (X_{\mathrm{uc}})_{\mathrm{BCD}}$: are the mass fractions of unburned carbon in CLA, BOA, FTA, and BCD, respectively
$\dot{m}_{\mathrm{CLA}}, \dot{m}_{\mathrm{BOA}}, \dot{m}_{\mathrm{FTA}}$, and $\dot{m}_{\mathrm{BCD}}$: are the mass flowrates of the ash streams, $(\mathrm{kg\ kg}_{\mathrm{fuel}}^{-1})$

Then, substitution of $\overline{m}_{\mathrm{uc}}$ in Eq. (3.29), and using the total carbon in fuel instead of the total combustibles, gives the correct carbon burnout, and substitution of $\overline{m}_{\mathrm{uc}}$ in Eq. (3.27), gives the correct combustion efficiency.

Chapter 4 Kinetic Theory & Reaction Models of the Pyrolysis & Char Combustion

4.1 Chapter Overview

Part of this study, is the investigation of the fundamental combustion kinetics, and the TGA data are employed for this purpose. This chapter presents the derivation of the mathematical models that will be used to calculate the kinetics parameters of the devolatilization and the char combustion steps. The kinetic theories behind these two steps are discussed. For the devolatilization, integral iso-conversional model of *Coats and Redfern* (*CR*) rate law is used to predict the non-isothermal kinetic parameters of the TGA data. Three models are examined to express the function of mass conversion; the n-power, the diffusion, and the particle contraction. More importantly, the intrinsic reactivity rate law of the char combustion is derived. In addition, the published data of the specific internal surface area of the char and the char densities are employed to predict these properties of the fuels in the current study by correlation to the original fuel properties and the temperature.

4.2 Pyrolysis Kinetics

The solid decomposition rates are assumed to be proportional to the remaining mass of the sample [71]. Therefore, the rate of mass loss is usually expressed by the ratio dw/dw_o, as w is the mass of the sample present at time t and (o) denotes the initial state. Usually w is expressed by the mass fraction converted (α) and α is:

$$\alpha = \frac{w_o - w}{w_o - w_f} \tag{4.1}$$

where,
α : is the fraction of reactant mass converted at time t
w_o : is the initial mass of sample, kg
w : is the mass of solid reactant at time t,
w_f : is the final mass of sample, kg

and (1-*α*) is the remaining unreacted mass. As far as this study concerned, the TGA data will be treated with the global power reaction model to determine the apparent kinetics parameters as follows:

$$\frac{\mathrm{d}\alpha}{\mathrm{d}t} = k.(1-\alpha)^n \tag{4.2}$$

where,
k: reaction rate constant, (s^{-1})
n : is the appearant reaction order
t: time, (s)

The rate constant can be expressed by the Arrhenius kinetic equation:

$$k = A.exp(-\frac{E_a}{RT}) \tag{4.3}$$

where,
A: pre − exponential factor, (s^{-1}).
E_a: apparent activation energy, (kJ mol^{-1}).
R: universal gas constant = 8.314459 (J mol^{-1} K^{-1})
T: the absolute temperature, (K)

The integral iso-conversional model of Coats and Redfern (CR) is widely used in the prediction of the non-isothermal kinetics parameters of the TGA data [11, 147, 148]. The CR method can fit the data of *(α,T)* to determine the kinetic parameters only if the rate law takes the form of an n-power law [149]. With an Arrhenius expression for the rate constant, the rate of conversion with the temperature change can be expressed as follows:

$$\frac{\mathrm{d}\alpha}{\mathrm{d}T}.\frac{\mathrm{d}T}{\mathrm{d}t} = A.(1-\alpha)^n.exp(-\frac{E_a}{RT}) \tag{4.4}$$

At constant heating rate, the rate equation can be written:

$$\frac{\mathrm{d}\alpha}{\mathrm{d}T} = \frac{A}{\theta}(1-\alpha)^n.exp(-\frac{E_a}{RT}) \tag{4.5}$$

w$here$,
θ: heating rate, (K min^{-1})

By integrating both sides of Eq. (4.5) and with simplifications described in other references [11, 149], we obtain a linear logarithmic relationship when the left-hand side is plotted against T^{-1}:

$$\mathrm{Ln}\frac{1-(1-\alpha)^{1-n}}{(1-n)T^2} = \mathrm{Ln}\frac{AR}{\theta E_\mathrm{a}} - \frac{E_\mathrm{a}}{RT} \tag{4.6}$$

Or in a more general form of *f(α)*:

$$\mathrm{Ln}\left(\frac{\mathrm{g}(\alpha)}{T^2}\right) = \mathrm{Ln}\frac{AR}{\theta E_\mathrm{a}} - \frac{E_\mathrm{a}}{RT} \quad (4.7)$$

$$g(\alpha) = \int \frac{\mathrm{d}\alpha}{f(\alpha)} \quad (4.8)$$

The intercept is $\mathrm{Ln}\left(\frac{AR}{\theta E_\mathrm{a}}\right)$ and the slope is $-\frac{E_a}{R}$

The function of the degree of conversion *f(α)* can take the form of a power law with a reaction of order n, or it can be expressed by the diffusion or contraction models listed elsewhere [11, 71]. In terms of the power law, the value of (*n*) giving the best fit is identified by the least square coefficient from the linear regression procedure. Values of *n* are expected to be 1, 4/3, 1.5, 5/3 and 2 because these can be reasonably explained by the geometrical, contracting or reaction order mechanisms of the chemical reaction [149]. The following models of *f(α)* are used in this study:

Power-Law: $f(\alpha) = (1-\alpha)^n$ (4.9)

3d-Diffusion: $f(\alpha) = \frac{3}{2}\left[(1-\alpha)^{\frac{2}{3}}(1-(1-\alpha)^{1/3}\right]^{-1}$ (4.10)

Grain contracting: $F(\alpha) = (1-\alpha)^{2/3}$ (4.11)

4.3 Char Combustion Kinetic Theory

There are many rate law models used to explain the char combustion in the literature. Generally, the char combustion data were treated with Arrhenius model as a global n-order reaction [91, 99, 150-152] and the char is assumed to be a sphere of pure carbon [153].

The char combustion is considered as a heterogeneous reaction of carbon with oxygen that occurs at the char particle's surface [154]. The overall reaction can occur in two mechanisms:

$$\mathrm{C_s} + \mathrm{O_{2g}} \rightarrow \mathrm{CO_{2g}} \qquad (\Delta H = -394\ \mathrm{kJ.mol^{-1}\ K^{-1}}) \quad (4.12)$$

$$2\mathrm{C_s} + \mathrm{O_{2g}} \rightarrow 2\mathrm{CO_g} \qquad (\Delta H = -111\ \mathrm{kJ.mol^{-1}\ K^{-1}}) \quad (4.13)$$

At elevated temperatures in the combustion flame zone, and for large particles, CO can react with O_2 in the boundary layer to form CO_2 as follows:

$$2\mathrm{CO} + \mathrm{O}_{2\mathrm{g}} \rightarrow 2\mathrm{CO}_{2\mathrm{g}} \qquad (\Delta \mathrm{H} = -283\ \mathrm{kJ.mol^{-1}\ K^{-1}} \tag{4.14}$$

When this reaction occur, the oxygen will be insufficient for the oxidation of carbon, and CO_2 will react with the carbon according to the following reaction, namely Boudouard Reaction [10]:

$$\mathrm{CO}_{2(\mathrm{g})} + \mathrm{C}_{(\mathrm{s})} \rightarrow 2\mathrm{CO}_{(g)} \qquad (\Delta H = +172\ \mathrm{kJ.mol^{-1}\ K^{-1}}) \tag{4.15}$$

This type of bimolecular reaction can be based on the elementary collision-controlled bimolecular reaction mechanism that assumes when two molecules of species collide with a certain level of energy, and in the right orientation, the reaction occurs [155]. During the reaction, the mass loss of the solid particles of char will reduce the surface area of the particle, hence reduce the reaction rate. In such reactions, the rate starts at its maximum then decay when the reaction is complete. There are many factors that determine the reaction rate of the char combustion, such as the particle size, char porosity, particle density, oxidising gas pressure and combustion temperature.

4.3.1 Essenhigh Model for Rate Equation of Carbon Combustion

For the combustion of porous carbon particles, Essenhigh [153], assumes that the complex reaction occurs in a sequence of steps starting with the diffusion of oxygen through the stagnant boundary layer of nitrogen outside the particle to reach the external surface of the particle, chemisorption of oxygen on the external surface of the particle, internal (pore) diffusion, then further reaction of the remaining oxygen and carbon, and finally the diffusional discharge of the reaction products. The char is assumed a uniform sphere of carbon, and the reaction rate is the mass of carbon consumed per unit area, and proportional to the oxygen pressure. He represents the reaction rate as follows:

$$R_A = -\rho_{\mathrm{p}}.\frac{\mathrm{d}r}{\mathrm{d}t} = -k.P_{\mathrm{O}_2} \tag{4.16}$$

where,
R_A: is the char combustion reaction rate, ($\mathrm{kg\ m^{-2}\ s^{-1}}$)
r : is the particle radius, (m)
ρ_{p} : is the particle density, ($\mathrm{kg\ m^{-3}}$)
k : is the specific reaction rate coefficient, ($\mathrm{s^{-1}}$)
P_{O_2}: is the oxygen pressure, ($\mathrm{kg\ m^{-2}}$)

4.3.2 Langmuir-Hinshelwood Rate Law

The Langmuir-Hinshelwood rate expression, assumes that the reaction rate is controlled by two kinetic mechanisms, first is a non-dissociative adsorption of oxygen particles on the carbon surface to form the complex C(O), and the second step is the desorption of C(O) [97, 150, 156] .

$$C + O_2 \rightarrow C(O) \quad (4.17)$$

$$C(O) \rightarrow CO \quad (4.18)$$

4.3.3 Semi-global Kinetics

It was found that both the single step global model and the Langmuir-Hinshelwood model do not describe the reaction order data of char combustion [97]. Observations of CO_2 forming in the reaction suggested the reaction of gaseous oxygen with the complex C(O) as an intermediate step [101, 157]:

$$C(O) + O_2 \rightarrow CO_2 + C(O) \quad (4.19)$$

$$C(O) \rightarrow CO \quad (4.20)$$

In the TGA, the rate of char combustion represents the rate of weight loss per unit of external surface area of the char. Few researchers have implemented the TGA technique under kinetic control regime (temperatures < 873 K, combustion Zone I) [158]. Other researchers have calculated the kinetic parameters of the biomass char combustion under higher temperatures (1173 – 1473 K, combustion Zone II) [107, 159, 160].

The reaction is controlled by the diffusion theory when the oxygen concentration is negligible on the carbon surface, and assumed under chemisorption control if the carbon is subject to an aerodynamic field, once the sample is subject to a stream of air or oxygen. In this case the oxygen concentration on the carbon surface is high and the diffusion boundary layer is negligible [156]. During the reaction, the mass loss of the solid particles of char reduces the surface area of the particle, hence reduces the reaction rate. In such reactions, the rate starts at its maximum then decays when the reaction is complete.

The factors that determine the char combustion rate are many, such as the particle size, char porosity, particle density, oxidising gas pressure and combustion

temperature. The main investigation of this study is the effect of the temperature on the kinetics behaviour. In terms of the temperature dependence, the reaction takes place in two rate-controlling zones: Zone I at low temperatures (<900 K) where the oxygen is adsorbed at the external and internal pores of the particle, that burns with a constant size but reduced density [91]. Therefore, the reaction rate is proportional to the particle size. The apparent activation energy (E_a) and order (m) are true values. Whereas Zone II reactions occur at higher temperatures (900<T <1500 K) at which the oxygen is mainly consumed on the surface with both size and density reduction. In these conditions, the reaction is both chemically and diffusion controlled [91, 150, 161]. Furthermore, the apparent order of the oxygen concentration is (m+1)/2, where m is the order observed in Zone I, and the observed activation energy is $E_a/2$. The mathematical model in the next section describes those relations.

4.3.4 Development of the Char Combustion Model

The char combustion rate obtained from the TGA data can be simply represented by the rate law of a single particle combustion as follows [69]:

$$R_m = \frac{1}{(1-\alpha)^z} . \frac{\mathrm{d}\alpha}{\mathrm{d}t} = K_o . [C_o]^n \tag{4.21}$$

where,
R_m: reaction rate, gram carbon reacted per gram of original char per second, (s^{-1})
K_o: is the reaction rate coefficient, (kg m^{-2} s^{-1} [kg. m^{-3}]$^{-n}$)
$[C_o]$: is the bulk reactant gas concentration, (kg m^{-3})
z: is the reaction order of the carbon

However, to understand the overall reactivity, the porous characteristics of the char require the consideration of the local gas concentration on the external and internal surface area of the char pores. In addition to the diffusion limitations of the reactant gas through the boundary layer, the gas diffusion to the internal pore voids is another factor of the reaction rate to be considered. Thus, the true chemical reaction rate of the char combustion (the intrinsic rate), is the reaction rate per unit surface area of the internal or external pore surface area where there is no heat or mass transfer limitations [106].

The global intrinsic surface reaction rate (per unit of surface area) $\ddot{R}$ is a function of the concentration of the carbon atoms per surface area of the pore and the local concentration of the oxidant gas. It was given by Laurendeau [90] as follows:

$$\ddot{R} = m_{\mathrm{c}} \,.\, r_s([C_t].[\mathrm{C_L}]\,.\,T) \tag{4.22}$$

where,
$\ddot{R}$: Intrinsic rate for the hetrogeneous char reaction, (kg carbon. $\mathrm{m^{-2}\ s^{-1}}$)
m_{c} : mass of carbon atom (kg. $\mathrm{atom^{-1}}$)
r_s : is the conversion rate of carbon atoms from solid to gas (carbon atom. $\mathrm{m^{-2}\ s^{-1}}$)
$[C_t]$: concentration of active carbon sites per unit area, (atom $\mathrm{m^{-2}}$)
$[C_{\mathrm{L}}]$: local gas concentration, (kg $\mathrm{m^{-3}}$)

If we approximate the carbon chemical rate as follows:

$$r_s = k.[C_t].[C_{\mathrm{L}}]^m \tag{4.23}$$

Then, we obtain

$$\ddot{R} = m_c.k.[C_t].[C_{\mathrm{L}}]^m \tag{4.24}$$

$$\ddot{R} = \dot{K}.[C_{\mathrm{L}}]^m \tag{4.25}$$

where,
m : is the true reaction order
k: chemical rate coefficient ($\mathrm{s^{-1}}$)
$\dot{K}$: is the intrinsic rate coefficient $= m_{\mathrm{c}}.k.[\mathrm{C_t}]$, (kg $\mathrm{m^{-2}\ s^{-1}(kg\ m^{-3})^{-m}}$)

The relation between the overall reaction rate and the intrinsic rate of the heterogeneous carbon oxidation on the particle surface $\ddot{R}_{\mathrm{s}}$ is frequently expressed as follows [90]:

$$R_m = (\eta.A_{\mathrm{i}} + A_{\mathrm{e}}).\ddot{R}_{\mathrm{s}} \tag{4.26}$$

where,
η: effectiveness factor ($\eta \leq 1$)
A_{i}: Specific internal pore surface area, ($\mathrm{m^2\ kg^{-1}}$)
A_{e}: Specific external particle surface area, ($\mathrm{m^2\ kg^{-1}}$)
$\ddot{R}_{\mathrm{S}}$: Intrinsic rate of char reaction on the particle external surface, (kg carbon. $\mathrm{m^{-2}\ s^{-1}}$)

Then we obtain

$$R_m = (\eta.A_{\mathrm{i}} + A_{\mathrm{e}}).\ddot{K}.[C_{\mathrm{s}}]^m \tag{4.27}$$

where,
$[C_{\mathrm{s}}]^m$: is the gas concentration at the particle surface, $(\mathrm{kg\ m^{-3}})^{\mathrm{m}}$

The effectiveness factor η represents the actual chemical reaction rate as a function of the maximum rate possible on the total internal surface area of the particle [162]. In char combustion, it is the fraction of the specific internal surface area A_i that is necessary for the reaction if the local intrinsic rate was identical to $\ddot{R}_s$.

In most cases $\eta . A_{\mathrm{i}} \gg A_{\mathrm{e}}$ then we obtain:

$$R_m = \eta . A_{\mathrm{i}} . \ddot{K} . [C_{\mathrm{s}}]^m \tag{4.28}$$

In order to calculate η, a correlation with the Thiele modulus ∅ can be used for this purpose as shown in Eq. (4.29) [69]. Thiele modulus is a function of the particle size, pore surface reaction rate and the diffusion coefficient [162].

$$\left[\frac{\eta \emptyset^2 . (m+1)}{2}\right] = \frac{\gamma . R_m (m+1)}{[8 . D_{\mathrm{e}} . C_{\mathrm{s}}]} \tag{4.29}$$

where,
∅: Thiele modulus
γ: the ratio between particle volume and particle surface area, (m)
D_{e}: Effective diffusion coefficient, ($\mathrm{m^2\ s^{-1}}$)

The right hand side of Equation (4.29) can be calculated from the experimental data, then η can be calculated from the relation between η and $\eta\phi^2$ as derived by Mehta and Aris [90].

The effective diffusion coefficient is related to the overall diffusion coefficient of the gas through the particle internal and external surface area as proposed by Satterfield [163]:

$$D_{\mathrm{e}} = \frac{D . \psi}{\tau^2} \tag{4.30}$$

where,
D : overall pore diffusion coefficient, ($\mathrm{m^2\ s^{-1}}$)
ψ : particle porosity
τ^2: tortuosity $= (\sin \Omega)^{-1}$
where Ω is the average angle of pore intersecting the external surface of the particle.

It is assumed that $\Omega = 45^o$ [90], hence, $\tau = \sqrt{2}$.

The overall diffusion coefficient D is calculated according to the capillary diffusion of the single pore theory [90]. According to this theory, the oxygen diffusion through a single cylindrical pore comprises the molecular diffusion and Knudsen diffusion modes. Molecular diffusion (D_{a}) is a function of both the temperature and pressure as in Equation (4.32). The Knudsen diffusion (D_{k}) characterizes the transport caused by the collision of oxygen atoms with the pore wall, and is given by Equation (4.33). When the pore size is very small (<1 μm), the Knudsen diffusion is predominant [69].

$$D = \left(\frac{1}{D_a} + \frac{1}{D_k}\right)^{-1} \quad (4.31)$$

where,
D_a: molecular diffusion coafficient, ($m^2\ s^{-1}$)
D_k: Knudsen diffusion coafficient, ($m^2\ s^{-1}$)

$$D_a = D_o \left(\frac{T}{T_o}\right)^{7/4} . \frac{P}{P_o} \quad (4.32)$$

where,
D_o: molecular diffusivity at standard temperature and pressure STP, ($m^2\ s^{-1}$)
P: gas pressure, (atm)

$$D_k = \frac{\delta}{3}\left(\frac{8RT}{\pi . M_{O_2}}\right)^{1/2} \quad (4.33)$$

where,
δ: pore diameter, (m)

The pore mean radius r_p can be calculated from the following expression [69]:

$$r_p = 2\psi\tau^{0.5}/A_i\rho_p \quad (4.34)$$

where,
r_p: pore mean radius, (m)

The surface concentration of the oxidant gas [C_s] can be calculated from the application of Fick's law to the boundary layer diffusion to calculate the overall mass transfer coefficient and it can be substituted into the overall particle reaction rate [90] to obtain the final relation as follows:

$$R_m = \frac{12\ \Lambda\ D_a}{\rho_P . d_p^2}(C_o - C_s) \quad (4.35)$$

Therefore,

$$C_s = C_o - \frac{R_m . \rho_P . d_p^2}{12\ \Lambda\ D_a} \quad (4.36)$$

where,
d_P : initial diameter of char particle , (m)
Λ : gravimetric stoichiometric coefficient $\Lambda = M_c . (\nu_g M_g)^{-1}$
M_c, M_g : molecular mass of carbon and oxidizing gas, ($kg\ kmol^{-1}$)
ν_g : molar stoichiometric coefficient

For the char combustion, the primary product is assumed to be CO therefore Λ=3/4.

The char particle size and density vary with the type of the parent fuel, the heating rate during devolatilization, and the combustion temperatures. The mass losses in the TGA samples are due either to the size reduction or density decrease. At any time in the char burn-off, we assume the particles are spherical:

$$1 - \alpha = \frac{d_{\mathrm{p}}^3 \rho_{\mathrm{p}}}{d_{\mathrm{po}}^3 \rho_{\mathrm{po}}} \tag{4.37}$$

where,
(o)denotes the initial state of the particle
d_{Po} : initial diameter of char particle , (m)
ρ_{Po} : initial density of char particle, (kg m^{-3})

In order to express both the particle size and density changes with burn off (α), Smith [69] assumed that σ and β the orders of dependence of particle size and density, respectively as follows:

$$\frac{d_{\mathrm{p}}}{d_{\mathrm{po}}} = (1 - \alpha)^{\sigma} \tag{4.38}$$

$$\frac{\rho_p}{\rho_{po}} = (1 - \alpha)^{\beta} \tag{4.39}$$

where,
σ and β : order of dependance ofparticle size and density and $3\sigma + \beta = 1$

When the particles burn with constant size and reducing density, σ =0 and β = 1. However, if the reaction occurs at elevated temperatures it will be very rapid to penetrate the internal pore surface and occurs only on the external surface of the particle. Hence the particle size reduces with burn off and the density remains constant, i.e. σ =1/3 and β = 0. Depending on the original fuel composition, and the combustion temperature, values of σ and β vary between those two extremes. Sergeant and Smith [164] found for the low-ash bituminous coal that σ = β = 0.25. Smith [161] reported the same results for semi-anthracite coals. In contrast, brown coal char (low rank) showed a constant density and third-order reduction in particle size (σ = 1/3 and $\beta = 0$) with the conversion increase [91].

4.3.4.1 Combustion Zone I

It is established that in Zone I (where the combustion occurs under chemical kinetic control) [97] that the reaction occurs with a deep penetration of the oxygen to the internal pores due to the slow reaction at the lower temperatures. Thus the pore

diffusion limitation is insignificant, and the rate coefficient $\ddot{K}$ is independent of the particle size [69, 90, 91, 164]. In this case $\eta = 1$ ($\emptyset \leq 0.5$) and the oxygen concentration at the surface is equal to the bulk concentration ($C_s = C_o$) and the value of $\ddot{K}$and m can be calculated from the overall reaction rate as follows:

$$R_m = A_g . \ddot{K} . [C_s]^m \quad (4.40)$$

where,
A_g : *the total specific surface area of the char particle,* $(m^2\ kg^{-1})$

Equation (4.40) has been widely used in the modelling of coal char combustion and gasification in literature [165-170]. Adanez et al. [158] illustrated the effectiveness of this model in predicting the kinetic parameters of five wood species. They used the TGA data to predict the intrinsic kinetic parameters of wood chars and applied the kinetic parameters on the fluidized bed combustion boilers. While Dupont et al. [107] expressed the reaction rate by calculating the activation energy E_a of a reference sample and applied it to 21 samples of wood chips multiplied by an integral parameter that represents the differences between the wood species due to the mineral content of each one. Then they demonstrated that this parameter is linked to the ratio of the potassium/silicon. Recently, Gao et al. [171] used the random pore model (RPM) to calculate the intrinsic reactivity of rice husk char gasification with CO_2. They determined the intrinsic reaction rate constant as a function of the gasification temperature and the oxidant partial pressure. However, they assumed that gasification of the char at 1223 K is in the combustion Zone I where there is no diffusion limitation. Therefore, they did not consider the effectiveness factor in the determination of the intrinsic reactivity. This assumption at such a high temperature does not comply with all the published data on combustion zone I that are reviewed by Smith [69].

4.3.4.2 Combustion Zone II

At high-temperature char combustion where the reaction is under both the control of the chemical kinetic rate and the oxygen diffusion rate to the pore walls, the effect of oxygen pressure and the particle size are both equally important. Thus both particle size and density are reduced [90]. The char pore structure is assumed to be large spherical vesicles with a porous structure on the walls [93]. The effectiveness factor decreases with increasing temperatures as the surface area available for the reaction decreases, hence, $\eta = \frac{1}{\emptyset}$ for $\emptyset \geq 5.0$. Essenhigh [172] approximated the Thiele modulus as follows:

$$\emptyset = \gamma . \left[\frac{A_g . \rho_{\mathrm{p}} . \ddot{K} . C_{\mathrm{s}}^{m}}{\Lambda . D_{\mathrm{e}} . C_{\mathrm{s}}}\right]^{1/2} \quad (4.41)$$

Substituting η, and $\gamma = d_p/6$ for spherical particles in Equation (4.28), the overall reaction rate for Zone II becomes:

$$R_m = \frac{6}{d_{\mathrm{p}}} \left[\frac{\Lambda . D_{\mathrm{e}} A_g . \ddot{K} . C_{\mathrm{s}}^{m+1}}{\rho_{\mathrm{p}}}\right]^{1/2} \quad (4.42)$$

From the experimental value of R_m the intrinsic rate coefficient $\ddot{K}$ can be calculated.

This model combines the effects of particle size and the oxygen pressure on the overall rate of the char combustion. It can be seen from Eq. (4.42) that the overall particle reaction rate is inversely proportional to the particle size and to the square rout of the particle density. Laurendeau [90] reached the same conclusion for the combustion in Zone II. Essenhigh [172] also concluded that there is a negative dependence of the char combustion rate on the initial char density.

However, from the mathematical derivation of the rate model, the dependence of the intrinsic reaction rate $\ddot{R}$ and coefficient $\ddot{K}$ on the initial char density is negligible, and the reason for this is the inverse dependence of the effectiveness factor η and the surface gas concentration [C_s] on the particle density and thus these two effects cancel each other.

Comparing Equations (4.40) and (4.42), the apparent order and activation energy can be related to the intrinsic values as follows:

$$n = \frac{m+1}{2} \quad (4.43)$$

and,

$$E_{\mathrm{a}} = \frac{E_{\mathrm{t}}}{2} \quad (4.44)$$

where,
E_{t} : true activation energy, (kJ mol^{-1})

4.4 Calculations of the Char Physical Properties for Intrinsic Reactivity

The structural composition of biomass (cellulose, hemicellulose, lignin and ash) and the petrography of coal constituents (vitrinite, exinite and intertinite) determine the physical properties of the char produced, thus affecting its initial and evolved values during char burn off. The physical properties such as internal pore surface area, particle apparent density, true density, porosity, pore diameter, and particle diameter, are important in order to explain the char behaviour during combustion. The char specific surface area is a defining parameter of its intrinsic reactivity in the chemical control zone as shown in Eq. (4.40). Whereas, the other properties are important in the diffusion limitations zone as shown in Eq. (4.42). Moreover, those properties can be different for the same char produced at different temperatures.

Due to the experimental design of the TGA data in this study, it was difficult to have the char samples tested for their physical properties before the char combustion step. In addition, the char amounts that are produced from the TGA experiments are very small to be tested for the physical properties. Therefore, a review of the published experimental data on white wood and coal particles is performed to examine the trend of the change in the physical properties of the char with the parent fuel ultimate and proximate analysis. This investigation can help to develop a model that can be applied on the fuels under study.

4.4.1 Modelling of the Char Surface Area

Gan et al. [173] related the coal surface area A_g to the carbon content of coal and found that the CO_2 surface area decreases with an increase of carbon wt% from 70 to 75% and then increases again with higher carbon content. However, A_g values are not on one line but in a band of 80 $m^2\ g^{-1}$. Chan et al. [93] plotted A_g for three bituminous coals versus the char preparation temperature. They found that the minimum surface areas were of chars produced in the temperature range 773 – 973 K. However, both correlations cannot be applied for all ranges of carbon percent and the temperatures. Consequently, the reviewed data in this study were examined for many constituents and the char preparation temperatures. Figure 4.1 illustrates the dependence of coal char surface area on various constituents of the coal such as the C_{daf}, the ash_{db} and the VM_{db} and the char preparation temperature. Interestingly, the data in Fig. 4.1-(a) shows

a slightly linear dependence in the specific char surface area A_g for the full range of carbon content (daf) of the coal, and with the temperature increase from 773 to 1073 K. However, at the temperature 1273 K, the A_g behaviour is completely different, as the A_g trend is parabolic and has a minimum at carbon content 86-87%, and then increases again with the carbon content increase. More clear effect of the ash content on the A_g can be observed in Fig. 4.1-(b). The linear increase of A_g with the ash content of the fuel is more consistent and compatible for the temperature range of the study. Like the carbon content, a trivial effect is observed on the A_g with the increase of the VM content of the fuel as can be seen in Fig. 4.1-(c). On the other hand, the preparation temperature effect on the A_g is linear as well until 1173 K, and then a sudden exponential increase or decrease occurs in the char surface area depending on the fuel carbon content as shown in Fig. 4.1-(d).

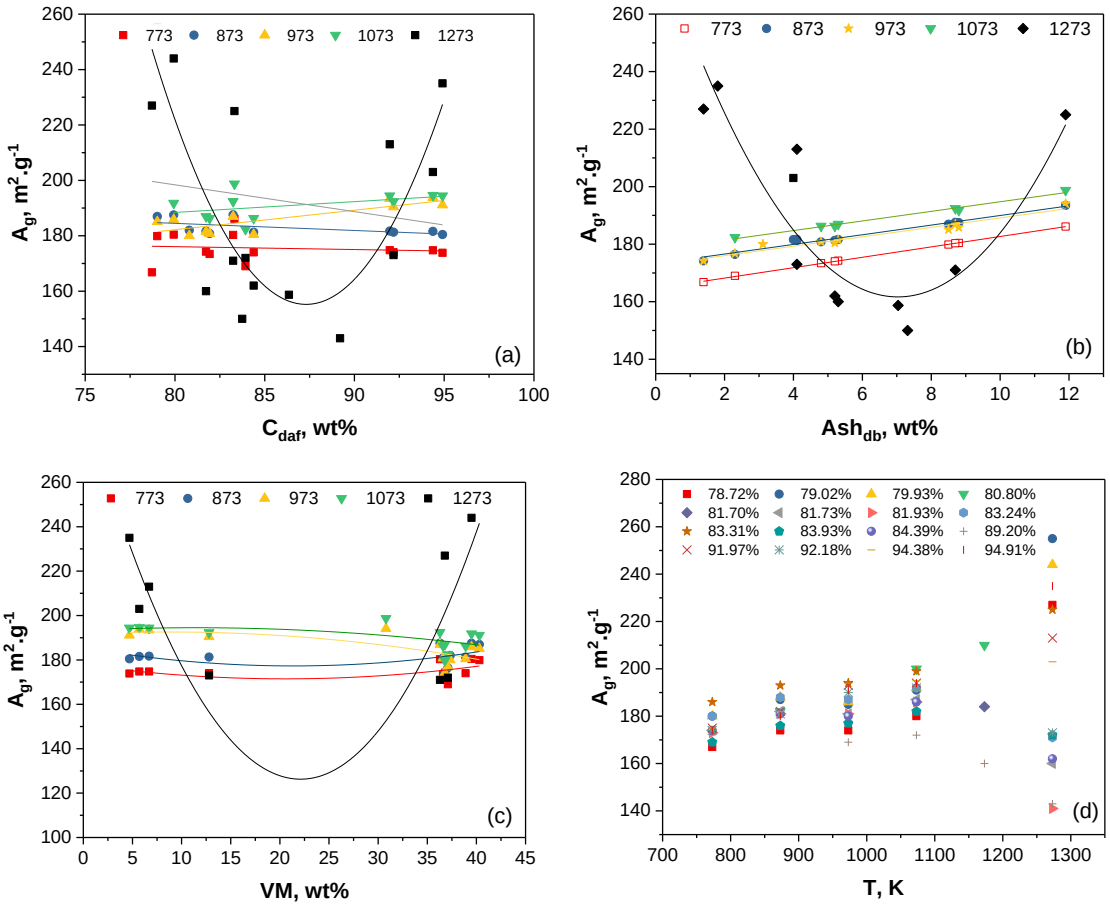

Figure 4.1 Correlation of the published data on the char surface area to the composition of the parent coal: (a) C_{daf} wt%, (b) Ash_{db} wt%, (c) VM_{db} wt%, and (d) temperature. [174]

These correlations suggest that at lower temperatures than 1100 K, the char preparation temperature and the ash content in the fuel have the most significant

effects on the char specific surface area, and at higher temperatures the carbon content is the leading parameter in the change of the char specific surface area.

Williams et al. [166] correlated the initial surface area of the coal chars produced at a temperature 1573 K in a drop tube reactor with the fixed carbon content of the parent coal and they found the following model:

$$A_g = 4764.2C^2 - 7324.9C + 2912.9 \quad (4.45)$$

However, this model cannot be applied to the temperature range 773-973 K of this study as it is based on data of higher temperatures.

Based on above observation, the published data were used to correlate the A_g to the coal properties in the temperature range under investigation. Different independent variables were examined for the correlation such as the carbon content (daf), ash and volatile matter contents, and the treatment temperature using OriginPro 2017 to find a non-linear multivariable fitting function for the correlation.

Data from Nandi [95], Gan [173], Harding et al. [174], Zhu et al. [89], Arenillas [175], Chan [93], and Masnadi [176], were selected for the correlation of the coal char surface area with the temperature and the fuel constituents.

In the case of biomass, data from Suliman et al. [177], Masnadi et al. [176], Lopez-Gonzalez et al. [160], Vallejos-Burgos et al. [178], Chowdhury et al. [160], and Abdul Halim & Swithenbank [179], were also correlated via OriginPro 2017 to find a non-linear multivariable fitting function for the wood pellets char surface area. The selected data from above-mentioned references of coal and wood pellets are listed in Appendix B. The criteria for selection were as follows: (a) the method of measurement was CO_2 absorption, (b) the particle size close to the particle size of the samples in this study, (c) the char preparation temperature and method, and (d) the temperature range (773 – 1473 K).

4.4.2 Modelling of the Char Density

In the same manner, data on the true and apparent densities of the coal char from Nandi et al. [95], Smith [180], Smith & Tyler [181], Lu et al. [182], Matsuoka et al. [183], and Chan et al. [93], and data of the biomass char true and apparent densities published by Suliman et al. [177], Guo & Lua [184], Vaughn et al. [185] Pastor-Villegas et al. [186] and other wood pellets data from the Energy research Centre of the Netherlands ECN database of biomass char [187-192] were selected to correlate the

char apparent and true density to the fuel composition. Data were plotted versus carbon content and temperature as shown in Fig. (4.2). Clearly, it can be seen from Fig 4.2 that the true density of the coal char increases with both C% and the temperature by a band of 1000 kg m^{-3}, and the variation of the density is significantly high for the same temperature (a band of 1100 kg m^{-3}). However, biomass has a different behaviour, the influence on the char density is less evident and more random on biomass char than on the coal char, and the char density increases up to a temperature 950 K then decreases at higher temperatures. These findings suggest that the biomass undergoes more complex reactions during the pyrolysis step than the coal. Again, the reviewed data were correlated to generate a multivariable function of the char density to the fuel constituents and the temperature, using OriginPro 2017 program. The published data that were used in the correlation of the char true and apparent densities are listed in Appendix C.

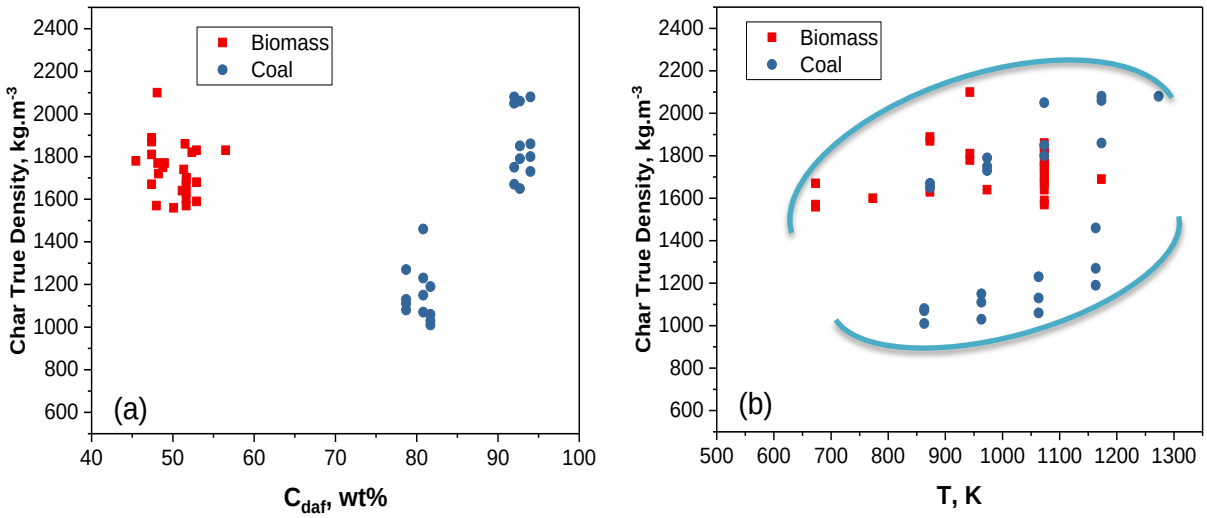

Figure 4.2 Dependence of the true density of biomass and coal chars on (a) C_{daf} wt%, and (b) temperature.

Chapter 5 Fundamental Kinetic Study Results & Discussion

5.1 Chapter Overview

This chapter provides new insights into the biomass reactivity during the thermal treatment of stagnant particles. Two primary aims are achieved in this chapter: the thermal behaviour of biomass at various devolatilization temperatures, and the reactivity of the biomass char combustion in comparison to coal. The intrinsic kinetic parameters of the biomass char combustion are determined and evaluated in comparison to coal chars. Furthermore, the effects of the char preparation conditions, parent fuel composition, and the ash content, on the char reactivity are investigated. Non-isothermal TGA data are used in the pyrolysis stage with the aim of producing chars at a certain temperature and burn them isothermally. Various sets of experiments are performed to produce char at different temperatures. By means of the TGA techniques this investigation has been conducted. The findings of this fundamental study provide an important opportunity to advance the understanding of the biomass thermal behaviour and the kinetic parameters that are necessary for the large scale combustion process design.

Two types of wood pellets; the USWWP, and the CAWWP, and two types of coal; the VC and the ELC are used in this comparison. The results of the compositional analysis of the four fuels are presented in this chapter.

5.2 Fuel Characterization

The proximate and ultimate analysis measurements were performed according to the methods outlined in Sections 3.3.2 and 3.3.4. Table 5.1 displays the proximate analysis and calorific values of the four fuel types as received (ar) with the standard deviation in the mean of triplicate sample tests.

The results in Table 5.1 show that the VC has the highest moisture content and highest ash content among the four fuel types. As expected, the wood pellet compositions vary significantly from that of the coal, however, both wood pellets have similar composition.

The USWWP and CAWWP have considerably high volatile matter (VM) (86.32 and 84.51%, respectively) and low ash content (0.67 and 0.74%), compared to ELC and VC VM (44.47 and 10.29%, respectively). The ELC has shown the highest calorific value (29,764 kJ kg^{-1}), the second highest is the VC that has 21,883 kJ kg^{-1}, and as expected the wood pellets has lower GCV at 18,587 and 18,882 kJ kg^{-1} for the USWWP and CAWWP, respectively. These results are in agreement with the published data on soft wood pellets and coal (see Table 2.3), and not too far from the ELC analysis reported by Jones et al. [193], as their results show 47.99% VM, 3.83% ash, and 41.55% FC. On the other hand, the VC has shown significantly high ash content (38.20%) and trivially higher GCV than wood pellets (21,883 kJ kg-1) although it has a higher fixed carbon. Apparently, the high ash content and low volatile matter in the VC have contributed to reduce the calorific value of the coal. The higher ash content in the coal suggests that the ash deposition problems with the coal combustion are expected to be greater than the case of the biomass combustion.

Table 5.1 Proximate analysis (ar) of USWWP, CAWWP, ELC, and VC.

Sample	MC%	STDV	Ash%	STDV	VM %	STDV	FC %	GCV kJ kg^{-1}	STDV
USWWP	5.48	±0.45	0.67	±0.07	86.32	±1.04	7.53	18,587	±68
CAWWP	6.37	±0.56	0.74	± 0.05	84.51	±1.37	8.37	18,882	±60
ELC	3.99	±0.11	2.90	±0.20	44.47	±0.41	48.64	29,764	±7
VC	7.52	±0.40	38.20	±0.27	10.29	±0.35	43.99	21,883	±107

The ultimate analysis was performed with a Perkin Elmer 2400 SII CHN/S analyser according to the method outlined in Section 3.3.4. The oxygen was determined by difference and the average of triplicate tests is recorded. Table 5.2 presents the results of the ultimate analysis as dry, ash-free (daf) composition. Due to the low content of the sulphur in all the fuels, the measurements were below the detection level of the CHNS analyser. However, the sulphur was detected by the XRF analysis of the fuel ashes.

Table 5.2 Ultimate analysis as wt% (daf) of the USWWP, CAWWP, ELC, and VC.

Sample	N	STDV	C	STDV	H	STDV	O*
USWWP	0.18	±0.03	49.34	±0.54	6.14	±0.10	44.34
CAWWP	0.76	±0.01	50.30	±0.23	6.18	±0.03	42.76
ELC	1.56	±0.10	77.40	±1.35	5.16	±0.07	15.88
VC	1.31	±0.00	92.57	±2.26	3.61	±0.07	2.51
* determined by difference							

As can be seen in Table 5.2, the elemental analysis of the USWWP and the CAWWP have shown slightly different composition in nitrogen 0.18% and 0.76%, in carbon 49.34% and 50.30%, in hydrogen 6.14% and 6.18%, and respectively in oxygen 44.34 and 42.76%. On the other hand, the ELC have shown higher carbon, nitrogen, and sulphur contents than the wood pellets (1.56% nitrogen, 77.40% carbon). The hydrogen was slightly lower in the coal than in the biomass (5.16% versus 6.14%).

The USWWP results are within the range of the published data, and very close to the white wood pellets characteristics (see Table 2.3). Jones et al. [193] have analysed samples of the ELC and found 75.94% C, 1.76% N, 4.26% H, and 0.64% S. Although, these results are slightly different from the ones in this study, both sets of results fall in the range of the US Geological Survey coal data tables of the ELC [64], that presents four different ranks of the ELC and their compositions are in the range 73.82-78.72%C, 1.15-1.73% N, 5.13-5.33% H, and 0.33-0.63% S, respectively.

5.3 Physical Char Properties

5.3.1 Initial Specific Char Surface Area

As shown in Section 4.4.1, published data on the specific surface area A_g of wood and coal chars were reviewed to correlate the fuel properties to the produced char surface area in the temperature range under investigation. Accordingly, the selected data on the char specific surface area were used for correlation with C_{daf} wt%, ash_{db} wt%, VM_{db} wt%, and the treatment temperature to find a non-linear fitting function for the correlation. The significance of correlation showed that the carbon and the ash

contents had trivial effects on the A_g of biomass and the best correlation was found, with an average error of ±11.0%, to be:

$$A_g = 1.65VM^{1.13} + 44T^{0.5} - 1248 \quad (5.1)$$

The sensitivity analysis showed that the leading parameter in the correlation is the temperature, with a 1-6% increase in A_g per every 10 K increase in the temperature. Also, the volatile matter is an important parameter as for every 1% increase in the *VM*, the A_g increases by 1%. In contrast, the carbon and ash contents had no considerable influence on the resultant surface area therefore they were eliminated from the correlation.

Similar correlation attempts for the coal was performed, however, due to the change in the char structure at a temperature higher than 1073 K, two correlations were found for the surface area of the coal char; one for the temperature region 773-973 K as in Eq. 5.2 with a ±13.8% error, and another correlation for the temperature region 1073-1273 K as shown in Eq. 5.3 with a ±15.3% error:

$$A_g = 0.1Ash^{0.7} + T^{0.07} + 103 \quad (5.2)$$

$$A_g = 2.5Ash^{0.89} + 43\,T^{0.5} - 1370 \quad (5.3)$$

Yet in this case, the sensitivity analysis showed that A_g of the coal char is more stable with the change of ash content and the temperature in the region of 773-973 K, as such for every 10 K increase in temperature there is only a 0.4% increase in the A_g. Also, the ash content had insignificant effect on A_g, in which every 5% increase in the ash content, the surface area increases by ±0.1%. It was found that the carbon and the volatile matter contents had no significant effect on the char surface area. In contrast, at higher region of the temperatures, the A_g is highly sensitive to the ash content as for every 1% increase in the ash content, the A_g increases by 2-4%, and for every 10 K increase in the temperature results to a 5.0% increase in the A_g.

Equations (5.1), (5.2) and (5.3) were used to predict the char specific surface area of each sample used in this study at different temperatures.

5.3.2 Initial True Char Density

Based on the discussion in Section 4.4.2, a correlation was derived for the true density of the char based on C% (daf) and the preparation temperature. For biomass, the true density formula was found to be the following, with ±4.76% error:

$$\rho_{\mathrm{t}} = 9750 - 386.0C + 4.221T + 3.70056C^2 + 0.00221T^2 \quad (5.4)$$

As expected, the sensitivity analysis showed a higher dependence of the true density on the carbon content than the temperature. The true density of the biomass varies by ±(0.0-2.4%) for every 1% increase in the carbon content, whereas a ±20 K change in the temperature results to a ±1.5% change in the true density.

A similar equation was found for the coal data with a higher dependence on the carbon content with an error of ±9.08% as follows:

$$\rho_{\mathrm{t}} = 3490 - 99.8C - 0.567T + 0.87496C^2 + 0.00071T^2 \quad (5.5)$$

Like the biomass, the sensitivity of the coal char true density to the carbon content was higher than to the temperature. The true density increases by 3.5% with the carbon content increase of 1%. On the other hand, the variance in the true density with temperature is like that of biomass, namely for every ±20 K change in temperature the true density undergoes a ±1.4% change.

5.3.3 Initial Apparent Char Density

Nandi et al. [95] observed an average increase in the apparent density of the anthracite coal char by 5% per 100 K increase in the preparation temperature. Also, Chan et al. [93] compared the mercury density of three bituminous coal chars with the temperature and found an increase in the apparent density between 2% to 8% with every 100 K increase from 673 to 1173 K. Both sets of data and other data from [91, 182] were used to determine the correlation of the apparent char density with parent fuel carbon content and temperature. A non-linear multivariable function was generated by OriginPro 2017. The resultant correlation for biomass char, with ±7.34% error is given as follows:

$$\rho_{\mathrm{a}} = 11581 - 393.7C + 1.441T + 3.301C^2 - 0.00059T^2 \quad (5.6)$$

And, for coal char with a maximum ±4.63% error:

$$\rho_{\mathrm{a}} = 10253 - 245.3\mathrm{C} - 0.085\mathrm{T} + 1.5956\mathrm{C}^2 + 0.00032T^2 \quad (5.7)$$

Analogous to the true density, the apparent density showed a high dependency on the carbon content. The increase in carbon content of 1% resulted in a 3.7% increase in the apparent density, whereas for every 20 K variance in the temperature, only a 0.0-1.0% increase in the apparent density is witnessed. This result is in agreement with the findings of Chan et al. [93].

5.3.4 Initial Char Particle Size

Although the particle size has a great influence on the char properties [69, 90, 91, 180], it was difficult to correlate the char particle size to the fuel constituents due to the limited available data. Nevertheless, Davidsson & Pettersson [194] formulated the longitudinal, tangential, and radial shrinkages of 5 mm wood cubes as a second degree function for each of those dimensions. They found final volume shrinkage of 60%. However, their results cannot be applied on ≤ 80 μm particles as the particle size can significantly change the shrinkage ratio. Yu et al. [139] and Fu et al. [195] examined the swelling behaviour of the coal particles during pyrolysis. They both found that, depending on the coal rank, that the maximum swelling occurs at pyrolysis temperatures 573- 723 K with a 40% to 200% swelling ratio, then the particles return to their original size in the temperature range 850-950 K. After 973 K, the particles start to shrink by up to 20% at a temperature 1273 K. In this study, the mean diameter of the char particles is determined from the relation between the degree of conversion (mass release) during devolatilization and the apparent density, using Equation (4.38).

The calculated initial physical properties of four fuel chars are listed in Table 5.3. Clearly, the surface area of the chars increases with the temperatures above 773 K, and the biomass samples showed a larger surface area increase with temperature than do the coal samples, and this is due to their crosslinked structure that constrain the reorganizing of the carbon lamella in the short time pyrolysis step maintaining higher porosity and surface area [196]. These results are in agreement with the Gan et al. [173] and Chan et al. [93] conclusions. Zhu et al. [89] reported the total surface area of the ELC sample at a temperature 1273 K as 227 $m^2\ g^{-1}$. Compared to the correlation results of 192 $m^2\ g^{-1}$, the variance falls within the expected 15.3% error. Ellis et al. [197]

reported the specific surface area of the Canadian wood pellets char prepared at 1173 K at 468.1 $m^2 g^{-1}$, which is only 8% different than the results of this study (507 $m^2 g^{-1}$). All the Ag results are within the expected range of the char surface area, i.e. 100- 600 $m^2 g^{-1}$, and the apparent density of coal char is within the expected range of 900-1400 kg m^{-3} [90]. To the best knowledge of the author, there is no published data on the physical properties of Vietnamese coal in the literature.

Table 5.3 Initial char physical properties in the temperature range 773-1273 K.

	T	Ag	Apparent density	True Density	Particle Size	Porosity
	K	$m^2 g^{-1}$	Kg m^{-3}	Kg m^{-3}	m	
USWWP	773	230	693	841	3.95E-05	0.18
	873	306	883	986	3.73E-05	0.10
	973	379	923	1151	3.61E-05	0.20
	1073	448	963	1335	3.50E-05	0.28
	1173	513	1003	1540	3.37E-05	0.35
	1273	576	1043	1764	3.17E-05	0.41
CAWWP	773	224	834	845	4.18E-05	0.10
	873	300	874	990	4.00E-05	0.12
	973	373	914	1154	3.88E-05	0.21
	1073	442	954	1339	3.72E-05	0.29
	1173	507	994	1544	3.62E-05	0.36
	1273	570	1034	1768	3.40E-05	0.42

Continued

	T	Ag	Apparent density	True Density	Particle Size	Porosity
	K	$m^2 g^{-1}$	Kg m^{-3}	Kg m^{-3}	m	
ELC	773	157	952	995	7.78E-05	0.04
	873	164	997	1055	7.46E-05	0.06
	973	171	1048	1130	7.29E-05	0.07
	1073	178	1106	1219	7.10E-05	0.09
	1173	185	1170	1322	7.07E-05	0.11
	1273	192	1241	1439	6.98E-05	0.14
VC	873	165	1390	1798	7.94E-05	0.23
	973	172	1441	1872	7.73E-05	0.23
	1073	179	1499	1961	7.67E-05	0.24
	1173	186	1563	2064	7.54E-05	0.24
	1273	233	1634	2181	7.40E-05	0.25

5.4 Pyrolysis Reactivity

5.4.1 Pyrolysis Profile

Samples of 5 mg ±5% of USWWP, CAWWP, VC, and ElC were treated in a Perkin Elmer Pyris 1 TG analyser at temperatures 773, 873, 973, 1073, 1273 K and at the heating rate of 100 K/min, under nitrogen with a flow rate of 40 mL/min. Then the isothermal conditions were continued for 3 minutes to reach a steady rate then the char gasification was performed by switching the purging gas to air at 40 mL/min to complete the char combustion until a final steady mass was obtained.

The complete thermal treatment profiles of the mass loss with time of the four samples are illustrated in Fig. 5.1. It can be seen from Fig. 5.1 that the wood samples showed a different thermal behaviour than the coal samples due to the differences in the structural composition of both types of fuel. Clearly, the biomass did not witness a

notable change in the volatile matter (VM) release with the increase of the final pyrolysis temperature in the range 773-1273 K.

The devolatilization curve of the biomass species USWWP and CAWWP appeared to have one global step without a shoulder, thus indicating that the global reaction approach proposed in the mathematical model of pyrolysis in Section 3.1 is acceptable. However, the ELC showed a clearly different mass loss with temperature increase. On the other hand, the VC had a very small devolatilization step due to its low volatile matter content.

The pyrolysis behaviour of any fuel can be revealed from the DTG profile (derivative of wt%, wt%/min) extracted from the TGA data through the peaks in the mass loss rates that occur during the pyrolysis step. The shape and area under the peak assists in the predicting of the reaction complexity and its temperature dependence. The DTG of the USWWP, CAWWP, VC and ElC samples during the pyrolysis step at various temperatures are shown in Fig. 5.2. Wood particles started to devolatilize at a temperature 479 K and 469 K for USWWP and CAWWP respectively. Colombian coal also started to lose mass at a temperature 469 K, whereas, the Vietnamese coal VC started to lose mass at 40 degrees higher, i.e. at 510 K.

The onset temperature of the DTG curve is defined when the mass loss rate is above 0.1%/min. The USWWP and CAWWP DTG curves had onset temperatures at 603 and 588 K, Whereas, the ELC onset was at a temperature 708 K. On the other hand, the VC samples failed to release significant amounts of volatiles at a temperature 773 K independent of the pyrolysis time. Therefore, it was eliminated from the study. The VC onset temperature was 726 K.

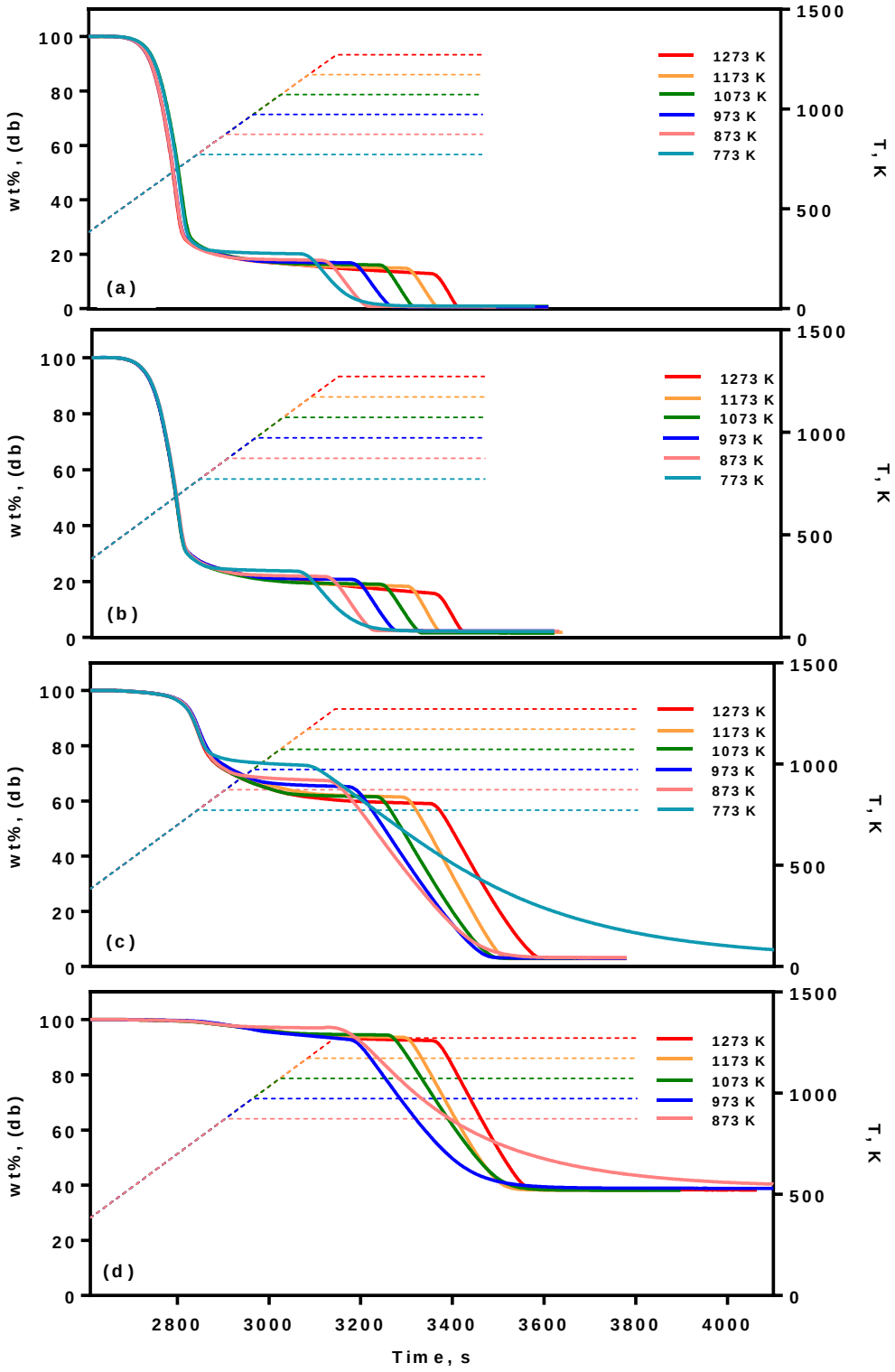

Figure 5.1 TGA profile for (a) USWWP, (b) CAWWP, (c) ELC, and (d) VC.

The DTG profile of the USWWP and CAWWP of mass loss with temperature exhibited a shoulder at 350 °C (623 K). This shoulder is resulting from the hemicellulose decomposition [85]. The maximum weight loss rate was observed at the temperatures 696, 693, 776 and 946 K for the USWWP, CAWWP, ELC and VC, respectively. For the biomass, this rate is attributed to the cellulose decomposition. Similar results for the biomass were obtained by Wang et al. [125] for birch and spruce woods [125]. They found that the maximum pyrolysis rate was at a temperature 673 K. Biagini et al. [198] found the beech wood maximum pyrolysis rate at 680 K. Also Lopez-Gonzalez et al. [160] found that the maximum pyrolysis rate of eucalyptus, pine and fir woods at a temperature 631, 637, and 641 K, respectively. All these types of wood are the main source of white wood pellets. The pyrolysis onset and the peak temperatures are listed in Table 5.4.

Table 5.4 Pyrolysis characteristic temperatures of four fuels.

Sample	Onset T K	Peak T K	Peak end T, K	Peak degree of conv. (α)
USWWP	603	696	731	0.68
CAWWP	588	693	728	0.67
EIC	708	776	849	0.39
VC	726	946	1273	0.51

Another observation from Fig .5.2 is that the biomass samples reached their maximum pyrolysis rate at lower temperatures than coal. The lower peak temperatures in the biomass imply higher reactivity [125]. The coal samples reached the maximum rate of mass loss at higher temperatures. As it can be seen, the ELC had a maximum rate at 776 K. Similar results were obtained for bituminous coal at 800 K [199], and lower temperature at 713 K for lower rank coal [148].

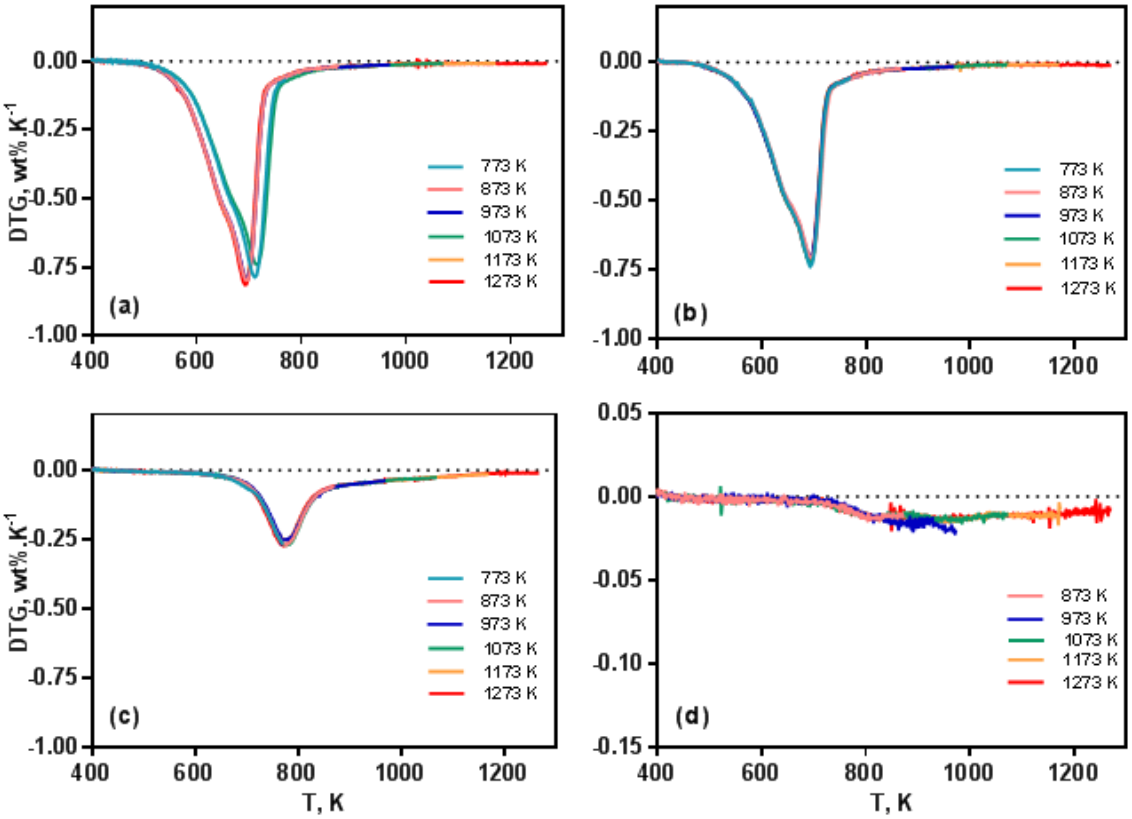

Figure 5.2 DTG curves of the devolatilization and gasification of : (a) USWWP (b) CAWWP (c) ELC (d) VC, at various pyrolysis temperatures.

The tails at the end of the peaks in the DTG profile of the USWWP and CAWWP are related to the lignin decomposition that ended at temperatures 731 and 728 K, respectively. The ELC DTG curve showed a smaller peak area at the lowest pyrolysis temperature (773 K), while the peak area did not change significantly at higher temperatures. The rapid mass loss of the wood pellets and the ELC at low temperatures is due to the high tar and aliphatic gas yields [78]. Also, the wood pellet peaks had a shoulder at 673 K and this implies more than one step reaction occurring concurrently or sequentially. Trommer and Steinfield [76] observed two-step pyrolysis of Petrozuata Delayed coke and Flexicoke; the first is at temperatures 860 and 956 K, and the second above 1210 K and 1090 K, respectively. On the other hand, the VC devolatilization did not exhibit a significant peak with the pyrolysis temperature increase.

The maximum rate of weight loss during pyrolysis of the four samples at temperatures 773, 873, 973, 1073, 1173, and 1273 K are listed in Table 5.5 and illustrated in Figure 5.3. From Table 5-3, both biomass samples and the ELC reactivity can be observed as being 2-3 times higher than the VC rate. The higher is the VM content of the fuel, the

higher is the maximum rate of the devolatilization step [199]. Therefore, the sequence of the maximum pyrolysis rate was USWWP>CAWWP>ELC>VC.

Table 5.5 Maximum rate of weight loss during pyrolysis step at various temperatures.

T, K	USWWP, 1/s	CAWWP, 1/s	ELC, 1/s	VC, 1/s
773	0.0164	0.0160	0.0165	
873	0.0161	0.0150	0.0136	0.0074
973	0.0159	0.0147	0.0120	0.0050
1073	0.0147	0.0149	0.0105	0.0038
1173	0.0145	0.0147	0.0109	0.0037
1273	0.0156	0.0142	0.0110	0.0032

In general, the low carbon and high volatile matter content of the biomass fuels resulted in a higher maximum rate of mass loss and decreases with an increase in the temperature from 773 K to 1073 K and then tended to stabilize at higher temperatures. Although the VC had significantly lower rates than biomass at all temperatures, both coal samples the ELC and VC have witnessed a higher reduction in the pyrolysis maximum rate in the temperature range 873-1073 K and being more severe in the VC case.

This discrepancy in the behaviour between the biomass and the coal can be attributed to the different structures of the biomass to that of the coal. The woody biomass is a highly porous species compared to coal due to its fibrous structure, lower carbon and higher oxygen content. At low temperatures (773 -873 K), the biomass char produced increases the macro porous size and its porosity due to the aliphatic H loss, and more aromatic layers are formed [93]. While at higher temperatures (873-1173 K), the carbon content increases, and the aromatic H starts to decrease. The resulting char has a more solid coke structure and more miso and micro pores are developed.

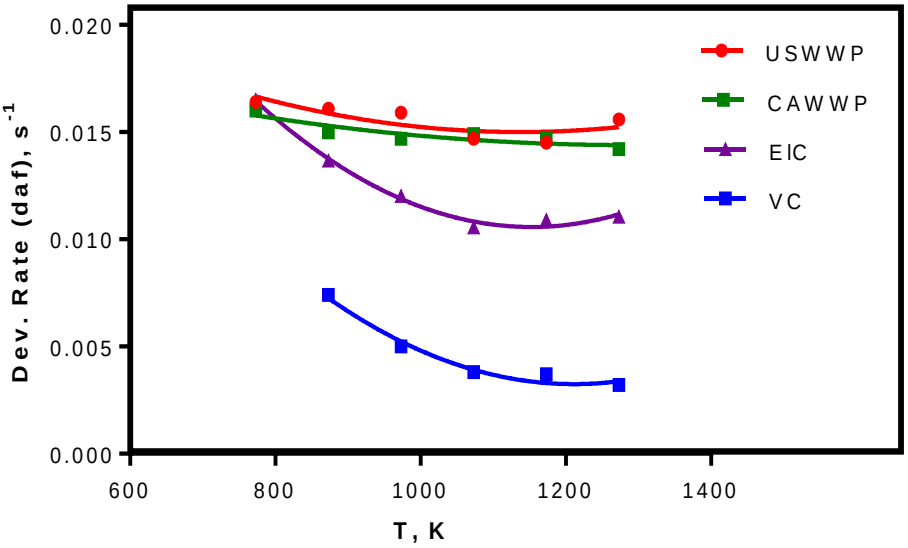

Figure 5.3 Maximum devolatilization rate of the USWWP, CAWWP, ELC, and VC at different final pyrolysis temperatures.

For coal samples, the surface area increases in the pyrolysis due to the chemisorption reaching smaller pores and then increases the diffusivity. Whereas at higher pyrolysis temperatures, the structural carbon crystallization increases, resulting in thermal annealing and loss of active sites.

On the other hand, the higher mineral content of the VC also differentiates the pyrolysis rate of the VC from the rate of the ELC pyrolysis. The higher mineral content, the more temperature sensitive is the devolatilization process. The main mineral constituents found in most types of coals are: (a) alumina-silicates, such as kaolinite ($Al_2Si_2O_5(OH)_4$ and illite $KAl_3Si_3O_{10}(OH)_2$ (b) oxides, such as SiO_2 and Fe_2O_3 (c) carbonates, such as $CaCO_3$, $MgCO_3$ and $FeCO_3$ and (d) sulphides and sulphates, such as FeS_2 and $CaSO_4$ [90]. During pyrolysis, the mineral compounds are transformed to metal oxides in the char forming ash component. The kaolinite start losing its hydroxyl groups at temperatures 823- 1123 K and forming aluminium silicate $Al_2Si_2O_7$ [200]. At higher temperatures, this compound causes sintering on the particle surface. The illite also decomposes and yields thin lamina of mica or polysilicate mineral $KAl_2(AlSi_3O_{10})(F, OH)_2$ which are highly elastic [201]. In addition, other metal compounds, such as NaCl, KCl, K_2O, $CaCO_3$, and $MgCO_3$ all start to melt at temperatures 1013-1098 K [202, 203]. Therefore, at temperatures about (1073 K) and above, the higher ash comprising coal faces mineral diffusion through the pores, thus causing resistance to the release of

volatile matter due to the blockage of the particle pores and the devolatilization rate ultimately decreases.

5.4.2 Devolatilization Yield

Figure 5.4 illustrates the increase of VM yield with temperature increase for the four fuels. As expected, the VM yield of the USWWP and CAWWP during devolatilization was 79-87% and 76-84%, respectively. Whereas the VM yield of the ELC increased from 27% to 41% and for the VC increased from 3% to 8%, with temperature increase from 773 K to 1273 K. The increase of volatile yield in both wooden biomass samples was 2% for every 100 K temperature increase. Whereas, the increase in both coal samples was 10% for the ELC and 33% for the VC, respectively.

These results imply that biomass can release 90% of its VM at low temperatures. The high release of VM from biomass species at lower temperatures compared to coal can be attributed to the difference in volatile matter composition in the two types of fuel. The linear chains of polysaccharides constituents of cellulose and hemicellulose, containing a high percent of oxygen and water content can be easily released in the temperature range 473–673 K. While the coal lamella consists of polynuclear aromatic, and hydroaromatic clusters linked together by aliphatic chains [90]. The aromatic clusters constitute 75% of the coal and they are responsible for the char formation. Whereas the hydroaromatic is 17% of the coal mass and this is responsible for the tar formation during pyrolysis. The aliphatic carbon chains are only 8% and produce CH_4, CO and CO_2 [204]. Therefore, coal requires higher temperatures to release heavier aromatic compounds during the devolatilization. This also applies to lignin where the aromatic part of the woody biomass starts to decompose at low temperatures but it will not reach its peak until 723 – 773 K. This property of the biomass gives more stability and higher reactivity during devolatilization step with less temperature dependence in the temperature range 800-1300 K. While for coal, a complete devolatilization occurs only at temperatures higher than 1173 K.

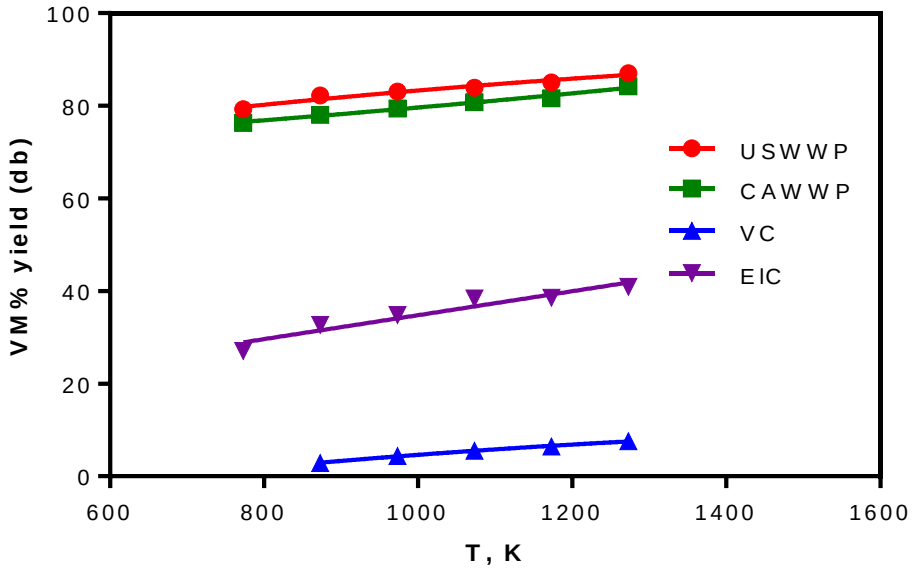

Figure 5.4 Volatile matter yield with the pyrolysis temperature increase.

The devolatilization results in the temperature range 1173-1273 K are comparable with the proximate analysis of the fuels listed in Table 5.1. Table 5.6 displays the volatile matter, char and ash yields of the four fuels in the temperature range investigated.

Table 5.6 Devolatilization yields of USWWP, CAWWP, VC and ELC at various pyrolysis temperatures.

	USWWP			CAWWP			ELC			VC		
T, K	**VM**	**Char**	**Ash**	**VM**	**Char**	**Ash**	**VM**	**Char**	**Ash**	**VM**	**Char**	**Ash**
773	79.25	18.32	0.95	76.33	21.53	2.13	**27.03**	**70.14**	**2.56**			
873	82.26	17.10	0.69	78.08	19.48	2.24	32.67	64.19	2.98	2.88	57.68	39.46
973	83.08	16.18	0.67	79.41	18.33	2.37	34.82	62.25	2.98	4.39	56.82	38.81
1073	83.89	15.14	0.89	80.80	17.46	1.57	38.36	58.49	2.94	5.55	56.29	38.11
1173	85.08	14.29	0.66	81.64	16.40	1.89	38.51	58.60	2.83	6.42	55.40	38.24
1273	87.06	12.59	0.34	84.20	13.63	2.13	40.91	55.96	3.17	7.59	54.15	38.28

5.4.3 Pyrolysis Kinetic Parameters

The devolatilization of two biomass samples and two coal samples were carried out at non-isothermal conditions up to various final pyrolysis temperature in the range 773 -1273 K at the same heating rate of 100 K min^{-1}. The heating rate was maintained

at the highest possible with the TGA instrument used to overcome the low heating rate influence on the heat and mass transfer. The data selected for each curve is the data points between the onset and the end of the peak where most of the decomposition step takes place and usually they are measured every second in the test period. The VM fractional conversion of the four fuel samples are compared for each pyrolysis temperature and plotted in Fig. 5.5. The difference between the biomass and coal behaviour during pyrolysis is clear. Both biomass samples maintain the same decomposition trend as the temperature increases with a 50% conversion time $t_{1/2}$ in about 50 seconds for all temperatures. However, higher decomposition rates for the second 50% of the conversion at higher temperatures, were observed. Interestingly, the ELC had the same behaviour as biomass, in terms of $t_{1/2}$ with a slower reactivity for the second half of the conversion. Although the biomass samples and ELC have different volatile matter and carbon content, this similarity in behaviour can be attributed to the low ash content in both fuels. Conversely, the degree of conversion of the VC samples varied strongly with the pyrolysis temperature increase. Knowing that at a temperature 773 K, the VC failed to decompose to a significant degree. This discrepancy of the VC behaviour from other fuels can only be explained by the difference in volatile matter complexity in each fuel and the higher mineral content in the VC that have been discussed in Section 5.2.

It is recommended to maintain the heating rate constant for several analysis tests to study the pyrolysis kinetics [205]. However, Conesa et al. 2001 recommended to use more than one technique to find the best kinetic mechanism [71]. In this study, the heating rates for all the experiments were constant at the highest possible rate of the instrument in the attempt to simulate the high heating rate in the pilot scale combustion. The mathematical method used could examine more than one reaction order for the best fitting of the data and more than one model for the reaction rate in terms of the function of mass loss. In addition to the power law model, the 3D-diffusion model and the grain contraction model were also tested to predict the reaction order.

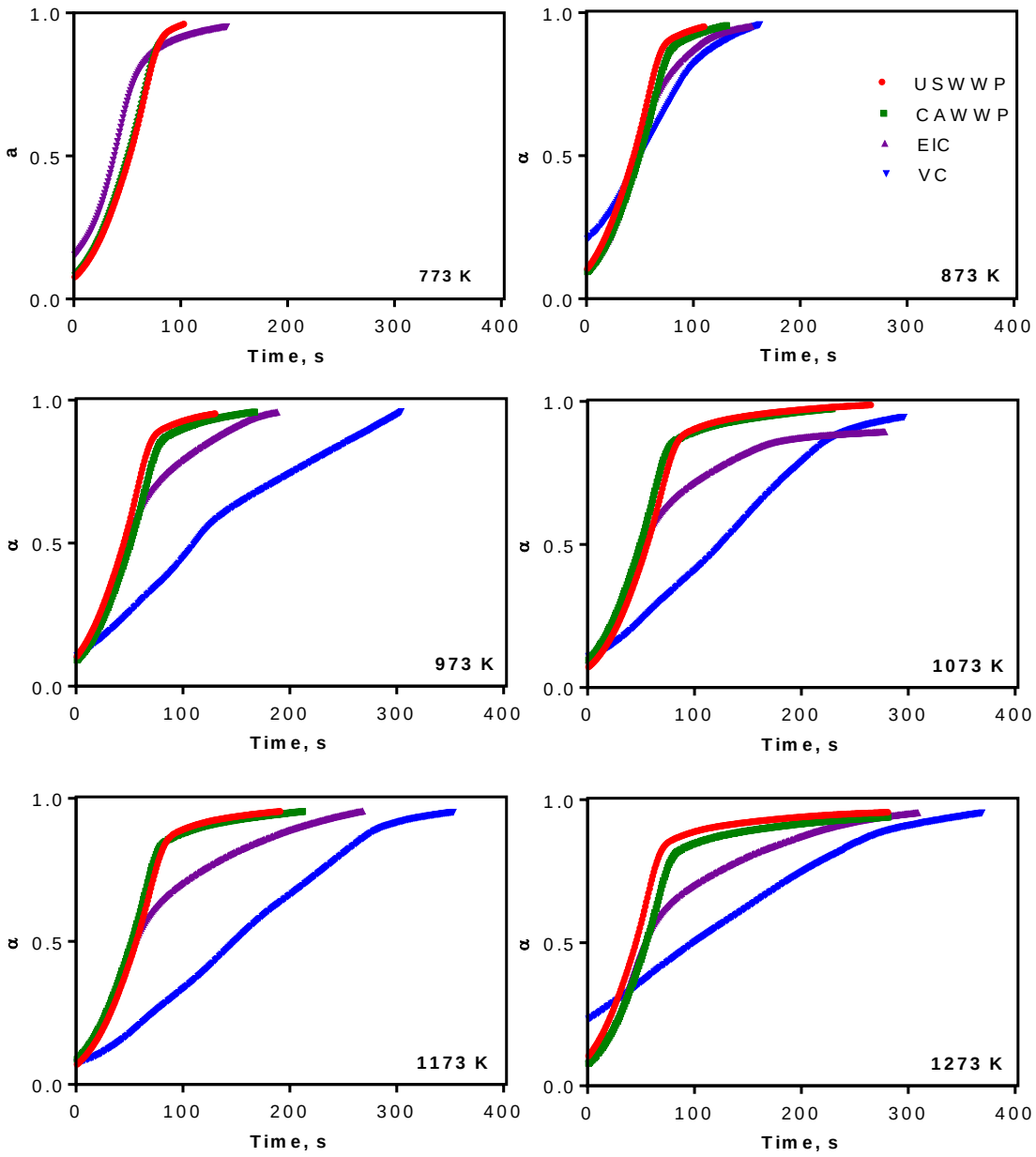

Figure 5.5 Degree of devolatilization (α) of the USWWP, CAWWP, ELC and VC as a function of time for each final pyrolysis temperature.

The integral Isoconversional single rate Coat and Redfern (CR) method with a global reaction model [11] was used to calculate the Arrhenius triplets (activation energy, pre-exponential factor and the reaction order) for the four samples that are listed in Table 5.7. The general trend of the activation energy in terms of the highest to lowest values, is ELC > USWWP > CAWWP > VC for all the temperature range. All samples witnessed a decrease of E_a with an increase in temperature from 773 K to 1273 K. The

E_a values of the USWWP and CAWWP decreased from 81 and 74 kJ mol^{-1} at 773 K to 75 and 68 kJ mol^{-1} at 1273 K, respectively. Similarly, the E_a of the ELC and VC decreased from 101 kJ mol^{-1} at 773 K, 95 kJ mol^{-1} at 873 K to 24 and 55 kJ mol^{-1} at 1273 K, respectively.

These results are not too different from published results. Zhang et al. [206] calculated the value of E_a for the wood chips pyrolysis and found it to be 85.39 kJ mol^{-1}. Munir et al. [73] have heated samples of cotton stock, sugarcane bagasse and shea meal to a temperature 1223 K under nitrogen atmosphere. Their results for the activation energy were in the range of 58 – 77 kJ mol^{-1}. They assumed a power-low reaction and found the reaction order of 0.5 for all biomass samples. Anthony et al. [79] calculated the lignite pyrolysis activation energy at 1273 K at 650 K min^{-1} heating rate as 37.66 kJ mol^{-1} and 55.65 kJ mol^{-1} for the bituminous coal. Based on their observations of two-step pyrolysis, Trommer and Steinfield [76] assumed two pseudo components mechanism with the E_a values 51.57 and 12.10 kJ mol^{-1} for flexicoke.

Like the common trend, the reaction order for both biomass samples was first-order for all the temperature range under study [11]. Interestingly both coal samples did not follow that trend. The ELC sample witnessed an increasing reaction order with temperature increase from n=0 at 773 K, to n=1 for 873-1073 K, then increased to n=1.335 at 1173-1273 K. These results indicate the complexity of the reactions, thus suggesting more than one step scheme, with less sensitivity to the fuel composition. The 3D-diffusion and grain contracting models failed to give a better prediction than the power low for the USWWP, CAWWP and ELC fuel samples.

On the other hand, the VC samples showed very low values of E_a with the first-order reaction model and better data fitting was found with the 3D-diffusion model. This result confirms the proposed inhibiting effect of the mineral content in the Vietnamese coal to release volatiles due to the diffusion limitations. Solomon and Hamblen [78] reviewed the parameters that affect the reaction rates of coal pyrolysis for various coal ranks and heating conditions. They concluded that the kinetic rate of volatile species released during pyrolysis, such as aliphatic, methyl and aromatic functional groups are rather insensitive to the coal rank, and this is opposite to the oxygen species that were found to be more rank-sensitive. Moreover, the heating conditions have a considerable influence on the results of the reaction rates.

Table 5.7 Apparent Arrhenius parameters of the pyrolysis step in the temperature range 773-1273 K.

	T, K	Ea, kJ mol^{-1}	A, 1/s	n	R-residue	Ea/Ea1273
USWWP	773	81.13	1.82E+23	1.0	0.9975	1.08
	873	78.08	1.65E+22	1.0	0.9984	1.04
	973	76.69	1.03E+23	1.0	0.9987	1.02
	1073	75.51	5.38E+22	1.0	0.9991	1.01
	1173	74.94	4.72E+22	1.0	0.9995	1.00
	1273	75.03	7.23E+22	1.0	0.9988	1.00
CAWWP	773	74.32	9.26E+21	1.0	0.9976	1.09
	873	71.57	4.98E+21	1.0	0.9988	1.05
	973	69.80	3.00E+22	1.0	0.9990	1.02
	1073	70.49	3.36E+22	1.0	0.9990	1.03
	1173	69.11	2.59E+22	1.0	0.9991	1.01
	1273	68.20	2.01E+22	1.0	0.9991	1.00
ELC	773	101.35	9.52E+22	0.0	0.9205	3.84
	873	91.14	1.36E+22	1.0	0.9869	3.46
	973	83.55	3.17E+21	1.0	0.9758	3.17
	1073	77.39	1.11E+21	1.0	0.9674	2.93
	1173	26.15	3.90E+23	1.335	0.9886	0.99
	1273	26.37	4.10E+23	1.335	0.9906	1.00
VC	873	94.69	3.45E+18	3D-Diffusion	0.9892	1.72
	973	109.96	5.45E+20	3D-Diffusion	0.9798	2.00
	1073	77.83	1.06E+19	3D-Diffusion	0.9932	1.42
	1173	75.61	4.20E+18	3D-Diffusion	0.9919	1.38
	1273	54.96	1.73E+17	3D-Diffusion	0.9967	1.00

These conclusions can explain the sensitivity of the calculated Arrhenius parameters to the reaction models used in this study. It has been found that the kinetic models used with the TGA data of pyrolysis might not represent this phenomena efficiently, and restrict the data fitting with a certain reaction order and the kinetic parameters [97, 150], and the single global reaction model produces lower activation energy for the coal pyrolysis than does the multi-step simultaneous reactions model, as each reaction has its individual kinetic parameter values [80, 207]. Aggrawal [208] found that at low pyrolysis temperatures, the n=0 or n=1 give the same results. However, this was not the case in this study.

The apparent activation energy E_a results for the devolatilization step are plotted against the final pyrolysis temperature in Fig. 5.6. The decrease in the value of Ea at higher temperatures can be explained by the two sets of reactions competing during thermal decomposition step; The first is the primary reaction that leads to non-reactive volatiles with lower activation energy, and the second is the reactive volatiles part of them passing through secondary reactions to produce char, or escape as tar, and these reactions have a higher activation energy [77, 79, 80]. The primary volatiles are the rate limiting step, therefore the overall reaction rate depends on the functional groups in the fuel and the pyrolysis temperature if other parameters are constant such as the heating rate and the gas flowrate as is the case in this study.

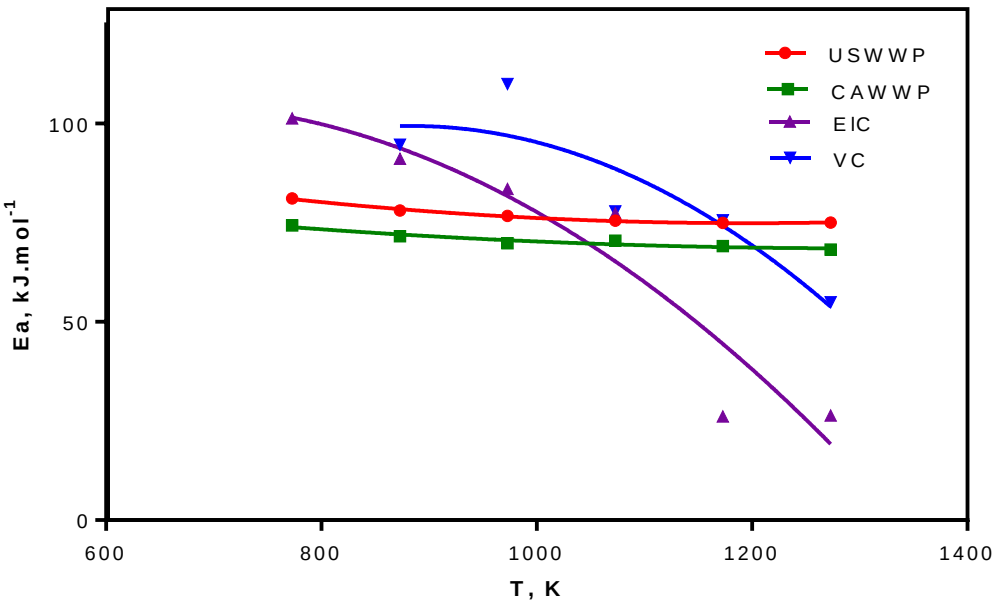

Figure 5.6 Apparent activation energy E_a of the USWWP, CAWWP, ELC, VC pyrolysis in the temperature range 773-1273 K.

At lower temperatures, the high activation energy is required for the secondary reactions to take place. Consequently, the fuel with higher non-reactive volatiles (CO, CO_2, CH_4 and other paraffins) will have a lower activation energy, such as the biomass fuels (known for having more oxygen and hydrogen functional groups) as well as tar. On the other hand, the coal samples have more reactive species (olefins and acetylenes), therefore release less volatiles and produce a higher yield of char. However, at higher temperatures, the energy barrier is overcome and more gases can be produced from the reactive volatiles of higher activation energy.

5.5 Char Combustion Reactivity

5.5.1 DTG Curves

Four fuel samples were thermally treated under an inert gas environment for the devolatilization at final temperatures 773 -1273 K, then after three minutes at that temperature the produced chars were burned with air at 40 mL min^{-1} at the same temperature until a constant mass is obtained. The DTG curves of the USWWP, CAWWP, ELC and VC are illustrated in Fig. 5.7.

The first observation from Fig. 5.7 is the significant increase in the char combustion rate of both biomass samples with the temperature increase, as well as the coal samples. The highest (peak) conversion rates of the four char samples at 1273 K are about twice the conversion rate at a temperature 773 K. Also, the peaks at low temperatures have a long tail with a longer half-time than the peaks at the higher combustion temperatures especially in the coal cases. This is an unmistakable evidence of the char combustion temperature dependence. The stretched peaks of the coal longer than the biomass can be explained by more diffusion limitation of the oxygen into the pore system due to the lower porosity of the coal char.

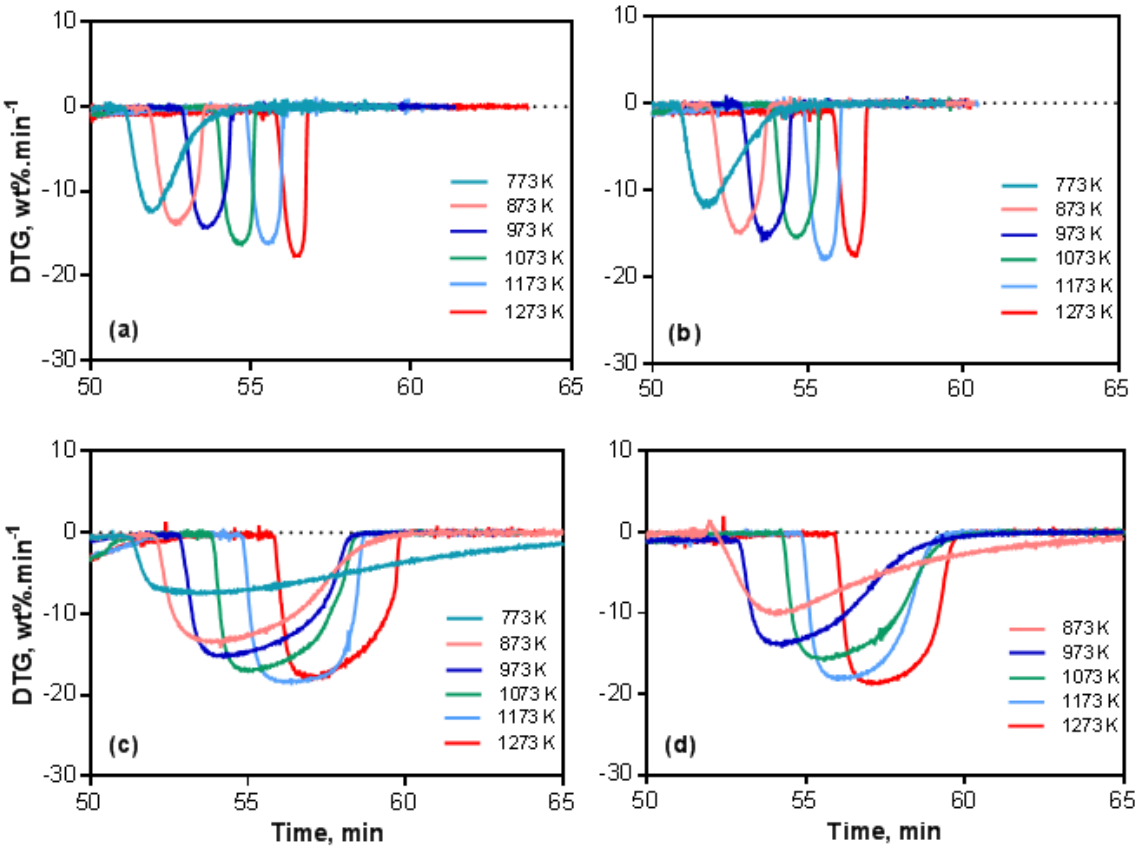

Figure 5.7 DTG curves of the char combustion: (a) USWWP, (b) CAWWP, (c) ELC, and (d) VC, at various combustion temperatures.

5.5.2 Maximum Char Combustion Rate

The maximum char combustion rates ($d\alpha/dt$, s^{-1}) of the four samples are illustrated in Fig. 5.8 and listed in Table 5.8. Evidently, the maximum char reactivity of the biomass samples USWWP and CAWWP are much higher than the maximum rate for the coal samples. This suggests that the char combustion is not only temperature dependant but also dependent on the fuel composition and structure. It was found that the higher the volatile matter content of a fuel, the higher is its char reactivity [209]. These results are in good agreement with the reported results in the literature [152, 159].

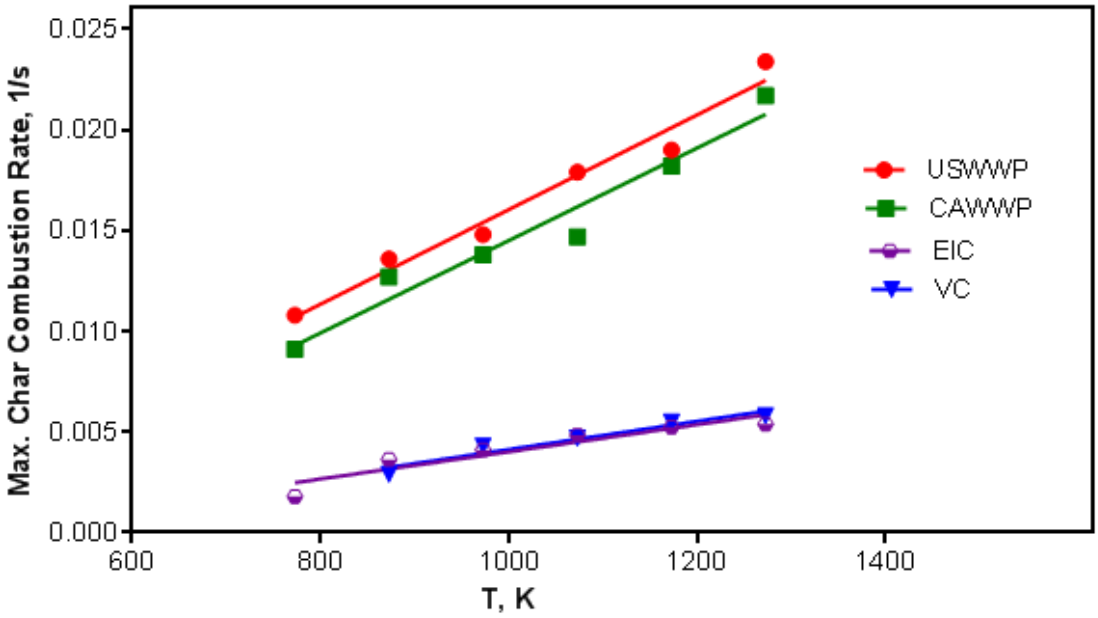

Figure 5.8 Maximum char combustion rates of the USWWP, CAWWP, ELC and VC samples at various temperatures.

For the biomass samples, the USWWP has shown a 10% higher reactivity than the CAWWP. On the other hand, both coal samples, the ELC and the VC show similar maximum rates in the temperature range investigated.

Table 5.8 Experimental maximum char combustion rates ($d\alpha/dt$, s^{-1}) of the USWWP, CAWWP, ELC and VC samples at various temperatures

	RR_{max} , s^{-1}			
T, K	USWWP	CAWWP	EIC	VC
773	0.0108	0.0091	0.0018	
873	0.0136	0.0127	0.0036	0.0029
973	0.0148	0.0138	0.0041	0.0043
1073	0.0179	0.0147	0.0049	0.0047
1173	0.0190	0.0182	0.0052	0.0055
1273	0.0234	0.0217	0.0054	0.0058

The fractional burn off of four fuel chars are calculated as dry-ash-free and plotted as a function of time in Fig. 5.9 to compare the char burn off trend for the four fuels. Clearly, both biomass chars have higher burn off rate than coal samples. Despite their parent biomass alteration in composition, it appears that the pyrolysis step has eliminated the differences and produced very similar char behaviour at all temperatures. The conversion at a temperature 773 K for the USWWP, CAWWP and ELC, and at 873 K for the VC increases rapidly to unity. However, the complete burn off time has decreased with the temperature increase subsequent to a higher burning rate at higher temperatures. A similar trend is observed for all the coal char samples investigated.

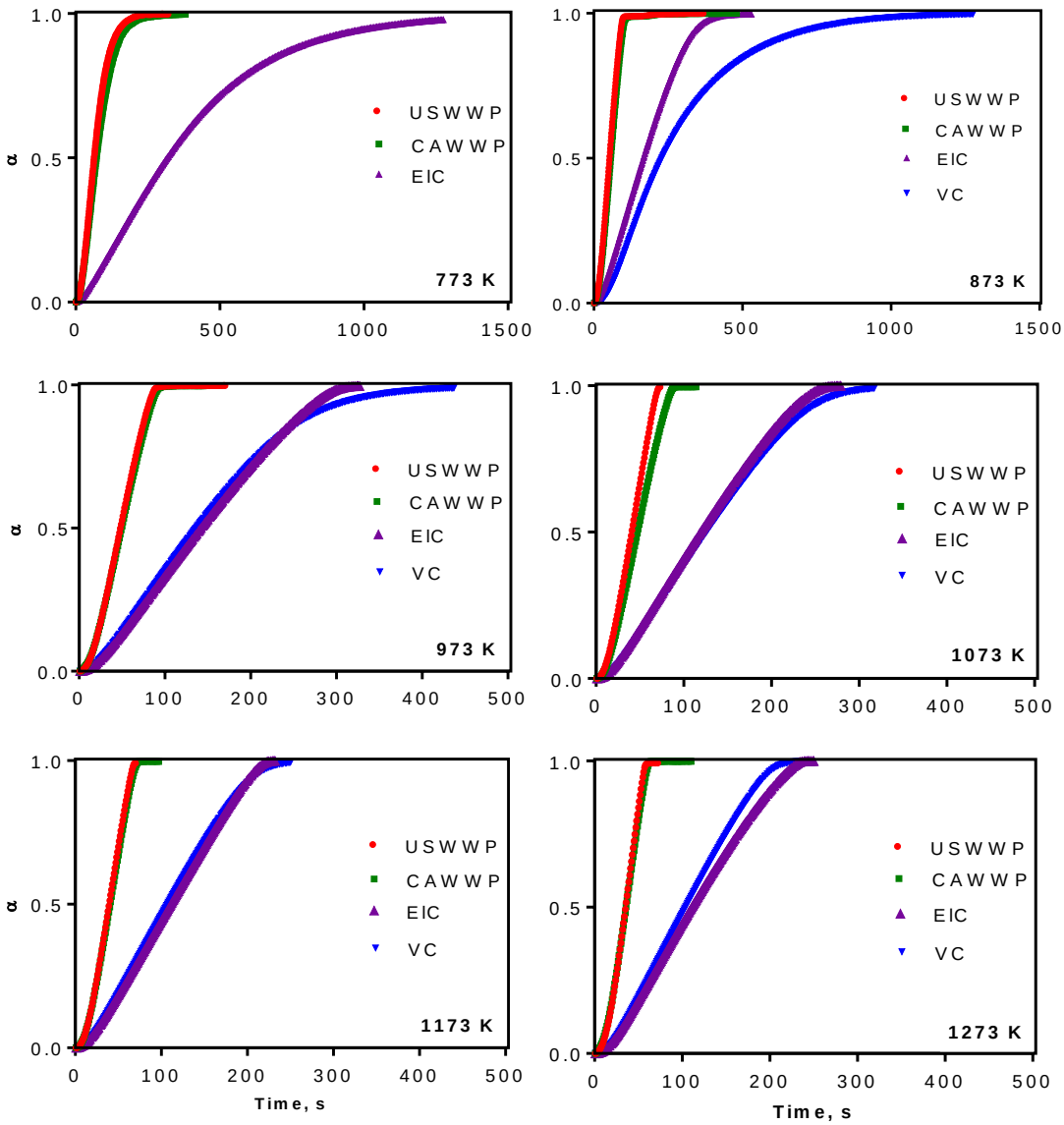

Figure 5.9 Char fractional burn out (α) of the USWWP, CAWWP, ELC and VC.

5.5.3 Char Burn-off Rate

The rate at which the burn off fraction (α) changes with the burn out progress for the four fuel samples, are plotted in Fig. 5.10. In general, the rate increases at the higher combustion temperatures at any degree of the burn off. At a temperature 773 K both biomass samples had the maximum rate at 30-40% burn off. Whereas, the ELC and VC had their maximum reaction rate at 10% and 20% conversion, respectively. This behaviour shows the chemical control mechanism of Zone I reactivity. Lizzio et al. [99] found the maximum rate of bituminous char at 30-40% burn off and Smith [69] reported the maximum rate of the anthracite coal at 21%.

At higher temperatures, the burn off rate did not have a maximum value but a steadier trend for the range of 20-80% conversion. There was a sharp increase in the burn off rate within the first 5% burn off for all samples. This increase can be attributed to the quick combustion of the remaining aromatic hydrocarbons that eliminates the diffusional limitations, thus enabling the reactant gas to reach the micropores. It was found that at temperatures higher than 1173 K, the char micropores increase at the first stages of burn off due to the rapid destruction of the molecular sieve structure and the total surface area increases [210, 211]. On the other hand, thermal annealing starts at temperatures between 973 K and at 1373 K, the micro porosity and carbon edges are lost, and the char structure becomes more graphitic, hence the active sites are lost [90].

With an increase in the burn off, a balance between the pore surface area increase due to pore merging and opening up, and the loss of active sites of carbon occurs. This balance results in an almost steady rate of burn off and a curve of elliptical shape is obtained until 80-90% conversion. Also, this means that the activation energy of the burn off range 20-80% is almost constant. After the 80% conversion, a dramatic decrease in char surface area occurs due to pore coalescence and the reaction rate rapidly reduces after the 95% conversion.

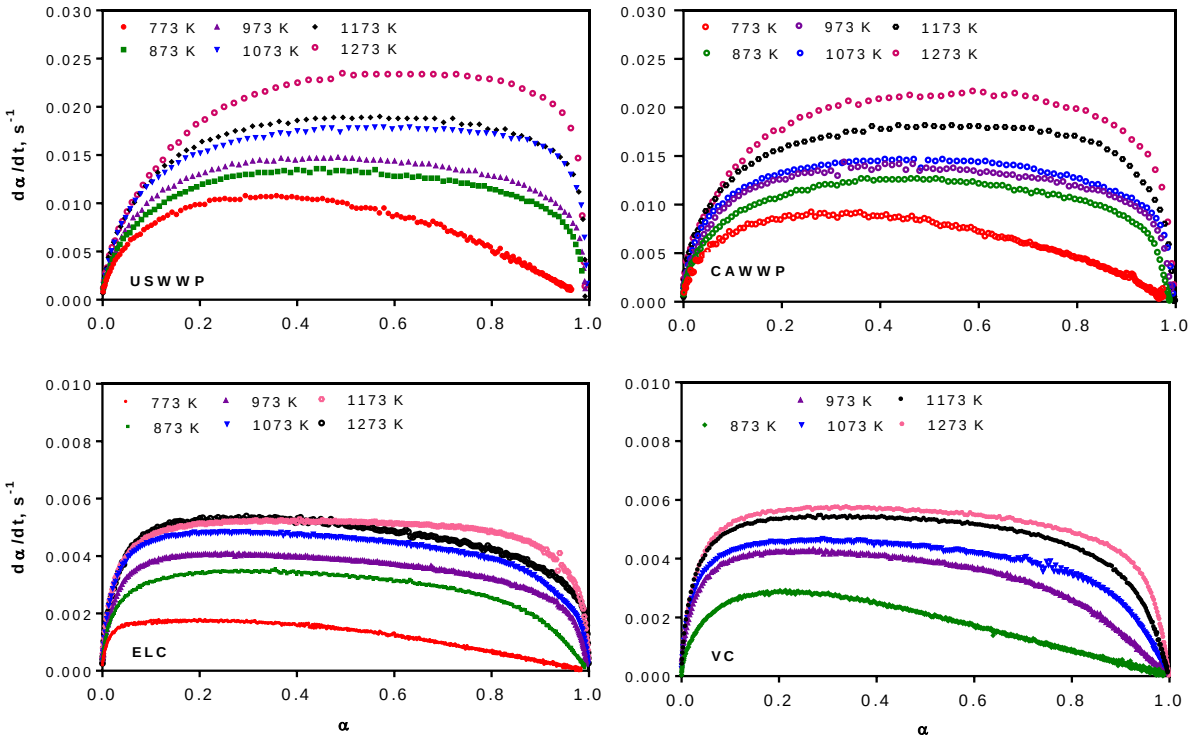

Figure 5.10 Rate of fractional burnout change da/dt with the fraction of burn out (α), for the USWWP, CAWWP, ELC and VC in the temperature range 773-1273 K.

As expected, the effects of the ash and volatile content of the coal samples are reflected on the char burning rate. The reaction rate of the VC char at higher temperatures is higher than the ELC corresponding values. This difference is due to the significantly higher mineral content that not only acts as a reaction catalyst but also inhibits the thermal annealing and graphitic structure formation by maintaining the dislocations and carbon edges, even at the higher temperatures of combustion. In favour of this explanation is the work of Solomon et al. [212] on the crosslinking behaviour during the coal pyrolysis. They found that demineralization of lignite decreases the crosslinking reactions while the bituminous coals undergo early crosslinking during pyrolysis due to the presence of carboxyl groups. A recent study on pinewood char reactivity, Nanou et al. [213] enhanced the steam gasification reactivity by impregnation of ash into the wood char. In other words, the higher oxygen content of biomass that exists as carboxyl group promotes early crosslinking during char combustion thus resulting in a higher reactivity, as well as the mineral content of the VC promoting crosslinking during char combustion leading to a higher reactivity.

5.5.4 Char Combustion Zones

The char combustion rate depends on the temperature, oxygen diffusion into the pore structure, the pore surface area and the concentration of the active sites on the carbon surface. The temperature dependence of the char oxidation can be explained by three temperature zones [90, 97], although they are not clearly specified as certain ranges of the temperature [159]. Never the less, the DTG curves and the reaction rate plots in this study could be used to determine the reactivity regions of the char combustion. From the DTG curves presented in Fig. 5.7, both biomass samples have a clear tail in the peak mainly at a temperature 773 K. The ELC has a wide peak with tail at both 773 and 873 K. On the other hand, the VC extended this behaviour up to a temperature 973 K. This behaviour can be used to identify combustion zones for each fuel. It appears that the biomass enters the combustion Zone II at lower temperatures due to the higher diffusion limitation caused by higher volatile matter content.

5.5.5 Reactivity Index

The reactivity index *RI* of the char oxidation rate is a parameter commonly used to compare the reactivity of different fuel chars [152]. The higher is the *RI*, the higher is the char reactivity:

$$RI = \frac{0.5}{t_{0.5}}, \quad s^{-1} \tag{5.8}$$

where, $t_{0.5}$: is the time of 50% carbon burn out.

The reactivity index values of the char oxidation at 0.2 oxygen partial pressure and temperature range 773 – 1273 K are listed in Table 5.9. As expected, the reactivity index of the biomass samples is higher than those of the coal samples. The USWWP and CAWWP have increased RI values from 0.008 and 0.007 s^{-1} at a temperature 773 K to 0.015 and 0.014 s^{-1} at 1273 K, respectively. The *RI* values of both coal samples increases more quickly, however they show less variability in temperatures above 973 K and increase from 0.002 to 0.005 s^{-1}.

Table 5.9 Reactivity index (*RI*) at 0.2 oxygen partial pressure and temperature range 773-1273 K.

	RI, s^{-1}			
T, K	USWWP	CAWWP	EIC	VC
773	0.008	0.007	0.002	
873	0.010	0.009	0.003	0.002
973	0.011	0.010	0.004	0.004
1073	0.013	0.011	0.004	0.004
1173	0.013	0.013	0.005	0.005
1273	0.015	0.014	0.005	0.005

Figure 5.11 shows the reactivity index variation with temperature. The trend RI increasing with the temperature can reveal the reactivity zones. From Fig. 5.11, biomass chars show 3-4 zones based on the rate of conversion. In a different way, the ELC char shows two different reactivity behaviours; the first is at a temperature 773-873 K and the second at 973-1273 K. Similarly, the VC char shows two behaviours; the first at a temperature 873 K then a different behaviour for the temperature range 973-1273 K. More accurately, the kinetic parameters can exhibit the distinct combustion zones as will be shown in the next section.

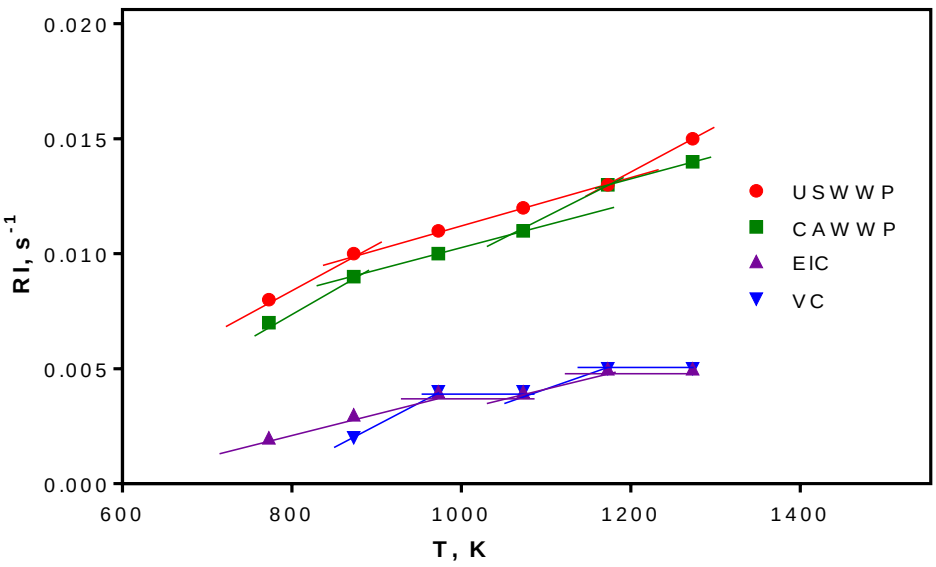

Figure 5.11 Reactivity index of USWWP, CAWWP, ELC and VC at 0.2 oxygen partial pressure and variable temperatures.

5.5.6 Intrinsic Char Reactivity

The derived intrinsic reactivity model in Section 4.3.4 for the char combustion is applied on the set of isothermal TGA experiments to calculate the intrinsic reaction rate and the Arrhenius triplet (activation energy, pre-exponential factor and the reaction order) of char combustion.

The overall reaction rate R_m was calculated according to Eq. (4.21) from the TGA data on the peak conversion. Then the global intrinsic reaction rate coefficient $\ddot{K}$ was calculated according to Eq. (4.40) and Eq. (4.42), and the Arrhenius rate constant (k) is calculated from Eq. (4.24). The intrinsic rate coefficients of char combustion at different temperatures are listed in Table 5.10. Evidently, the rate constant of the four fuels are close to each other at low temperatures (773- 873 K) thus indicating chemically controlled reaction. At higher temperatures, in addition to the chemical rate effect, the diffusion limitations contribute to the differences in reactivity from one fuel to another due to the differences in the pore system. It can be observed that the biomass char reactivity at these temperatures is 2-3 times higher than that of the coal char. The highly porous structure of biomass is dominated by the macro pores in which the oxygen can penetrate mainly by the bulk diffusion. Conversely, the coal char structure includes a higher ratio of the microporous system in which the oxygen transfer by Knudsen diffusion dominates. From the calculations, it was found that the latter is lower than the former by two orders of magnitude.

Table 5.10 Intrinsic rate coefficient in the temperature range 773-1273 K.

	$\ddot{K}$, kg m^{-2} s^{-1} (kmol m^{-3})$^{-m}$			
T, K	USWWP	CAWWP	EIC	VC
773	4.82E-07	4.04E-07	7.21E-07	
873	1.19E-05	1.03E-05	1.10E-05	1.10E-05
973	6.09E-04	3.95E-04	1.07E-04	1.17E-04
1073	7.57E-04	9.00E-04	2.28E-04	1.84E-04
1173	1.59E-03	1.27E-03	4.84E-04	4.77E-04
1273	1.83E-03	1.60E-03	7.41E-04	9.88E-04

Interestingly, the dependence of the intrinsic reactivity on the initial particle density, whether apparent or true, is proved to be negative through the calculations. This finding supports the theoretical conclusion made earlier in Section 4.3.4.2.

The Arrhenius plots of the rate constant k as a function of the temperature reciprocal T are shown in Figure 5.12. Significantly, all the fuel types have exhibited more than one linear region. These regions are correlated by linear functions with least square coefficients ≥ 0.90. The biomass samples exhibited three regions of reactivity; and, the coal samples have shown mainly two regions. Never the less, all the samples had the same reactivity in the temperature region 773-873 K, and this is supported by the conclusion of chemically controlled reactivity in the combustion Zone I. In the temperature range 873-973 K, the biomass samples exhibited a notable change in reactivity, where the higher porosity resulting from the pyrolysis step increases the char surface area and ultimately increases the char reactivity. On the other hand, the coal char samples exhibited a continuous behaviour in the temperature range 773- 973 K, and this can be attributed to the significantly lower surface area than the biomass.

The clear divergence in reactivity of the four fuels in the temperature range 973-1273 K can be interpreted as the transition from chemical-controlled mechanism to diffusion-controlled mechanism where both influence the char reactivity. These characteristics represent the combustion Zone II behaviour. As shown in Section 5.5.5, the reactivity of the coal chars is lower than the biomass char reactivity. Respectively, the intrinsic reactivity of combustion Zone II of the coal chars is lower than the intrinsic reactivity of the biomass char, however, tending to exceed the biomass reactivity at higher temperatures than 1273 K (combustion Zone III), where the diffusion limitations dominate the reaction rate.

5.5.7 Arrhenius Kinetic Parameters

The reaction order for oxygen in the temperature Zone I (773-873 K) was assumed to be 0.5-order for all samples. In the case of the VC, the sample failed to devolatilise at 773 K due to its high ash and low volatile matter contents, however at a temperature 873 K the reaction order was 0.5. This assumption is based on the published data that assumes the intrinsic reaction order value is between 0.5 – 1.0 for Zone I combustion [97, 180]. The reaction order of char combustion rate in Zone II was assumed to be first-order as reported in the literature for the chars of various coal ranks [69], and assumed to be first-order in the absence of experimental data [106]. Young & Smith

[214] experimentally found a value of n=0.4 for the char combustion at a steady-state flow combustor in a temperature range of 940-1420 K (combustion Zone II). However, the discrepancy of these results with the assumption in this study can be explained by the effect of the transport phenomena that is eliminated in the TGA kinetics.

The intrinsic activation energy and pre-exponential factor were calculated from the slop and intercept of the regression lines in the combustion Zone I. As it has been shown earlier in section 4.3.4.2, the activation energy in Zone II is expected to be half of the activation energy observed in Zone I [91, 97]. The results of the intrinsic activation energy E_t and the pre-exponential factor A in Zones I and II are summarized in Table 5.11.

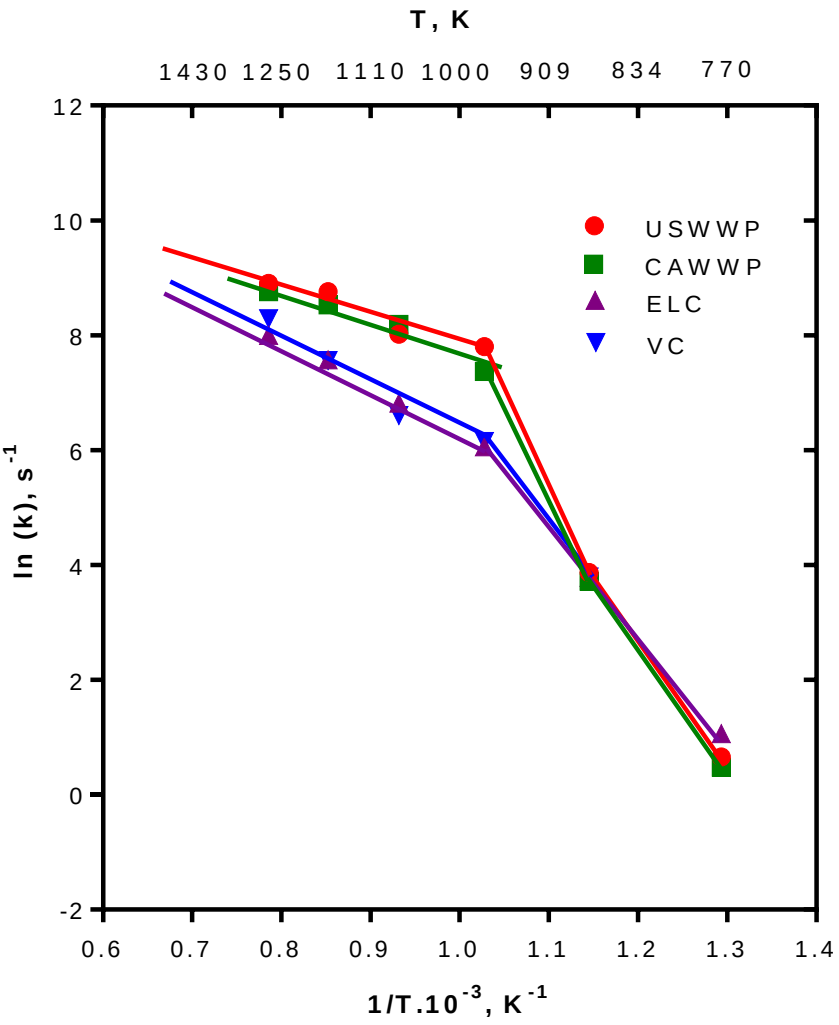

Figure 5.12 Arrhenius plot of ln (k) with the temperature reciprocal.

As it can be seen from Table 5.11, the intrinsic activation energy E_t in the combustion Zone I of the USWWP and CAWWP are 180 and 182 kJ mol^{-1} respectively, and the

pre-exponential factor was 2.85E+12 and 3.04E+12 for the USWWP and CAWWP, respectively. The published work on biomass intrinsic reactivity is rarely found in the literature. Recent studies on wood pellets char reactivity under CO_2 and steam gasification, used the Random Pore model (RPM) to calculate the kinetic parameters, and found a value for the E_t of 220-251 kJ mol^{-1} at temperatures in the range 873-1173 K [197, 215]. However, these results cannot be directly compared to the results of this study due to the different combustion conditions. In the same manner, a recent study by Fang et al. [216], applied the RPM on bituminous coal char combustion to calculate the intrinsic kinetic parameters. They examined the reliability of the TGA data with a microfluidized bed (MFB) data and found that the two methods produced similar kinetic parameters in the low-temperature range 693-783 K. Their data have shown lower values for the E_t 128-137 kJ mol^{-1}, and lower values for the pre-exponential factor A at 5.8 $\times 10^4$ to 6.40 $\times 10^6$. The disagreement of these results with the results of this study can be referred to the model they used and the higher char preparation temperature than the char combustion temperature that might produce different char porosity and pore surface area.

The ELC and VC have values of E_t 153 and 167 kJ mol^{-1}, and the A values are 6.15E+10 and 4.23E+11, respectively. These results are in a good agreement with the published data on the intrinsic coal char reactivity at atmospheric pressure of oxygen. The intrinsic activation energy E_t of semi-anthracite was found to be 167 kJ mol^{-1} [161]. This can be compared to the VC value as it is also considered as semi-anthracite. Other published data such as 134 kJ mol^{-1} for brown-coal char [91], 136 kJ mol^{-1} for lignite char [106], 138 kJ mol^{-1} for sub-bituminous coal [153], and 155 kJ mol^{-1} for anthracite coal [170] are comparable to the coal data in this study.

Table 5.11 Global intrinsic kinetic parameters.

	ZONE I			**ZONE II**			
	E_t kJ mol^{-1}	A, s^{-1}	R-residue	E_a kJ mol^{-1}	A, s^{-1}	R-residue	E_a / E_t
USWWP	180	2.85E+12	0.99	42	3.87E+05	0.93	0.23
CAWWP	182	3.04E+12	0.98	47	6.33E+05	0.99	0.26
ELC	153	6.15E+10	0.97	67	1.79E+06	0.99	0.44
VC	167	4.23E+11	0.99	75	4.17E+07	0.96	0.45

Although the values of the coal char E_t are lower than the biomass corresponding values, the higher values of the pre-exponential factors for the biomass chars appear to be inversely affecting the reaction rates, namely increasing the collision frequencies. Ultimately, the resultant reactivities are very similar as shown in Fig. 5.12.

In combustion Zone II, as expected from the reactivity index curves, the biomass char needs lower activation energy to burn than the coal char needs. The values of E_a for the USWWP, CAWWP, ELC and VC are 42, 47, 67 and 75 kJ mol^{-1}, respectively. The biomass chars show a reduction in the activation energy to 0.25 E_t from Zone I to Zone II, while the ratio for the coal chars are similar to the theoretically expected values at 0.5 i.e. 0.44 and 0.45 for the ELC and the VC, respectively.

5.5.8 Validation of the Intrinsic Char Reactivity Results

Smith [69, 106] reviewed all the published data on intrinsic char reactivity. He unified the intrinsic reaction rate $\ddot{R}$ data on the basis of the oxygen pressure being 1atm and plotted the intrinsic rate versus the reciprocal of the temperature. His plot exhibited a regression line of activation energy at 179 kJ mol^{-1} for chars of various ranks of coal. Although the differences in the pore size and surface area have been eliminated, the variation of the reactivity fell in the range of four orders of magnitude. He attributed these variations to the carbon structure and catalytic or inhibition effects of the impurities.

Accordingly, the reactivity of the chars in this study is recalculated at1atm oxygen pressure at g cm^{-2} s^{-1} units to examine the uncertainty in the calculated intrinsic kinetic parameters, and pointed the results on Smith's plot. Figure 5.13 presents the reactivities of four fuels, namely the USWWP, CAWWP, ELC and VC on the Smith reactivity plot.

The temperature dependence of the four fuel chars is clearly shown in Fig. 5.13, and the alignment with the 179 kJ mol^{-1} activation energy fitted line is very good and this supports the assumptions made for the reaction order. All the char reactivity values were comparable in the combustion Zone I. However, the biomass samples showed higher intrinsic reactivity than the coal char samples in the combustion Zone II. This reflects the lower activation energy of the biomass than the corresponding values of the coal.

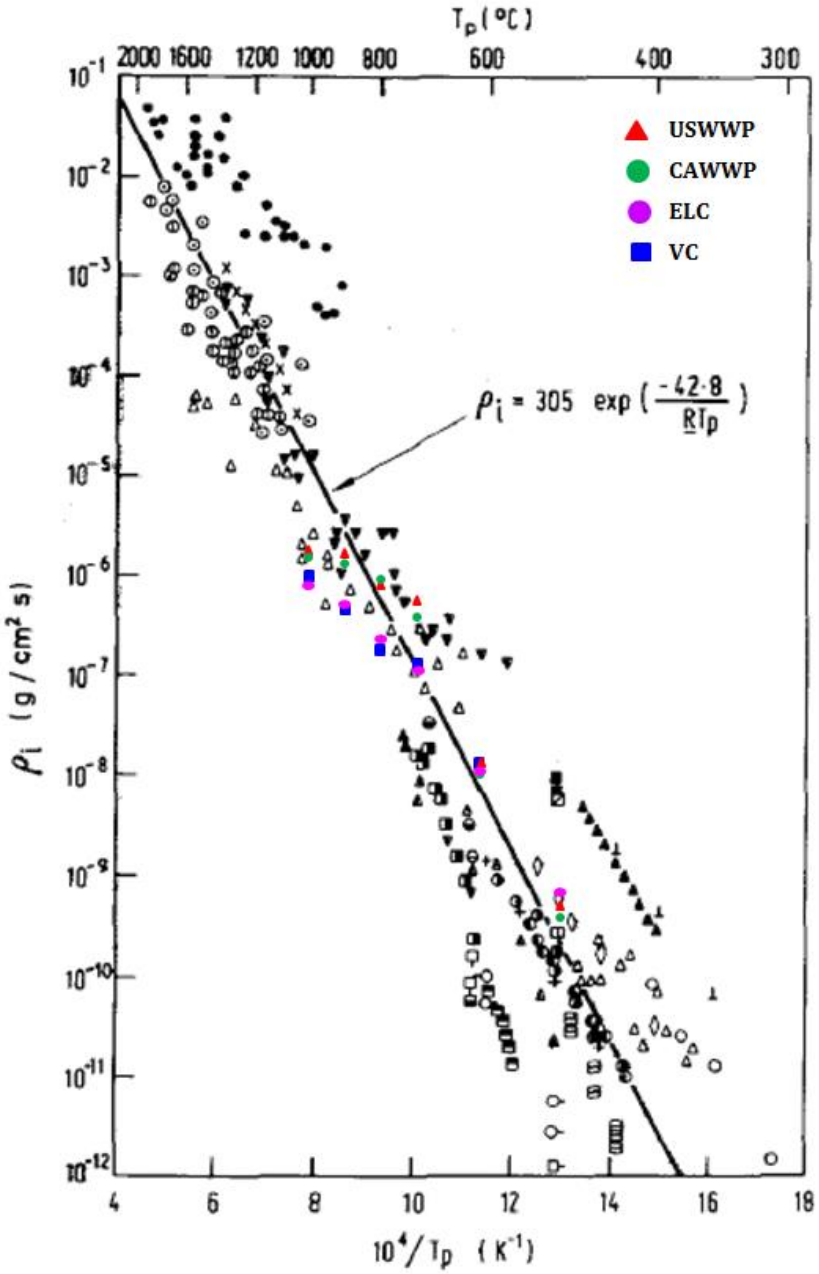

Figure 5.13. Char intrinsic reactivity of USWWP, CAWWP, ELC and VC highlighted on Smith reactivity plot (Smith [69]).

Although the Smith plot was used to verify the char reactivity results of this study, it is important to bear in mind the possible error in the experimental data that were used to generate the plot due to neglecting the effect of the CO_2 absorption in the boundary layer on the intrinsic char reactivity.

5.6 Sources of Errors

In addition to the experimental errors, the assumptions made in the mathematical model could also be a source of error in the resulting kinetic parameters.

i. Biomass particles from milled wood pellets are not spherical even at very small size (<80 micron). It is also difficult to identify the shape factor of the biomass particles. The intrinsic reactivity model of the coal chars assumes the particle is spherical. However, this can be a reasonable assumption for the coal particles not biomass. From Thiele modulus graph [162] the value of η in a plate is 0.3 lower than of a sphere. Therefore, in combustion Zone II, this assumption has generated higher effectiveness factor for the biomass than the actual one and this can decrease the intrinsic reactivity of biomass by one order of magnitude.

ii. The use of the developed surface area model in this study with ±20% error could generate ±10% error in the biomass rate constant k and ±16% error in the coal char rate constant. However, this error did not affect the slope of Ln(k) in the Arrhenius plot and the E_t values were unchanged.

iii. The char pore structure is bi-modal size distribution that combines macro-porous structure where the oxygen penetrates by means of bulk diffusion, and a microporous system in which the Knudsen diffusion controls. However, the effective diffusivity was calculated using the uni-modal pore distribution that assumes mean pore diameter. This assumption can also generate unmeasurable error. However, Smith & Tylor [181, 217] concluded that there was no significant change in char reactivity with simplifying the bi-modal with uni-modal pore structure.

5.7 Summary of Findings

The work of this chapter resulted into the following findings:

i. Wood pellet composition varies significantly from that of the coal. The USWWP and CAWWP have considerably high volatile matter VM compared to ELC and VC. The USWWP has twice the VM of the ELC and 8 times of the VC volatile matter. On the other hand, the ELC has shown the highest calorific value (29,764 kJ kg^{-1} versus 18,587 kJ kg^{-1} for USWWP), i.e. wood pellets have 37%

lower gross calorific value (on dry basis) than ELC. Instead, the VC has shown significantly high ash content (38.20%) and trivially higher GCV than the wood pellets (21,883 kJ kg^{-1}) although it has a higher fixed carbon.

ii. The dry ash-free elemental analysis has shown that the wood pellets have 25% and 42% lower carbon content than the ELC and VC, respectively. The VC rank is found to be anthracite coal due to its high carbon content (92.57%).

iii. Wood pellets start devolatilization at lower temperature than coal, and reach the maximum rate at 170-240 K lower temperatures than the maximum rate temperatures of coal.

iv. Wood pellets have shown higher maximum pyrolysis rates than coal. Also, the increase in the pyrolysis temperature from 773 K to 1273 K has decreased the maximum rates of the wood pellets devolatilization by only 5-10%, whereas in the coal case the maximum rate has decreased by 35-55% with the temperature increase from 773 K to 1273 K.

v. Based on above observation, wood pellets can release 90% of their volatile matter in a temperature about 773 K. While the coal releases less than 38-66% of its volatile matter in this temperature, thus needs higher temperatures for complete devolatilization and this depends on the coal rank.

vi. This variance in behaviour of wood pellets than the coal is translated kinetically into a more stable apparent activation energy E_a during the pyrolysis step in the temperature range under study (only 8% decrease in the E_a value). Whereas, the activation energy of the coal samples exhibited a decrease of 50-25% for the E_a values of the ELC and VC from a temperature 773 K to a temperature 1273 K, respectively.

vii. The integral Isoconversional method with a global power reaction scheme was successful in predicting the pyrolysis kinetics of the USWWP, CAWWP and the ELC. Conversely, the devolatilization of the high ash content coal (VC) was better predicted by the 3D-diffusional reaction model rather than the power model and this indicates the effect of the mineral matter on the release of the volatiles even at low temperatures.

viii. Wood pellets chars produced and burned at temperatures higher than 973 K possess higher reactivity than the corresponding coal chars.

ix. Although the apparent char burn off rate of the wood pellets was higher than the coal rate, both types of fuel have shown similar intrinsic reactivity in the combustion Zone I. This proves the independence of the intrinsic reactivity on the fuel type and rank. Conversely, wood pellets char reactivity was 2-3 times higher than the coal chars in the combustion Zone II due to the highly porous char structure produced at higher temperatures. Both wood pellets and coal chars exhibited an intermediate combustion zone between 973 K and 1173 K.

x. The intrinsic activation energy of the char combustion is found to be 180, 192, 153, and 167 $kJ.mol^{-1}$ for the USWWP, CAWWP, ELC and VC, respectively. It is the first in the literature to report the char intrinsic kinetic parameters of the Vietnamese coal.

xi. The mathematical models of the char surface area and the density that are developed in this study have been proven satisfactory to be used in the prediction of the intrinsic char reactivity. It is the first time in the literature a model for the char surface area and the char density are generated as a function of two parameters.

xii. TGA procedure of a sequential two-step method is found satisfactory to produce a char with an intrinsic reactivity and activation energy being consistent with the chars produced under transport phenomena conditions.

Chapter 6 Pilot Scale Biomass Combustion Results & Discussion

6.1 Chapter Overview

Part of the objectives of this study is to investigate the combustion performance of wood pellets in comparison to coal at pilot scale. In this chapter, the results of the pilot scale experimental work that has been performed in PACT facility on the pulverized combustion rig are presented. The effect of the oxygen environment on the combustion performance is investigated by utilizing two oxidants: air and an oxygen-carbon dioxide mixture. Hence, four combustion cases are included in the investigation: two air-fuel and two oxy-fuel cases.

The first part of this chapter is the fuel particle size distribution, ash composition and the deposition tendencies results. These properties were specifically examined for the only two fuels used in the pilot scale experimental work due to their influence on the results.

The biomass combustion experiments were performed simultaneously with the coal combustion runs on the same rig and with the same thermal input, to create a baseline for data for comparison. Substantial amounts of new data were generated and published in the literature that contributes to a better understanding of the wood pellets combustion in terms of advantages and limitations over that of coal. However, the fuel ash composition is of special importance for this study to answer the question about the combustion behavior of wood pellets. Therefore, as far as this research study is concerned, only the data related to the ash distribution pattern and the deposition formation are presented.

Also, comparisons of the char morphology between the biomass and coal chars generated by the bench scale TGA tests and the pilot scale bottom chars are conducted via a SEM analysis.

6.2 Particle Size Distribution

The particle size distribution (PSD) of the USWWP and ELC (as received) were measured by sieve shaker analysis. The results of the PSD for both samples are shown in Table 6.1 and 95% of the USWWP and 99% of the ELC sample weight, has a diameter less than 500 μm. However, 58.8% of the ELC falls below 60 μm, whereas only 16% of the USWWP particles falls below 60 μm, also 93% of ELC particles falls below 250 μm, whereas, only 67% of USWWP falls below this size. Although these values are normal for milled wood [3], this PSD of the wood pellets is considerably different than the PSD of the pulverized coal used in the combustion power plants. This variation should be considered in the design of biomass combustion plants in comparison to coal in terms of air/fuel flowrates, primary to secondary air staging, and the biomass feeding system with the primary air. It should be noted that there was a 1.5% weight loss in both samples due to the trapped particles in the sieve mesh.

Table 6.1 Particle size distribution of USWWP and ELC

PS Category	**USWWP**			**ELC, wt%**		
Mm	wt.%	STDV	cum. wt.%	wt.%	STDV	cum. wt.%
<25	3.10	± 0.06	3.10	23.09	± 1.55	23.09
25-60	12.48	± 0.31	15.58	35.73	± 2.58	58.82
60-125	26.67	± 0.50	42.25	6.93	± 0.57	65.75
125-200	14.20	± 0.25	56.45	19.28	± 1.34	85.03
200-250	10.31	± 0.21	66.76	7.96	± 0.65	92.99
250-500	27.79	± 0.56	94.55	5.43	± 0.42	98.42
500-1000	3.89	± 0.07	98.44	0.08	± 0.00	98.50
Losses	1.56		100.000	1.50		100.000

Figure 6.1-(a), shows the percentage of PSD categories of both fuels. It is interesting to note that there are two modes of distribution for both biomass and coal particles. Particles of size 25-60 μm, and 125-200 μm have dominated the coal PSD, whereas higher particle size categories have dominated the wood pellets at 60-125 μm and 250-500 μm, respectively. This mode of distribution may have an influence on the

combustion mechanism and the slag deposition and aerosols formation in the fly ash. Figure 6.1-(b) clearly illustrates the differences in particle size of the biomass from coal by 20% in the range 50-300 μm.

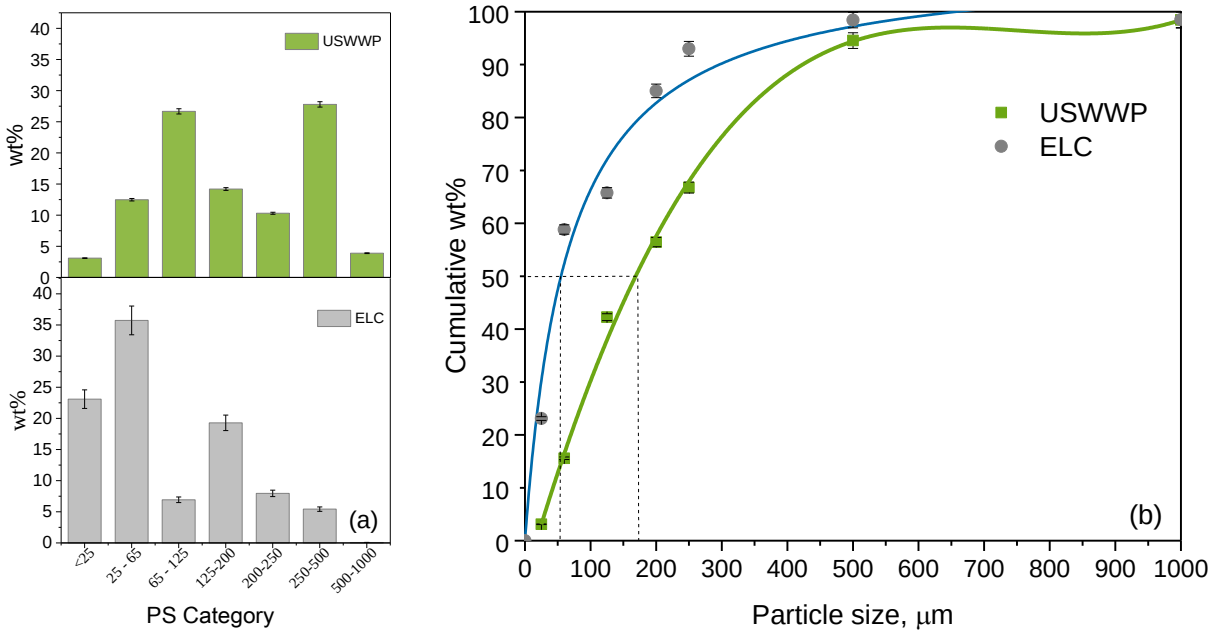

Figure 6.1 Particle size distribution of USWWP and ELC: (a) particle size categories in wt.%, and (b) cumulative particle size distribution in wt.%.

6.3 Fuel Ash Composition

Samples of USWWP and ELC ashes were tested for elemental composition to enable the prediction of the slagging and fouling tendencies for both the biomass and coal. The ash compositional analysis data was generated according to the procedure outlined in Section 3.6.10. The elemental analysis of the fuel ashes for silicon (Si), aluminum (Al), calcium (Ca), magnesium (Mg), barium (Ba), potassium (K), sodium (Na), iron (Fe), manganese (Mn), titanium (Ti), phosphorous (P), Sulphur (S), and chlorine (Cl); were performed with the XRF method and the results are given in Table 6.4. From the data in Table 6.4, a diverse composition of the two fuel ashes can be observed. The USWWP ash is significantly higher in calcium and potassium contents than the ELC (28.82% Ca and 11.74% K in the USWWP, vs. 12.63% Ca and 1.23% K in the ELC). Also, the USWWP ash is higher in Mg, Mn, P, and Cl contents (5.38% Mg, 2.98% Mn, 2.19% P, and 0.27% Cl in the USWWP vs. 1.46% Mg, 0.15% Mn,0.59% P, and 0.02% Cl in the ELC). In contrast, the ELC coal ash contains higher silicon, iron, aluminum, sodium, and sulphur (12.45% Si, 11.76% Fe, 9.62% Al, 2.58% Na, and

4.05% S in the ELC vs. 5.87% Si, 3.14% Fe, 2.67% Al, 1.41% Na, and 1.72% S in the USWWP).

Closer inspection of the data in Table 6.2 shows that the USWWP has higher potassium, alkaline earth metals and chlorine, and lower silica and alumina than coal. Potassium is the foremost source of alkali in the wood pellets. Therefore, it can be expected that the biomass can cause higher fouling and corrosion problems in the boiler tubes, and lower slagging problems in the radiation sections of the furnace. Whereas, the high silicon, aluminum, and iron contents in the coal are expected to increase the furnace slagging. The high sulphur content in the coal can promote alkali sulfates that may increase the tendency of slagging on the furnace walls. However, from the literature review in Section 2.8.3, it has been shown that there are various possibilities of chemical reactions in the multi-element composition, not only depending on the fuel composition, but on the combustion temperature as well. The chemical equilibrium at the combustion temperature can steer the reaction preference towards a certain product rather than another for the same elements. The ash composition results of the USWWP are within the range of the published wood pellets data [116, 218], aspen (white wood) [49], and willow wood and hybrid poplar [2].

For a better prediction of the slagging, fouling and corrosion tendencies of the USWWP, and the ELC in the pilot scale pulverized combustion process, a comparison of the deposition indices are discussed in the next section.

Table 6.2 Ash composition of the USWWP, and ELC, via XRF analysis.

	Ash composition			
Element	USWWP	STD Error	ELC	STDV
Si	5.87	± 0.08	12.45	± 0.94
Al	2.67	± 0.03	9.62	± 0.05
Ca	28.82	± 0.01	12.63	± 0.82
Mg	5.38	± 0.01	1.46	± 0.10
Ba	0.29	± 0.01	0.29	± 0.04
K	11.74	± 0.01	1.23	± 0.11
Na	1.41	± 0.02	2.58	± 0.18
Fe	3.14	± 0.09	11.76	± 0.43
Mn	2.98	± 0.04	0.15	± 0.05
Ti	0.29	± 0.00	0.57	± 0.02
P	2.19	± 0.01	0.59	± 0.04
S	1.72	± 0.01	4.05	± 0.31
Cl	0.27	± 0.01	0.03	± 0.02

6.3.1 Slagging and Fouling Tendencies

The tendency to slagging and fouling in the combustion of wood pellets and the coal have been an issue in the power industry [193]. In this study, the slagging and fouling tendencies of the USWWP and the ELC were compared. Empirical indices, such as the base/acid ratio, slagging index, alkali index, ash melting ratio, high-temperature chlorine corrosion ratio and the potassium slagging ratio were used in the assessment, (see Table 2.5) and the results are listed in Table 6.3.

The data in Table 6.3 shows that the base-to-acid ratio of the USWWP ash is significantly higher than that of the ELC (3.86 for USWWP and 0.92 for ELC), thus indicating a higher slagging tendency for biomass. Also, the silica slagging index R_{SL} indicates a high tendency for slagging for both fuels wood pellets and coal due to the high content of low-melting point basic compounds. However, these two indices neglect the preferences between the basic compounds to form the metal silicates. It was found

that CaO is the primary bonding oxide with silica leading to the release of the alkali to the gas phase [113]. The higher calcium and magnesium in the fuel, the lower alkali silicate deposition can occur. In addition, the phosphorus that is notably high in the USWWP is neglected in these two indices as they were originally formulated for very low phosphorus coals. The increased P_2O_5 in the fuel can bind with K_2O, MgO, and CaO to form a low-melting temperature complex in the fly ash [114, 120]. P_2O_5 is a highly dehydrating agent that sublimes at 633 K, forming H_3PO_4 in the moist combustion gases. Phosphoric acid can react with the basic oxides to form cementing phases of K_3PO_4, Na_3PO_4, Zn_3PO_4, and $AlPO_4$. Therefore, the results of $R_{B/A}$ and R_{SL} need to be interpreted with caution. Barroso et al. [219] suggested not to use the $R_{B/A}$ ratio with biomass fuels that have high calcium content as those in this study.

Table 6.3 Slagging and fouling indices of USWWP and ELC

	Slagging and Fouling Tendencies					
	Low			High		
	$R_{B/A}$	R_{SL}	*AI*	R_{AM} (molar)	R_{CC} (molar)	R_{KS}
USWWP	3.86	0.19	0.058	0.41	14.31	2.16
ELC	0.92	0.42	0.048	0.24	N/A	0.32

In contrast to the $R_{B/A}$ and R_{SL}, the *AI*, R_{AM}, and R_{CC} results have shown low tendency to fouling, potassium slagging, and high-temperature corrosion for both USWWP and ELC. The *AI* is significantly low for both fuels, and this indicates low fouling tendencies. The AI value of the ELC is in good agreement with the published data by Xing et al. [193] on ELC ash (0.04), and the result of USWWP R_{AM} is in good agreement with the published data as well. De Fusco et al. [220] studied the deposition propensity of a wood species, and their results showed R_{AM} values at a range 0.25-0.56. The high value of R_{CC} in the USWWP (14.31) puts forward the assumption of low corrosion risk in the elevated temperature zones due to the low chlorine content in the wood pellets. The R_{CC} does not have a statistical meaning for coal as the S content is significantly higher than chlorine in most of the coal ranks (see Table 2.3). On the other hand, the alkali to silicon ratio R_{KS} for the wood pellets was higher than that of the coal. This can be interpreted as lower tendency of USWWP for slagging than ELC. Winnika et al.

[116] found a high slagging in the combustion of wood pellets with R_{KS} 0.5, and found no slagging with wood pellets that have a value of R_{KS} at 3.1.

In summary, the deposition indices have given contradicted tendencies for the biomass and coal ash depositions. These contradictory results may be due to the uncertainty in the XRF data, especially for the low content elements such as the S and Cl, or to the experimental basis that these indices were derived from. In addition, a lack of characteristic differences between biomass and coal can be observed despite their complete difference in the ash composition. The results of the deposition tendencies therefore, need to be interpreted with caution. The only distinguishing index between the two fuels is the R_{KS}. Thus, the judgement on the deposition propensity through the empirical deposition indices is not revealing.

6.4 Pilot Scale Combustion Experimental Design

The data of the air and oxy combustion experiments were collected from the baseline cases of combustion. The baseline cases were achieved by optimizing the burner performance with fuel-oxidant flowrates, in-flame temperatures, and the exit oxygen and gas emissions. The oxy-fuel runs were designed to compare with the air-fuel runs in the input oxygen ratio and the primary oxidant fraction of the total gas. Both qualitative and quantitative analyses of the collected data were used in this investigation.

The thermal input of the four combustion cases were set at 200 kW, and the oxy-fuel case was enriched with 27% weight oxygen in order to simulate the air composition of oxygen at 21% vol. The fuel and oxidant flowrates were adjusted to maintain a 3.5-4.0% exit oxygen (on dry basis). The USWWP-air test run continued for 9.85 hours and consumed 412 kg biomass. Similarly, the USWWP-oxy test run continued for 10.77 hours and consumed 451 kg biomass. Likewise, the ELC-air, and ELC-oxy runs took place for 7.8, and 10.0 hours and consumed 194 and 251 kg coal, respectively.

6.4.1 Ash Stream Flowrates

When each baseline case was achieved, the ash samples were collected for a certain time from the bottom of the FG pipe (BOA), and the cyclone ash (CLA) as shown in Fig.3.7. However, the flowrate of each stream is the average over the total experimental time. The samples of CLA and BOA have shown fluctuations from the all

day average value by ±5%, and this is due to the fluctuation of the air and fuel flowrates. In addition, the unburned fuel/char particles and the deposited ash particles in the water tray (BCD) at the bottom of the furnace are also collected at the end of the testing day, as this comprises a considerable fraction of the unburned fuel, especially in the biomass case. Traditionally, this residue is the main source of the thermal losses in the biomass combustion due to its high carbon content.

Visually, the FTA sample was lighter in weight and with a finer particle size than the CLA for all combustion cases. The BOA had a higher char percentage in the USWWP-oxy combustion than the USWWP-air case. Figure 6.2 displays photographs of the BOA, char and the deposition particles collected from both USWWP-air (Left) and USWWP-oxy (right) cases. The char particles in the BOA of air combustion case were finer than the ones in the oxy combustion case, indicating better combustion and higher burnout in the former than the latter case. Similarly, the furnace bottom residue (BCD) consisted of higher amounts of char and unburned fuel in the oxy case than those in the air case. The reason for this can be explained by the difference in the residence time of the biomass particles in the furnace. The total air flowrate in the air-biomass case is higher than the oxy-fuel case therefore, larger particles can drop down to the furnace bottom due to the lower oxidant speed in the case of USWWP-oxy. In both cases of combustion, refractory particles and large deposition agglomerates were found. From the photographs in Fig. 6.2-(e)&(f) we can see that the deposition particles combine various types of deposits as well as considerable amounts of the refractory deposition. These varied in hardness, colour, and structure.

In both of the coal combustion cases there were difficulties in collecting the furnace deposition from the bottom water tray, and the use of the deposition probe was out of the scope of this study. However, the same calculations of the biomass BCD were applied to calculate the BCD compositions of the coal cases. In the same time, the bottom char and unburned coal particles dropped in the water tray were insignificant.

It is worth noting that the bottom opening of the furnace is only 150 mm in diameter. And the area of this opening represents only 2.77% of the total area of the furnace base. Therefore, the amount of BCD that is collected from this opening does not represent the total amount of unburned fuel or the adjacent depositions. The actual amount can be estimated from the ash mass balance as will be shown later in this chapter.

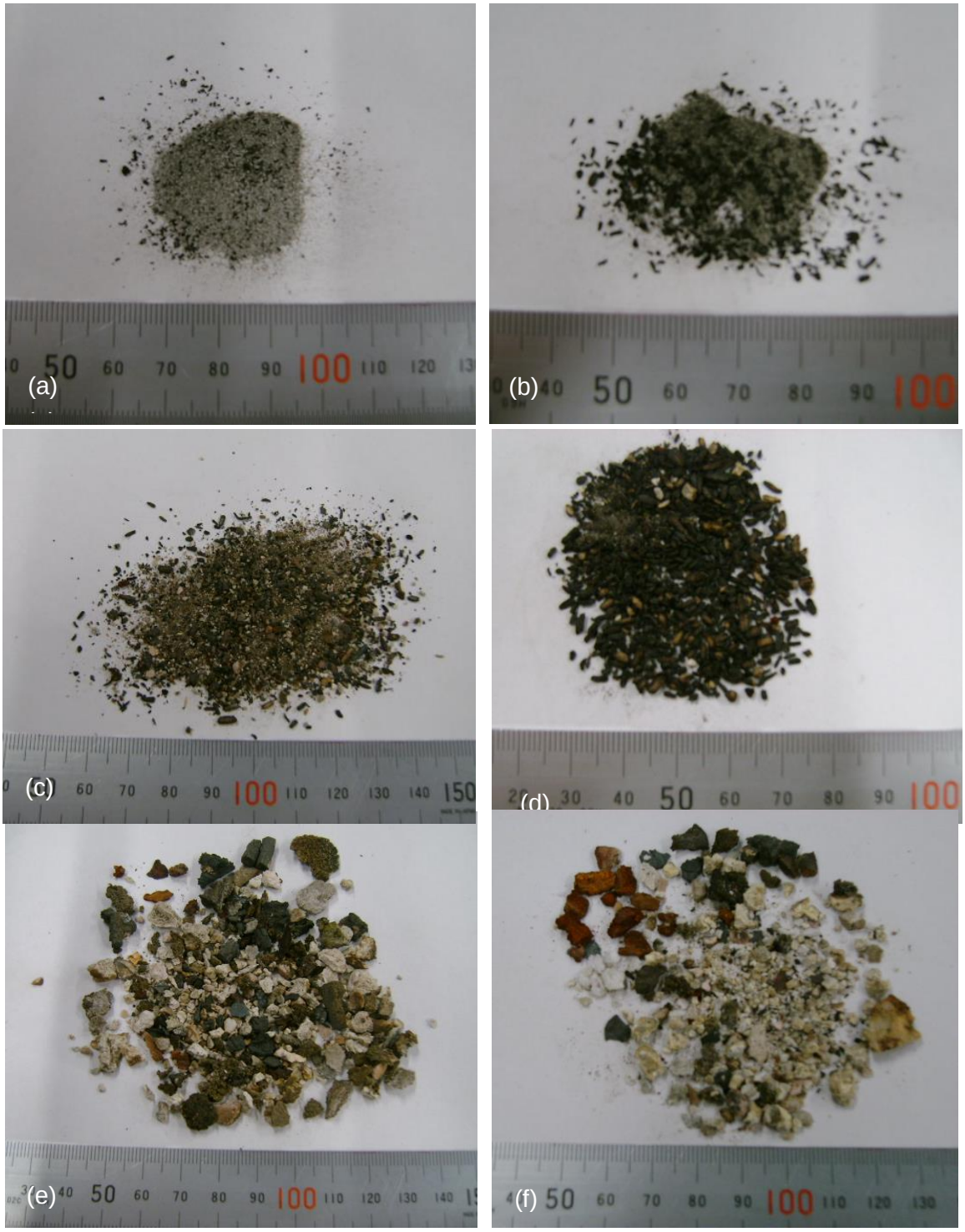

Figure 6.2 Photographs of the biomass combustion ashes in air-biomass (left) and oxy-biomass (right) cases; (a) &(b) BOA, (c)&(d) BCD char, and (e)&(f) depositions.

Table 6.4 shows the ash flowrates at each sampling point for the four combustion cases. It can be seen from the data in Table 6.4 that the cyclone has collected the main part of the fuel ashes. This result can be explained by the fact that the cyclone ash contains higher amounts of the large particles (metal oxides) and these comprise the majority of the ash composition, rather than the amounts of the fine particles (metal chlorides and sulphates) that are mainly collected by the candle filter. Interestingly, the biomass-air had lower CLA, FTA, and BOA than the oxy combustion case, suggesting a different path of chemical reactions in the two combustion environments. The higher percentage of the large particles in the wood pellets, with the low FG mass flowrate, are the reasons for this discrepancy, as the large ash particles can easily fall by gravity close to the walls of the rising FG pipe where gas velocities are lower.

On the other hand, the coal had a higher CLA and FTA, but lower BOA in the air combustion than those in the oxy combustion case. These results may partly be explained by the different mineral composition of the initial fuels.

Table 6.4 Ash flowrates in g h^{-1} from different collection points for the four combustion cases

	CLA	**FTA**	**BOA**
Combustion case	g h^{-1}	g h^{-1}	g h^{-1}
USWWP-Air	84.73	38.77	7.03
USWWP-Oxy	89.81	51.91	10.42
ELC-Air	287.85	120.65	4.66
ELC-Oxy	251.00	114.62	11.51

Figure 6.3 illustrates the ash flowrates of the three ash collection points in the biomass and coal combustion cases. Interestingly, the USWWP-air combustion had higher bottom ash than the bottom ash in the ELC-air case. The reason for this difference can be attributed to the different particle size distribution.

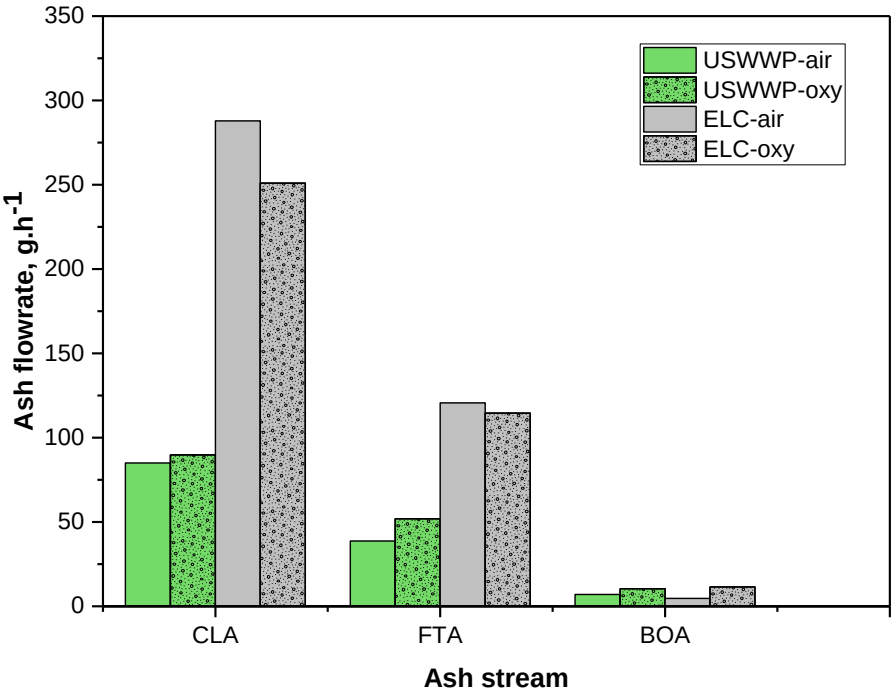

Figure 6.3 Comparison of ash flowrates in the combustion cases; USWWP-air, USWWP-oxy, ELC-air, and ELC-oxy, in $g.h^{-1}$ from collection points CLA, FTA, and BOA.

The fractional distribution of the fuel ash among the different fly ash streams and the deposits depend on many factors such as the fuel particle size distribution, fuel ash composition, adiabatic flame temperature of the combustion process, and the heat transfer in the furnace. Thus, it is expected to see differences between biomass and coal ash distribution in both cases air and oxy-fuel combustions. To illustrate the ash distribution pattern, the mass in part per million (ppm) of pure CLA, FTA, and BOA, are normalized to the original fuel ash content. This method served to calculate the remaining ash parts (BCD) that is anticipated mainly as bottom depositions on the furnace walls and base, and insignificant amounts of submicron aerosols that could be transported with the stack gases.

In the USWWP-oxy case, the CLA, FTA, and BOA were found to be higher at 31.57%, 18.03%, and 3.49%, respectively. Accordingly, the calculated deposition fraction (BCD) in the USWWP-air is higher than that of the combustion with the O_2/CO_2 mixture (54.57% vs. 46.91%).

Opposite trends were found for the ELC cases, the ELC-air has produced higher fly ash in the ELC-air than in the ELC-oxy case (38.64%, 16.24%, for the CLA and FTA, respectively), except in the BOA case, the oxy-fuel case produced higher bottom ash. Consequently, the bottom depositions are expected to be higher in the oxy-fuel case than in the air-fuel case (49.35% vs. 44.61%).

Table 6.5 Fractional distribution of the fuel ash on CLA, FTA, BOA, and BCD streams for the USWWP and ELC combustion cases.

	A_{fuel}	CLA		FTA		BOA		BCD	
	ppm	ppm	wt%	ppm	%	ppm	%	ppm	%
USWWP-Air	6700	1973	29.45	907	13.54	164	2.45	3656	54.57
USWWP-Oxy	6700	2115	31.57	1208	18.03	234	3.49	3143	46.91
ELC-Air	29000	11205	38.64	4710	16.24	148	0.51	12938	44.61
ELC-Oxy	29000	9836	33.92	4479	15.44	374	1.29	14311	49.35

Figure 6.4 compares the fractional distribution of the fuel ash on the four ash streams in the four combustion cases. The pie chart in Fig. 6.4 shows that, in comparison to coal, the USWWP-air has a lower percentage of fly ash (CLA + FTA), and a higher percentage of the bottom ash and depositions than the ELC-air case. A possible explanation for the discrepancy is the particle size distribution. As shown in Fig. 6.1, the USWWP has larger particles with high abundance rather than the ELC. Higher amount of the large ash particles is expected to reside in the bottom ash more than being conveyed with the fly ash. Further, the high content of the earth alkaline metals in the wood pellets may result in a higher carbonate and silicate depositions in the bottom of the furnace. It is important however, to mention that other factors may contribute to the deposition occurrence such as the fuel ash composition and the combustion temperature.

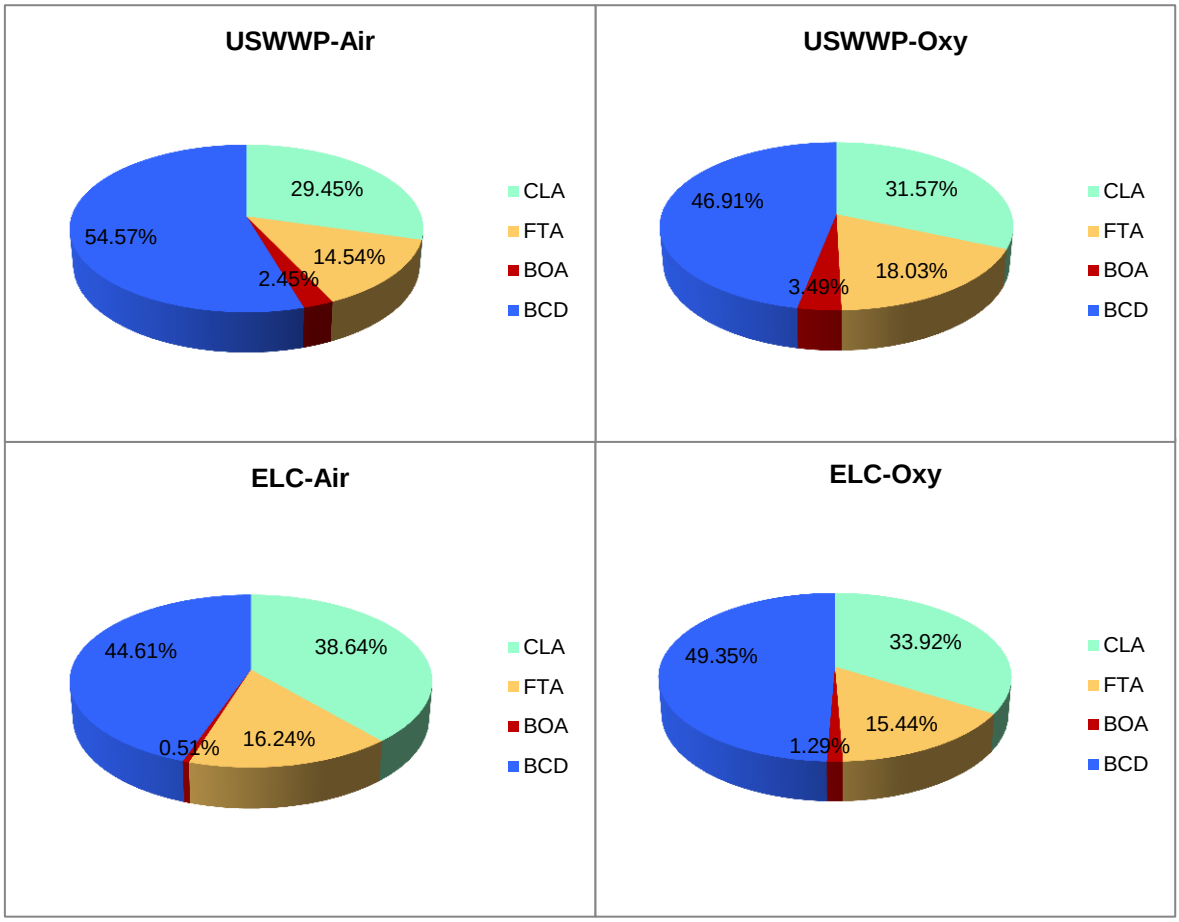

Figure 6.4 Ash fractional distribution as CLA, FTA, BOA, BCD in four combustion cases USWWP-air, USWWP-oxy, ELC-air, and ELC-oxy

6.4.2 Ash Compositional Analysis

Further investigation on the ash distribution is performed by the data collected from the XRF analysis of the different ash streams. Each ash sample was analyzed for the elemental composition (Si, Al, Ca, Mg, Ba, K, Na, Fe, Mn, Ti, P, S, and Cl). The XRF analyses have shown absolute errors in the readings ranging between 0.01% for Ti, and 0.20% for Ca, the other elements fell in this range. The repeatability of each test was in the range 0.00–1.60 standard deviation in the mean of duplicate readings. The highest errors were in the Ca for the USWWP and the Si for the ELC. To estimate the BCD composition, mass balance of each element in the fuel ash and the produced ash streams was performed. The analysis results are presented in Table 6.6.

Table 6.6 Elemental analysis (wt%) of CLA, FTA, BOA, and BCD for the four combustion cases USWWP-air, USWWP-oxy, ELC-air, and ELC-oxy.

Combustion case	Element	CLA %	FTA %	BOA %	BCD %	Av. STDV
USWWP- Air	Si	4.75	2.82	5.80	7.22	± 0.43
	Al	1.66	2.32	0.91	3.38	± 0.13
	Ca	40.22	16.25	35.58	25.47	± 1.60
	Mg	4.58	1.43	3.22	6.88	± 0.21
	Ba	0.27	0.32	0.22	0.30	± 0.02
	K	2.68	21.69	3.20	14.54	± 0.52
	Na	0.63	2.11	0.58	1.69	± 0.03
	Fe	2.57	4.42	1.80	3.18	± 0.37
	Mn	3.89	1.88	3.36	2.73	± 0.15
	Ti	0.17	0.15	0.17	0.39	± 0.01
	P	2.04	1.51	1.66	2.46	± 0.13
	S	0.45	6.20	0.90	1.32	± 0.19
	Cl	0.10	1.70	0.13	0.00	± 0.05
USWWP - Oxy	Si	6.76	3.92	9.03	5.78	± 0.37
	Al	1.95	3.09	1.69	3.07	± 0.20
	Ca	34.87	17.11	37.36	28.61	± 1.50
	Mg	3.71	1.56	4.21	8.05	± 0.23
	Ba	0.27	0.31	0.32	0.30	± 0.01
	K	4.65	21.96	3.52	13.20	± 1.09
	Na	0.83	2.00	0.65	1.62	± 0.18
	Fe	3.17	4.57	2.85	2.58	± 0.25
	Mn	3.19	1.47	3.66	3.36	± 0.14
	Ti	0.25	0.21	0.28	0.35	± 0.01
	P	1.78	1.57	1.98	2.72	± 0.12
	S	1.13	7.20	0.75	0.08	± 0.41
	Cl	0.26	0.91	0.18	0.03	± 0.02
ELC - Air	Si	15.08	11.75	17.31	10.36	± 0.25
	Al	8.75	9.46	7.16	10.46	± 0.13
	Ca	13.28	15.26	13.58	11.10	± 0.15
	Mg	1.11	1.45	0.95	1.76	± 0.04
	Ba	0.25	0.36	0.17	0.29	± 0.00
	K	0.82	1.51	1.97	1.46	± 0.03
	Na	1.15	2.32	0.67	3.92	± 0.05

Continued

Combustion case	Element	CLA %	FTA %	BOA %	BCD %	Av. STDV
	Fe	10.96	14.19	8.85	11.59	± 0.12
	Mn	0.11	0.22	0.32	0.15	± 0.00
	Ti	0.61	0.61	0.51	0.52	± 0.02
	P	0.40	0.72	0.56	0.70	± 0.01
	S	0.41	2.35	2.54	7.84	± 0.02
	Cl	0.04	0.12	0.32	0.00	± 0.01
ELC - Oxy	Si	18.43	13.40	16.24	7.93	± 1.01
	Al	9.69	10.10	8.33	9.46	± 0.62
	Ca	13.37	15.81	13.47	11.11	± 0.97
	Mg	0.98	1.22	0.73	1.87	± 0.13
	Ba	0.26	0.31	0.20	0.30	± 0.02
	K	0.97	1.10	1.05	1.44	± 0.05
	Na	1.09	1.56	0.70	3.96	± 0.13
	Fe	11.04	12.67	10.73	11.99	± 0.85
	Mn	0.12	0.16	0.16	0.17	± 0.01
	Ti	0.69	0.59	0.60	0.47	± 0.04
	P	0.41	0.67	0.48	0.68	± 0.04
	S	0.42	2.03	1.88	7.23	± 0.13
	Cl	0.03	0.02	0.31	0.03	± 0.01

A first glance at the data in Table 6.6 reveals the variation in composition of all ash streams from the original fuel ash composition, as well as from each other. Firstly, the USWWP-air CLA contains essentially calcium (40.22%), silicon (4.75%), magnesium (4.58%), and manganese (3.89%). Very little sulphur, chloride, and sodium were found in the CLA. Whereas, the candle filter ash FTA was abundant with potassium, calcium and sulphur (21.69%, 16.25%, and 6.20%, respectively), and lower abundant in iron (4.42%). Like the cyclone ash, the bottom ash had a high content of calcium (35.58%) and silicon (5.80%), whereas the ash deposition (BCD) of USWWP-air consisted mainly of calcium, potassium, and silicon. In a similar trend, the USWWP-oxy ash has the same mineral distribution pattern in the four ash streams, with slight differences in some elements such as higher calcium and lower silicon were found in the BCD deposition.

On the other hand, ELC-air combustion produced a different ash pattern. Surprisingly, the CLA and FTA had almost the same composition as the fuel ash, except the silicon and sulphur, silicon was pronounced in the CLA (15.08%), and the sulphur was 0.41%. In the same pattern, the FTA and BOA had high abundance in calcium, silicon, iron,

and aluminium. In contradiction to wood pellets, the coal BCD had a significant percentage of sulphur (7.84%) compared to the other ash streams, as well as the iron, calcium, aluminium and silicon. The same observations were found on the ELC-oxy ash compositions.

The data presented in Table 6.6 are mapped in Fig. 6.5 for the USWWP-air and USWWP-oxy, and Fig. 6.6 for ELC-air, and ELC-oxy, respectively. These figures illustrate the abundance of each element in the various ash streams. The colored lines connecting the data points are for easier tracking only.

The appropriate explanation of the elemental distribution trend in each fly ash stream and the bottom deposition requires a closer inspection to the melting points as well as the condensation points of the commonly identified compounds of the ash minerals. The condensation temperatures of the potential mineral compounds could be a major factor in the deposition incidence as well as the melting temperatures. It is possible, that the mineral form with the highest condensation temperature is expected to slag and stick to other ash solid particles (metal oxides) or stick to the furnace walls by inertial impaction, earlier than other forms of that mineral. Not all these particles will reach the wall, therefore the remaining particles will either freeze with the temperature decrease and remain in the fly ash, or deposit on the first surface they impact upon, such as the furnace bottom and FG pipe (in this study case). The deposition site depends on the melting point. The lower melting point of a compound extends the deposition to further surfaces of the heat exchange, whereas the high melting point ends the deposition occurrence at an earlier stage. On the other hand, the low condensation-temperature compounds can remain in the vapor phase to be conveyed with the flue gases to further cooling stages, then condense and deposit on the heat exchanger tube surfaces. Taking into consideration the effect of the chemical equilibrium and stability of each compound, the deposition prediction can be closer to the actual occurrence. Hence, a review of all the condensation and melting points of the potential mineral compounds was conducted, bearing in mind that the flue gases in this study case leave the furnace at 1073-1273 K.

In the combustion furnace, alkali, sulphur and chlorine are expected to be released as vapors and react in the gas phase in the presence of oxygen and water vapor to form alkali sulfates and chlorides [50]. K_2SO_4 is expected to be the first slagging precursor as it has the highest condensation temperature (1962 K). Then, these sticky particles

adhere to the furnace walls and trapping the metal oxides (CaO, MgO, FeO, Al_2O_3) to form a thin fused glassy film on the walls [48]. Downstream the furnace, the dissociation of K_2CO_3 to K_2O occurs at 1173 K, where K_2O bonds with silica to form potassium silicate K_2O_3Si that has a low melting point, hence may initiate the agglomeration on the furnace bottom and tube surfaces. Potassium silicate is a corrosive, irritant material that can cause severe corrosion to the boiler surfaces. In general, the basic oxides (CaO, MgO, K_2O, Na_2O, P_2O_5) can react with the acidic oxides (SiO_2, Fe_2O_3, MnO, Al_2O_3) to form a ceramic-form deposition. K_2O is the least stable among the potassium compounds, as it decomposes at 573 K. Therefore, potassium vapors are found in the initial stages of the combustion process.

Wood pellets are primarily rich with calcium and potassium. Calcium is pronounced in all the fly ash streams CLA, FTA, BOA, as well as the bottom deposition BCD. The melting point of CaO and $CaSO_4$ are 2886 K, and 1733 K, respectively, thus they are expected to comprise the fly ash calcium, whereas the calcium in the deposit is expected to be $CaCl_2$, as its liquid phase occurs in the range 1045-2208 K. Most of the fuel ash potassium, was collected with the filter ash and the bottom deposition (21.69% FTA, and 14.54% BCD). The high abundance of potassium and sulphur in the FTA suggests that the K_2SO_4 is the main form of potassium in the fly ash, as it is in the solid phase at the exit of the furnace (high freezing point 1342 K), and the particle size is small enough to be conveyed to the candle filter. Previous studies on wood and wood pellets combustion observed potassium sulfate in the upper furnace sections, and in the convective passes [50, 116, 221].

However, the sulphur is not enough to react with all the potassium. Therefore, a large fraction of the potassium has deposited in the furnace bottom BCD, and the expected forms are K_2SiO_3, KCl, K_2O and KOH, as their freezing points are lower than 1073 K (1023, 1043, 1013, and 633 K, respectively). Considering the chemical stability of the three compounds, KCl is the most stable and has a high boiling point (1693 K), and therefore the particles are sticky at the furnace exit temperature, and can be found attached to the fly ash particles passing the cyclone to be captured with the aerosols in the filter ash FTA. In support of this explanation is the high chlorine content in the FTA relative to the other fly ash streams. In the industrial boilers, KCl was found in the fouling deposition on the super heater tubes [2]. For the USWWP-oxy, Fig. 6.5 shows clearly the similarity with the air combustion case in the elemental distribution, except the silicon as it was higher in the bottom ash than in the bottom deposition BCD.

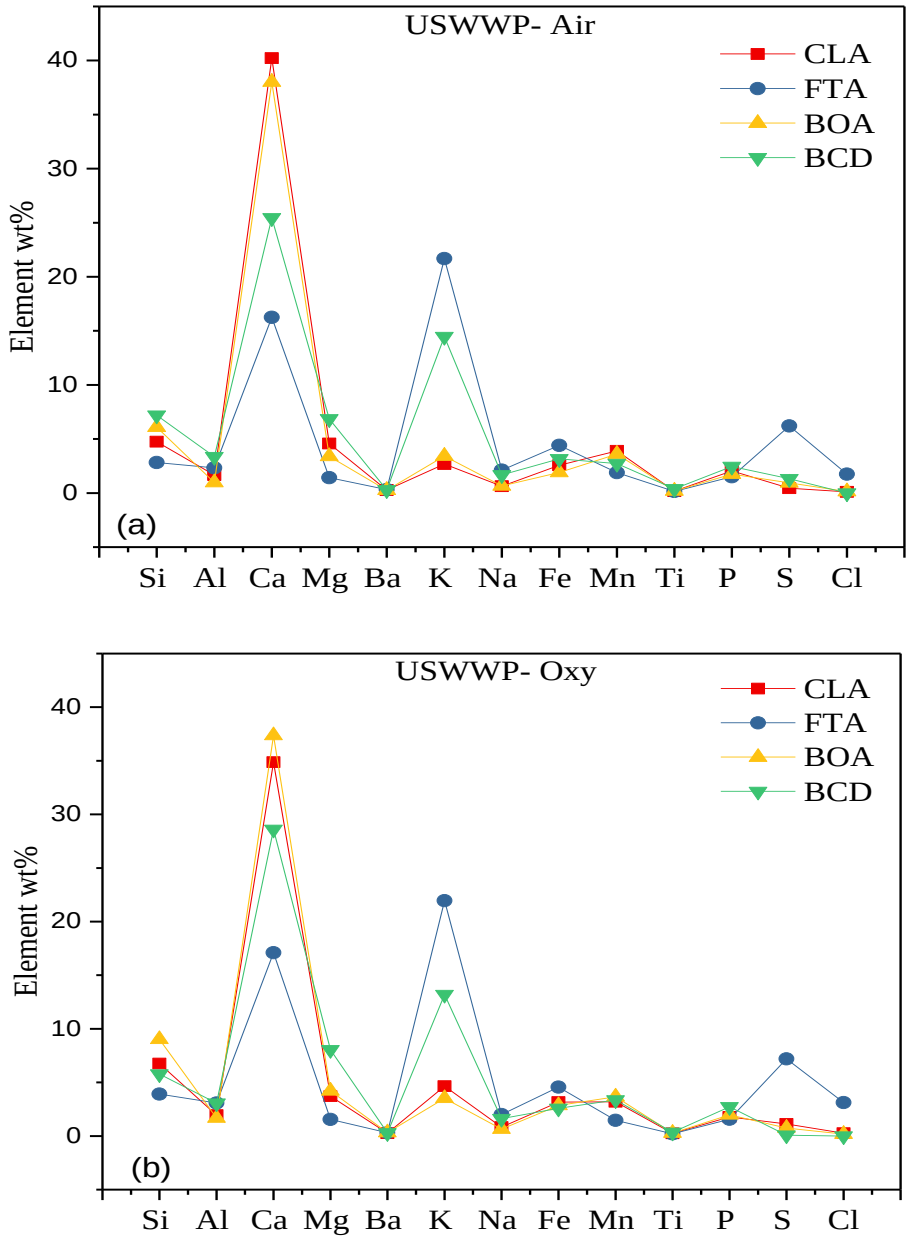

Figure 6.5 Elemental analysis of the ash in CLA, FTA, BOA, and BCD of (a) USWWP-air, and (b) USWWP-oxy, combustion cases.

In the absence of chlorine, K_2O can react with silica to form K_2SiO_3 that freezes at about 1023 K, or react with CO_2 to form K_2CO_3, and then initiates the bottom agglomeration. Therefore, the potassium and silicon are abundant in the BCD.

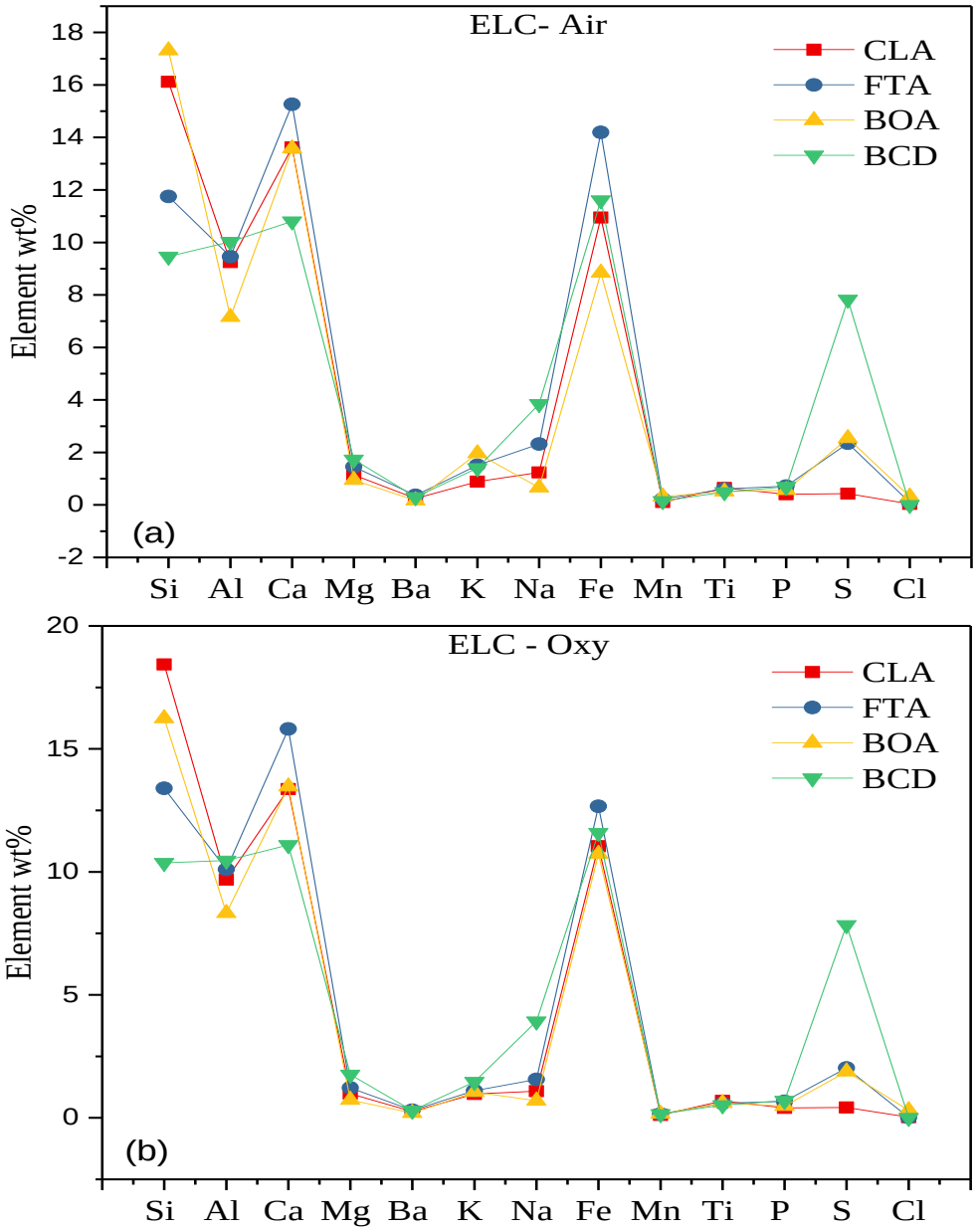

Figure 6.6 Elemental analysis of the ash in CLA, FTA, BOA, and BCD of (a) ELC-air, and (b) ELC-oxy, combustion cases.

In contrast to the wood pellets, coal is abundant with silica, alumina, iron oxide and sulphur, and less abundant in calcium. Clearly, from Fig 6.6, similar compositions of Al, Mg, Ba, K, Fe, Mn, Ti, and P in the fly ash streams and the bottom deposition can be observed. The CLA and FTA are dominated by the Si, Ca, Fe and Al, thus indicating enrichment with metal oxides. Whereas, alkali and sulphur enrichment are significantly lower in the CLA, and higher in the FTA, suggesting the formation of alkali sulphates that is the main cause of fouling in the heat exchanger tubes [50].

The high concentrations of Si, Al, Ca, Fe in the BCD, suggests the formation of complex metal silicates due to the high silicon content that may have captured the metal oxides. Whereas, the high sulphur and sodium concentrations in the BCD, suggest the formation of Na_2SO_4, and less amounts of K_2SO_4, indicating higher tendency for fused alkali sulfate to form agglomeration with other metal oxides and silicates.

Table 6.7 shows the ash compositions as metal oxides and it shows that the ash mineral oxides do not add up to 100%. The undetected fractions of the ash could be attributed to the presence of carbon in the form of metal carbonates that decomposes at temperatures higher than 973 K to the metal oxides. On the other hand, higher total metal oxides than 100%, can be explained by complex silicates and oxides formation of multi elements during the deposition process that requires lower amounts of oxygen that are over predicted by individual oxides.

Table 6.7 Elemental oxides composition of the fuel ash, CLA, FTA, BOA and BCD

		USWWP - Air				**USWWP - OXY**			
	A_{fuel}	CLA	FTA	BOA	BCD	CLA	FTA	BOA	BCD
SiO2	12.55	10.17	8.38	12.41	15.45	14.45	8.38	19.31	12.37
Al2O3	5.04	3.14	5.83	1.72	6.39	3.68	5.83	3.18	5.80
CaO	40.32	56.28	23.93	49.78	35.64	48.78	23.93	52.27	40.03
MgO	8.91	7.60	2.58	5.34	11.41	6.15	2.58	6.98	13.35
BaO	0.32	0.31	0.34	0.24	0.33	0.30	0.34	0.35	0.33
K2O	14.14	3.23	26.45	3.85	17.52	5.60	26.45	4.23	15.90
Na2O	1.89	0.84	2.70	0.79	2.27	1.11	2.70	0.88	2.19
Fe2O3	4.48	3.67	6.53	2.58	4.55	4.53	6.53	4.07	3.69
MnO2	4.71	6.16	2.33	5.32	4.32	5.04	2.33	5.78	5.32
TiO2	0.48	0.29	0.35	0.29	0.65	0.41	0.35	0.47	0.59
P2O5	5.02	4.68	3.59	3.80	5.64	4.07	3.59	4.54	6.24
SO3	4.28	1.12	17.98	2.25	3.30	2.81	17.98	1.86	0.19
Total	102.16	97.49	100.98	88.39	107.48	96.94	100.98	103.93	105.99
Undetected	-2.16	2.51	-0.98	11.61	-7.48	3.06	-0.98	-3.93	-5.99

Continued

		ELC - Air				ELC - Oxy			
	A_{fuel}	CLA	FTA	BOA	BCD	CLA	FTA	BOA	BCD
SiO2	26.62	32.25	25.14	37.03	22.17	39.44	28.66	34.75	16.97
Al2O3	18.18	16.53	17.87	13.52	19.77	18.30	19.08	15.73	17.87
CaO	17.67	18.59	21.35	19.00	15.53	18.70	22.12	18.84	15.54
MgO	2.41	1.84	2.41	1.58	2.92	1.63	2.02	1.21	3.10
BaO	0.32	0.28	0.40	0.19	0.33	0.29	0.34	0.22	0.34
K2O	1.48	0.99	1.82	2.37	1.76	1.17	1.33	1.26	1.74
Na2O	3.47	1.55	3.13	0.90	5.29	1.46	2.11	0.94	5.34
Fe2O3	16.81	15.67	20.29	12.65	16.57	15.79	18.11	15.34	17.14
MnO2	0.24	0.18	0.36	0.50	0.24	0.18	0.25	0.25	0.27
TiO2	0.95	1.01	1.01	0.84	0.86	1.15	0.99	1.01	0.79
P2O5	1.34	0.91	1.64	1.28	1.60	0.93	1.54	1.09	1.57
SO3	10.11	1.03	5.87	6.34	19.57	1.05	5.06	4.70	18.06
Total	99.60	90.83	101.28	96.19	106.62	100.10	101.62	95.35	98.74
Undetected	0.40	9.17	-1.28	3.81	-6.62	-0.10	-1.62	4.65	1.26

6.4.3 Fuel Ash Partitioning

The relative abundance of each element to the fuel ash is shown in Fig. 6.7 and Fig. 6.8 for the USWWP and ELC, respectively. These values are calculated by normalizing the elemental concentrations in the fly ash streams and the bottom deposit by those in the fuel. The effect of the oxidant environment on the ash behaviour is more recognized here. As can be seen from Fig. 6.7, the fractional distribution of the ash elements among the four streams is clearly different between the air and oxy-fuel cases, mainly the alkali, chlorine and sulphur. Higher fractions of alkali and sulphur are in the BCD in the air-fuel case, indicating higher amounts of alkali sulphates and chlorides can be seen in the furnace bottom deposition. In addition, more metal oxides such as silica, alumina, iron oxide, and titanium oxide are conveyed with the FTA in the air-fuel case than those in the oxy-fuel case.

These correlations suggest that the oxy-fuel combustion inhibits the release of volatile elements to the gas phase in the early stages of the combustion, reducing the alkali slagging, and hence reducing the furnace wall deposition, increasing however, the alkali fouling in later stages of the heat exchange.

Furthermore, the high chlorine fraction in the BCD of the oxy-fuel case suggests higher alkali chlorides are trapped on the furnace walls and the bottom, whereas, the air-fuel releases more chlorine with the FTA and CLA indicating higher corrosion problems could be expected on the heat exchanger surfaces.

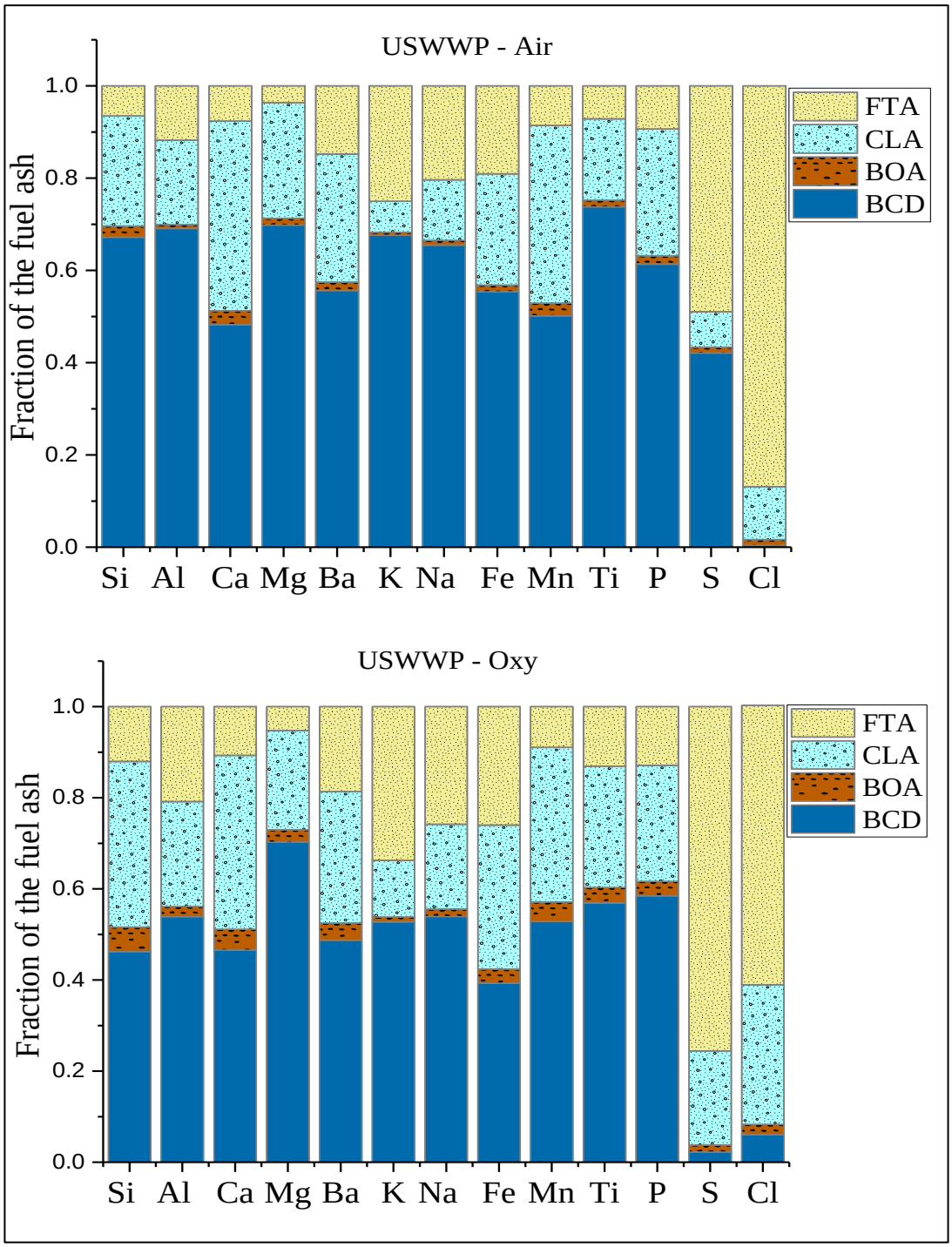

Figure 6.7 Relative abundance of ash elements normalized by the fuel ash for the USWWP–air and USWWP-oxy cases.

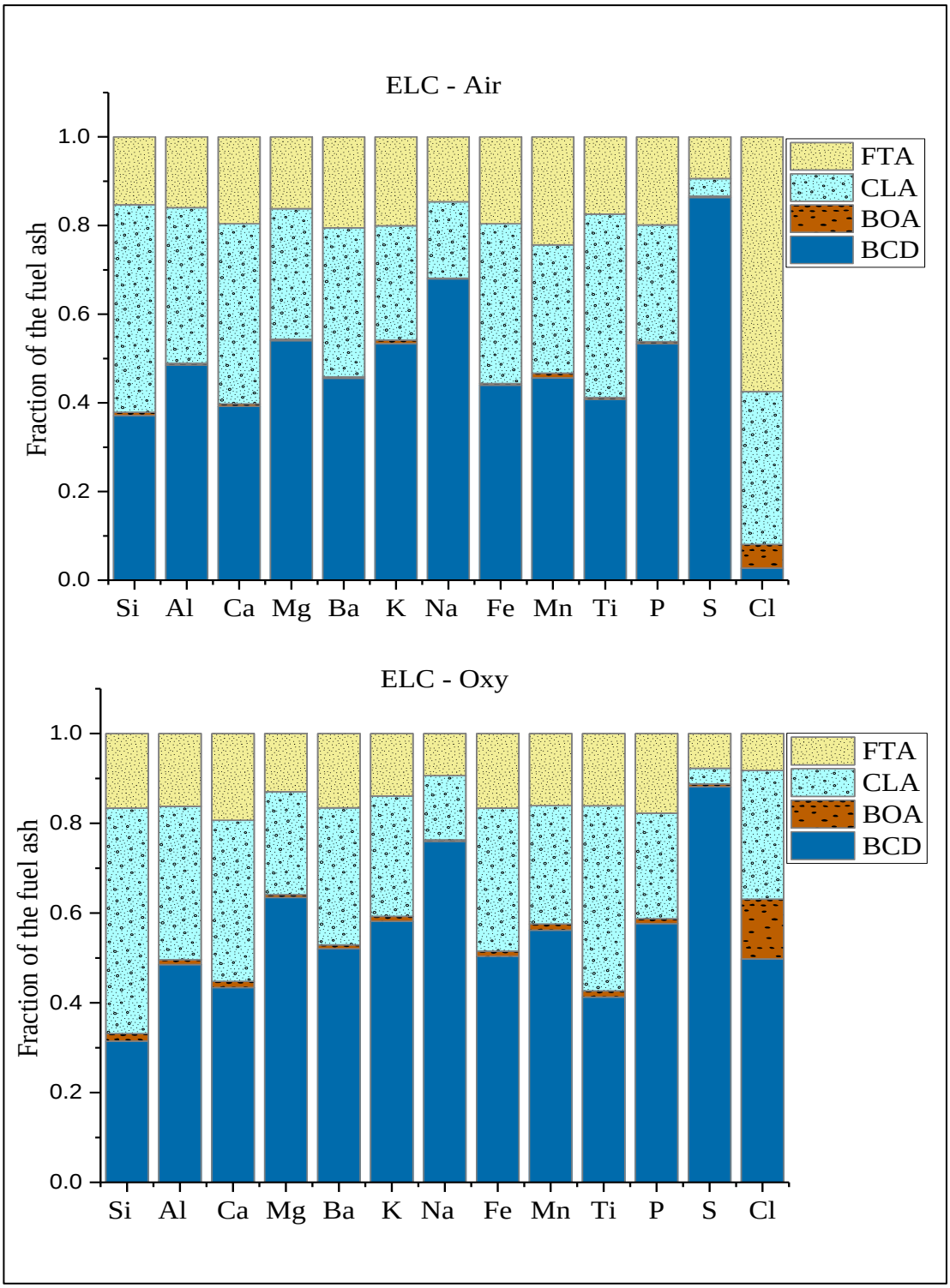

Figure 6.8 Relative abundance of ash elements normalized by the fuel ash for the ELC–air and ELC-oxy cases.

Surprisingly, the two coal combustion cases have shown significantly similar abundance of the ash elements in the various ash streams. Two exceptions from this trend are the sodium and chlorine, as they are mainly released with the fly ashes in the air-fuel, whereas, in the oxy-fuel case they were trapped in the BCD suggesting more sodium chlorides are trapped in the bottom deposition. This behaviour is relatively similar to the chlorine behaviour in the USWWP case. In general, the effect of the oxy-fuel case on the ash behaviour is less significant on the ELC than its effect on the USWWP combustion.

6.4.4 Deposition Growth Index

In addition to the empirical indices, the experimental data can be employed to indicate the slagging and fouling tendencies of the fuels used in this study, such as the energy-based deposition growth index *(DGI)* that can express the deposition tendency of a specific fuel. The *DGI* is the ratio of the total mass of deposit to the product of total mass of the fuel burned in the test and the NCV_{db} of the fuel as shown in the following equation [219]:

$$DGI = \frac{BCD}{NCV_{\mathrm{db}}} \ (\mathrm{kg\ GJ^{-1}}) \qquad (6.1)$$

Applying Eq. (6.1) on the BCD values listed in Table 6.5, the *DGI* values of the USWWP-air, USWWP-oxy, ELC-air, and ElC-oxy are 0.21, 0.18, 0.45, and 0.50, respectively. These values can be interpreted to be that the USWWP has half of the slagging propensity of the ELC in the air combustion and third of the slagging propensity of the ELC in the oxy-combustion case. A comparison between the *DGI* trends and the predicted slagging tendencies that are listed in Table 6.3 is shown in Fig. 6.9. The agreement between the R_{SL} and the *DGI* for both cases of air and oxy-fuel combustion is reasonably good. This agreement translates the validity of the R_{SL} as a reasonable slagging prediction index, and the *DGI* as an experimental slagging index for the biomass as well as the coal. The R_{AM} did not correlate with the *DGI* for both fuels. Barroso et al. [219] found an agreement between *DGI* and the base-to-acid ratio for coal ranks that have low calcium content and did not correlate with high calcium coals. This may explain the case of the biomass in which high calcium content was found.

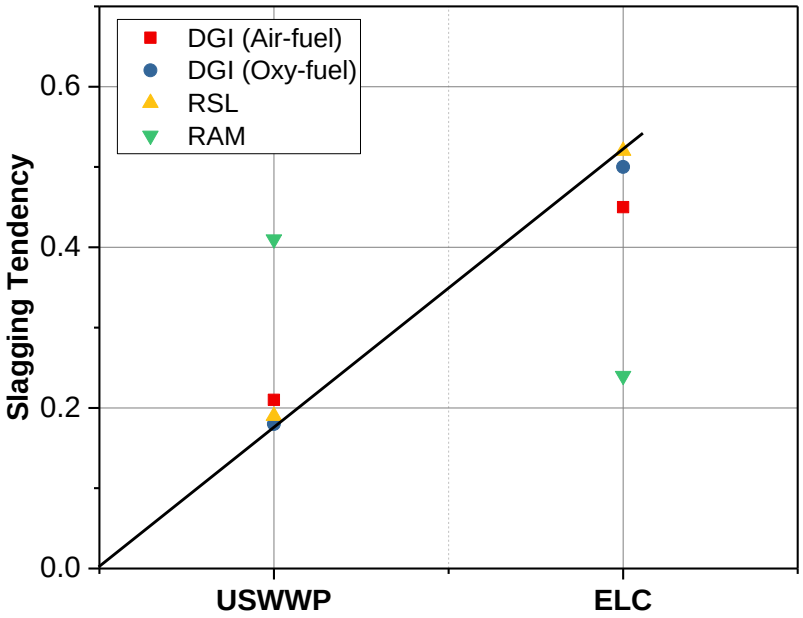

Figure 6.9 Predicted slagging tendencies in relation to the experimental deposition growth index (DGI)

6.4.5 Carbon-in-ash Analysis

To estimate the combustion efficiency and the carbon burnout of a certain fuel, the measurement of the carbon-in-ash is required. Therefore, the CLA, FTA, BOA, and BCD (in the case of USWWP) samples were analysed by the CHNS analyser for total carbon content. Ash samples were dried according to the standard methods, milled for less than 80 μm, and then analysed for the total carbon. The analysis results are listed in Table 6.7 and illustrated in Fig. 6.10. Interestingly, the data in Table 6.7 shows that the biomass-air has lower carbon content in all the ash streams than for the biomass-oxy combustion case. What stands out in the data is the bottom char and deposition BCD. Clearly, the air combustion has lower carbon losses with the bottom char than the oxy-fuel case, and the photograph of the samples shown in Fig. 6.1, confirms this result. These findings suggest that, the biomass burns better with the air than with the O_2/CO_2 oxidant. Thus, from the kinetics of the combustion explained in Section 4.3.3, and the collected ash data, it is possible to hypothesise that the presence of CO_2 in the oxy-fuel case may play an inhibiting role to the fuel carbon oxidation by reducing the oxygen diffusion rate to the carbon surface and reducing the combustion temperature by the endothermic reaction of CO_2 with carbon (Boudouard Reaction). However, the sound explanation for this discrepancy can be found when these results are correlated

to the actual furnace temperature distribution and to the CO_2, NO_x and CO emissions for both cases of combustion oxidants.

Furthermore, the biomass combustion has shown to have lower carbon content in the CLA and BOA, than the coal in both of the air and oxy-fuel cases. In contrast, the FTA in both cases of the biomass has shown higher content of carbon than the FTA of the coal. A significant discrepancy between the USWWP and the coal carbon-in-ash is in the BOA. As shown in the previous sections these two cases have opposite trends in the flowrate, and ash composition patterns that can explain the discrepancy in the carbon in the ash as well. Although, the char content in the BOA is significantly lower in the biomass cases than in the coal combustion, the bottom deposit of the biomass contained a large fraction of unburned fuel char, whereas the coal had insignificant char deposition in the water tray. The effect of this discrepancy in the carbon-in-ash between the two fuels, can be seen on the total carbon burnout and combustion efficiency as will be discussed in the next section. As mentioned in Section 6.4.1, the carbon in the BCD was negligible in both of the coal cases.

Table 6.8 Carbon-in-ash as wt% of the CLA, FTA, BOA in four combustion cases, and the BCD in the wood pellet cases.

	CLA	STDV	FTA	SE	BOA	SE	BCD	STDV
	Wt%		Wt%		Wt%		Wt%	
USWWP- Air	1.75	±0.04	1.48	±0.05	1.63	±0.28	12.30	±0.52
USWWP-Oxy	2.22	±0.14	1.98	±0.03	3.45	±0.59	23.95	±1.35
ELC- Air	2.19	±0.14	1.29	±0.00	19.62	±0.18	negligible	
ELC- Oxy	3.26	±0.43	1.11	±0.04	7.00	±0.67	negligible	

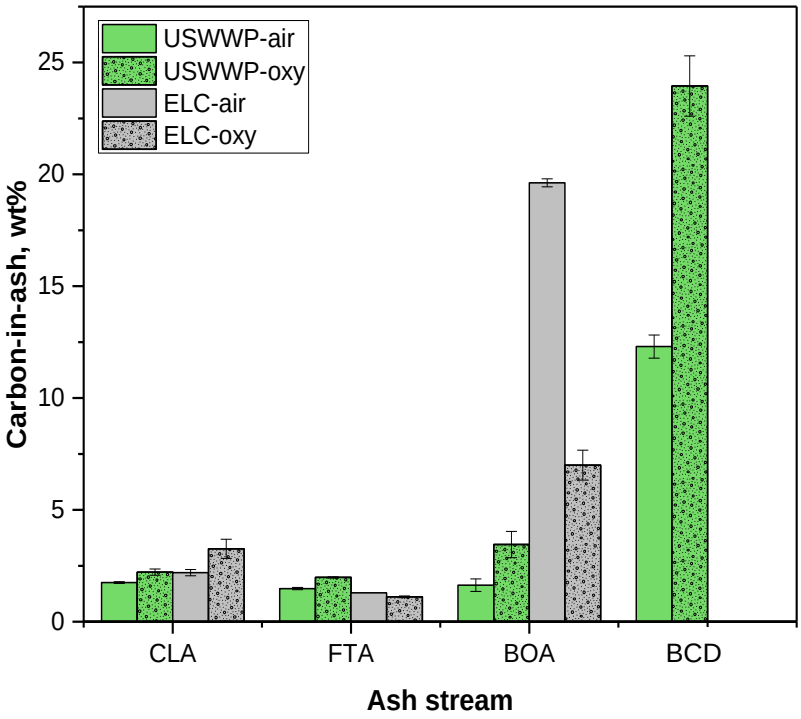

Figure 6.10 Carbon-in-ash of the CLA, FTA, BOA, and BCD in the USWWP-air, USWWP-oxy, ELC-air, and ELC-oxy combustion cases.

6.4.6 Carbon Burnout & Combustion Efficiency

This study set out with the aim of assessing the combustion performance of the USWWP, with different oxidants, in comparison to coal. The combustion efficiency η_{Comb} is one of the process indices that are used to serve this purpose. As shown in Section 3.5.14.5, the combustion efficiency depends on the carbon burnout and the carbon oxide emissions in the flue gases.

During the testing day, the flue gas emissions were measured online by the gas analyzer at 5 second intervals. When a steady state is achieved, the emission data for 10 minutes are recorded and immediately the mean value can be obtained. In general, the carbon monoxide CO emissions were very low in all the combustion cases, and the measurements in the flue gas were 16, 15, 15, and 12 ppm for the USWWP-air, USWWP-oxy, ELC-and air, ELC-oxy, respectively, with an average error ±2 ppm. According to Eq. (3.29) and Eq. (3.27), the carbon burnout (C_{BO}) and the combustion efficiency η_{Comb} of all the four cases were calculated and the results obtained are listed in Table 6.9.

As can be seen from Table 6.9, the carbon burnout and the combustion efficiency of the four combustion cases are higher than 99.7%. However, the biomass had slightly

lower C_{BO} than the coal in both of the combustion cases and this is due to the large amounts of char accumulated in the bottom water tray. Similar results of the USWWP-air $\boldsymbol{\eta_{Comb}}$ compared to the ELC-air were found. Interestingly, the oxy-fuel environment has the opposite effect on the USWWP from the ELC combustion, as it produced lower efficiency than the air-fuel case with the wood pellets but higher efficiency with the coal case. A probable reason for these slightly different effects is the opposite difference in the flame temperatures between the oxy and air-fuel in both of the fuel cases.

Table 6.9 Combustion performance parameters of USWWP-air, USWWP-oxy, ELC-air, and ELC-oxy combustion cases

Combustion case	**C_{BO}**	**η_{Comb}**
	%	%
Air- USWWP	99.88	99.88
Oxy - USWWP	99.77	99.87
Air - ELC	99.93	99.94
Oxy - ELC	99.95	99.95

6.4.7 Char Morphology

To assess the validity of the predicted char kinetic reactivity in Chapter 5, one thing that can be done within the capacity of this study is to examine the porous structure changes of the fuel during the air and oxy-fuel pulverized combustion processes and compare the char morphology with the char particles that are produced in the TGA analysis at 1273 K as a maximum available temperature in the TGA instrument. Accordingly, the BOA char samples of the USWWP and ELC were tested by scanning electron microscope (SEM) for particle morphology.

Figure 6.11 illustrates the SEM images of the USWWP TGA, air-fuel, and oxy-fuel chars in two magnifications; x30 (left), and x500 (right). Figure 6.11 is quite revealing in several ways. First, the fibrous structure of the wood pellets is clear in the TGA char, see Fig. 6.11-(a) & (b), the particles have retained the original shape and the internal walls of the fuel particles. The porous structure has mainly cylindrical cavities along the particle length, and the pores open up to larger cavities. Although, the internal particle

walls are retained, the internal smaller pores are accessible due to the large feeder pores. Whereas, Fig. 6.11-(c) & (d) reveals a clear difference in the air-fuel combustion char than the TGA char. More erupted particle walls with larger central cavities and very few internal walls remained. The particles lost the fibrous shape, and the outer walls are more rounded and porous. The pore system is clearly macro porous, but with higher pore volume. These differences can be explained by the more rapid pyrolysis in the air-combustion that releases higher amounts of volatile matter.

Figure 6.11-(e) & (f), show the SEM images of the wood pellets oxy-fuel char. It can be seen from Fig. 6.11-(e) that, similar to the air-fuel char, the particles are deformed and more rounded than angular with large internal cavities that replaced most of the internal walls. However, Figure 6.11-(f) shows the difference between the two combustion cases. Apparently, most of the pore system on the walls is non-accessible, and the porous system is not fully developed. These findings may be explained by incomplete devolatilization and the thermal annealing that can occur at higher temperatures of the oxy-fuel environment. This implies the oxygen diffusion limitation to the internal pores.

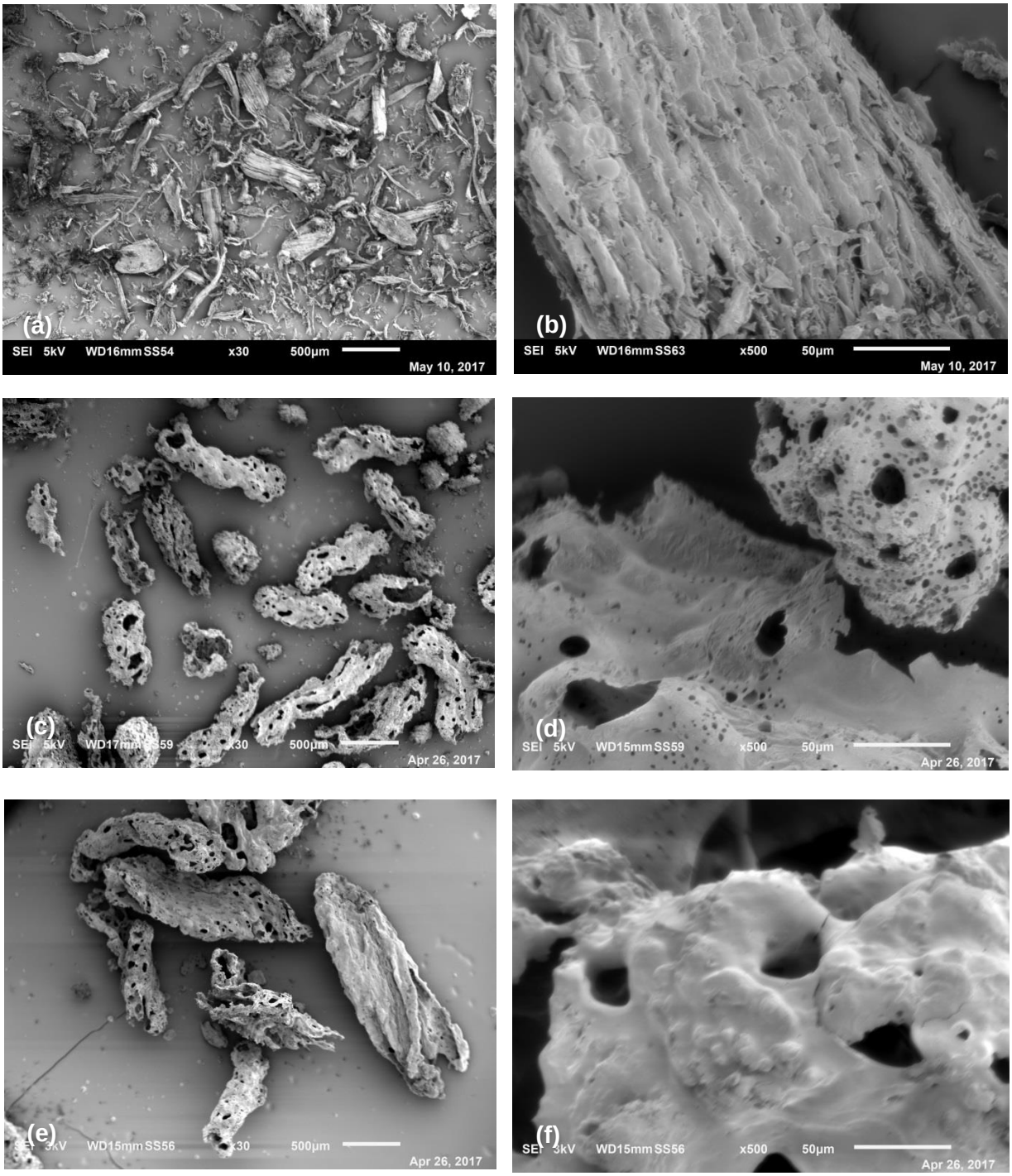

Figure 6.11 SEM micrographs of the USWWP chars; (a) TGA char produced at 1000 °C (x30), (b) TGA char (x500), (c) air-fuel char (x30), (d) air-fuel char (x500), (e) oxy-fuel char (x30), and (f) oxy-fuel char (x500).

Figure 6.12 compares the SEM images of the ELC chars. It can be seen that most of the TGA char particles have an angular shape; however, there are some particles with rounded shape. The internal walls are retained and apparently there are blind pores with few in the micro size on the outer walls. On the other hand, the air-fuel char has more opened pores. The particle shapes are mainly spherical with high pore volume and a fully developed porous structure. This has been observed on many bituminous coals [181]. Similarly, the oxy-fuel char particles were mainly spherical indicating cenosphere particle formation that occur due to the plasticising then release of the volatile matter commonly observed in the bituminous coal chars [222]. However, the particle is more deformed and more internal walls are broken with higher volume cavities. This difference between the oxy-fuel char and the air-fuel char may be explained by the longer residence time in the oxy-fuel case that allows for more devolatilization and structure deformation.

The SEM images in Figs. 6.11 and 6.12 reveal, substantial differences between the USWWP chars and the ELC chars in the particle shape and the pore structure. The coal char particles are spherical and highly porous, whereas the USWWP char is more fibrous with long cavities and consists mainly of an opened up flat cavities system. The effect of the oxy-fuel on the wood pellets char formation was relatively higher than the effect on the coal char, and this confirms the different results in the ash partitioning, the carbon burnout and the combustion efficiencies between the two fuel cases.

The TGA char particle of the wood pellets has shown higher porosity and surface area from the coal char, and this finding supports the trend of the calculated surface area and porosity of the two fuel chars in Section 5.2.1 and presented in Table 5.1.

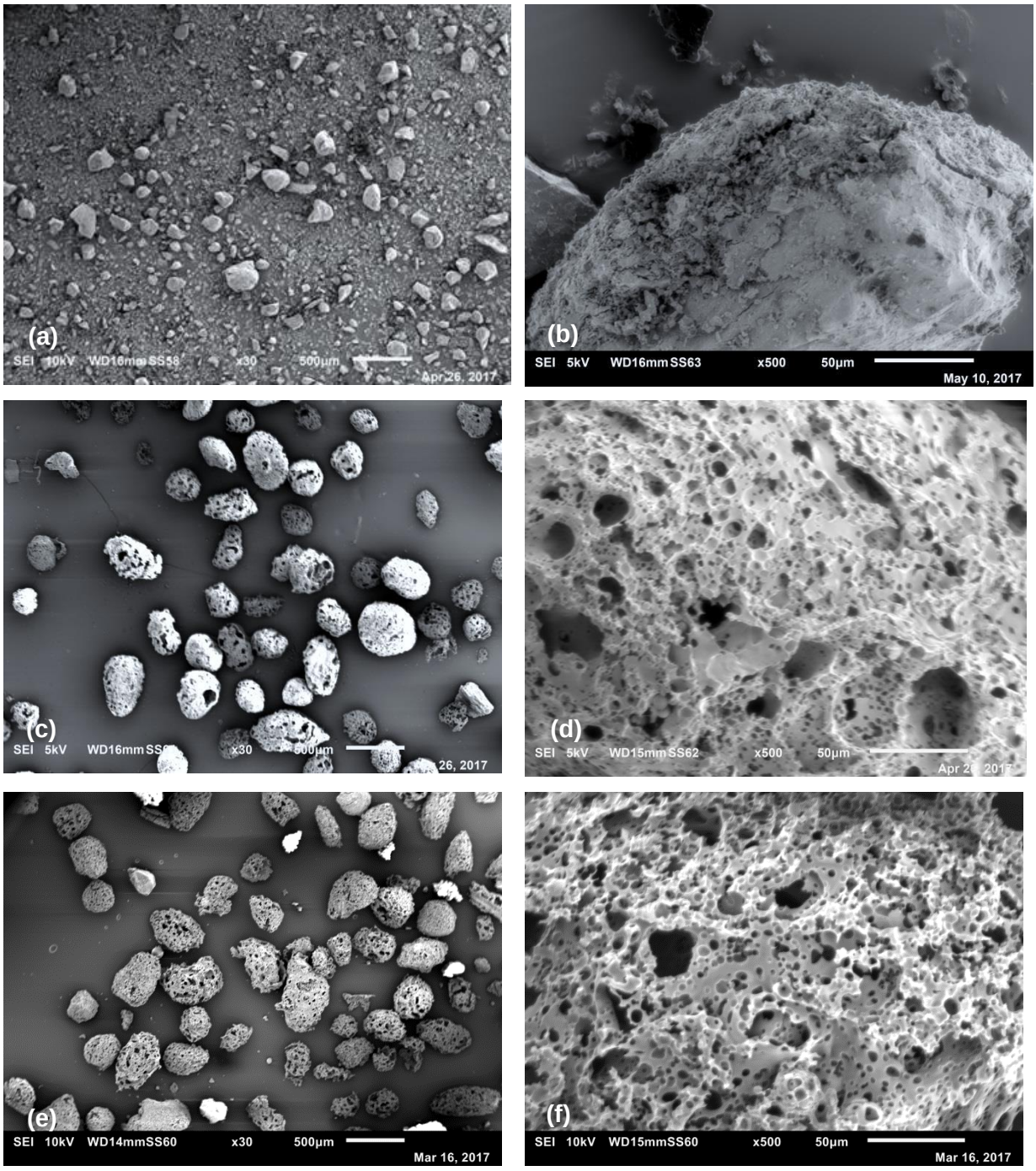

Figure 6.12 SEM micrographs of the ELC chars; (a) TGA char produced at 1000 °C (x30), (b) TGA char (x500), (c) air-fuel char (x30), (d) air-fuel char (x500), (e) oxy-fuel char (x30), and (f) oxy-fuel char (x500).

6.5 Summary of Findings

This chapter has presented the pilot scale 250 kW combustion test results, for the US white wood pellets and the El-Cerrejon coal fuels in two cases, namely air-fuel and oxy-fuel combustion. In addition, the fuel composition data were discussed and employed in the data analysis of the combustion tests. The main concern of this study was the ash behaviour, the char and deposition formation during the combustion process.

6.5.1 Fuel Properties

The fuel characterization results have shown that the wood pellets are substantially different from the coal in the particle size distribution and the ash mineral composition.

i. Different modes of particle size distribution were found for the wood pellets than for the coal. 60% of the ELC particles were below 60 μm in diameter, whereas only 16% of the USWWP particles were below this size, also 93% of ELC particles were below 250 μm, whereas, only 67% of USWWP falls below this size.

ii. The wood pellet ash composition has shown to have higher potassium, alkaline earth metals and chlorine, and lower silica, alumina, iron and sodium than coal.

iii. An important finding from the ash composition analysis is the total elemental content as metal oxides in the 550 ºC ash does not add up to 100%. The undetected fractions of the ash could be attributed to the presence of carbon in the form of metal carbonates that decomposes at higher temperatures than 700 ºC to the metal oxides.

iv. These results were employed to assess the slagging and fouling tendencies of the two fuels. The results of the deposition indices have given reversed deposition tendencies for both wood pellets and the coal. In addition, there was a lack of characteristic significance between the biomass and the coal despite the high discrepancy in their ash composition. Only the potassium slagging ratio (R_{KS}) emerged as a distinguishing index between the two fuels. Thus, the judgement on the deposition propensity through the empirical deposition indices is not revealing.

6.5.2 Pilot Scale Combustion Tests

The wood pellet combustion tests have shown substantial differences between the air-fuel and the oxy-fuel cases than the coal corresponding cases in the following aspects:

i. The USWWP generated lower fly ash and bottom ash in the air-fuel case than in the oxy-fuel case, and, respectively, the bottom deposition of the air-fuel case is expected to be higher than that of the oxy-fuel case.

ii. In contrast, the coal had a higher fly ash and lower bottom ash and bottom depositions in the air combustion than those in the oxy combustion case by 5%, 0.78%, and 4.74%, respectively. Respectively, the coal produced five times higher fly ash, 3.5 folds higher depositions, than the wood pellets, and 40% higher bottom ash, than the wood pellets in the oxy-fuel case. However, the wood pellets have produced 10% higher bottom ash than the coal in the air-fuel case.

iii. The other major findings to emerge from this chapter are the partitioning of the fuel ash elements on the different ash streams, and the effect of the oxidant environment on this partitioning. In the case of wood pellets, the change in the oxidant from air to O_2/CO_2 had a substantial effect on the individual composition of each ash stream; dissimilar concentrations of most of the elements were found in both air and oxy-fuel cases. Possible reasons for this discrepancy are the flame temperature and the residence time differences in the two cases. Further, a greater effect was revealed on the ash elemental partitioning, mainly the alkali, chlorine and sulphur. Whereas, in the coal case, the effect was insignificant on the composition of the individual ash streams and the elemental partitioning of the fuel ash on the various streams.

iv. In the wood pellets case, most of the fuel alkaline earth and silicon were found in the bottom depositions and the cyclone ash for both air and oxy-fuel cases. Whereas, higher fractions of alkali and sulphur could be found in the deposition in the air-fuel case than in the oxy-fuel case, indicating higher amounts of alkali sulphates can be seen in the furnace bottom deposition.

v. In addition, heavy metals such as Fe, Ti, Mg, and other metals such as Al, Ba, and P were less abundant in the fly ashes in the air-fuel case, and this explains the lower fly ash mass flowrates in the air-fuel case.

vi. In the same time, most of the fuel ash chlorine was released in the filter and the cyclone ashes in the air-fuel case, whereas, a considerable fraction of the chlorine could be found in the bottom deposits.

vii. The coal-air combustion produced different ash pattern than the wood pellets. More than 50% of the Si, Al, Ca, Ba, Fe, Mn and Ti were found in the cyclone and the filter ashes, whereas only 25% of the alkali was conveyed with the fly ash streams. In addition, very small amounts of sulphur were found in the fly ash, which is expected to be in the bottom depositions. The same observations were found for the ELC-oxy ash compositions. The only exception from this similarity was chlorine, where an abundance of the chlorine was found in the cyclone and filter ash in the air-fuel case, whereas about 50% of the chlorine could be trapped in the bottom deposition in the oxy-fuel case.

viii. The carbon burnout and the combustion efficiency of the wood pellets and the coal were higher than 99.7%. However, the biomass had slightly better carbon burnout and combustion efficiency in the oxy-fuel than in the air-fuel case. In contrast, the coal had better combustion performance in the oxy-fuel than in the air-fuel case.

ix. The effect of oxy-fuel on the wood pellets char formation was significantly higher than the effect on the coal char, and this confirms the different results in the ash partitioning, the carbon burnout and the combustion efficiencies between the two fuel cases.

x. The TGA char particle of the wood pellets has shown higher pore volume and surface area from the coal char, and this validates the calculated *Ag* and porosity of the two fuel chars in Section 5.2.1 and presented in Table 5.1.

Chapter 7 Techno-Economic Analysis of BECCS

7.1 Chapter Overview

The technical performance and cost effectiveness of white wood pellets (WWP) combustion in comparison to coal are investigated in this chapter. The aim of this comparative study is to assess the current challenges and the future opportunities of the bioenergy with carbon capture and storage (BECCS) as one of the solutions to the global warming and climate change problems. The performance of white wood pellets in the combustion power plants, versus three types of imported coal to the UK; Colombian, Russian, and US coal fuels, to assess the viability of BECCS technology with the current market prices and the projected fuel prices in the next 15 years is examined. Two carbon capture technologies are selected for this comparison, and more than one scenario of governmental incentives are examined to booster the BECCS technology. The IECM program was employed to perform the plant-level performance and cost estimates. The assumption of co-firing in three levels 25%, 50%, and 85% were investigated in terms of plant efficiency, cost of electricity, and the total levelized annual cost. In addition, the sensitivity of plant economics to the fuel prices, renewable obligation credits, and carbon price variations was also examined.

As this study is self-contained, the introduction and the literature review on the economics of BECCS studies is included in this chapter.

7.2 Introduction

Global warming is an issue of concern to the international community due to the climate change resulting from the temperature increase of the Earth atmosphere. The report of the Intergovernmental Panel on Climate Change (IPCC) in 2007, stated that in order to keep global warming below 2 K, and avoid the most dangerous consequences of climate change, global greenhouse gas (GHG) emissions must be reduced by 50-85% by 2050 – and peak no later than 2015 [6].

The largest contributor to GHG emissions is, the energy supply sector [223]. In 2010, approximately 35% of the total anthropogenic GHG emissions were attributed to this

sector. The reasons for the vast expanding in energy sector are, the rapid economic growth (with the associated higher demand for power, heat, and transport services) and an increase of the share of coal in the global fuel mix [5].

For the reduction of GHG emissions from the energy supply sector, multiple mitigation options are available, such as energy efficiency improvements and fugitive emission reductions in energy conversion, transmission, and distribution systems, replacement of fossil fuel with less GHG emitting technologies such as renewable energy, nuclear power, and carbon dioxide capture and storage (CCS) [5]. According to the EIA World Energy Outlook report in 2009, Carbon Capture and Storage (CCS) in the power sector and in industry represents 10% of the total emissions savings in 2030 [224], and could provide almost 20% of the global emission cuts required by 2050 [6]. The only up to date large scale technology solution for CO_2 negative emissions is Bio Energy with Carbon Capture and Storage (BECCS) [6, 15, 225]. This conclusion is based on the assumption that biomass combustion releases the same quantity of CO_2 that is required for its growth; therefore emissions from biomass combustion are considered to be CO_2 neutral [226]. Moreover, the capture and long term storage of these CO_2 emissions would effectively result in the net removal of atmospheric CO_2, and biomass with CCS is potentially one of the few options for negative emissions [7].

In this study, the sensitivity of Plant efficiency, cost of electricity and Levelized Annual Cost towards the fuel price, capacity factor, fixed charged factor and Carbon Price will be examined. In addition, the uncertainty analysis of renewable obligation credit in biomass-firing plants will be investigated and discussed herein.

7.3 CO_2 Capture & Storage Technology (CCS)

CO_2 Capture and Storage defines a technological process by which at least 90% of CO_2 emissions is captured from large stationary sources (e.g. fossil fuel-fired power plants, refineries, and heavy industry), transported and injected into a suitable deep geological formation (at least 800m and up to 5,000m), then a suitable measurement, monitoring, and verification (MMV) technologies are applied to ensure the safety, and permanence of the captured CO_2's isolation from the atmosphere [5, 6].

7.4 Challenges & Incentives of BECCS Deployment

Up to date, deployment of BECCS technology has not been at full scale, except in the United States with three demonstration projects with a total capacity of 1055,000 $tCO_2\,yr^{-1}$ [227]. Among those projects, the Illinois I million $tCO_2\,yr^{-1}$ capacity project that is considered the world first industrial scale, has started commissioning in 2011 and sequestered 1M tonnes of CO_2 up to the end of 2014. The so far narrow deployment can be attributed to the high cost of the technology, the lack of dedicated financial incentives for BECCS found in any country or region, and the decrease in the carbon price (carbon tax) on fossil fuels, from 18 £ $tonne^{-1}$ CO_2 in 2011 to 9.55 £ $tonne^{-1}$ CO_2 in 2014 [228]. Furthermore, the technical potential of BECCS is conditioned by the availability of sustainable biomass, CO_2 storage capacity and the performance of biomass conversion and CO_2 capture technologies [229]. The net energy conversion efficiency and the carbon removal efficiency then determine the potential of BECCS in terms of negative GHG emissions. In other words, carbon-negative equals carbon abatement only if BECCS replaces zero-emission technologies. If it replaces carbon-emitting technologies, the abatement of their emissions is then added for the total carbon abatement [6]. In this regard, many scientists have emphasized the need for governmental incentives to boost the adaptation of the BECCS technology. Such incentives are the specific subsidy on captured emissions from BECCS (renewable obligation certificates ROCs price), in addition to the carbon tax on fossil fuel emissions [15, 230-232]. Consequently, IPCC 2014 5^{th} Assessment Report has recommended certain regulations for fossil fuel facilities that enforce deployment of CCS power plants in the market place, or the cost reduction breach between them and their unabated counterpart (e.g. via sufficiently high carbon prices or subsidies) [5]. At the same time, the report emphasized the requirement of clear regulations concerning short- and long-term responsibilities for transportation and storage along with MMV standards for the large-scale future deployment of CCS.

7.5 Biomass Supply Chain

Although BECCS has gained a lot of attention in the power generation sector, with support and incentives from many governments, there has been a lot of criticism to the logic that BECCS produces negative carbon emissions and the bioenergy is carbon neutral. In the same time, concerns about the sustainability of forestry as the main

source of biomass were raised. In 2012, Smolker & Ernsting from Biofuel watch [233] criticised these reasoning since large scale plants of biomass combustion produce more CO_2 emissions than fossil fuels, and more fuel demand could cause deforestation and change the land-use. Furthermore, BECCS with underground storage has uncertainty of future leakages and rejected by some communities like in the Netherland. However, oil-enhanced-recovery by injecting CO_2 under oil reservoirs found the solution for this concern in the oil-producing countries like the USA and North Sea states, and this is considered as a form of CCS. Therefore, the report suggest the bio-ethanol that produces pure CO_2 if burned, that can be cheaply and easily captured [233]. In 2016, another critic article by Alfonso Arranz [234] specifically analysed the CCS as a hype of elevated expectations and then more disappointments. He suggested prioritizing CCS to industrial use, and replacing the conventional power plants with non-CCS technologies.

A recent report published by Chatham House in 2017 [235] discussed in details the projections of biomass supply chain for the short-term and long-term future. The report indicates that the EU; the main producer of bioenergy, anticipates a hold in the bioenergy share of the EU total energy consumption after 2020, because of competition with cheaper renewable energy (particularly PV and wind) and improvement in energy efficiency. Further, the report raises the concerns of the woody biomass supply chain emissions from harvesting, processing and transportation, in addition to the influence of deforestation on the forest carbon stock and land-use. Deforestation, as the editor believes, will reduce the future natural sequestration of CO_2 and increase the release of soil carbon to the atmosphere. Even with replantation, we need to wait for 10-20 years to return the absorption capacity of the mature trees i.e. a very long carbon payback period. Therefore, the argument that biomass is zero emission fuel is questioned by the report.

Alternatively, using the forest residues without harvesting can have less impact, however, there will be GHG emissions and maybe higher than the long-term decay emissions if the residues are left to decay in the forest (unmanaged forest). The sawdust can be a good replacement for energy to the forest wood, as long as it will not reduce the other mill residue industries such as fibreboard and particle boards due to its minimum carbon payback period. Another ideal replacement feedstock is the black liquor, a waste from pulp and paper industry that has no other use. Finally the report gives some recommendations to the EU policy makers on sustainability criteria of

woody biomass with a comprehensive forest management plans and interstate regulations.

In contrast to this report, the fifth assessment report of IPCC profoundly counts on the BECCS as the best mitigation option for carbon emissions [5]. Taeroe et al. [236] studied the difference between carbon emissions of managed forests and unmanaged forests and found that the first had less cumulative carbon emissions for 200 years than the latter one. The Chatham House report was later criticized by Wilson from the Institute of Chartered Foresters [237] for failure to provide realistic scenarios and objective assumptions. His argument is based on the fact that carbon emissions from biomass are part of the carbon cycle in nature not an addition to it as the case of emissions from fossil fuels. Also, the carbon stock should be considered on a regional scale not on a single tree. Another argument can be said here, is that the pulp and furniture industries are also contributing to remove large areas of forests around the world and reducing the natural carbon sink.

Economically, in a recent study, Boukherroub et al. [238] designed a wood pellets supply chain optimization model that showed a profitable wood pellet mill of 100,000 tonnes yr^{-1} if located in the same forest provided that the harvesting costs are shared with the mill and a governmental support in road development is available. More profits can be obtained if sawmill is mixed with the forest waste.

7.6 BECCS Incentives in the United Kingdom

According to the 2008 Climate Change Act that obligated a reduction of the UK's greenhouse gas emissions by at least 80% by 2050, in July 2011, the UK Department of Energy and Climate Change, has set a carbon management plan that includes a budget target to cut carbon emissions by 50% (from the 1990 baseline) by 2027 [239]. The plan presented a vision for energy efficiency and low carbon technologies in heat and electricity production, low carbon industry, and low carbon transport. In the future, more gas-fired generation will be replacing coal., and 40-70 GW of the new capacity is required by 2030 including more renewable and CCS technologies. In other words, the strategic goal of the carbon plan is to move to a sustainable low carbon economy without sacrificing living standards, but by investing in new cars, power stations and buildings.

An early outcome of this plan was a significant increase in the bioenergy production and the low carbon electricity deployment since 2013. The 2016 energy statistics report published by the Department of Energy and Climate Change, exhibits an increase of +23.7% in biofuel used to produce electricity from 2014 to 2016-quarter 3, and a 2.2% increase in the low carbon electricity generated from biofuels [240]. Figure 7.1 shows the increase in low carbon electricity generation in the last three years.

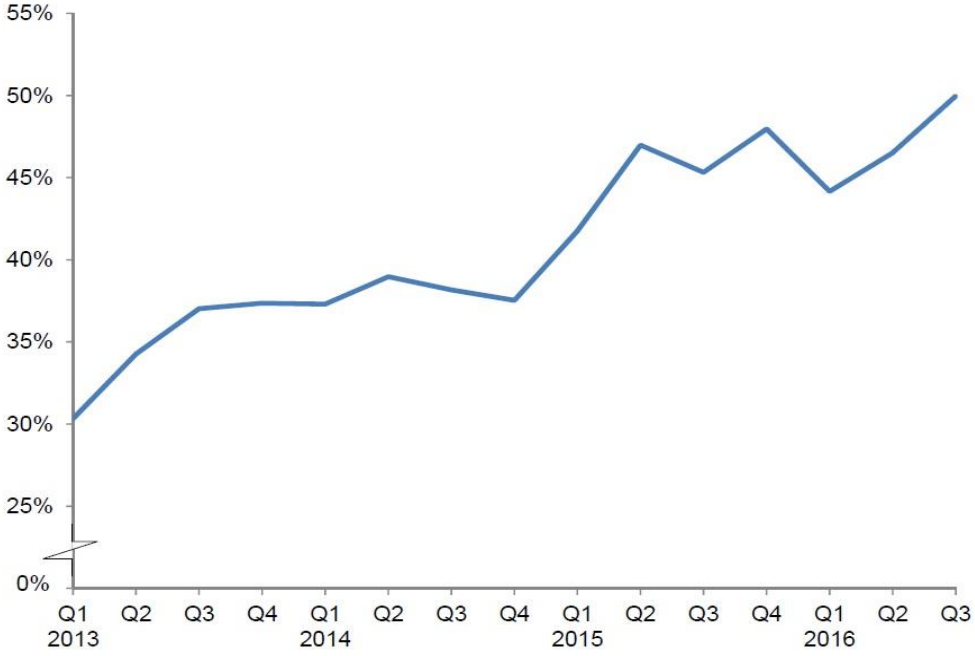

Figure 7.1 Percentage of the low carbon electricity share of generation in the UK in the years 2013-2016. [241]

7.7 Review of Recent Techno-economic Studies on BECCS

There has been a reasonable amount of economic analysis and cost effectiveness studies on power plants firing fossil fuels with CCS since the beginning of this century [232, 242-249]. Some of these researches included co-firing biomass with coal and with the deployment of carbon capture technologies [231, 250-254]

However, very limited research work on BECCS economic viability and economic deployment with coal and natural gas power generation, has been published in the literature. In recent studies that have been published in peer reviewed journals, the CCS cost based on technologies that are now commercially developed such as mono-ethanolamine (MEA) and ammonia have been estimated [34, 231, 251, 253-256]. However, less research work has been performed on the techno-economic potential of

the latest technologies of CCS such as oxy-fuel and membrane systems. Only a few of these studies, have investigated the pulverized wood as a fuel for co-firing, or pure wood combustion power plants in the United Kingdom. For instance, Bridgwater et al. [255] concluded that fast pyrolysis of wood can be profitable. They also concluded that although the capital costs are high in the first innovative plant, the specific plant cost can be decreased by 20% if the plant capacity is doubled, the feedstock is considered as a waste disposal rather than a cost, and the by-product chemicals are traded. Further, Rhodes [15] presented a new model to calculate the carbon mitigation cost with biomass power plants versus conventional fuels, such as coal and combined cycle gas turbine (CCGT). His model showed that at a carbon price 60 £ tonne^{-1} CO_2, 73 £ tonne^{-1} CO_2 , BECCS cost of electricity equals the corresponding cost of natural gas combined cycle (NGCC) and coal combustion plants, respectively [15]. Also, he concluded that BECCS can be cost-competitive via emissions offset where the mitigation cost was 605 £ tonne^{-1} CO_2 at that time.

In 2011, Patel et al. [257] compared the techno-economic performance of three combustion plants for energy recovery from three different biomass fuels including wood waste, and they found that the calorific value, steam turbine efficiency, capital cost, and operational costs are the most affecting parameters to the levelised cost of electricity. In the same year, McIlveen-Wright et al. [252] also evaluated the co-combustion of biomass with the pulverised coal in three different combustion technologies, in terms of mechanism to support the use of biomass in power plants. Their work showed that applying the Renewable Obligation Credit (ROC) is more transparent and cost-effective than the carbon price in the co-firing power plants. Similar techno-economic assessments of co-firing biomass with coal were performed by Catalonotti et al. and Meerman et al. [253, 254]. They both found that for wood pellets integrated gasification combined cycle (IGCC) with CCS technology was the cheapest BECCS technology with a significant impact of the biomass price on the production cost.

A recent techno-economic study in 2016 [258], suggested that deploying the BECCS will be dominant in the energy consumption at the end of the 21st century, and there are two scenarios for using the CCS technology. The first scenario assumes bioenergy without CCS technology that will lead to a higher carbon price and the demolition of fossil fuels trade. In this case, the demand for biomass will be higher and the competition for land-use will result in a rise of the food prices. On the other hand, if the

bioenergy is deployed with CCS to meet the 2 °C goal, the carbon price will be reduced and the fossil fuel consumption will remain consistent until the end of the century.

7.8 Objectives of Current Assessment Study

The main aim of this study is to investigate the performance and economic feasibility of dedicated large scale BECCS technology for power generation, in comparison to coal. Accordingly, the study examines the following areas: (i) quantify and compare the technical performance and cost effectiveness of combustion based power plants using white wood pellets, coal and co-firing fuel, with and without CCS technologies; (ii) explore the impact of key assumptions on both of these comparisons; (iii) evaluate the role of CC technology on the plant cost; and (iv) evaluate the role of carbon price policy and Renewable Obligation Certificate (ROC) in accelerating CCS deployment in the framework of GHG emissions mitigation.

7.9 Integrated System Approach for Current Assessment

Operational factors affecting CCS costs and emissions at power generation plants are taken into consideration in this study. Hence, the Integrated Environmental Control Model (IECM 8.0.2) is employed for a systematic estimation of plant performance, costs and emissions of different scenarios of fuel and carbon capture technologies. IECM is a widely used computer-modelling program developed by Carnegie Mellon University for the US Department of Energy's National Energy Technology Laboratory (DOE/NETL) [65]. It has been exploited to estimate the performance, costs and GHG emissions of pulverized coal, NGCC, and the integrated gasification combined cycle (IGCC) plants both with and without CCS [243, 253]. The model also provides an uncertainty analysis to key performance and cost criteria. In addition, the fundamental mass and energy balances are applied with the empirical data to quantify the overall plant performance, resource requirements, and emissions [243]. Plant performance and emissions are linked to engineering-economic models that calculate the capital cost, annual operation & maintenance costs, and the total levelized cost of electricity for the overall plant. However, the IECM does not have the option to use a biomass fuel that neglects the required modifications to the boiler, ash handling system and flue gas treatment systems to control emissions for biomass cases. In addition, the emission constraints in the IECM determine the removal efficiencies of control

systems for SO2, NOx, and particulate matter required to comply with the US emission constraints. When changing the limits to the UK limits, the removal efficiency of pollutants will change. Never-the-less, the IECM developers have confirmed the applicability of the program on the biomass fuels without any significant errors. Detailed technical information on the IECM program can be found in the Carnegie Mellon University website [65].

In this study, we evaluate the influence of fuel properties, cofiring blend ratios and CCS technology on the plant performance in terms of plant efficiency (high heating value HHV basis), CO_2 removal efficiency, and energy penalty. While the key cost measures are the capital cost, the total levelised cost of electricity (£ $MW^{-1}h^{-1}$), added cost of CCS, and cost of CO_2 avoided. Also, we examine the sensitivity of the total cost of white wood power plant to different scenarios of fuel price, carbon taxes and credits. To achieve these predictions, IECM version 8.0.2 is employed.

Taking into consideration the UK regulatory policies for power generation and local market prices, the performance and cost parameters are updated accordingly. The performance assumptions were modified according to the Levelised Cost Model (LCM) of electricity generation published by the Department of Energy and Climate Change in 2013 [259].

7.9.1 Limitations of IECM to Biomass Application

The IECM program was primarily designed for pulverised coal as the combustion fuel. Applying the program on biomass dedicated combustion or co-firing with coal over 50% energy content from biomass, requires some modifications to the boiler, ash handling system and flue gas treatment systems to control emissions [259], and this option is not available in the IECM. Thus, an error that is not significant in the net plant efficiency and performance of carbon capture plant may occur. In addition, the plant cost parameters are set for new (retrofit equals 1 basis), while this is not 100% true for existing coal plants. At the same time, the biomass power plants are mostly new as they have not been commercially commissioned until the present. Moreover, the ROC is not taken into consideration in the input interface screens that a manual correction had to be performed to the cost of electricity results. Another limitation is the maximum fuel price that is lower than current biomass fuel prices. A series of correspondences with the IECM development team has been made to clarify these

points, and they confirmed that the program can accurately generate the results of biomass fuels in the pulverized coal combustion plants model.

Moreover, the emission constraints in the IECM determine the removal efficiencies of control systems for SO_2, NO_x, and particulate matter required to comply with the US emission constraints. When changing the limits to match the UK limits, the removal efficiency of pollutants will change. This is explained by the developers of IECM as the user-specified values for control technology performance and this may cause the plant to over-comply or under-comply with the emission constraints specified by the model [260].

7.10 Baseline Comparison

7.10.1 White Wood Pellets-fired Power Plant Configuration

The IECM is employed to establish a new milled white wood pellet power plant without CCS, as the reference plant named here as the Ref Plant. The pulverized coal plant option in the program is selected for this purpose, utilizing the same combustion, purification and cooling technologies used for coal combustion. However, the baseline configuration for a biomass-fired power plant in the electricity generation cost model (LCM), 2013 [261] is reflected in the performance parameters of the IECM program in this study. The plant configuration is illustrated in Fig. 7.2. A Super-Critical boiler (SC) is used to generate steam at the super-critical conditions. In support to this selection, other energy studies have used the super-critical boiler as the typical boiler type in the UK power plants [253, 262]. The boiler is designed to have tangential firing and about 90% efficiency. The air/oxy gases are preheated before inlet to the boiler. The pollutants removal technologies are applied to meet the Large Combustion Plant Directive **2001/80/EC** (LCPD) of the European Parliament issued in 2001 and amended in 2009 for the emission ceiling of large combustion plants [263]. Selective Catalytic Reduction (Hot-side SCR) is used for NO_x removal plus, the inside furnace control. Also, SO_2 removal is performed via wet Limestone Flue Gas Desulphurization (FGD), and Cold-side Electrostatic Precipitation (CESP) for particulate removal at 99.5% efficiency. Up-to-date there are no mercury emission limitations for combustion power plants in the UK, however, a Mercury removal system via carbon injection is included in the plant configuration to comply with the global agreement of Minamata Convention on Mercury held in 2013, to install the best available technologies on new

power plants and facilities with plans to be drawn up to bring emissions down from their existing levels [264].

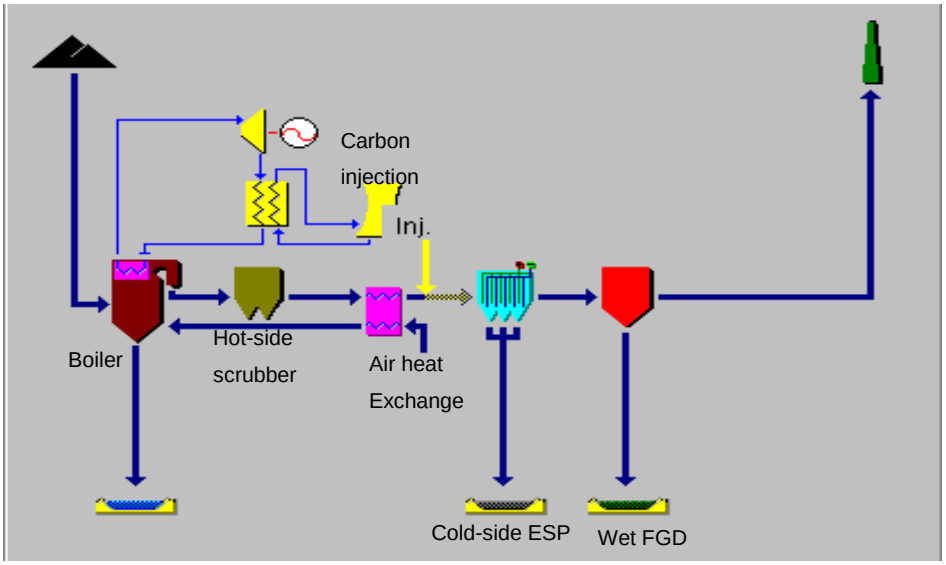

Figure 7.2 Plant configuration of pulverized biomass combustion without CCS [65].

Table 7.1 shows the European Parliament and the UK governmental emission ceiling for the coal-firing and biomass-firing power generation plants [263].

By far the largest proportion of imported wood pellets by the UK power stations came from Canada for the last four years and reached 1.72 million tonnes of pellets in 2012 [16]. Therefore, the WWP fuel properties and costs, used herein are of the Canadian white wood pellets.

Table 7.1 EU and UK emissions ceiling for coal and biomass firing power generation plants.

Parameter	**SO_2 [263]**	**NO_x [263]**	**CO_2 [265]**	**Fly Ash [266]**
	mg Nm^{-3}	mg Nm^{-3}	g CO_2 MJe^{-1}	LOI, wt%
Power plant Size, MW_{th}	>300	50-500	>50 kW	>50 kW
Plant Type	Biomass/Coal	Biomass/Coal	Coal	Biomass/Coal
Emission Ceiling	200	300 / 200	≤79.2	5

7.10.2 Coal-fired Power Plant Configuration

The same operation conditions of the biomass reference plant are applied to three different coal-fired combustion plants. The Colombian El-Cerrejon, Russian steam, and US Appalachian coal types, referred to as COC, RUC, and USC were selected for comparison with the WWP. These fuel types were selected based on actual data of the most imported coal types to the UK in the last few years [267]. Since the second half of 2010, the British coal production has declined by 30% and this mainly due to the closure of several coal mining companies. As a result the dependence on imported coal has increased by 10% from 2012 to 2013.

The fuel properties of WWP and three types of coal were cited from the literature and the US Geological Survey database [64]. Fuel prices were extracted from the Department of Energy and Climate Change database [268], Energy Information Administration (EIA) Coal Database – Export Prices to the UK [269], and the Index Mundi website [270]. The prices were corrected to the UK plants location by the addition of £13 for shipping to the UK shores, and £16 for discharging, shipping to local plant and storage. These rates were taken from the local coal buyer of SEMBCORP Co. The fuel properties and cost prices as fired in plant are listed with references in Table 7.2.

Table 7.2 Fuel costs and properties [64-66, 268-270].

Fuel Type	**WWP**	**RUC**	**COC**	**USC**
GCV, kJ kg^{-1} (db)	18,660	27,290	32,000	30,842
Fuel Cost FOB, £ $tonne^{-1}$	189.91	54.00	55.45	53.18
Fuel Cost (£ GJ^{-1})	10.18	1.98	1.73	1.72
Moisture, wt%	8.03	10.65	3.09	5.63
Ash, wt% (db)	0.29	15.67	1.39	9.79
Carbon, wt% (daf)	46.61	60.36	78.72	71.74
Hydrogen, wt% (daf)	5.70	4.50	5.18	4.62
Oxygen, wt% (daf)	40.18	8.35	9.71	6.09
Nitrogen, wt% (daf)	0.07	1.84	1.52	1.42
Sulphur, wt% (daf)	0.01	0.3	0.39	0.64

db: dry basis. daf: dry ash-free

7.11 Post-Combustion Carbon Capture Plant

The post-combustion amine-capture plant technology is added to each reference plant with 90% assumed removal efficiency, along with transportation and storage processes referred here as the CC plant. There are other technologies using ammonia as the sorbent or polymer membrane penetration technology, however they are not considered in this study as the Econamine FG+ technology is a mature and well commercially established technology while the other technologies have been proven in other research work to be more expensive and less efficient [36, 247]. The IECM assumes a 99.9% pure CO_2 will be compressed after the CC plant with traces of other gases, such as HCl, NO_x and SO_3. The plant CO_2 gas pressure is 13.79×10^5 pascal, and the pumped gas through pipelines is under 11.86 MPa pressure with minimum pressure of 10.30 MPa.

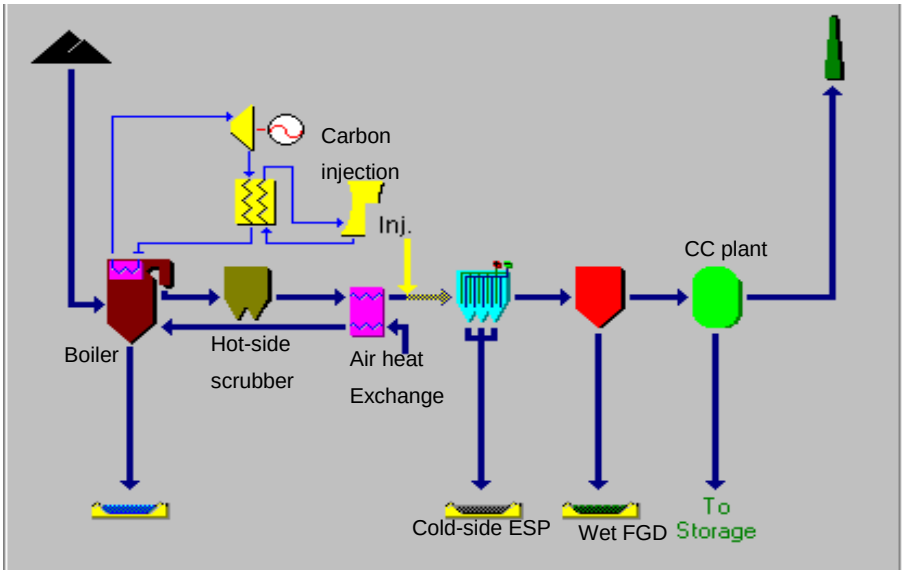

Figure 7.3 Plant configuration of the pulverized combustion with CCS [65].

7.12 Oxy-fuel Combustion Plants

Another carbon mitigation technology is considered in this study namely the oxy-Fuel Combustion (Oxy plant) for wood pellets and coal, with an integrated Air Separation Unit (ASU), and the offshore storage of CO_2 in a depleted oil or gas field, with a new infrastructure. The plant baseline CO_2 gas pressure is 13.79 MPa, and the pumped gas through pipelines is under 11.79 MPa pressure with minimum pressure of 10.30 MPa.

The impact of the carbon capture and oxy-fuel technologies on the plant performance and cost of electricity for different fuel plants is also examined herein in this study.

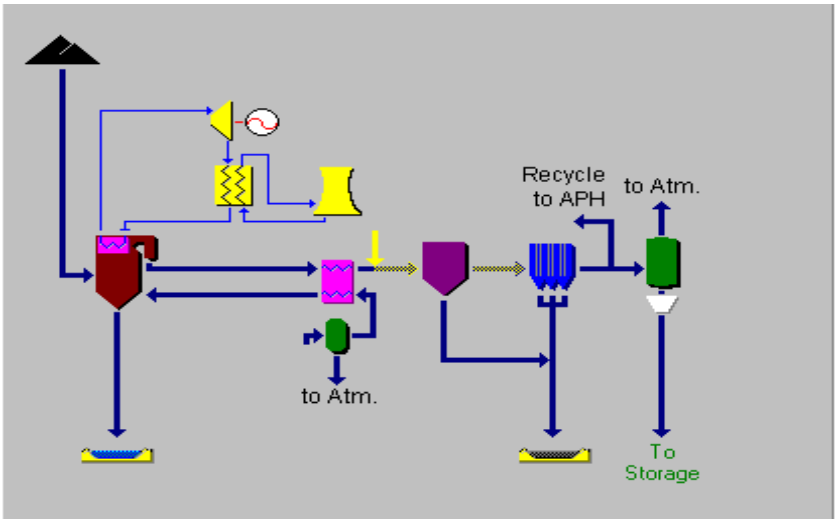

Figure 7.4. Plant configuration for the oxy-fuel combustion [65].

7.13 Operational & Economic Assumptions

For the purpose of performance and cost evaluation at the large-scale power plants, the performance and cost parameters of coal/biomass-firing plants are defined as follows:

i. The reference plant is set to 650 MW gross power output. This capacity was selected to match the typical existing capacity of coal firing power plants. This will help the comparison of exact power plant scales between coal and biomass fuel performances, knowing that the advanced supercritical steam turbine scale can be 400 -1000 MW power [271].
ii. The capacity factor (CF) for coal is assumed 70%, that is in line with the EIA monthly capacity factor data of power generation from various fuels and technologies, and the biomass CF is equal to 62.3% according to the Digest of UK Energy Statistics (DUKES) [272, 273].
iii. All fuel prices are based on current data as received by the UK power plants.
iv. The plant life for coal is assumed to be 25 years and for biomass dedicated power plant is 20 years according to the LCM criteria [259]. The reason for the deference in lifetime is due to the sever fouling, slagging and high temperature corrosion of the boiler tubes when biomass fuels are used, those can lead to

tube leakages, tube clogging, and unplanned shutdowns of the boiler that would cause a shorter lifetime [274].

v. The discount rate is 10% based on the LCM [259].

vi. The effective tax rate (ETR) is the effective rate of tax by reference to pre-tax and post-tax rates of return. The value of ETR for biomass is 21% and for the coal is 13.5%. The difference in values is referred to the lifetime of the plant and the capital cost

Tables 7.3 and 7.4 list the performance and cost parameters for the biomass and coal fired power plants. Although, some of these parameters are associated with errors and uncertainties in real applications such as the capacity factor and fixed charge factor, they are considered as deterministic values in the nominal cases.

Table 7.3 Key operational assumptions for baseline Analysis.

Parameter	**WWP**			**Coal**		
	Ref - WWP	CC-WWP	Oxy-WWP	Ref-PC	CC-PC	Oxy-PC
Performance						
Gross plant size (MW)	650	650	650	650	650	650
Plant life (yr) **[259, 261]**	20	20	20	25	25	25
Construction Period **[259]**	3.0	3.5	3.5	3.0	3.5	3.5
Capacity Factor CF (%) **[259, 272]**	62.3	62.3	62.3	70	70	70
Unit Type	Super Critical					
Boiler firing Type	Tangential					
Boiler Efficiency (%)	86	86	90	91	91	94
Fuel Flowrate, tonne h^{-1}	312.0	385.3	299.9	182.8	219.3	175.6
Boiler Efficiency, %	86.69	86.69	90.17	90.77	90.77	94.44
Excess air for furnace (% stoich.)	20	20	5	20	20	20
Gas Temp. Exiting Economizer(K)	593					
Gas Temp. Exiting Preheater(K)	403					

Continued

NO_x removal (%)	**61**	**61**	**15**	**73**	**73**	**15**
SO_2 removal Efficiency (%)	60	98	69	69	98	75
SO_3 removal efficiency (%)	66	66	99	69	69	100
Fly Ash removal efficiency (%)	90	90	72	96	96	96
Mercury removal efficiency (%)	72	72	56	100	100	72
CO_2 capture efficiency (%)	0.0	90	87	0.0	90	87
ASU recovery efficiency	-	-	95	-	-	95
CO_2 produced gas pressure (MPa)	-	13.79	13.79	-	13.79	13.79
Power Requirement						
Base Plant (% MWg)	4.167	4.094	4.167	2.917	3.362	2.917
Hot-side SCR (% MWg)	0.505	0.566	0.000	0.442	0.535	0.000
CESP (% MWg)	0.102	0.102	0.191	0.112	0.112	0.164
Wet FGD (% MWg)	1.656	2.600	0.351	1.510	2.515	0.307
Activated Carbon Inject (% MWg)	0.014	0.020	0.010	0.009	0.011	0.012
Cooling Tower Use (% MWg)	1.250	2.800	1.250	1.250	2.800	1.250
CCS (% MWg)	0.00	32.68	17.11	0.00	30.10	25.67

Table 7.4 Economic model parameters for biomass and coal combustion.

Parameter	**WWP**	**Coal**
Fuel Price (£ $tonne^{-1}$)	189.9	55.0
Discount Rate (%) **[259]**	10	10
Labour rate, £ h^{-1} **[275]**	30.25	30.25
Effective tax rate (%) **[259]**	21	13.5
Inflation rate (%) **[259]**	2	2
Operating shifts per day **[262]**	4	4
Operation & Maintenance Cost(%TCP) **[276]**	5%	5%
CO_2 transport cost (£ $MW^{-1}h^{-1}$) **[259, 261]**	33.70	33.03
CO_2 transport & storage cost (£ $tonne^{-1}$ CO_2) **[277]**	25.28	25.28

7.14 Co-Firing Options

Biomass co-firing can be a near-term mitigation solution to the GHG emissions [232]. Co-firing is defined as the firing of a renewable fuel (i.e. biomass) along with the primary fuel (coal, natural gas, furnace oil, etc.). Recent studies in Europe and the United States [2–5] have established that burning biomass with fossil fuels has a positive impact both on the environment and the economics of power generation. The emissions of SO_2 and NO_x were reduced in most co-firing tests (depending on the biomass fuel used). The CO_2 net production was also inherently lower, and this is because biomass is considered as CO_2-neutral. In addition, total fuel costs can be reduced in some cases if the biomass processing costs (transportation, grinding, etc.) are lower than the primary fuel processing costs on an energy basis.

Co-firing of biomass and coal at coal-fired power plants has been considered to be one of the most attractive strategies to reduce CO_2 emissions [278]. On the other hand, co-firing has been sought to negatively affect the plant efficiency due to the reduction of the boiler efficiency [279]. Co-firing can be implemented by co-milling, direct co-firing with separate feeding systems, or parallel co-firing via separate combustion units [232].

In this study, co-firing is applied to investigate the sensitivity of using cheap price coal with biomass as a method to reduce the cost of electricity generated from biomass fuels and study the overall plant efficiency behaviour. The life cycle assessment (LCA) of CO_2 emissions is not considered in this study, only the plant emissions are assessed.

Table 7.5 WWP-USC blending for co-firing plants.

Fuel type	**CO_2 Capture Technologies**
100% US Coal	
25% White Wood Pellets Cofiring	Air-fuel,
50% White Wood Pellets Cofiring	Oxy-fuel, and
85% White Wood Pellets Cofiring	Amine FG+
100% White Wood Pellets	

As shown in Table 7.2, the US coal has the lowest price per tonne as received in the UK power plants, and accordingly is cheaper in terms of cost per GJ of energy produced. Therefore, three cases of co-firing US coal with 25%, 50%, and 85% of WWP will be studied to measure the impact of fuel price on plant efficiency and cost of electricity (COE) (see Table 7.5). The 85% is selected to reflect the change of carbon price at this ratio as regulated by the UK Department of Energy.

7.15 Variability & Uncertainty Analysis

Although, many CCS techno-economic studies produce deterministic values of cost with a high degree of confidence and accuracy, the plant-level studies tend to include a sensitivity analysis for certain assumptions on the parameters that can take more than one value, such as the fuel price, capacity factor, fixed charge factor, and carbon price [243, 248, 253, 262]. Such studies employ the probability distributions or assign a range of values to the uncertain parameters. On the other hand, “Uncertainty” reflects a lack of knowledge about the precise value of one or more of the parameters affecting the CCS costs. For example, a study that incorporates the concept of contingency cost factor on capital cost when investigating new methods or new solvents, or even new plant size that have not been commercialized yet [231, 244]. Other studies went further in assuming scenarios for the future policies or incentives of CCS especially when biomass is deployed in the co-firing or a conversion plant [229, 254, 280].

In this study, the sensitivity of Plant Efficiency towards the fuel type, the *COE* towards the fuel price, and Carbon Price will be examined. In addition, the uncertainty analysis of ROCs in biomass-firing plants will be investigated and discussed herein.

7.15.1 WWP Price Variation

Biomass fuels, including wood pellets, cost consistently less than oil fuels although at 2009 prices are only marginally cheaper than the mains gas. While woodchips are always cheaper than wood pellets on a per kWh basis variable fuel quality, as the high moisture content can erode the margin significantly. Other factors in the woodchip price are the number of times timber is handled between standing as a tree and being delivered into a silo, and the distance woodchips are transported. A crude rule of thumb is that it costs up to £10 every time a tonne of wood is handled. In respect of wood pellets this cost is 0.20 pence per kWh whereas for woodchips, the cost is

0.29 pence per kWh at 30% moisture content and 0.44 pence at 50% moisture content. Another rule of thumb applied across Europe is that it is uneconomic to transport woodchips more than about 30 miles because the fuel cost per kWh increases disproportionately above that distance [281]. Prices of imported wood pellets are listed in Table 7.6.

Table 7.6 Prices of wood pellets available at the UK markets.

Type of Wood Pellets	Price, £ tonne^{-1}	Price, £ GJ^{-1}	Ref.
UK Wood Pellets	182.66	11.03	[268]
Russian Wood Pellets	184.41	10.03	[282]
Canadian Wood Pellets	189.90	10.18	[283]
US Wood Pellets	200.00	11.93	[268]

To make the WWP more profitable as combustion fuel in power plants, there must be some reduction in the fuel cost. This can be achieved if local wood pellets are used with a reduction of processing, drying, and pelleting costs. Also, the fuel properties such as the moisture and bulk density have a profound influence on its heating value and ultimately its cost per unit of heat or electricity produced. Another way to reduce the fuel cost is by looking for much cheaper sources of imported pellets, such as from African or south Asian countries instead of Canadian and Russian sources.

The impact of wood pellets cost on *COE* produced compared with coal is also investigated in this study within the range of 1-11 £ GJ^{-1} that both fuels fall in.

7.15.2 Coal Price Variation

The projected coal prices for the next 15 years published by the DECC were used in this study to calculate the breakeven fuel price that gives cost-effectiveness to the BECCS in power generation plants [284]. The projection has three scenarios, low, central and high. The low price projection is based on importing from South Africa as the cheapest supplier for steam coal to the European countries in 2020 (55.2 £ tonne^{-1}). The central projection, accounts for updated historical data on the relationship between coal and gas prices (73.0 £ tonne^{-1}), whereas, the high scenario is based on lower productivity growth rates, higher mining wages, higher transportation costs and higher mine equipment costs (98.5 £ tonne^{-1}).

7.16 Results & Discussion of Model Analysis

7.16.1 Effect of CC and Oxy-fuel Processes on Plant Efficiency

The combustion plant performance relies on the fuel quality in terms of heating value (GCV), composition, and the capacity factor which is the annual average value, representing the percentage of equivalent full load operation during a year depending on the number of operating hours [260]. The plant efficiency is then calculated as the percentage ratio of net electrical output (MW) to the total plant heat input (GJ h^{-1} or MW yr^{-1}). The low plant efficiency elucidates high losses in the power generated due to the plant equipment and pollution equipment consumption, in other words represents the energy penalties. The plant efficiency results are listed in Table 7.7.

A comparison between the plant efficiency of three types of coal fuels: Colombian, Russian and US coal have been made with the white wood pellets combustion plant in three cases; first the reference plant without carbon capture, second with the amine FG+ CC plant, and the third of the oxy-fuel plant.

Table 7.7 Net output power and net plant efficiency of the Ref, CC, and Oxy plants.

	Ref. Plant		**CC Plant**		**Oxy Plant**	
Fuel	Net MW_e	Plant Eff.	Net MW_e	Plant Eff.	Net MW_e	Plant Eff.
Wood Pellets	607	37.56	375[a]	26.44	470	30.20
Colombian Coal	616	39.78	404[a]	28.89	481	32.39
Russian Coal	614	39.48	426[a]	29.68	488	32.57
US Coal	615	39.81	414[a]	29.36	484	32.63

a : the net electrical value does include the electricity required for the amine plant

Figure 7.5 illustrates the comparison results. The WWP plant showed a 2%, 3%, and 2% lower efficiency than the three types of coal in the Reference, Amine and Oxy plants, respectively. This is due to the lower heating value of the WWP, the lower boiler efficiency for biomass plants, and the higher capacity factor of the coal plants (see Table 7.3. The lower capacity factor is translated into lower electricity generated per year and this leads to lower plant efficiency. Although there are variations in the heating value and carbon content among the three types of coal, the plant efficiency

showed a low sensitivity to the type of coal in all three cases, with only a range of 0.7-2.7% differences between the three cases under investigation.

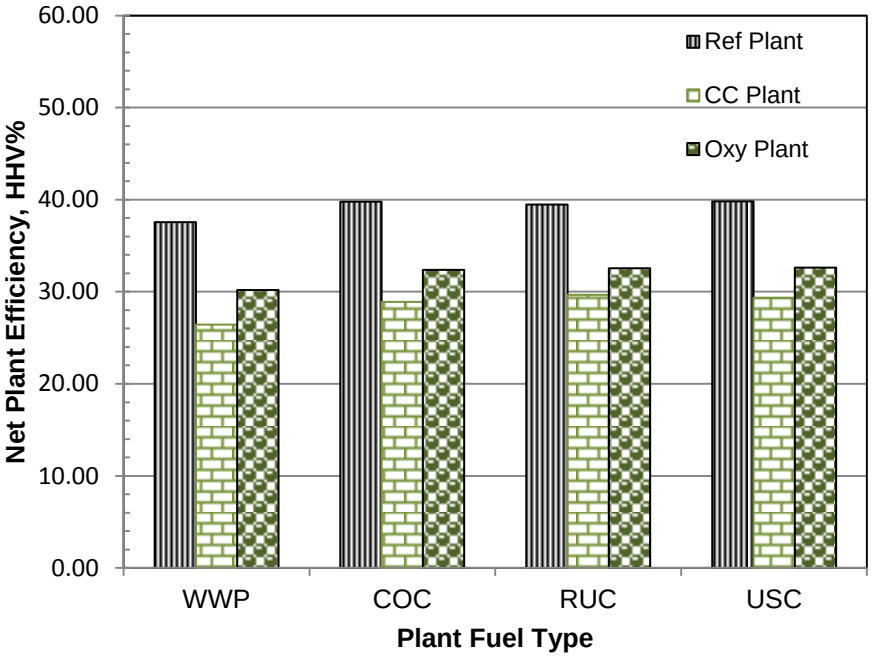

Figure 7.5 Net plant efficiency of WWP, Colombian, Russian, and US coal fuels in the three study cases: Reference, CCS and oxy-fuel plants.

Interestingly, the oxy-fuel plants showed a higher efficiency than the amine CC plants and the reason for that, the amine capture process and sorbent regeneration consume a large portion of the electricity generated. The efficiency difference of the Oxy and CC plants was the highest with the biomass fuel as of 14.2% increase, then the COC, USC and RUC as 12%, 11% and 9%, respectively. These results are in agreement with other research work performed by Catalonotti et al. [253] for coal-fuelled plants, and the Electricity Generation Model submitted to the Department of Energy and Climate Change [261]. Also, Dominichini et. al. [251] reached to the same plant efficiency of biomass-CCS case, i.e. 25.8% in comparison to 26.44% in the corresponding case in this study. To the best knowledge of the author, there is not enough data in economic comparison between post-capture and oxy-fuel technologies on biomass combustion in the literature.

7.16.2 Effect of CC and oxy-fuel on Carbon Emissions

The annual carbon emissions of 650 MW WWP, COC, RUC and USC plants without CCS technology are 2.91M, 3.08M, 2.78M, and 2.95M tonne CO_2 respectively. These results are commonly translated into emission factors kg CO_{2e} per unit of electricity produced. The CO_2 emission factor for the net electricity is a function of fuel property and plant efficiency. The results are listed in Table 7.8.

Table 7.8 Carbon emissions in kg $kW^{-1}h^{-1}$ from WWP, COC, RUC and USC plants.

	Ref Plant	**CC Plant**	**Oxy Plant**
WWP[a]	0.878	0.125	0.109
COC	0.816	0.112	0.100
RUC	0.739	0.098	0.089
USC	0.781	0.106	0.095

a: these are the calculated emissions, however, biomass is considered a neutral carbon fuel.

The actual emission factors for biomass and coal Ref-WWP, Ref-COC, Ref-RUC, and Ref-USC plants are 0.878, 0.816, 0.739, and 0.781 kg $kW^{-1}h^{-1}$, respectively. However, the net specific emissions of dedicated biomass (WWP) are zero regardless of the actual production [35, 3]. On the other hand, the emissions from the three coal plants are higher than the regulatory emission factor for electricity generation in the UK that is 0.544 kgCO_{2e} per kWh [9]. When applying the CCS technologies on the four plants, the emissions are reduced by 85-90% with final ranges that meet the regulatory set values. Figure 7.6 shows the carbon emissions results and the CC plants produce slightly higher emissions than the Oxy plants. In the same time, the carbon removal from the CC plant is also higher than the Oxy plant for the same energy output. The reason for these differences is the higher fuel input used in the first rather than in the latter. 0

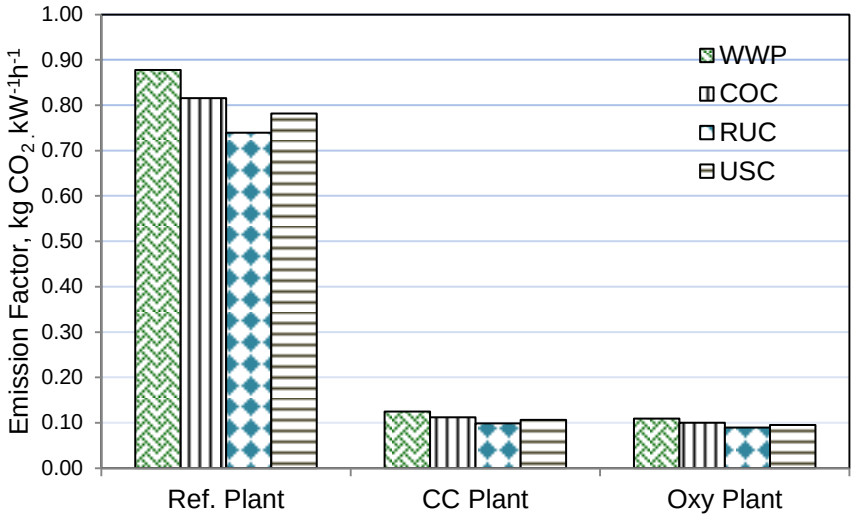

Figure 7.6 Carbon emission factor of WWP, Colombian, Russian, and US coal fuels in the three study cases: Reference, CC and Oxy-fuel plants.

The carbon captured from the WWP plant is 3.2M and 2.5M tonnes per year for the CC and Oxy plants respectively. Considering the biomass as a neutral carbon emission fuel, these quantities can be considered negative emissions that contribute to the mitigation of GHG for the long term. The actual emission factors for biomass Ref-WWP, CC-WWP, and Oxy-WWP are 0.8775, 0.125, 0.109 kg $kW^{-1}h^{-1}$, respectively. However, the net specific emissions of dedicated biomass (Ref-WWP) are considered zero regardless of the actual production [35, 3]. In addition, the utilization of carbon capture technologies with the biomass in the electricity generation industry in a 650 MW power plant can annually capture about 3.2M tCO_2 by post carbon capture and 2.5M tCO_2 by oxy-biomass combustion that are considered negative emissions. This assumption is further illustrated in Fig. 7.7.

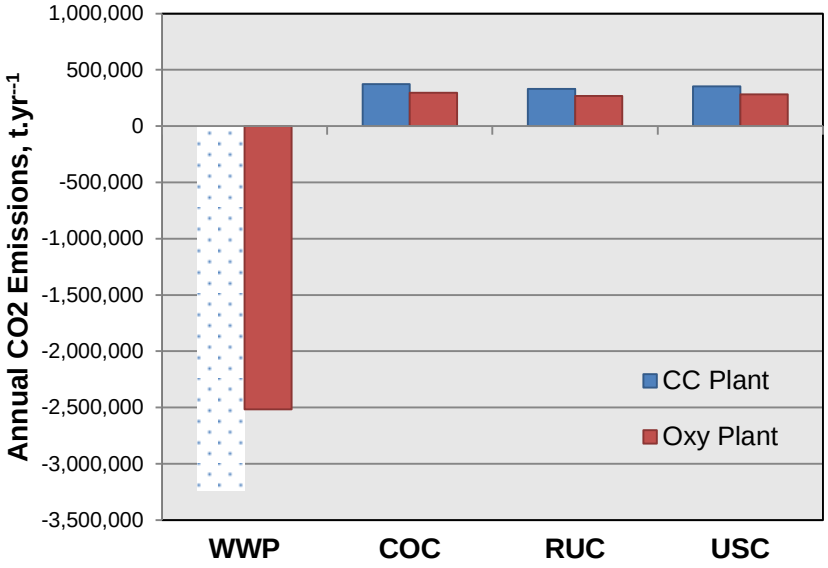

Figure 7.7 Annual Negative emissions of WWP, in comparison to positive emissions from coal fuels.

7.16.3 Capital Cost of Dedicated Biomass Plant versus Coal Plants.

The capital required for WWP and the three types of coal used in the UK are calculated based on the plant description in the IECM with a capacity of 650 MW and for three cases investigated of Reference, Amine capture and oxy-fuel plants. Table 7.9 shows the total capital investment for the reference, CC and oxy-fuel plants. It is found that without CCS, the capital required for the WWP plant is not significantly higher than the capital required for the three coal plants. Basically, the difference in the capital cost of WWP plant over the three coal plants is due to the assumption that the biomass plants are the first of a kind while the coal plants are Nth of a kind which is reflected in the depreciation and amortization costs of the plant equipment. However, the reason for these proximate results is due to the high capital required for pollutant removal units from the coal due to the high ash content compared to the wood biomass (see Table 7.2), especially the Russian coal.

From Table 7.9 it can be observed that the capital required for the Reference WWP plant is only higher by 7.7%, 4%, and 5.3% than the capital required for the COC RUC and USC plants, respectively. The higher capital required for RUC among the other coal types is attributed to the higher capital required for the total solid particles (TSP) removal unit; CESP, as observed from Table 7.2 that the fly ash content of the Russian coal is 54, 11, and 1.6 times higher than the WWP, COC, and USC respectively.

Figure 7.8, shows the results obtained for the capital required for the subunits of three cases of Reference, Amine and oxy-fuel plants with the four types of fuels.

Table 7.9 Economic results of Reference, CC and Oxy plants for four different fuels.

	Total Capital, £M			Cost of Electricity, £ $kW^{-1}h^{-1}$		
Fuel type	Ref	CC	Oxy	Ref	CC	Oxy
WWP	736	1151	1257	108.88	203.95	192.20
COC	683	1065	1202	59.47	97.69	103.62
RUC	707	1072	1198	61.60	86.88	104.81
USC	699	1079	1203	60.24	84.63	103.09

When applying the post-combustion carbon capture process with amine FG+, the capital costs of the four CC plants and the Oxy plants have increased by 40-50% from the Reference plants, and the capital cost of the CO_2 control is approximately the same for WWP and the three types of coal.

A comparison of the two carbon capture technologies, CC and Oxy processes on the four fuel cases shows that, the capital cost of oxy-fuel process is around 10% higher than post-combustion CCS with amine plant for the same 90% CO_2 removal and a 99% pure gas to be compressed for storage. The reason for this difference in capital cost is the cost of the air separation unit and flue gas recycling equipment and piping that are approximately 1.5 times higher than the amine plant equipment costs [252]. On the contrary, the base plant and SO_x removal costs are higher for the CC plant than the corresponding costs in the oxy-fuel plants, due to the smaller flue gas flow in the oxy-fuel resulting a smaller unit size and completely different separation process of sulphur when removed after gas recycling. The same conclusions were reached by Rubin et al. and Catalonotti et al. [244, 253] with a slight variance in capital costs between both technologies than the results in this study.

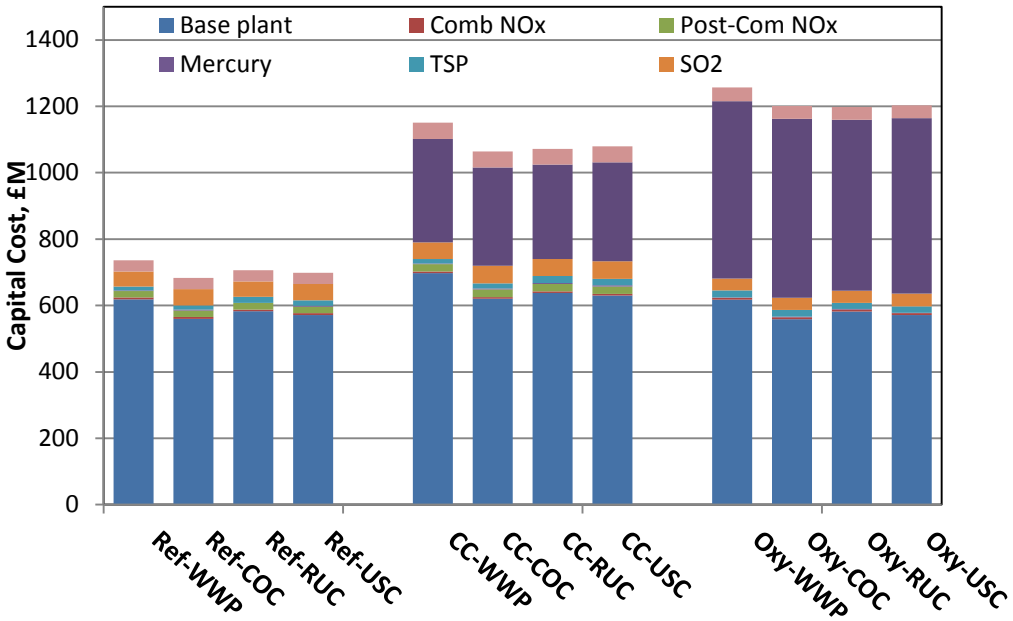

Figure 7.8 Capital required (£M) for WWP, Colombian, Russian, and US coal fuels in the three study cases: Reference, CCS and oxy-fuel plants.

7.16.4 Cost of Electricity (*COE*)

The levelized cost of electricity (*COE*, £ MW^{-1} h^{-1}) is calculated by the IECM, from the annual levelized total cost (*TLAC*, £M yr^{-1}) that is the sum of the total annual O&M cost and annualized capital cos, divided by the total number of working hours and the net electrical output [248], namely

$$Levelized\ COE\ (\text{£ MW}^{-1}\text{h}^{-1}) = \frac{TLAC\ (\text{£M yr}^{-1})}{(\text{no.ofhours per yr} * \text{Net Electrical output MW})} \qquad (7.1)$$

where,
COE: cost of electricity generation, (£ $MW^{-1}h^{-1}$)
$TLAC$: annual levelized total cost, (£M yr^{-1})

As a result, the plant with the higher capital required is predicted to have a higher levelized *COE* which is in this case the oxy-fuel plants. As shown in Table 7.9, the *COE* of the oxy-coal plants are higher than the *COE* of the amine plants by 20 £ $MW^{-1}h^{-1}$ for the COC, RUC, and USC coal types, respectively. In contrast, the WWP fuel showed a lower value of *COE* in the oxy-fuel plant than the *COE* of the amine plant by a difference 11.75 £ $MW^{-1}h^{-1}$ (5.76%).

This contradiction in the results is attributed to the second factor of *TLAC*, i.e. the variable operating cost component, which was higher in the amine plant than the oxy-WWP plant that dominated the opposite effect of the capital cost. The variable operation cost is mainly dependent on the fuel cost that is higher in the amine plant as more fuel is required to overcome the energy loss within the carbon capture process. In addition, the costs of the emissions control (SO_2, CO_2, and NO_x) are consequently higher in the amine plant than in the oxy plant. Figure 7.9 illustrates the *COE* as a function of plant and fuel types.

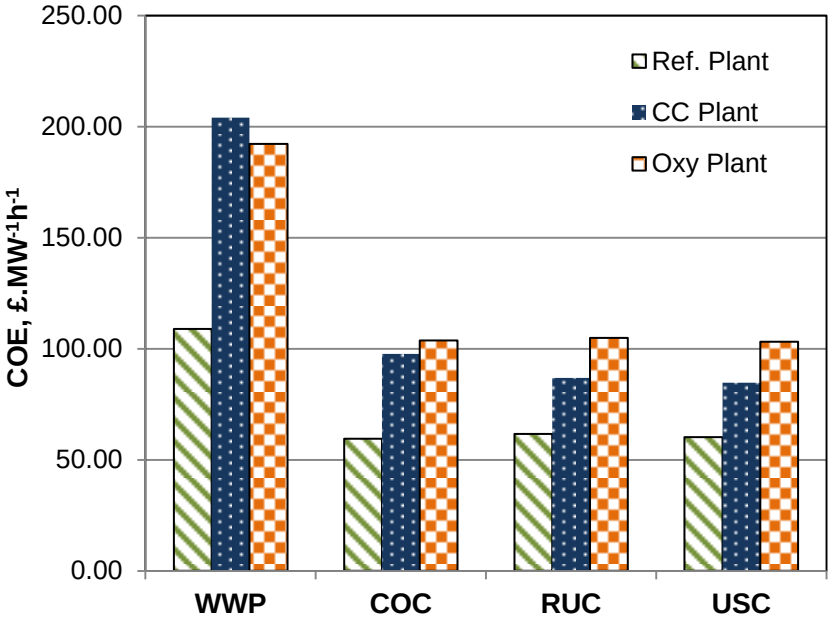

Figure 7.9 Levelized *COE* for WWP, COC, RUC and USC, in three cases; REF, CCS and Oxy-fuel plants.

7.16.5 Cost of CO_2 Avoided & Cost of CO_2 Captured

The cost of CO_2 avoided (£ $MW^{-1}h^{-1}$) is one of the common economic measures of the CCS plants [248, 253, 254]. It denotes the cost of avoiding or removing a ton of atmospheric CO_2 emission while producing one MWh of electricity [248].

$$\text{Cost of } CO_2 \text{avoided } (£\ MW^{-1}h^{-1}) = \frac{(COE)_{CCS} - (COE)_{Ref}}{(tCO2\ MW^{-1}h^{-1})_{Ref} - (tCO2\ MW^{-1}h^{-1})_{CCS}} \qquad (7.2)$$

where,

$tCO_2\ MW^{-1}h^{-1}$: CO_2 mass emission rate to the atmosphere

Meanwhile, the cost of CO_2 captured is another cost measure for a certain capture technology and plant type [248]. This measure is used to evaluate the economic sustainability of a CO_2 capture system relative to a market price for CO_2 as an industrial commodity. For a power plant, it can be defined as follows:

$$\text{Cost of } CO_2 \text{captured } (£.tCO_2^{-1}) = \frac{(COE)_{CC} - (COE)_{ref}}{(tCO_2\ MW^{-1}h^{-1})_{captured}} \quad (7.3)$$

where,
$(tCO_2\ MW^{-1}h^{-1})_{captured}$: total mass of CO_2 captured per net MWh for a power plant with $CC = CO_2$ produced $- CO_2$ emitted.

It is imperative to distinguish between the cost of CO_2 avoidance and the cost of CO_2 capture, as many readers may mistake one for the other. The cost of CO_2 captured excludes the costs of CO_2 transport and storage since the purpose of this measure is only to calculate the cost of the capturing process. Hence, the cost of CO_2 captured is always lower than the cost of CO_2 avoided. The cost of carbon avoidance and cost of carbon capture values for all fuels are listed in Table 7.10.

The three types of coal exhibited a slight variation in the cost of CO_2 avoided. However, the oxy plants showed higher costs than the amine capture plants in terms of CO_2 cost of avoidance corresponding to the same trend of capital costs and *COE* in the three coal plants. The CC plant with the US coal has the lowest cost of CO_2 avoided, i.e. 34.34 £ tonne^{-1}, then the Russian and Colombian coal at 37.70 £ tonne^{-1} and 52.56 £ tonne^{-1}, respectively. Whereas, the Oxy-COC, Oxy-RUC, and Oxy-USC has 60.06 £ tonne^{-1}, 64.87 £ tonne^{-1}, and 60.83 £ tonne^{-1}, respectively. These results agree with the conclusions of Berghout et. al. [249], as they found that the costs of CO_2 avoided for three different plant types were lower for the post-capture than the oxy-fuel process, especially in the long term which is similar to the case of our study.

Table 7.10 Cost of carbon capture, avoidance and negative emissions (in case of WWP).

	WWP		**COC**		**RUC**		**USC**	
	CC	**Oxy**	**CC**	**Oxy**	**CC**	**Oxy**	**CC**	**Oxy**
Cost of CO_2 avoidance, £ $\mathbf{tCO_2^{-1}}$	124.75	105.34	52.56	60.06	37.70	64.87	34.34	60.83
Cost of CO_2 Capture, £ $\mathbf{tCO_2^{-1}}$	67.24	65.70	19.82	30.80	23.62	35.42	20.81	31.79

As mentioned in Section 7.8, the IECM does not include the option of biomass fuels in the combustion plant model. Thus, the fact that BECCS can be a negative emission process is not translated here in the calculations of the cost of CO_2 avoided and cost of CO_2 captured. The model treats the biomass as the coal fuels and calculates the costs similarly. As expected, the results showed higher costs of CO_2 avoidance in plants with WWP than the costs of the three coal-fuelled plants in both cases of oxy and amine capture technologies. This is due to the higher *COE* of WWP plants. However, the CC-WWP plant has a higher cost than the Oxy-WWP plant, while the CC-Coal plants of the three coal fuels have lower costs than the Oxy-coal plants. These opposite trends are attributed to the higher *COE* and higher tonnes of CO_2 emitted from the CC-WWP plant against the Oxy-WWP plant. In the same manner, the cost of CO_2 capture is also higher for WWP plants than for coal plants, and these results are shown in Fig. 7.10.

7.16.6 Proposed New Concept of CCS Cost for Biomass

Despite the above results, an argument can be raised about the concept of the cost of CO_2 avoidance for any biomass plant and in this case the WWP plant. The argument is about considering the biomass as a neutral CO_2 fuel. Then, one can say, the CO_2 produced in the reference plant should have zero value as the trees already have taken the CO_2 from the atmosphere. In this case, the cost of CO_2 avoided in Eq. 7.2 will have a negative value. Therefore, the author believes that Eq. 7.2 in its current form does not apply correctly to biomass fuels.

The same argument could possibly be raised on the cost of CO_2 captured when applying on biomass fuels. As the carbon captured from a biomass power plant is considered as negative emissions, Eq. 7.3 can be used to express the *cost of negative emissions* of BECCS as follows:

$$\text{Cost of negative emissions } (£\,\mathbf{tCO_2^{-1}}) = \frac{(COE)_{\text{CC}} - (COE)_{\text{ref}}}{(\text{tCO}_2\ \text{MW}^{-1}\ \text{h}^{-1})_{\text{captured}}} \quad (7.4)$$

The author believes that this definition is more appropriate for the BECCS. Accordingly, a new understanding and economic assessment to the BECCS can be approached in comparison to coal.

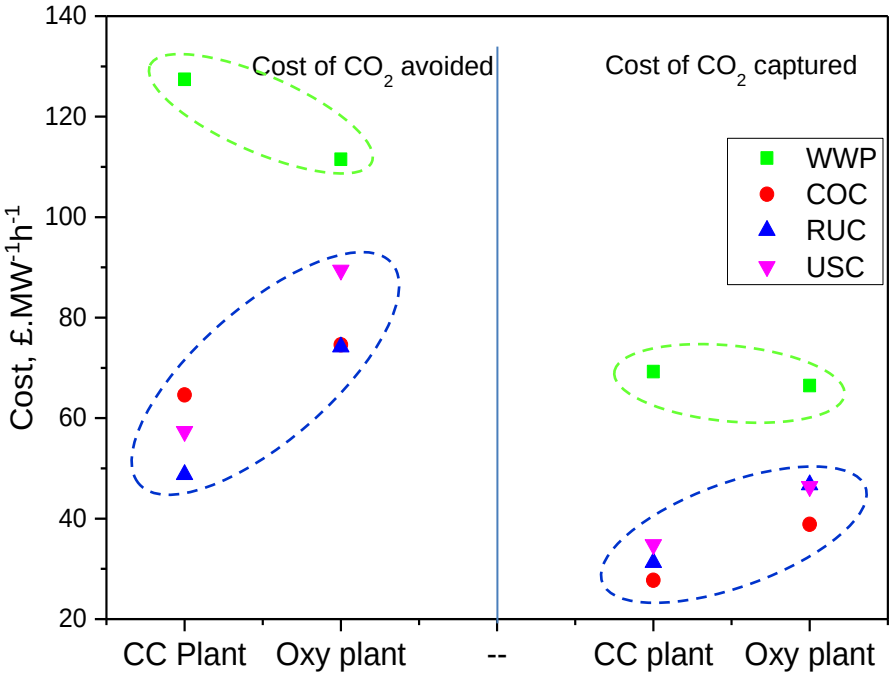

Figure 7.10 Cost of CO_2 avoidance and cost of CO_2 capture in CC and oxy-fuel plants with WWP, COC, RUC, and USC fuels.

7.16.7 Effect of Co-firing on Plant Efficiency

Co-firing biomass with coal is one of the methods to mitigate the carbon emissions of fossil fuels, and at the same time reduce the cost of electricity produced from dedicated biomass power plants. In this analysis, blends of 25%, 50% and 85% of WWP with the Appalachian low sulphur US coal are used as the fuel for combustion power plant. The results of plant efficiency at co-firing are illustrated in Fig. 7.11.

Co-firing at 25% WWP reduces the coal plant efficiency of Ref, Amine and Oxy plants by 0.39%, 0.5%, and 0.44%, respectively. The increase of WWP from 25% to 50% results in a larger reduction in plant efficiency by 0.48%, 0.6%, and 0.52%, while at 85% WWP, the reductions in plant efficiency were 0.9%, 1.14%, and 0.98% for the Ref, Amine, and Oxy plants, respectively.

The efficiency drop of the amine plant was the highest among the three cases at all WWP blending ratios. The reason for this is the higher energy losses in the amine plants that requires more fuel to keep the output energy constant, and that will result in lower heating value of the fuel blend due to the lower heating value of WWP. Also it

can be observed from Fig.7.11 that the Oxy plant has higher efficiencies than the Amine plant in all blending ratios.

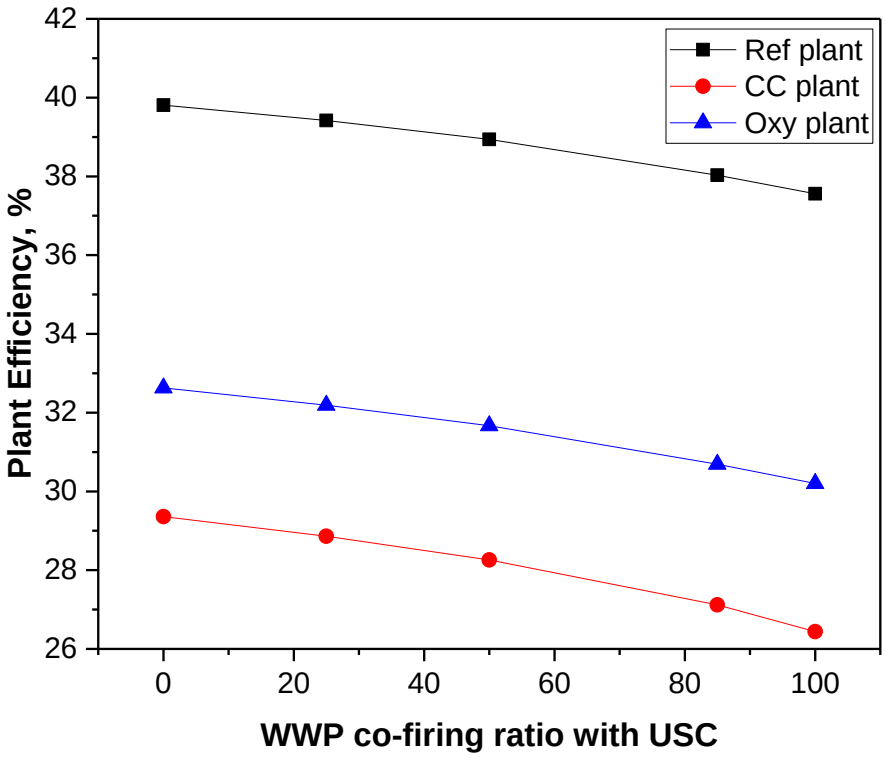

Figure 7.11 Effect of Co-firing WWP with US coal on plant efficiency in the three cases; Reference plant; amine plant and Oxy-fuel plant.

7.16.8 Effect of Co-firing on *COE*

The application of CCS on co-firing plants has revealed some interesting findings in terms of the *COE*. First, for base plant without CCS, the cost of electricity is reduced at 25% blending with WWP because of the Renewable Obligation credit (ROC), i.e. 0.5 ROC at blending below 50% (ROC = 42.02 £ $MW^{-1}h^{-1}$ produced). The same reason maintained the *COE* of the CCS plants at 25% WWP, also the same as the Ref plant. While at higher levels of WWP blending, the cost is dramatically increased for the three cases of Ref, Amine and Oxy plants.

On the other hand, a comparison between the two CCS technologies shows that at low co-firing ratios (less than 50% WWP) the *COE* of the Amine plant is lower than that of the Oxy plant, while at blending higher than 50% WWP, the Oxy plants has lower *COE*

than the Amine capture plant. The explanation for this change in *COE* proportionality of Oxy to Amine plants is the trade off the capital cost of Oxy plants with the increasing fuel cost at higher blending ratios. The results of the *COE* of the three cases of co-firing plants are shown in Fig. 7.12.

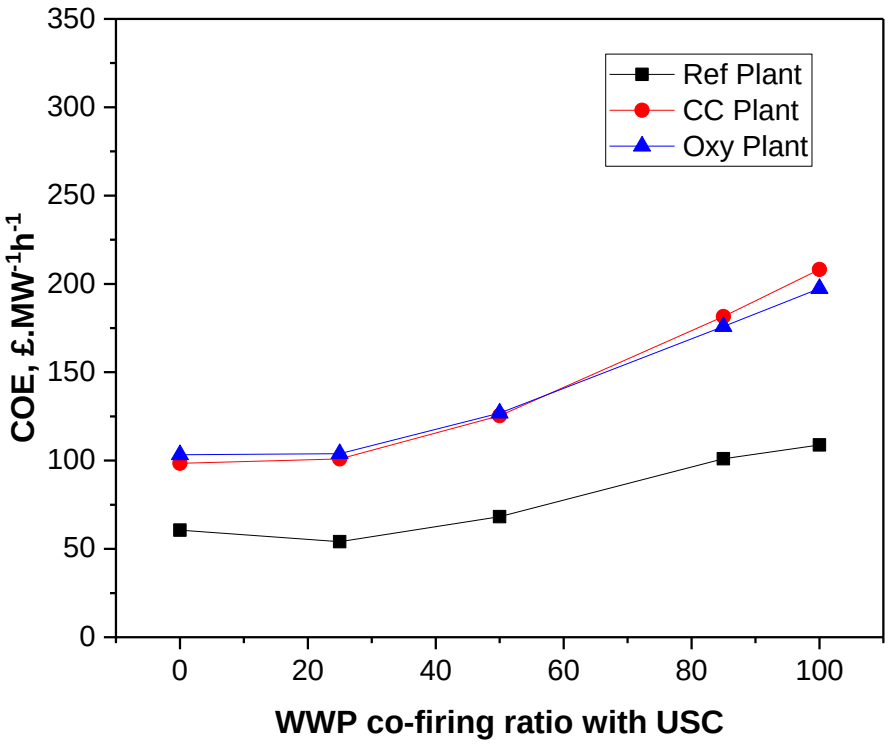

Figure 7.12 Effect of Co-firing WWP with USC on COE in three cases; Reference, CC, and oxy-fuel plants.

7.16.9 Effect of Co-firing on Total Annual Levelized Cost

The Total Levelized Annual Cost (*TLAC*) is the sum of the total annual O&M cost and annualized capital cost components. For the three cases of Ref, CCS, and oxy plants with various fuels, the results are shown in Figure 3.12. Interestingly, co-firing WWP with coal at 25% or less, in retrofit coal combustion plants has a positive effect in reducing the TLAC of Ref and oxy plants. In contrast, at higher percentages of WWP the TLAC considerably increases due to the high fuel cost until the 85% WWP then a drop in the cost value occurs when the fuel become 100% WWP. The last change in the cost is due to the change of RO value for dedicated biomass plants that increases to 1 ROC from 0.75 RO after 85% biomass.

Similar to the trend in the *COE* proportionality in the oxy and amine plants, the *TLAC* is higher in the latter at all co-firing ratios except the very low WWP percentage; less than 8% in the fuel blend, the amine plant has a lower *TLAC*.

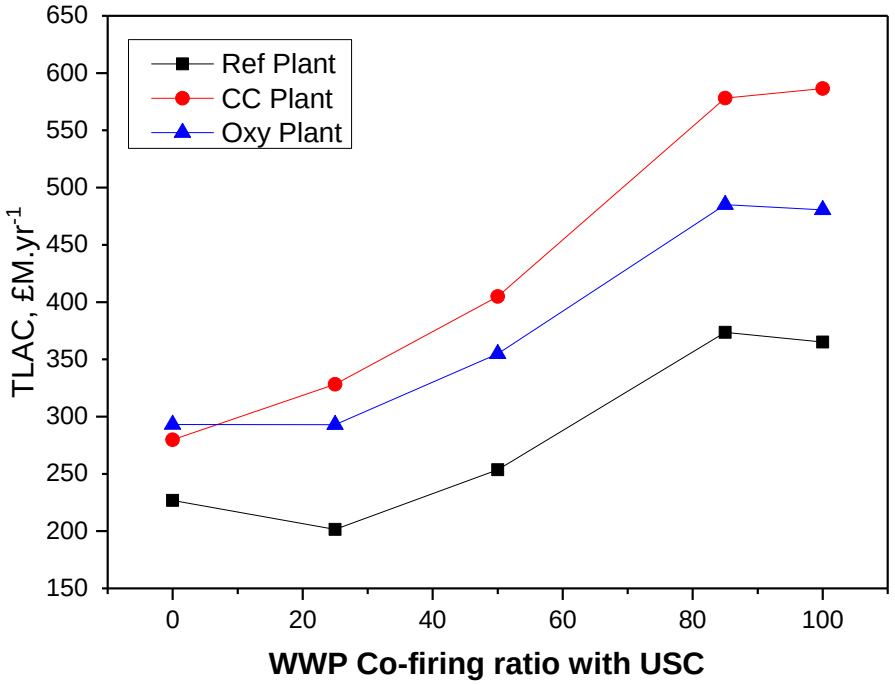

Figure 7.13 Effect of co-firing on *TLAC* in three cases; Reference plant without CC, Amine CC plant and Oxy-fuel plant.

7.16.10 Economic Scenarios

As mentioned in Section 7.14, the sensitivity of the WWP combustion plant to the fuel prices, and the subsidies offered by the government is examined in this study to conclude that the viability of BECCS as an economic CO_2 mitigation method for the long-term planning.

7.16.10.1 WWP Cost Variability

Investing in WWP versus coal in the combustion power plants for electricity generation is influenced by the WWP price as the main cost-effectiveness factor that the power plant companies should consider [285]. With the current coal prices (1.7–2.9 £ GJ^{-1}) and WWP price with 5 times higher (10.2 £ GJ^{-1}), the breach is too high. Thus, an outlook at how low the WWP prices could thriftily sustain the BECCS deployment in the power generation industry is presented in this section.

Figure 7.14 shows the current prices of coal and WWP as received at the UK power plants; 53 £ tonne^{-1} and 189.9 £ tonne^{-1} represented by black and green lines with stars on the x-axis. The horizontal lines represent the *COE* of the coal plant cases at Ref, amine and oxy plants, respectively.

For the WWP reference plant, the breakeven WWP price is 108 £ tonne^{-1}, while applying the carbon capture technologies requires more reduction in the fuel price to reach the breakeven price at approximately 65 £ tonne^{-1}, and 69 £ tonne^{-1} for Amine and oxy plants respectively. Also, the CCS technologies showed more variation at higher WWP prices, the larger the fuel price the less *COE* can be gained from the oxy plant than the CC plant.

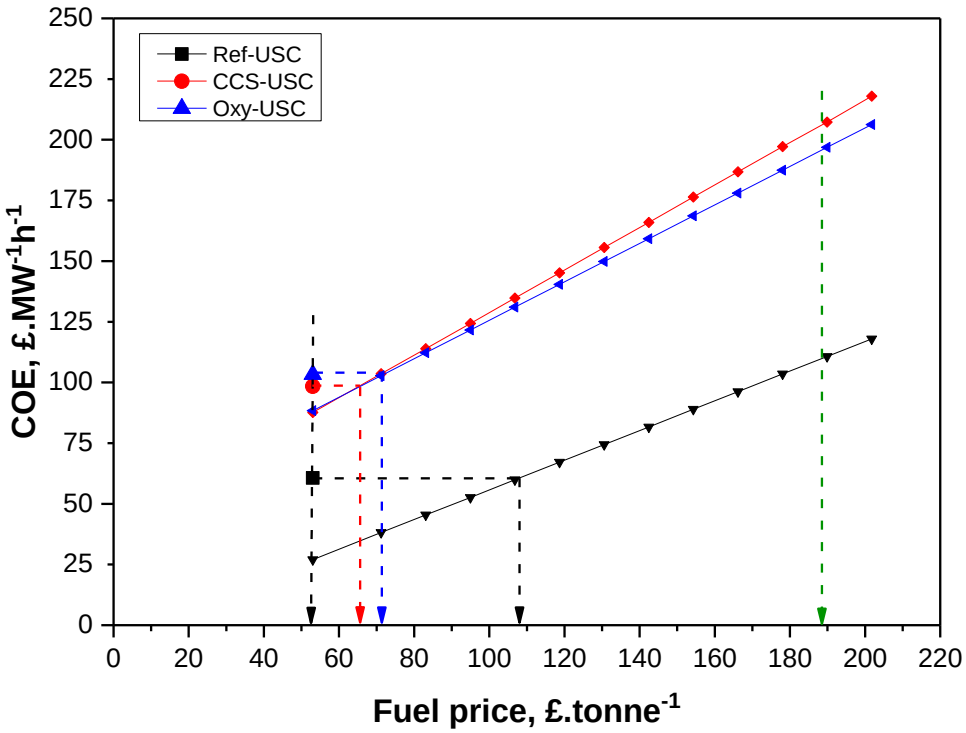

Figure 7.14 Breakeven WWP prices to facilitate BECCS deployment at coal power generation plants.

7.16.10.2 Coal Cost Variability

A second scenario could booster the viability of BECCS in the near future and that is the potential increase in coal prices. As mentioned in Section 7.14.2, the projected coal prices for the next 15 years fall into three scenarios, low, central and high. Those projections are reflected on the *COE* variance with the WWP prices to predict the breakeven price of the fuel as shown in Fig. 7.15. The vertical long dash-dot lines in

Fig. 7.15 represent the low, central and high projected prices of coal in 2030. The horizontal dashed lines represent the breakeven price of WWP in the case of the Reference plant without CCS. The low coal price scenario is discussed in the previous section. At the central and high price scenarios, the breakeven WWP price is 120 £ tonne^{-1} and 130 £ tonne^{-1} respectively, that is higher by £47 and £32 than the coal prices. The results of Fig. 7.15 are listed in Table 7.11.

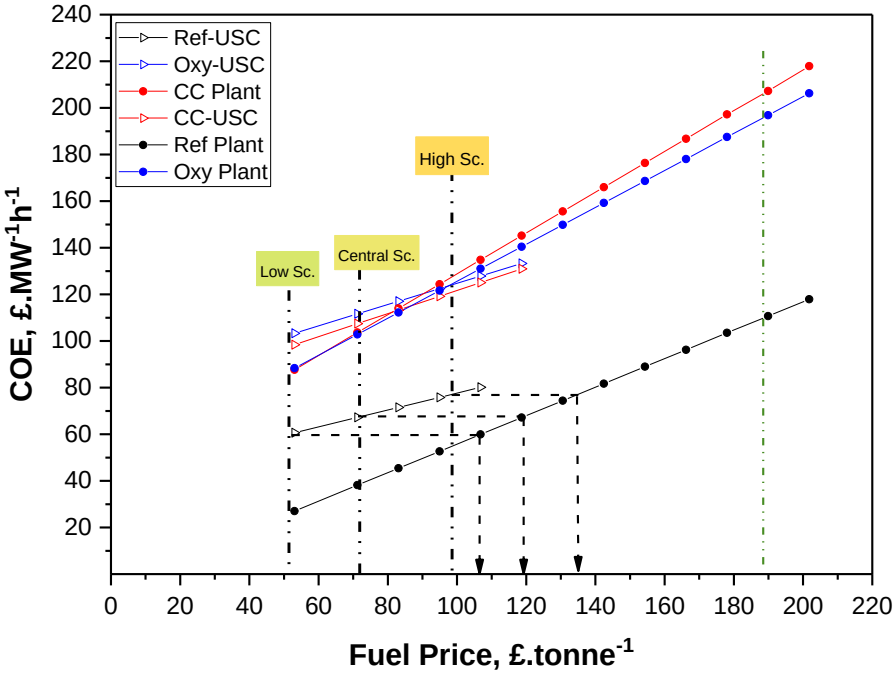

Figure 7.15 Breakeven WWP prices at low, central and high coal prices scenarios in 2030 at power generation plants.

The application of CCS technologies on coal and biomass reduces the gap between the two fuel prices at the breakeven point, especially at the high price scenario in which the fuel prices at the oxy plants will have the same value at £98, while the amine plant will have a breakeven WWP price at £85. In the central scenario, the breakeven price is 85 £ tonne^{-1} and 78 £.tonne^{-1} for oxy and CCS plants, respectively.

Table 7.11 Breakeven prices of WWP in response to different scenarios of projected coal prices.

	Low Scenario Coal price =55.2 £ tonne^{-1}			Central Scenario Coal price =73 £ tonne^{-1}			High Scenario Coal price =98.5 £ tonne^{-1}		
	Ref.	**CC**	**Oxy**	**Ref.**	**CC**	**Oxy**	**Ref.**	**CC**	**Oxy**
Breakeven WWP price	108	65	69	120	78	85	130	85	98

7.16.10.3 Effect of Renewable Obligation Credit (ROC) on *COE*

The Renewable Obligation Credit (ROC) is the main current financial support scheme for renewable electricity in the UK [16]. The current value of ROC is equal to 42.02 £ $MW^{-1}h^{-1}$ for electricity generation [228] burning 100% biomass.

In this section, the effect of multiplying the ROC by 1, 2, and 3 times on the *COE* is examined. From Fig. 7.16 it can be shown that deploying biomass (WWP) in power plants without CCS can only compete with the conventional coal power plants when the ROC subsidy is multiplied 3.7 times the current value to become 155.5 £.$MW^{-1}h^{-1}$. In comparison with the coal-CCS plants, the dedicated biomass competes the *COE* of coal with a lower subsidy that is 2.7 and 1.8 ROC for the amine and oxy-coal plants respectively. On the other hand, the WWP-CCS plants with the current fuel price are extremely far from the competition with the coal prices even with 4 times ROC value.

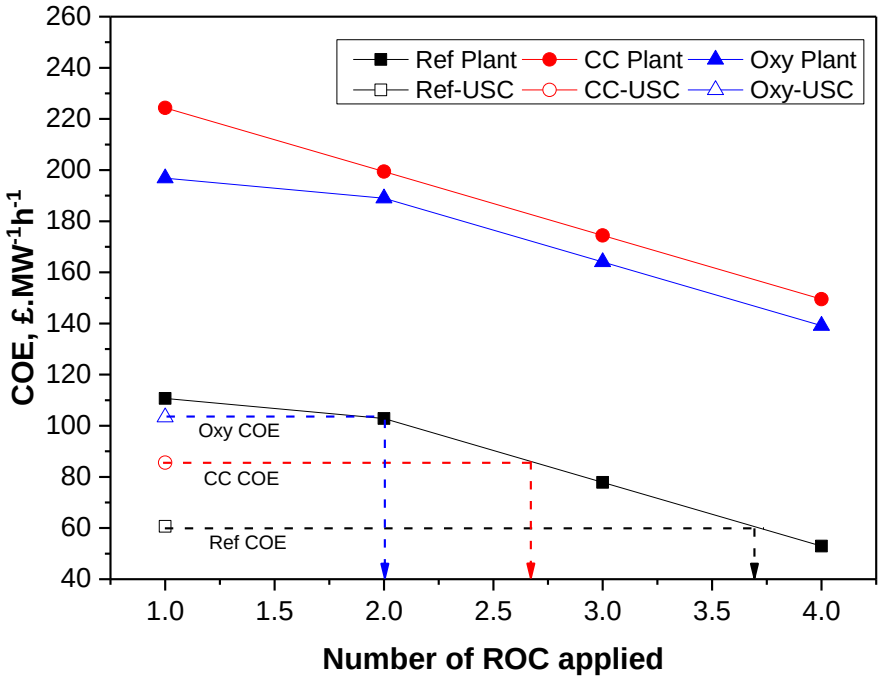

Figure 7.16 Effect of ROC value on the Breakeven WWP price with coal at power generation plants.

7.16.10.4 Effect of Carbon Price on *COE*

Currently, the UK government has set a fixed limit of carbon price on power generation from coal combustion plants as 9.55 £ tCO_2e^{-1} [228]. However, increasing the carbon tax will drive the power companies to deploy renewable alternatives such as wood pellets. In this scenario, the sensitivity of *COE* with carbon tax is examined assuming an increase in the carbon tax from the current value to 2, 3, 4, 5,…10 times increases.

Figure 7.17 shows the plant levelized *COE* as a function of the carbon price units added to the coal plant taxes per one MWh produced. The resulting carbon breakeven price is 6.65 times the current value that is approximately 64 £ $MW^{-1}h^{-1}$. However, the increase of *COE* with carbon price will tend to increase the electricity bills for the consumers, and that makes this scenario likely to be undesirable at present. Rhodes [15] has reached to a £10 higher breakeven carbon price (123 $ $tonne^{-1}$ CO_2 i.e. 73 £ $tonne^{-1}$ CO_2), and this is due to the different biomass fuel used and the fuel prices at that time.

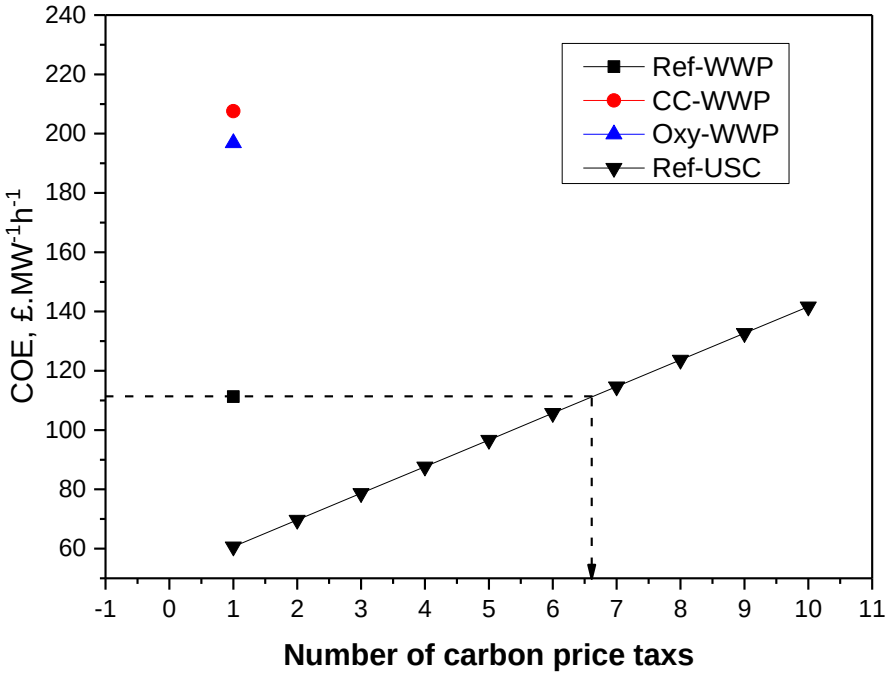

Figure 7.17 Breakeven number of carbon price tax of coal power generation plants in respect to the *COE* of WWP power plants.

On the other hand, if the carbon price is used as a reward to the negative carbon emissions of the BECCS, it will become an important incentive for the commercialization of the BECCS. Therefore, the negative emissions calculated in this study are costed with the same price of carbon emissions and deducted from the annual costs, as a showcase of increasing CO_2 price can result in a reasonable breakeven *COE* between CC-USC plants and the BECCS plants. Figure 7.18 shows the impact of the Negative Emissions Incentive on the breakeven COE of Oxy-WWP and CC-WWP with both CC-USC and Oxy-USC values of COE 65 £ $MW^{-1}h^{-1}$ and 121 £ $MW^{-1}h^{-1}$, for a 72 £ $tonne^{-1}$, and 124 £ $tonne^{-1}$ CO_2 captured prices respectively. Obviously, the Oxy-WWP plant needs much lower incentives to compete with the Oxy-Coal plant.

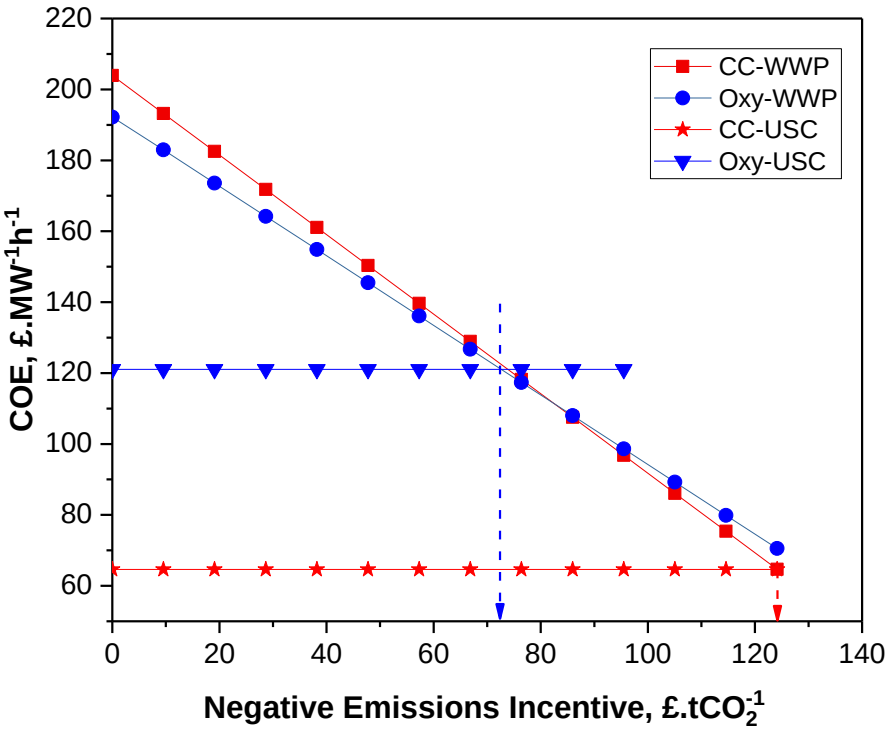

Figure 7.18 Sensitivity of *COE* of BECCS and Oxy-USC and CC-USC plants to the negative emissions incentive of BECCS.

7.17 Summary of Findings

The results of the techno-economic analysis that was performed on the wood pellets power plant in comparison to coal, are summarised as follows:

i. The utilization of white wood pellets WWP in electricity generation without CCS can annually eliminate about 4.6 tonnes CO_2 per each MW of power produced in a large scale power plant. However, the plant efficiency is reduced from 39.5% to 37.5% if substituting the coal with wood pellets. And, the *COE* is increased by 150%, although the capital cost does not witness a significant rise when moving from coal to wood pellets.

ii. The application of CCS technology had a higher negative effect on the wood pellets plant efficiency than the oxy-fuel technology. The CCS reduced the plant efficiency of wood pellets by 30% of the reference plant efficiency versus 20% reduced by the oxy-fuel. Whereas both CC technologies reduced the coal plant efficiency by 20%.

iii. Also, there was a rapid rise in the capital cost and the *COE* of the wood pellets and coal plants with the use of CCS and oxy-fuel technologies. The capital costs of the four reference plants have increased by equivalent 55% and 70% with the use of CCS and oxy-fuel, respectively. However, the effect of the CCS technology on the *COE* was different between wood pellets and the coal. The increase in the *COE* of wood pellets plant was 87%, whereas the corresponding increase in the coal plants was 40%. On the other hand, the oxy-fuel technology equally increased the *COE* of wood pellets and coal plants by about 70%.

iv. Co-firing WWP with coal is best to occur at low blending levels as the plant efficiency and the *COE* are trivially affected by the 25% biomass blending. Higher blending ratios would dramatically increase the *COE* and total annual levelized cost.

v. When the CCS technologies are applied, similar results were obtained. However, the comparison between the two CCS technologies showed that at low co-firing ratios (less than 50% WWP) the *COE* and *TLAC* of Amine plant was lower than their values in the oxy-fuel plants, while at blending higher than 50% WWP, the Amine plant showed a higher *COE* and *TLAC* than the oxy plant.

vi. Knowing that the predictions of WWP prices at 2020-2030 assumes an increase in the imported fuel price up to 200 £ $tonne^{-1}$ [267], there will be a continuous challenge to the BECCS deployment unless new global sources with lower prices can be approached.

vii. The critical price range of WWP that booster the BECCS deployment is 70-100 £ $tonne^{-1}$. In the three plant cases, the oxy-WWP plant has higher breakeven price, and that translates more economic viability of the oxy-biomass than the amine capture technology.

viii. The deployment of biomass (WWP) in power plants without CCS can only compete the conventional coal power plants when the ROC subsidy is multiplied by 3.7 times the current value. While utilizing the CC technologies with coal-fired plants, reduced the ROC required for WWP to compete with coal to 2.7 and 1.8 ROC for the Amine and Oxy-coal plants respectively.

ix. Equally, the increase of carbon price is another method to booster the BECCS. Hence, the current carbon price (9.55 £ tCO_{2e}^{-1}) should be increased. The carbon breakeven price is calculated as 6.7 times the current value that is approximately 64 £ MWh^{-1}.

x. The current cost assessment methods of cost of CO_2 avoided and cost of CO_2 captured do not take into consideration the net values of carbon emissions that is theoretically equal to zero for biomass fuels. Therefore, the author suggests a new concept of “Cost of Negative Emissions” for the biomass fuels.

Chapter 8 Conclusions & Recommendations

This experimental research study makes a noteworthy contribution to the literature by generating new data on the 100% conversion of white wood pellets in the power generation industry. Moreover, the study provides new insights into the actual problems faced by the power generation companies during burning the biomass, such as burn out efficiency, combustion efficiency, and NO_x emissions in comparison to coal.

8.1 Literature Review

The literature review has shown that there is a technical potential in using biomass as a part of the solution to the energy generation demand due to its environmental preferences on th e conventional solid fuels. Also, sufficient data on biomass characterization is available to identify the methods with which the characterization investigation can be conducted in this study. However, there are relatively few historical studies on the topic of biomass char combustion, the intrinsic reactivity of biomass char in comparison to coal and the ash behaviour during combustion. Thus, in this study, the main research focus is the investigation of biomass (particularly wood pellets) combustion behaviour of the particle and the pulverized fuel pilot combustion scales. In comparison to coal, these aspects and the techno-economic feasibility of white wood pellets as a fuel for combustion are evaluated.

8.2 Biomass Characterization

A full characterization analysis has been performed on white wood pellets (USWWP) that are imported from the USA. The aim of this characterization was to quantify the design and modelling properties of the biomass oxy-fuel combustion experiments. The testing procedures were mainly performed according to the British Standard methods of solid biofuel characterization. All the procedures were repeated 2-3 times at a minimum.

8.2.1 Conclusions

The findings of the current analysis have shown that:

I. The particle size distribution of both wood pellets and coal is bimodal, however, with different size categories. This mode of distribution may have an influence on the combustion mechanism and the slag deposition and aerosols formation in the fly ash.

II. The higher ash content in the coal suggests that the ash deposition problems with the coal combustion are expected to be greater than the case of the biomass combustion.

III. The chemical compositional analysis showed that wood pellets have higher alkali and earth alkaline minerals, and higher chlorine content than coal. Whereas the coal has silica, alumina, iron, titanium, and sulphur content higher than the wood pellets. This alteration in the mineral composition is reflected on the slagging and fouling tendencies predicted by the deposition indices. Wood pellets have a lower tendency for the radiation zone slagging than coal, never-the-less have higher fouling tendency in the convective passes.

IV. Overall, the slagging and fouling indices that are used to predict the deposition tendencies of the coal were not successful on biomass. New indices specifically used for biomass, were better in the prediction of the ash deposition when correlated to the experimental growth index of deposition.

8.2.2 Recommendations

I. It is recommended that further investigation on the wood pellets mineral composition be conducted on the fuel itself rather than its ash. Using wet chemical analysis or other analytical methods than XRF can produce more reliable data on the low content elements such as the chlorine, sulphur, and trace elements.

II. Further experimental investigations are needed on the fouling and slagging tendencies of the biomass ash to develop new deposition indices that can give a better prediction of the biomass deposition propensity.

8.3 Fundamentals of the Solid Particle Combustion

The pyrolysis behaviour and the char combustion kinetics of the USWWP, CAWWP, ELC and VC were experimentally investigated in Chapter Five of this thesis. For the pyrolysis, different global reaction models were used to predict the Arrhenius kinetic parameters, and for the char reactivity the intrinsic kinetic parameters were determined.

8.3.1 Conclusions

The results of this part of the thesis have shown that:

I. A noteworthy finding in this study is that the biomass can release 90% of its volatile matter at a temperature of about 773 K. Whereas, the coal releases less than 38-66% of its volatile matter at this temperature, thus the coal needs higher temperatures than 1273 K for complete devolatilization and this depends on the coal rank.

II. The results of this study support the notion that the higher oxygen content of the biomass promotes early crosslinking during pyrolysis thus resulting in a higher porosity and surface area of the char produced. Equally, the high mineral content of the VC promotes the catalytic effect during the char combustion, therefore leading to a higher char reactivity.

III. The Integral Isoconversional method with a global power reaction scheme was successful in predicting the pyrolysis kinetics of the USWWP, CAWWP and the ELC. Conversely, the devolatilization of the high ash content coal (VC) was better predicted by the 3D-diffusional reaction model than the power model and this indicates the effect of the mineral matter on the release of the volatiles even at low temperatures.

IV. Although the char burn-off rate of the biomass was higher than that of the coal, both types of fuel have shown similar intrinsic reactivity in combustion Zone I. This proves the independence of intrinsic reactivity on the fuel type and rank. Conversely, in combustion Zone II (at a temperature of 1273 K), the intrinsic biomass char combustion reactivity was 2-3 times higher than that of the coal char due to the highly porous char structure produced at higher temperatures. Both biomass and coal chars exhibited an intermediate combustion zone between 973 K and 1173 K. It is the first time in the literature that it has been reported the char intrinsic kinetic parameters of the Vietnamese coal.

V. The TGA procedure of a sequential two-step method is found to satisfactorily produce a char with an intrinsic reactivity and activation energy being consistent with the published data on chars produced under transport phenomena conditions.

8.3.2 Recommendations

I. A limitation of this study is that the assumptions of the spherical shape and the pore model of the coal char were applied on the biomass particles to predict the actual kinetic parameters knowing that biomass particles are fibrous and have a longitudinal shape. Thus, it is recommended that further work be carried out to determine a better pore structure model, and determine the particle shape factor of the biomass for better prediction of the char reactivity.

II. Further investigations can be performed on the effect of the oxygen pressure on the intrinsic reaction order, particularly of the biomass char combustion.

III. A further analysis of the gaseous products from the TGA experiments can improve the understanding of the complexity of the biomass pyrolysis and char combustion mechanisms.

8.4 Pilot Scale Experimental Work

Part of this thesis is to determine the differences in the ash behavior during the pilot scale combustion between biomass and coal. The results obtained were presented and discussed in Chapter Six.

8.4.1 Conclusions

The following conclusions can be drawn from the findings in Chapter Six:

I. The variation of the mode of particle size distribution between the wood pellets and the coal has been reflected on the partitioning pattern of the fuel ash elements, and ultimately could affect the deposition tendencies and the aerosols formation in the fly ash streams.

II. It is possible that the oxy-fuel combustion inhibits the release of volatile elements to the gas phase in the initial stages of the combustion, thus reducing the alkali sulphates slagging, increasing however, the alkali sulphate fouling

tendencies on the convective passes. On the other hand, higher alkali chlorides are expected to be found on the furnace walls and bottom, whereas, less chlorine is released to the fly ash, thus indicating lower propensity of high-temperature corrosion problems on the heat exchanger surfaces.

III. The effect of the oxy-fuel environment on the ash formation is less significant on the coal than its effect on the wood pellets. The oxy-fuel environment had slightly reduced the combustion efficiency of the USWWP, and improved the ELC combustion efficiency from the air-fuel cases. However, these effects were insignificant compared to the overall efficiency.

IV. Although the pore structure of the TGA chars of both fuels did not completely represent the actual pore system that has been observed in the pulverized combustion char particles, it did reflect the differences in the char properties and the char combustion kinetics that were found in Chapter Five. Thus, the results of the kinetic parameters can be used for qualitative and quantitative comparison between different fuel reactivities.

8.4.2 Recommendations

I. Although this study was performed on a pilot scale, the findings are noteworthy to be further investigated on a larger scale of the pulverized fuel combustion. Being limited to the ash analysis data; this study lacks the supporting evidence of the observed findings and concluded results. Compiling the ash results with the other experimental data can add insight to the overall biomass behaviour in the pulverized combustion.

II. Further research could usefully explore the actual deposition occurrence of the wood pellets, in different combustion environments. In addition, using the current data with a chemical equilibrium modelling program such as FactSage could also validate the results.

III. Another possible topic of future research would be to investigate more biomass fuels with oxy-fuel combustion to conclude general behaviour for biomass. Also, the influence of different oxidant mixtures on the ash formation and combustion behaviour can be further explored.

8.5 Techno-economic Study

In chapter Seven, an investigation of the techno-economic performance of white wood pellets as the biomass fuel for combustion power plants both with and without CCS, versus three types of imported coal to the UK; Colombian, Russian, and US coal fuels, was performed to assess the viability of the BECCS technology with the current market prices and any projected fuel prices in the next 15 years.

8.5.1 Conclusions

The following observations were concluded:

I. To produce carbon-neutral electricity, WWP is one of the proposed options. However, for sustainable biomass supply chain and sustainable forest carbon sink, the use of sawdust, industrial waste wood, pulp waste liquor, and forest residues as biomass sources for wood pellets in the bioenergy sector is the optimum choice for the short term use of BECCS. Further, there is a need for a global consensus on biomass supply chain to be developed. Governments need to agree on international forest management plans and land-use policies, to adopt more BECCS projects as one of the few solutions to carbon emissions.

II. The utilization of white wood pellets in electricity generation without CCS can annually eliminate about 3M tonnes CO_2 from a 650 MW plant. However, the *COE* is rather higher by about 150%. In other words, the cost of CO_2 abatement by this method is very high at the present and more advanced and cost-effective mitigation technologies are necessary to search for in the near future.

III. The application of CCS technologies with coal-fired power plants is necessary to meet the regulatory emission factors applied in the UK. Meanwhile, using biomass with CCS can produce negative-emissions of CO_2. The BECCS using white wood pellets with oxy-fuel technology has more economic potential to compete the oxy-coal plants than the post-combustion CCS technology.

IV. Knowing that the predictions of WWP prices at 2020-2030 assumes an increase in the imported fuel price up to 200 £ $tonne^{-1}$ [267], there will be a continuous challenge to the BECCS deployment unless new global sources of biomass with lower prices can be approached.

V. The ROC has a more positive impact than the carbon price on the *COE* from the point of customers view without adding more burdens on the power

generation companies, and this conclusion is in agreement with the conclusion of McIlveen-Wright et al. [252].

VI. A general conclusion from the above is that BECCS using white wood pellets is more efficient and more cost-effective with the oxy-fuel technology than the post-combustion technology.

8.5.2 Recommendations

I. More research studies on the carbon life cycle and the sequestering capacity of the forests on a long term in comparison to use as a fuel are needed.

II. The deployment of BECCS on a large scale requires more incentives from the government, such as the ROC, the CP, and a new incentive that this study suggests; the Negative Emission Incentive (NEI).

III. The author suggests for the cost of carbon capture to be considered as the cost of negative emissions in the case of biomass fuels. Further mathematical development and cost parameters analysis is recommended for biomass fuel correction.

IV. For the electricity generation from co-firing systems, the amine post capture technology is recommended for low blending levels, while the oxy-fuel process is recommended for higher blending than 50% WWP.

References

1. Vassilev, S.V., et al., *An overview of the chemical composition of biomass.* Fuel, 2010. **89**(5): p. 913-933.

2. Jenkins, B.M., et al., *Combustion properties of biomass.* Fuel Processing Technology, 1998. **54**(1-3): p. 17-46.

3. Ragland, K.W., D.J. Aerts, and A.J. Baker, *Properties of Wood for Combustion Analysis.* Bioresource Technology, 1991. **37**(2): p. 161-168.

4. Demirbas, A., *Combustion characteristics of different biomass fuels.* Progress in Energy and Combustion Science, 2004. **30**(2): p. 219-230.

5. Bruckner, T., Bashmakov, I.A., and Mulugetta, Y., *Climate Change Report IPCC WGIII, 5th Assessment Report :Climate Change 2014*. 2014: Berlin, Germany. p. 1-137.

6. EBTP, *Zero Emissions Platform Report: Biomass with CO2 Capture and Storage (Bio-CCS).* 2012: p. 4-29.

7. IEA, *Technology Roadmap Bioenergy for Heat and Power Report.* 2012.

8. IEA, *Tracking Clean Energy Progress 2013,* IEA Input to the Clean Energy Ministerial, 2013.

9. Sjostrom, E., *Wood Chemistry. Fundamentals and Applications.* Second Edition ed. 1993, San Diego: Academic press.

10. Glassman, I.Y., R. A., *Combustion*. 4th ed. Combustion. Vol. Chapter 2. 2008, London, UK: Elsevier Academic Press. 34.

11. White, J.E., W.J. Catallo, and B.L. Legendre, *Biomass pyrolysis kinetics: A comparative critical review with relevant agricultural residue case studies.* Journal of Analytical and Applied Pyrolysis, 2011. **91**(1): p. 1-33.

12. Carpenter, D., et al., *Biomass feedstocks for renewable fuel production: a review of the impacts of feedstock and pretreatment on the yield and product distribution of fast pyrolysis bio-oils and vapors.* Green Chemistry, 2014. **16**(2): p. 384-406.

13. Teixeira, G., et al., *Gasification of char from wood pellets and from wood chips: Textural properties and thermochemical conversion along a continuous fixed bed.* Fuel, 2012. **102**: p. 514-524.

14. Vamvuka, D., et al., *Gasification of Waste Biomass Chars by Carbon Dioxide Via Thermogravimetry-Effect of Catalysts.* Combustion Science and Technology, 2012. **184**(1): p. 64-77.

15. Rhodes, J.S. and D.W. Keith, *Engineering economic analysis of biomass IGCC with carbon capture and storage.* Biomass & Bioenergy, 2005. **29**(6): p. 440-450.

16. Ofgem, *Annual Sustainability Report 2011-2012.* 2013.

17. Edge, P.J., et al., *A reduced order full plant model for oxyfuel combustion.* Fuel, 2012. **101**: p. 234-243.

18. Black, S., et al., *Effects of firing coal and biomass under oxy-fuel conditions in a power plant boiler using CFD modelling.* Fuel, 2013. **113**: p. 780-786.

19. Alvarez, L., et al., *Biomass co-firing under oxy-fuel conditions: A computational fluid dynamics modelling study and experimental validation.* Fuel Processing Technology, 2014. **120**: p. 22-33.

20. Nimmo, W., Daood, S.S., and Gibbs, B.M., *The effect of O2 enrichment on NOx formation in biomass co-fired pulverised coal combustion.* Fuel, 2010. **89**: p. 2945-2952.

21. Smart, J.P., R. Patel, and G.S. Riley, *Oxy-fuel combustion of coal and biomass, the effect on radiative and convective heat transfer and burnout.* Combustion and Flame, 2010. **157**(12): p. 2230-2240.

22. Badour, C., et al., *Combustion and air emissions from co-firing a wood biomass, a Canadian peat and a Canadian lignite coal in a bubbling fluidised bed combustor.* Canadian Journal of Chemical Engineering, 2012. **90**(5): p. 1170-1177.

23. Diaz-Ramirez, M., et al., *Influencing factors on NOX emission level during grate conversion of three pelletized energy crops.* Applied Energy, 2014. **115**: p. 360-373.

24. Alanne, K., et al., *Analysis of a wooden pellet-fueled domestic thermoelectric cogeneration system.* Applied Thermal Engineering, 2014. **63**(1): p. 1-10.

25. Pickard, S., et al., *Bio-CCS: Co-firing of established greenfield and novel, brownfield biomass resources under air, oxygen-enriched air and oxy-fuel conditions.* Ghgt-11, 2013. **37**: p. 6062-6069.

26. Jones, J.M., *Combustion properties of torrefied willow compared with bituminous coals.* Fuel Processing Technology, 2012. **101**: p. 9.

27. Ndibe, C., J. Maier, and G. Scheffknecht, *Combustion, cofiring and emissions characteristics of torrefied biomass in a drop tube reactor.* Biomass & Bioenergy, 2015. **79**: p. 105-115.

28. Klemm, D., Heublein, B., Fink, H-P. and Bohn, A., *Cellulose: Fascinating Biopolymer and Sustainable Raw Material.* Angew. Chem. Int. Ed., 2005. **44**: p. 35.

29. Nishiyama, Y., P. Langan, and H. Chanzy, *Crystal structure and hydrogen-bonding system in cellulose 1 beta from synchrotron X-ray and neutron fiber diffraction.* Journal of the American Chemical Society, 2002. **124**(31): p. 9074-9082.

30. Scheller, H.V.a.U., P., *Hemicelluloses.* Annual REview of Plant Biology, 2010. **61**: p. 26.

31. Yaser AZ, C.T., Hairul MA, Shazwan AS, *Current Review on the Coagulation/Flocculation of Lignin Containing Wastewater.* Int J Waste Resources 2014. **4**(153).

32. BSI, *Solid biofuels - Fuel specifications and classes, BS ENISO 17225*, in *Specification of graded wood pellets*. 2012, BSI Group Headquarters: London, UK. p. 7.

33. Fitzpatrick, E.M., et al., *The mechanism of the formation of soot and other pollutants during the co-firing of coal and pine wood in a fixed bed combustor.* Fuel, 2009. **88**(12): p. 2409-2417.

34. Swithenbank, J., et al., *Wood would burn.* Biomass & Bioenergy, 2011. **35**(3): p. 999-1007.

35. Vamvuka, D. and D. Zografos, *Predicting the behaviour of ash from agricultural wastes during combustion.* Fuel, 2004. **83**(14-15): p. 2051-2057.

36. Munir, S., W. Nimmo, and B.M. Gibbs, *The effect of air staged, co-combustion of pulverised coal and biomass blends on NO(x) emissions and combustion efficiency.* Fuel, 2011. **90**(1): p. 126-135.

37. Vassilev, S.V. and C.G. Vassileva, *A new approach for the combined chemical and mineral classification of the inorganic matter in coal. 1. Chemical and mineral classification systems.* Fuel, 2009. **88**(2): p. 235-245.

38. Dai, J.J. and J.R. Grace, *Biomass granular screw feeding: An experimental investigation.* Biomass & Bioenergy, 2011. **35**(2): p. 942-955.

39. Mermoud, F., et al., *Experimental and numerical study of steam gasification of a single charcoal particle.* Combustion and Flame, 2006. **145**(1-2): p. 59-79.

40. Lu, H., et al., *Comprehensive study of Biomass particle combustion.* Energy & Fuels, 2008. **22**(4): p. 2826-2839.

41. Evans, D.G.H., J. A., *The porosity of brown-coal char.* Fuel Processing Technology, 1970. **49**(2): p. 110-118.

42. Linge, H.G., *The surface area of coal particles.* Fuel Processing Technology, 1989. **68**(1): p. 111-113.

43. Orlanders, B.a.S., BM., *Characterization of Ashes from Wood and Straw.* Biomass and Bioenergy, 1995. **8**(2): p. 105-115.

44. Gubba, S.R., et al., *Numerical modelling of the co-firing of pulverised coal and straw in a 300 MWe tangentially fired boiler.* Fuel Processing Technology, 2012. **104**: p. 181-188.

45. Lu, H., et al., *Effects of particle shape and size on devolatilization of biomass particle.* Fuel, 2010. **89**(5): p. 1156-1168.

46. Li, J., et al., *Flame characteristics of pulverized torrefied-biomass combusted with high-temperature air.* Combustion and Flame, 2013. **160**(11): p. 2585-2594.

47. Etiegni, L. and A.G. Campbell, *Physical and Chemical Characteristics of Wood Ash.* Bioresource Technology, 1991. **37**(2): p. 173-178.

48. Misra, M.K., K.W. Ragland, and A.J. Baker, *Wood Ash Composition as a Function of Furnace Temperature.* Biomass & Bioenergy, 1993. **4**(2): p. 103-116.

49. Ragland, K.W., et al., *ASH DEPOSITION IN A WOOD-FIRED GAS-TURBINE.* Journal of Engineering for Gas Turbines and Power-Transactions of the Asme, 1995. **117**(3): p. 509-512.

50. Miles, T.R., et al., *Boiler deposits from firing biomass fuels.* Biomass & Bioenergy, 1996. **10**(2-3): p. 125-138.

51. Vamvuka, D., D. Zografos, and G. Alevizos, *Control methods for mitigating biomass ash-related problems in fluidized beds.* Bioresource Technology, 2008. **99**(9): p. 3534-3544.

52. Vassilev, S.V., et al., *An overview of the composition and application of biomass ash. Part 1. Phase-mineral and chemical composition and classification.* Fuel, 2013. **105**: p. 40-76.

53. Demirbas, A., *Calculation of higher heating values of biomass fuels.* Fuel, 1997. **76**(5): p. 431-434.

54. Channiwala, S.A. and P.P. Parikh, *A unified correlation for estimating HHV of solid, liquid and gaseous fuels.* Fuel, 2002. **81**(8): p. 1051-1063.

55. KOPPEJAN, S.J.V.L.J., *The Handbook Of Biomass Combustion & Cofiring*. 2008, UK: Earthscan.

56. Musinguzi, W.B., et al., *Thermal characterization of Uganda's Acacia hockii, Combretum molle, Eucalyptus grandis and Terminalia glaucescens for gasification.* Biomass & Bioenergy, 2012. **46**: p. 402-408.

57. Center, B.E., *Typical Calorific Values of Fuel.* http://www.biomassenergycentre.org.uk/portal/page?_pageid=75,20041&_dad=portal&_schema=PORTAL.

58. Haykiri-Acma, H., *Combustion characteristics of different biomass materials.* Energy Conversion and Management, 2003. **44**(1): p. 155-162.

59. Hallgren, A.L., K. Engvall, and B.J. Skrifvars, *Ash-induced operational difficulties in fluidised bed firing of biofuels and waste.* Biomass: A Growth Opportunity in Green Energy and Value-Added Products, Vols 1 and 2, 1999: p. 1365-1370.

60. Wei, X.L., U. Schnell, and K.R.G. Hein, *Behaviour of gaseous chlorine and alkali metals during biomass thermal utilisation.* Fuel, 2005. **84**(7-8): p. 841-848.

61. Gaur, S.a.R., T.T., *Thermal data for natural and synthetic fuels*. 1998, New York: Marcel Dekker.

62. Kitani, O.a.H., C.W., *Biomass Handbook*. 1989, New York: Gordon and Breach Science Publishers.

63. Clasification, E.-P. *Wood pellets, fir (#3257)*. 2009.

64. U.S. Geological Survey Open File Report 2006-1241: Susan J. Tewalt, R.B.F., Ivette E. Torres, and Fiorella Simoni, *World Coal Quality Inventory.* 2006: p. 132-157.

65. Mellon, U.o.C. *Integrated Environmental Control Model (IECM 8.0.2)*. Available at http://www.cmu.edu/epp/iecm/download_8.0.2.html 2012.

66. Classification, E.P., *Wood pellets white (#3075)* https://www.ecn.nl/phyllis2/Browse/Standard/ECN-Phyllis#wood pellets, 2006.

67. Francescato, V., Antonini, W., *Wood Fuels Handbook.* Publications of the Italian Agriforestry Energy Association, 2008.

68. Di Blasi, C., F. Buonanno, and C. Branca, *Reactivities of some biomass chars in air.* Carbon, 1999. **37**(8): p. 1227-1238.

69. Smith, I.W., *The Combustion Rates of Coal Chars: A Review*, in *Nineteenth International Symposium on Combustion*. 1982, The Combustion Institute. p. 1045-1065.

70. Ghetti, P., L. Ricca, and L. Angelini, *Thermal analysis of biomass and corresponding pyrolysis products.* Fuel, 1996. **75**(5): p. 565-573.

71. Conesa, J.A., et al., *Analysis of Different Kinetic-Models in the Dynamic Pyrolysis of Cellulose.* Thermochimica Acta, 1995. **254**: p. 175-192.

72. Bennadji, H., et al., *Effect of Particle Size on Low-Temperature Pyrolysis of Woody Biomass.* Energy & Fuels, 2014. **28**(12): p. 7527-7537.

73. Munir, S., et al., *Thermal analysis and devolatilization kinetics of cotton stalk, sugar cane bagasse and shea meal under nitrogen and air atmospheres.* Bioresource Technology, 2009. **100**(3): p. 1413-1418.

74. Findorak, R., et al., *Thermal degradation and kinetic study of sawdusts and walnut shells via thermal analysis.* Journal of Thermal Analysis and Calorimetry, 2016. **125**(2): p. 689-694.

75. Samuelsson, L.N., et al., *Pyrolysis of kraft pulp and black liquor precipitates derived from spruce: Thermal and kinetic analysis.* Fuel Processing Technology, 2016. **149**: p. 275-284.

76. Trommer, D. and A. Steinfeld, *Kinetic modeling for the combined pyrolysis and steam gasification of petroleum coke and experimental determination of the rate constants by dynamic thermogravimetry in the 500-1520 K range.* Energy & Fuels, 2006. **20**(3): p. 1250-1258.

77. Anthony, D.B. and J.B. Howard, *Coal Devolatilization and Hydrogasification.* Aiche Journal, 1976. **22**(4): p. 625-656.

78. Solomon, P.R. and D.G. Hamblen, *Finding Order in Coal Pyrolysis Kinetics.* Progress in Energy and Combustion Science, 1983. **9**(4): p. 323-361.

79. Anthony, D.B., et al., *Rapid Devolatilization and Hydrogasification of Bituminous Coal.* Abstracts of Papers of the American Chemical Society, 1975. **170**(Aug24): p. 31-31.

80. Braun, R.L. and A.K. Burnham, *Analysis of Chemical-Reaction Kinetics Using a Distribution of Activation-Energies and Simpler Models.* Energy & Fuels, 1987. **1**(2): p. 153-161.

81. Agrawal, R.K., *Kinetics of Reactions Involved in Pyrolysis of Cellulose .2. The Modified Kilzer-Broido Model.* Canadian Journal of Chemical Engineering, 1988. **66**(3): p. 413-418.

82. Kilzer, F.J. and A. Broido, *Speculations on Nature of Cellulose Pyrolysis.* Pyrodynamic, 1965. **2**(2-3): p. 151-&.

83. Diebold, J.P., *A Unified, Global-Model for the Pyrolysis of Cellulose.* Biomass & Bioenergy, 1994. **7**(1-6): p. 75-85.

84. Manya, J.J., E. Velo, and L. Puigjaner, *Kinetics of biomass pyrolysis: A reformulated three-parallel-reactions model.* Industrial & Engineering Chemistry Research, 2003. **42**(3): p. 434-441.

85. Branca, C., A. Albano, and C. Di Blasi, *Critical evaluation of global mechanisms of wood devolatilization.* Thermochimica Acta, 2005. **429**(2): p. 133-141.

86. Martin-Lara, M.A., et al., *Kinetic study of the pyrolysis of pine cone shell through non-isothermal thermogravimetry: Effect of heavy metals incorporated by biosorption.* Renewable Energy, 2016. **96**: p. 613-624.

87. Rukthong, W., Thanatawee, P., Sunphorka, A., Piumsumboon, P., and Chalermsinsuwan, B., *Computation of Biomass Combustion Characteristic and Kinetic Parameters by Using Thermogravimetric Analysis.* Engineering Journal of Chulalongkorn University- Thiland, 2015. **19**(2): p. 16.

88. Knight, A.T. and G.D. Sergeant, *Reactivity of Australian Coal-Derived Chars to Carbon-Dioxide.* Fuel, 1982. **61**(2): p. 145-149.

89. Zhu, Q., et al., *The predictions of coal/char combustion rate using an artificial neural network approach.* Fuel, 1999. **78**(14): p. 1755-1762.

90. Laurendeau, N.M., *Heterogeneous Kinetics of Coal Char Gasification and Combustion.* Progress in Energy and Combustion Science, 1978. **4**(4): p. 221-270.

91. Hamor, R.J., I.W. Smith, and R.J. Tyler, *Kinetics of Combustion of a Pulverized Brown Coal Char between 630 and 2200 Degrees K.* Combustion and Flame, 1973. **21**(2): p. 153-162.

92. Khan, M.R. *Reactivity of low-Temperature Chars: Significance of char active surface area as a reactivity parameter*. in *6th Annual Gasification Contractors Meeting*. 1986. Morgantown, West Virginia.

93. Chan, M.L., et al., *The oxidative reactivity of coal chars in relation to their structure.* Fuel, 1999. **78**(13): p. 1539-1552.

94. Branca, C. and C. Di Blasi, *Combustion Kinetics of Secondary Biomass Chars in the Kinetic Regime.* Energy & Fuels, 2010. **24**: p. 5741-5750.

95. Nandi, S.P., V. Ramadass, and P.L. Walker, *Changes in the Ultrafine Structure of Anthracites Upon Heat Treatment.* Carbon, 1964. **2**(3): p. 199-210.

96. Razouk, R.I., F.Z. Saleeb, and A.M. Youssef, *Effect of Thermal Treatment on Surface Area of Coal.* Carbon, 1968. **6**(3): p. 325-&.

97. Hurt, R.H. and J.M. Calo, *Semi-global intrinsic kinetics for char combustion modeling.* Combustion and Flame, 2001. **125**(3): p. 1138-1149.

98. Cooney, J.D., M. Day, and D.M. Wiles, *Thermal-Degradation of Poly(Ethylene-Terephthalate) - a Kinetic-Analysis of Thermogravimetric Data.* Journal of Applied Polymer Science, 1983. **28**(9): p. 2887-2902.

99. Lizzio, A.A., A. Piotrowski, and L.R. Radovic, *Effect of Oxygen-Chemisorption on Char Gasification Reactivity Profiles Obtained by Thermogravimetric Analysis.* Fuel, 1988. **67**(12): p. 1691-1695.

100. Ashman, P.J., et al., *Interactions of gaseous NO with char during the low-temperature oxidation of coal chars.* Proceedings of the Combustion Institute, 2000. **28**: p. 2171-2179.

101. Haynes, B.S. and T.G. Newbury, *Oxyreactivity of carbon surface oxides.* Proceedings of the Combustion Institute, 2000. **28**: p. 2197-2203.

102. Liu, L., et al., *The isothermal studies of char-CO2 gasification using the high-pressure thermo-gravimetric method.* Journal of Thermal Analysis and Calorimetry, 2015. **120**(3): p. 1877-1882.

103. Niu, Z., Liu, G., Yin, H., Wu, D. and Zhou, C., *investigation of mechanism and kinetics of non-isothermal low temperature pyrolysis of prehydrous bituminous coal by in-situ FTIR.* Fuel, 2016. **172**: p. 1-10.

104. Khare, P., B.P. Baruah, and P.G. Rao, *Application of chemometrics to study the kinetics of coal pyrolysis: A novel approach.* Fuel, 2011. **90**(11): p. 3299-3305.

105. Yang, Y.B., et al., *Combustion of a single particle of biomass.* Energy & Fuels, 2008. **22**(1): p. 306-316.

106. Smith, I.W., *Intrinsic Reactivity of Carbons to Oxygen.* Fuel, 1978. **57**(7): p. 409-414.

107. Dupont, C., et al., *Kinetic modelling of steam gasification of various woody biomass chars: Influence of inorganic elements.* Bioresource Technology, 2011. **102**(20): p. 9743-9748.

108. Widell, H., *Industrial scale biomass combustion plants: engineering issues and operation*. 2013, Denmark: Aalborg Energie TEchnik (AET).

109. Nussbaumer, T., *Combustion and co-combustion of biomass: fundamentals, technologies, and primary measures for emission reduction.* Energy & Fuels, 2003. **17**(6): p. 1510-1521.

110. Bowman, C.T. *Control of combustion-generated nitrogen oxide emissions: Technology driven by regulation*. in *International Symposium on combustion*. 1992. Pittsburgh, PA: The Combustion Institute.

111. Dayton, D.C., et al., *Release of inorganic constituents from leached biomass during thermal conversion.* Energy & Fuels, 1999. **13**(4): p. 860-870.

112. Leckner, B. and M. Karlsson, *Gaseous Emissions from Circulating Fluidized-Bed Combustion of Wood.* Biomass & Bioenergy, 1993. **4**(5): p. 379-389.

113. Sommersacher, P., Brunner, T., Obernberger, I. , *Fuel indexes: a novel method for the evaluation of relevant combustion properties of new biomass fuels.* Energy Fuels 2012. **26**: p. 11.

114. Pronobis, M., *Evaluation of the influence of biomass co-combustion on boiler furnace slagging by means of fusibility correlations.* Biomass and Bioenergy, 2005. **28**: p. 8.

115. Gruber, T., R. Scharler, and I. Obernberger, *Application of an empirical model in CFD simulations to predict the local high temperature corrosion potential in biomass fired boilers.* Biomass & Bioenergy, 2015. **79**: p. 145-154.

116. Wiinikka, H., et al., *Influence of fuel ash composition on high temperature aerosol formation in fixed bed combustion of woody biomass pellets.* Fuel, 2007. **86**(1-2): p. 181-193.

117. Gudka, B., Jones, J.M., Lea-Langton, A.R., Williams, A., and Saddawi, A., *A review of the mitigation of deposition and emission problems during biomass combustion through washing pre-treatment.* Journal of the Energy Institute, 2015. **xxx**: p. 13.

118. Acharya, B., Dutta, A., Mahmud, S., Tushar, M., and Leon M., *Ash Analysis of Poultry Litter, Willow and Oats for Combustion in Boilers.* Journal of Biomass to Biofuel, 2014. **1**: p. 10.

119. Obeenberger, I., *Strategy for the Application of Novel Characterization Methods for Biomass Fuels: Case Study of Straw.* Energy & Fuels, 2014. **28**: p. 12.

120. Sommersacher, P., Brunner, T., Obernberger, I. Kienzl, N., and Kanzian, W., *Application of Novel and Advanced Fuel Characterization Tools for the Combustion Related Characterization of Different Wood/Kaolin and Straw/Kaolin Mixtures.* Energy & Fuels, 2013. **27**: p. 15.

121. De Fusco, L., Defoort, F., Rajczyk, R., Jeanmart, H., Blondeau, J., and Contino, F., *Ash Characterization of Four Residual Wood Fuels in a 100 kWth Circulating Fluidized Bed Reactor Including the Use of Kaolin and Halloysite Additives.* Energy & Fuels, 2016. **30**: p. 12.

122. Viskanta, R.a.M., M. P>, *Radiation Heat Transfer in Combustion Systems.* Progress in Energy and Combustion Science, 1987. **13**: p. 97-160.

123. Wolf, J.P., *Biomass combustion for power generation: an introduction*. Vol. Ch 1. 2013: Woodhead Publishing Limited.

124. Charles, E., and Baukal, Jr., *Oxygen-enhanced Combustion*. 2nd edition ed. Industrial Combustion Series. 2013, London New York: CRC Press.

125. Wang, L., G. Varhegyi, and O. Skreiberg, *CO2 Gasification of Torrefied Wood: A Kinetic Study.* Energy & Fuels, 2014. **28**(12): p. 7582-7590.

126. Trabadela, I., H. Chalmers, and J. Gibbins, *Oxy-biomass ignition in air and relevant oxy-combustion atmospheres for safe primary recycle and oxy-burner development.* 12th International Conference on Greenhouse Gas Control Technologies, Ghgt-12, 2014. **63**: p. 403-414.

127. Farrow, T.S., C.G. Sun, and C.E. Snape, *Impact of CO2 on biomass pyrolysis, nitrogen partitioning, and char combustion in a drop tube furnace.* Journal of Analytical and Applied Pyrolysis, 2015. **113**: p. 323-331.

128. Wilen, C.R., A., *Handling and feeding of biomass to pressurized reactors- safety engineering.* Bioresource Technology, 1993. **46**(1-2): p. 77-85.

129. Council, E.P., *Handbook for the Certification of Wood Pellets for Heating Purposes ENPlus* in *Pellet Quality*. 2013, European Pellet Council (EPC): Brussels, Belgium. p. 11.

130. Koppejan, J., Lonnermark, A., Persson, H., Larsson, I., Blomqvist, P., Arshadi, M., et al., *Health and Safety Aspects of Solid Biomass Storage, Transportation and Feeding*, in *Biomass Combustion and Cofiring*, J. Koppejan, Editor. 2013, International Environmental Agency: Netherland.

131. Babrauskas, V., *Ignition Handbook, principles and applications to fire safety engineering*. 2003, Issaquah, WA, USA: Fire Science Publishers.

132. Müllerová, J., *Health and Safety hazards of biomass storage*, in *SGEM 2014, Ibena, Bulgaria, Volume: 5000*. 2014, Research Gate: Albena, Bulgaria.

133. Ottaway, M., *Use of Thermogravimetry for Proximate Analysis of Coals and Cokes.* Fuel, 1982. **61**(8): p. 713-716.

134. Van Loo, S.K., Jaap. , *The handbook of biomass combustion and co-firing* 2008: Earthscan. 442.

135. BSI, *Solid Biofuels-Determination of the Content of Volatile Matter, ISO DIS 18123*. 2013, BSI Group Headquarters: London - UK. p. 11.

136. BSI, *Solid Biofuels-Determination of ash content-ISO DIS 18122 (14775)*. 2013, British Standard Institute: London - UK. p. 5-9.

137. BSI, *Solid Biofuel- Determination of the Calorific Value BS EN 14918:2009*. 2009, British Standarad Institute: London, UK.

138. Jones, J.M., et al., *Modelling the relationship of coal structure to char porosity.* Fuel, 1999. **78**(14): p. 1737-1744.

139. Yu, J.L., et al., *Swelling behaviour of individual coal particles in the single particle reactor.* Fuel, 2003. **82**(15-17): p. 1977-1987.

140. Yu, J.L., et al., *Swelling and char structures from density fractions of pulverized coal.* Energy & Fuels, 2003. **17**(5): p. 1160-1174.

141. Howard, J.B. and Essenhig.Rh, *Pyrolysis of Coal Particles in Pulverized Fuel Flames.* Industrial & Engineering Chemistry Process Design and Development, 1967. **6**(1): p. 74-&.

142. Szuhanszki, J., *Advanced Oxy-fuel Combustion for Carbon Capture and Sequestration*, in *School of Chemical and Process Engineering*. 2014, University of Leeds: Leeds, UK. p. 205.

143. Pickard, S., *Oxygen-enriched biomass combustion studiesand an analysis of the development of the carbon capture and storage industry in the UK*, in *School of Process, Environmental and Material Engineering*. 2013, University of Leeds: Leeds, UK. p. 314.

144. ASTM, *Loss on Ignition (LOI) of Solid Combustion Residues*. 2013, ASTM International: PA, USA. p. 7.

145. Fan, M.H. and R.C. Brown, *Comparison of the loss-on-ignition and thermogravimetric analysis techniques in measuring unburned carbon in coal fly ash.* Energy & Fuels, 2001. **15**(6): p. 1414-1417.

146. Burris, S.C., D. Li, and J.T. Riley, *Comparison of heating losses and macro thermogravimetric analysis procedures for estimating unburned*

carbon in combustion residues. Energy & Fuels, 2005. **19**(4): p. 1493-1502.

147. Pickard, S., et al., *Robust Extension of the Coats-Redfern Technique: Reviewing Rapid and Rea liable Reactivity Analysis of Complex Fuels Decomposing in Inert and Oxidizing Thermogravimetric Analysis Atmospheres.* Energy & Fuels, 2013. **27**(5): p. 2818-2826.

148. Niu, Z.Y., et al., *Investigation of mechanism and kinetics of non-isothermal low temperature pyrolysis of perhydrous bituminous coal by in-situ FTIR.* Fuel, 2016. **172**: p. 1-10.

149. House, J.E., *Principles of Chemical Kinetics*. 1st ed, ed. S. Inc. 1997, Dubuque, IA USA: Wm. C. Brown Publishers.

150. Murphy, J.J. and C.R. Shaddix, *Combustion kinetics of coal chars in oxygen-enriched environments.* Combustion and Flame, 2006. **144**(4): p. 710-729.

151. Ranish, J.M. and P.L. Walker, *High-Pressure Studies of the Carbon-Oxygen Reaction.* Carbon, 1993. **31**(1): p. 135-141.

152. Fermoso, J., et al., *Kinetic models comparison for non-isothermal steam gasification of coal-biomass blend chars.* Chemical Engineering Journal, 2010. **161**(1-2): p. 276-284.

153. Essenhigh, R.H., *Rate-Equations for the Carbon-Oxygen Reaction - an Evaluation of the Langmuir Adsorption-Isotherm at Atmospheric-Pressure.* Energy & Fuels, 1991. **5**(1): p. 41-46.

154. Beeston, G.E., R. H. , *KINETICS OF COAL COMBUSTION: THE INFLUENCE OF OXYGEN CONCENTRATION ON THE BURNING-OUT TIMES OF SINGLE PARTICLES.* Journal of Physical Chemistry, 1963. **67**(6): p. 6.

155. Date, A.W., *Analytic Combustion*. Vol. Chapter 5. 2014, UK: Cambridge University Press.

156. Fortsch, D., Essenhigh, R.H., Schnell, U., and Hein K.R.G., *On the application of the Thiele/Zeldovich Analysis to porous Carbon Combustion.* Energy & Fuels, 2003. **17**: p. 901-906.

157. Zhuang, Q.L., T. Kyotani, and A. Tomita, *Desorption behavior of surface oxygen complexes on carbon in an inert gas and in O-2-gasification atmosphere.* Energy & Fuels, 1996. **10**(1): p. 169-172.

158. Adanez, J., et al., *Determination of biomass char combustion reactivities for FBC applications by a combined method.* Industrial & Engineering Chemistry Research, 2001. **40**(20): p. 4317-4323.

159. Daood, S.S., et al., *Char oxidation study of sugar cane bagasse, cotton stalk and Pakistani coal under 1% and 3% oxygen concentrations.* Biomass & Bioenergy, 2010. **34**(3): p. 263-271.

160. Lopez-Gonzalez, D., et al., *Gasification of lignocellulosic biomass char obtained from pyrolysis: Kinetic and evolved gas analyses.* Energy, 2014. **71**: p. 456-467.

161. Smith, I.W., *The Kinetics of Combustion of Pulverized Semi-Anthracite in Temperature-Range 1400-2200 Degrees K.* Combustion and Flame, 1971. **17**(3): p. 421-&.

162. Thiele, E.W., *Relation between catalytic activity and size of particle.* Industrial and Engineering Chemistry, 1939. **31**: p. 916-920.

163. Satterfi.Cn and D.H. Cortez, *Mass Transfer Characteristics of Woven-Wire Screen Catalysts.* Industrial & Engineering Chemistry Fundamentals, 1970. **9**(4): p. 613-&.

164. Sergeant, G.D. and I.W. Smith, *Combustion Rate of Bituminous Coal Char in Temperature-Range 800 to 1700 K.* Fuel, 1973. **52**(1): p. 52-57.

165. Williams, A., M. Pourkashanian, and J.M. Jones, *The combustion of coal and some other solid fuels.* Proceedings of the Combustion Institute, 2000. **28**: p. 2141-2162.

166. Williams, A., et al., *Modelling coal combustion: the current position.* Fuel, 2002. **81**(5): p. 605-618.

167. Gharebaghi, M., et al., *Large eddy simulation of oxy-coal combustion in an industrial combustion test facility.* International Journal of Greenhouse Gas Control, 2011. **5**: p. S100-S110.

168. Hong, J., W.C. Hecker, and T.H. Fletcher, *Modeling high-pressure char oxidation using Langmuir kinetics with an effectiveness factor.* Proceedings of the Combustion Institute, 2000. **28**: p. 2215-2223.

169. Hong, J.H., W.C. Hecker, and T.H. Fletcher, *Improving the accuracy of predicting effectiveness factors for mth order and Langmuir rate equations in spherical coordinates.* Energy & Fuels, 2000. **14**(3): p. 663-670.

170. Alvarez, L., et al., *CFD modelling of oxy-coal combustion in an entrained flow reactor.* Fuel Processing Technology, 2011. **92**(8): p. 1489-1497.

171. Gao, X.Y., et al., *Determination of the intrinsic reactivities for carbon dioxide gasification of rice husk chars through using random pore model.* Bioresource Technology, 2016. **218**: p. 1073-1081.

172. Essenhigh, R.H., *Influence of Initial Particle Density on the Reaction Mode of Porous Carbon Particles.* Combustion and Flame, 1994. **99**(2): p. 269-279.

173. Gan, H., P.L. Walker, and S.P. Nandi, *Nature of Porosity in American Coals.* Fuel, 1972. **51**(4): p. 272-&.

174. Harding, A.W., S.D. Brown, and K.M. Thomas, *Release of NO from the combustion of coal chars.* Combustion and Flame, 1996. **107**(4): p. 336-350.

175. Arenillas, A., et al., *Modelling of NO formation in the combustion of coal blends.* Fuel, 2002. **81**(5): p. 627-636.

176. Masnadi, M.S., et al., *Fuel characterization and co-pyrolysis kinetics of biomass and fossil fuels.* Fuel, 2014. **117**: p. 1204-1214.

177. Suliman, W., et al., *Modification of biochar surface by air oxidation: Role of pyrolysis temperature.* Biomass & Bioenergy, 2016. **85**: p. 1-11.

178. Vallejos-Burgos, F., et al., *On the structural and reactivity differences between biomass- and coal-derived chars.* Carbon, 2016. **109**: p. 253-263.

179. Halim, S.A. and J. Swithenbank, *Characterisation of Malaysian wood pellets and rubberwood using slow pyrolysis and microwave technology.* Journal of Analytical and Applied Pyrolysis, 2016. **122**: p. 64-75.

180. Smith, I.W., *Kinetics of Combustion of Size-Graded Pulverized Fuels in Temperature-Range 1200-2270 Degrees K.* Combustion and Flame, 1971. **17**(3): p. 303-&.

181. Smith, I.W. and R.J. Tyler, *Internal Burning of Pulverized Semi-Anthracite - Relation between Particle Structure and Reactivity.* Fuel, 1972. **51**(4): p. 312-&.

182. Lu, L.M., V. Sahajwalla, and D. Harris, *Coal char reactivity and structural evolution during combustion - Factors influencing blast furnace pulverized coal injection operation.* Metallurgical and Materials Transactions B-Process Metallurgy and Materials Processing Science, 2001. **32**(5): p. 811-820.

183. Matsuoka, K., et al., *The physical character of coal char formed during rapid pyrolysis at high pressure.* Fuel, 2005. **84**(1): p. 63-69.

184. Guo, J. and A.C. Lua, *Characterization of chars pyrolyzed from oil palm stones for the preparation of activated carbons.* Journal of Analytical and Applied Pyrolysis, 1998. **46**(2): p. 113-125.

185. Vaughn, S.F., et al., *Physical and chemical characterization of biochars produced from coppiced wood of thirteen tree species for use in horticultural substrates.* Industrial Crops and Products, 2015. **66**: p. 44-51.

186. Pastor-Villegas, J., et al., *Study of commercial wood charcoals for the preparation of carbon adsorbents.* Journal of Analytical and Applied Pyrolysis, 2006. **76**(1-2): p. 103-108.

187. ECN. *Biochar Beech wood (#3518)*. ECN Phyllis classification [Database] 2015 [cited 2016; Available from: https://www.ecn.nl/phyllis2/Browse/Standard/ECN-Phyllis#3518.

188. ECN. *Biochar from a blend of greenhouse waste (tomato leaves and stems) and clean wood (#3522)*. ECN Phyllis classification 2015 [cited 2016; Available from: https://www.ecn.nl/phyllis2/Browse/Standard/ECN-Phyllis#3522.

189. ECN. *Biochar from greenhouse waste (pepper residues) 400/60/0 (#3536)*. ECN Phyllis classification 2015 [cited 2016; Available from: https://www.ecn.nl/phyllis2/Browse/Standard/ECN-Phyllis#3514.

190. ECN. *Biochar from greenhouse waste (pepper residues) under gasification (1) (#3519)*. ECN Phyllis classification 2015 [cited 2016; Available from: https://www.ecn.nl/phyllis2/Browse/Standard/ECN-Phyllis#wood.

191. ECN. *Biochar from greenhouse waste (pepper residues) 600/60/0 (#3535)*. ECN Phyllis classification 2015 [cited 2016; Available from: https://www.ecn.nl/phyllis2/Browse/Standard/ECN-Phyllis#wood.

192. ECN. *Biochar from greenhouse waste (pepper residues) under gasification (2) (#3520)*. ECN Phyllis classification 2015 [cited 2016; Available from: https://www.ecn.nl/phyllis2/Browse/Standard/ECN-Phyllis#wood.

193. Xing, P., et al., *Experimental and theoretical methods for evaluating ash properties of pine and El Cerrejon coal used in co-firing.* Fuel, 2016. **183**: p. 39-54.

194. Davidsson, K.O. and J.B.C. Pettersson, *Birch wood particle shrinkage during rapid pyrolysis.* Fuel, 2002. **81**(3): p. 263-270.

195. Fu, Z.X., et al., *Swelling and shrinkage behavior of raw and processed coals during pyrolysis.* Fuel, 2007. **86**(3): p. 418-425.

196. Borrego, A.G., et al., *Coal char combustion under a CO(2)-rich atmosphere: Implications for pulverized coal injection in a blast furnace.* Fuel Processing Technology, 2008. **89**(11): p. 1017-1024.

197. Ellis, N., et al., *Mineral matter interactions during co-pyrolysis of coal and biomass and their impact on intrinsic char co-gasification reactivity.* Chemical Engineering Journal, 2015. **279**: p. 402-408.

198. Biagini, E., et al., *Devolatilization rate of biomasses and coal-biomass blends: an experimental investigation.* Fuel, 2002. **81**(8): p. 1041-1050.

199. LeBlanc, J., J. Quanci, and M.J. Castaldi, *Experimental Investigation of Reaction Confinement Effects on Coke Yield in Coal Pyrolysis.* Energy & Fuels, 2016. **30**(8): p. 6249-6256.

200. Bellotto, M., et al., *Kinetic-Study of the Kaolinite-Mullite Reaction Sequence .1. Kaolinite Dehydroxylation.* Physics and Chemistry of Minerals, 1995. **22**(4): p. 207-214.

201. Brearley, A.J., *An Electron-Optical Study of Muscovite Breakdown in Pelitic Xenoliths during Pyrometamorphism.* Mineralogical Magazine, 1986. **50**(357): p. 385-397.

202. Perry, R.H.a.G.D.W., *Perry's Chemical Engineers Handbook*. Perry's Chemical Engineers Handbook, ed. R.H. Perry. 2007, New York USA: McGraw-Hill. 2640.

203. Haynes, W.M., *Handbook of Chemistry and Physics*. 91st ed. Handbook of Chemistry and Physics, ed. W.M. Haynes. Vol. 1. 2010-2011: CRC Press. 2610.

204. Mookherjea, S.K. and B.K. Mazumdar, *Some Aspects of Low Temperature Pyrolysis Behaviour of Coal.* Fuel, 1969. **48**(3): p. 277-+.

205. Lazaro, M.J., R. Moliner, and I. Suelves, *Non-isothermal versus isothermal technique to evaluate kinetic parameters of coal pyrolysis.* Journal of Analytical and Applied Pyrolysis, 1998. **47**(2): p. 111-125.

206. Zhang, X.D., et al., *Study on biomass pyrolysis kinetics.* Journal of Engineering for Gas Turbines and Power-Transactions of the Asme, 2006. **128**(3): p. 493-496.

207. Anthony, D.B., et al., *Rapid Devolatilization and Hydrogasification of Bituminous Coal.* Fuel, 1976. **55**(2): p. 121-128.

208. Agrawal, R.K., *Kinetics of Reactions Involved in Pyrolysis of Cellulose .1. The 3-Reaction Model.* Canadian Journal of Chemical Engineering, 1988. **66**(3): p. 403-412.

209. Smith, S.E., et al., *Dtga Combustion of Coals in the Exxon Coal Library.* Fuel, 1981. **60**(6): p. 458-462.

210. Johnson, J.L., *Relationships between Coal-Char Gasification Reactivities and Physical and Chemical Coal and Coal-Char Properties.* Abstracts of Papers of the American Chemical Society, 1975. **170**(Aug24): p. 30-30.

211. Tomkow, K., et al., *Formation of Porous Structures in Activated Brown-Coal Chars Using O-2, Co2 and H2o as Activating Agents.* Fuel, 1977. **56**(2): p. 121-124.

212. Solomon, P.R., G.V. Deshpande, and M.A. Serio, *Crosslinking Reactions in Coal Pyrolysis.* Abstracts of Papers of the American Chemical Society, 1988. **195**: p. 99-Fuel.

213. Nanou, P., et al., *Intrinsic reactivity of biomass-derived char under steam gasification conditions-potential of wood ash as catalyst.* Chemical Engineering Journal, 2013. **217**: p. 289-299.

214. Young, B.C. and I.W. Smith, *The Combustion of Loy Yang Brown Coal Char.* Combustion and Flame, 1989. **76**(1): p. 29-35.

215. Lin, L.T. and M. Strand, *Investigation of the intrinsic CO2 gasification kinetics of biomass char at medium to high temperatures.* Applied Energy, 2013. **109**: p. 220-228.

216. Fang, Y., et al., *Kinetic Study on Coal Char Combustion in a Microfluidized Bed.* Energy & Fuels, 2017. **31**(3): p. 3243-3252.

217. Smith, I.W., *Kinetics of Combustion of Pulverized Semi-Anthracite in Temperature-Range 1400-2200 Degrees K.* Combustion and Flame, 1971. **17**(3): p. 421-&.

218. Tafur-Marinos, J.A., et al., *Comparison of inorganic constituents in bottom and fly residues from pelletised wood pyro-gasification.* Fuel, 2014. **119**: p. 157-162.

219. Barroso, J., J. Ballester, and A. Pina, *Study of coal ash deposition in an entrained flow reactor: Assessment of traditional and alternative slagging indices.* Fuel Processing Technology, 2007. **88**(9): p. 865-876.

220. De Fusco, L., Defoort, F., Rajczyk, R., Jeanmart, H., Blondeau, J., and Contino, F., *Ash Characterization of Four Residual Wood Fuels in a 100 kWth Circulating Fluidized Bed Reactor Including the Use of Kaolin and Halloysite Additives.* Energy & Fuels, 2016. **30**: p. 11.

221. Baxter, L.L., et al., *The behavior of inorganic material in biomass-fired power boilers: field and laboratory experiences.* Fuel Processing Technology, 1998. **54**(1-3): p. 47-78.

222. Gneshin, K.W., R.L. Krumm, and E.G. Eddings, *Porosity and Structure Evolution during Coal Pyrolysis in Large Particles at Very Slow Heating Rates.* Energy & Fuels, 2015. **29**(3): p. 1574-1589.

223. Report, I.F.A., *Contribution of Working Group III to the Fourth Assessment Report of the Intergovernmental Panel on Climate Change, 2007. B. Metz, O.R. Davidson, P.R. Bosch, R. Dave, L.A. Meyer (eds).* Cambridge University Press, Cambridge, United Kingdom and New York, NY, USA., 2007.

224. EIA, *World Energy Outlook.* 2009.

225. Azar, C., Lindgren, K., Obersteiner, M., Riahi, K., van Vuuren, D. P., den Elzen, K. M. G. J., Mollersten, K., Larson, E. D., *The feasibility of low CO2 concentration targets and the role of bio-energy with carbon capture and storage (BECCS).* Climatic Change, 2010. **100**(1): p. 195-202.

226. Demirbas, M.F., M. Balat, and H. Balat, *Potential contribution of biomass to the sustainable energy development.* Energy Conversion and Management, 2009. **50**(7): p. 1746-1760.

227. Karelsson, H., *The Current Status of BECCS.* GCEP Workshop on Energy Supply with Negative Carbon Emissions 2012. Stanford University, 2012.

228. OFGEM, *Renewables Obligation - total obligation levels for 2012-13.* 2013.

229. Kraxner, F., et al., *BECCS in South Korea-Analyzing the negative emissions potential of bioenergy as a mitigation tool.* Renewable Energy, 2014. **61**: p. 102-108.

230. Ricci, O., *Providing adequate economic incentives for bioenergies with CO2 capture and geological storage.* Energy Policy, 2012. **44**: p. 362-373.

231. Laude, A. and C. Jonen, *Biomass and CCS: The influence of technical change.* Energy Policy, 2013. **60**: p. 916-924.

232. Wiley, D.E.K., Z., Ho, M.T. , *The impact of biomass quality and quantity on the performance and economics of co-firing plants with and without CO2 capture., 21, 191-202.* International Journal of Green House Gas Control, 2014. **21**: p. 12.

233. Smolker, R.a.E., A., *BECCS (Bioenergy with Carbon Capture and Storage): Climate saviour or dangerous hype?*, in *BECCS*, R. Smolker, Editor. 2012, Biofuelwatch.

234. Arranz, A.M., *Hype among low-carbon technologies: Carbon capture and storage in comparison.* Global Environmental Change-Human and Policy Dimensions, 2016. **41**: p. 124-141.

235. Brack, D., *The Impacts of the Demand for Woody Biomass for Power and Heat on Climate and Forests*, in *Bioenergy*, D. Brack, Editor. 2017, Chatham House: UK.

236. Taeroe, A., et al., *Do forests best mitigate CO2 emissions to the atmosphere by setting them aside for maximization of carbon storage or by management for fossil fuel substitution?* Journal of Environmental Management, 2017. **197**: p. 117-129.

237. Wilson, P. *Chatham House biomass report: dancing on a pinhead!* Opinoin 2017 [cited 2017 12/07/2017]; Available from: http://www.charteredforesters.org/2017/04/chatham-house-biomass-report/.

238. Boukherroub, T., L. Lebel, and S. Lemieux, *An integrated wood pellet supply chain development: Selecting among feedstock sources and a range of operating scales.* Applied Energy, 2017. **198**: p. 385-400.

239. Dell, K., *Carbon Management Plan.* Department of Energy and Climate Change- UK -Carbon TRust, 2011: p. 8.

240. DECC, E.S., *Energy trends section 5: electricity.* https://www.gov.uk/government/uploads/system/uploads/attachment_data/file/295355/5_Electricity.pdf 2014: p. p 43.

241. Ashcroft, S., Singh, R. *Electricity Statistics*. 2014 [cited 2014 Sep 2014]; Available from: https://www.gov.uk/government/uploads/system/uploads/attachment_data/file/579519/Electricity.pdf.

242. Rubin, E.S., Rao, A.B., and Chao Chen, *Comparative Assessments of Fossil Fuel Power Plants with CO_2 Capture and Storage.* Preceedings of 7th International Conferenceon Green House Gas Control TEchnologies(GHGT-7), 2004. **1**(September): p. 5-9.

243. Rubin, E.S., C. Chen, and A.B. Rao, *Cost and performance of fossil fuel power plants with CO2 capture and storage.* Energy Policy, 2007. **35**(9): p. 4444-4454.

244. Rubin, E.S., et al., *Use of experience curves to estimate the future cost of power plants with CO2 capture.* International Journal of Greenhouse Gas Control, 2007. **1**(2): p. 188-197.

245. Rubin, E.S., et al., *A proposed methodology for CO2 capture and storage cost estimates.* International Journal of Greenhouse Gas Control, 2013. **17**: p. 488-503.

246. Mores, P., et al., *CO2 capture in power plants: Minimization of the investment and operating cost of the post-combustion process using*

MEA aqueous solution. International Journal of Greenhouse Gas Control, 2012. **10**: p. 148-163.

247. Mores, P., N. Scenna, and S. Mussati, *CO2 capture using monoethanolamine (MEA) aqueous solution: Modeling and optimization of the solvent regeneration and CO2 desorption process.* Energy, 2012. **45**(1): p. 1042-1058.

248. Rubin, E.S., *Understanding the pitfalls of CCS cost estimates.* International Journal of Greenhouse Gas Control, 2012. **10**: p. 181-190.

249. Berghout, N., M. van den Broek, and A. Faaij, *Techno-economic performance and challenges of applying CO2 capture in the industry: A case study of five industrial plants.* International Journal of Greenhouse Gas Control, 2013. **17**: p. 259-279.

250. De, S. and M. Assadi, *Impact of cofiring biomass with coal in power plants - A techno-economic assessment.* Biomass & Bioenergy, 2009. **33**(2): p. 283-293.

251. Domenichini, R., et al., *Techno-Economic Evaluation of Biomass Fired or Co-Fired Power Plants with Post Combustion CO2 Capture.* 10th International Conference on Greenhouse Gas Control Technologies, 2011. **4**: p. 1851-1860.

252. McIlveen-Wright, D.R., et al., *A Techno-economic assessment of the reduction of carbon dioxide emissions through the use of biomass co-combustion.* Fuel, 2011. **90**(1): p. 11-18.

253. Catalanotti, E., Hughes, K.J., Porter, R.T.J., Price, J. and Pourkashanian, M., *Evaluation of Performance and Cost of Combustion-Based power Plants with CO_2 Capture in The United Kingdom.* Environmental Progress & sustainable Energy, 2013. **DOI 10.1002/ep.**: p. 7.

254. Meerman, J.C., Knoope, M., Rameriz, A., Turkenburg,, W.C., and Faaij, A.P.C., *Technical and economicprospects of coal- and biomass-fired integrated gasification facilities equiped with CCS over time.* International Journal of Greenhouse Gas Control, 2013. **16**: p. 311-323.

255. Bridgwater, A.V., A.J. Toft, and J.G. Brammer, *A techno-economic comparison of power production by biomass fast pyrolysis with gasification and combustion.* Renewable & Sustainable Energy Reviews, 2002. **6**(3): p. 181-248.

256. Klemes, J., Bulatov, I., and Cockerill, T., *Techno-economic modelling and cost functions of CO_2 capture processes.* Computers and Chemical Engineering, 2007. **31**: p. 445-455.

257. Patel, C., et al., *Techno-economic performance analysis of energy production from biomass at different scales in the UK context.* Chemical Engineering Journal, 2011. **171**(3): p. 986-996.

258. Muratori, M., et al., *Global economic consequences of deploying bioenergy with carbon capture and storage (BECCS).* Environmental Research Letters, 2016. **11**(9).

259. DECC, *Eelctricity Generation Costs 2013.* 2013.

260. NETL, *Integrated Environmental Control Model User Manual.* DE-AC26-04NT41917, 2009: p. 29.

261. DECC, *Eelctricity Generation Cost Model- 2013 update of Non-Renewable Technologies.* 2013: p. 13-15, 36-47.

262. Gharebaghi, M., *Numerical and Experimental Investigation of the Oxy-coal Combustion in Carbon Caapture Technologies.* 2011: p. 224-254.

263. Union, T.E.P.a.T.C.o.t.E., *Directive 2001/80/EC Of The European Parliament and The Council of the European Union of 23 October 2001, on the limitation of emissions of certain pollutants into the air from large combustion plants.* Oficial Journal of the European Communities, 2009. **L309**.

264. UNEP, *Minamata Convension on Mercury.* 2013.

265. Ling, A., Pearson, M., *RO: Sustainability Criteria for Solid and Gaseous Biomass for Generators (greater than 50 kilowatts) Guidance.* 2011: p. 18.

266. European Standard for fly ash, B.E.r., 2008.

267. DECC, *Energy Trends Section 2: Solid Fuels and supplied Gasses.* 2014.

268. E4tech, D.-. *Biomass prices in the heat and electricity sectors in the UK.* 2010: p. 19.

269. EIA, *Coal Data Browser- Eport Price to United Kingdom.* 2014.

270. Indices., i.M.C.P.; Available from: http://www.indexmundi.com/commodities/?commodity=colombian-coal.

271. STYRELSEN, E., *Generatin of Energy and district heating, Energy storage carrier generation and conversion.* , in *Technology data for eneergy plants*. 2012, Energi Styrelsen: Denmark. p. 30-36.

272. DECC, *Calculating the Level of the Renewables Obligation for 2013/14.* 2012.

273. EIA, *Monthly Generator capacity factor data now available by fuel and technology.* 2014.

274. Oksa, M., Tuuma, S., and Varis, T, *Increased lifetime for biomass and waste to energy power plant boilers with HVOF coatings: High temperature corrosion testing under chlorine-containing molted salt.* Journal of Thermal Spray Technology, 2013. **22**(5): p. 783-796.

275. Statistics, O.f.N., *Table 6_SIC07 : Full-timea,b employees' pay by industry sector (SIC 2007)c, United Kingdom, April 2008 - 2013.* 2014.

276. Walsh, C., and Thornley, P., *The environmental impact and economic feasibility of introducing an organic Ranking Cycle to recover low grade heat during the production of metallurgical coke.* Juournal of Cleaner Production, 2012. **34**: p. 29-37.

277. DECC, *The costs of CCS for UK industry - A high level review.* 2013.

278. Lu, G., et al., *Impact of co-firing coal and biomass on flame characteristics and stability.* Fuel, 2008. **87**(7): p. 1133-1140.

279. Tillman, D.A., *Biomass cofiring: the technology, the experience, the combustion consequences.* Biomass & Bioenergy, 2000. **19**: p. 365-384.

280. Welfle, A., Gilbert, P., and Thornley, P., *Securing a bioenergy future without imports.* Energy Policy, 2014. **68**: p. 1-14.

281. Center, B.E., *Biomass fuels cost: : Technical Answers*. 2009.

282. http://pellets-wood.com, *Wood pellets prices.* 2013.

283. Markets, A.B., Argus Media Ltd., 2014. **14-013**.

284. DECC, *Fossil fuel Price Projections 2012- 2030.* 2013.

285. Strauss, W., Kingsley, E. , *Hedging Input Price Risk for Biomass Power Plant and Pellet Export Projects.* A paper presented at the Risk Conference 2011, 2011. **Las Vegas, USA**.

Appendix – A: Pilot Scale Combustion Flowrates: USWWP-Air

Basis: 100 kg biomass, complete combustion											
100% fuel Oxygen Availability											
Vol Fraction of N_2 in air	78.084										
Vol Fraction of O_2 in air	20.946										
Vol Fraction of Ar in air	0.934										
Vol Fraction of CO_2 in air	0.041										
Air : Fuel ratio	1.202										
Excess air%	20										
Fuel Flowrate Calculations											
NCV_{db}, MJ/kg	17.200										
1 kW = 3.60000 MJ/hr											
Thermal input, kW	**150**	**160**	**170**	**180**	**190**	**200**	**210**	**220**	**230**	**240**	**250**
Fuel Thermal input MJ/hr	540	576	612	648	684	**720**	756	792	828	864	900

Mass flowrate of fuel, kg/hr	**31.40**	**33.49**	**35.58**	**37.67**	**39.77**	**41.86**	**43.95**	**46.05**	**48.14**	**50.23**	**52.33**

Stoichiometric Oxygen calculations

$C + O_2$ ----------> CO_2

$2H + 1/2\ O_2$----> H_2O

$S + O_2$ ----------> SO_2

$N + 1/2\ O_2$ ----------> NO

Composition % by mass	**kg/100 kg F**	**M.wt**	**Kmols**	**Kmol O_2**	**Kmol CO_2**	**Kmol H_2O**	**Kmol NO**	**Kmol SO_2**	**Excess O_2**	**Kmol N_2**	**kmol FG**
C	46.45	12.011	3.867	3.867	3.867						
H	5.78	1.008	5.734	1.434		2.867					
O	41.73	15.999	2.608	-1.304							
N	0.17	14.007	0.012	0.006			0.012				
S	0.02	32.064	0.00062	0.00062				0.001			
Ash	0.67										
Moist	5.48	18.020	0.304			0.304					
Total	**100.3**			**4.003**	**3.867**	**3.171**	**0.012**	**0.001**	**0.809**	**17.939**	**25.799**
Total %					**14.99**	**12.29**	**0.05**	**0.002**	**3.13**	**69.53**	**100.000**

Total m3 at 273 K, 1 atm		89.678	86.628	71.037	0.272	0.014	18.115	401.837	176.066
Flue Gas Composition Calculations									
Thermal Input (kW)	**F, kg/hr**	**Kmol O_2**	**Kmol CO_2**	**Kmol H_2O**	**Kmol NO**	**Kmol SO_2**	**Excess O_2**	**Kmol N_2**	**kmol FG**
150	31.40	1.257	1.214	0.996	0.004	0.000	0.254	5.632	8.100
160	33.49	1.341	1.295	1.062	0.004	0.000	0.271	6.007	8.640
170	35.58	1.424	1.376	1.128	0.004	0.000	0.288	6.383	9.180
180	37.67	1.508	1.457	1.195	0.005	0.000	0.305	6.758	9.720
190	39.77	1.592	1.538	1.261	0.005	0.000	0.322	7.134	10.260
200	41.86	1.676	1.619	1.328	0.005	0.000	0.339	7.509	10.799
210	43.95	1.760	1.700	1.394	0.005	0.000	0.355	7.885	11.339
220	46.05	1.843	1.781	1.460	0.006	0.000	0.372	8.260	11.879
230	48.14	1.927	1.862	1.527	0.006	0.000	0.389	8.636	12.419
240	50.23	2.011	1.943	1.593	0.006	0.000	0.406	9.011	12.959
250	52.33	2.095	2.024	1.659	0.006	0.000	0.423	9.387	13.499

Appendix – B: Published Data of Biomass & Coal Char Surface Area

Ref.	Coal Type	Ash% db	VM% db	FC% db	C% db	c% daf	Prep. T	Ag
Coal							**K**	**m2/g**
Nandi 1964	St. Nicolas	9.1	4.5			94.0	973.0	215
		9.1	4.5			94.0	1073.0	198
		9.1	4.5			94.0	1173.0	104
		9.1	4.5			94.0	1273.0	24
	Dorrance	9.9	5.8			92.7	773	235
		9.9	5.8			92.7	873.0	250
		9.9	5.8			92.7	973.0	273
		9.9	5.8			92.7	1073.0	187
		9.9	5.8			92.7	1173.0	26
	Treverton	9.7	9			92.0	773	222
							873.0	243
							973.0	216
							1073.0	208
							1173.0	61
Gan 1972	PSOC-80					90.8	1273	408
	PSOC-127					89.5	1273	253
	PSOC-135					88.3	1273	214
	PSOC-4					83.8	1273	213
	PSOC-105 A					81.3	1273	114
	Rand					79.9	1273	147
	PSOC-26					77.2	1273	133
	PSOC-190					75.5	1273	96
	PSOC-141					71.7	1273	250
	PSOC-87					71.2	1273	268
	PSOC-89					63.3	1273	238
Harding 1996	Cynheidre	1.80	4.70	93.5	93.2	94.91	1273	235
	Narcea	4.00	5.70	90.3	90.6	94.38	1273	203
	San Jose	4.10	6.70	89.2	88.2	91.97	1273	213
	Tilmanstone	5.50	16.1	78.4	86.7	91.75	1273	107
	Taff Merthyr	4.10	12.80	83.2	88.4	92.18	1273	173
	Crosswell	2.30	37.10	60.7	82	83.93	1273	172
	Maria Luisa	4.80	36.60	58.6	78	81.93	1273	141
	Kellingley	5.20	38.90	55.8	80	84.39	1273	162
	Lieres	8.70	36.30	55	76	83.24	1273	171

	Bagworth	8.80	39.50	51.7	72.9	79.93	1273	244
	Bickershaw	10.10	34.2	55.6	79	87.88	1273	118
	Thoresby	5.20	36.20	58.6	79.2	83.54	1273	312
	Sabina	10.00	46.00	44	68.1	75.67	1273	293
	Ollerton	5.30	36.80	57.8	77.4	81.73	1273	160
	Daw Mill	4.70	38.00	57.3	76.8	80.59	1273	284
	Coventry	4.10	38.10	57.7	79.1	82.48	1273	503
	Longannet	11.90	30.80	57.3	73.4	83.31	1273	225
	Nadins	8.50	40.30	51.2	72.3	79.02	1273	255
Zhu 1999	El Cerrejon	1.39	36.79	58.73	49.76	78.72	1273	227
	Pitsburgh 8	7.31	38.08	54.61	51.86	83.75	1273	168
Arenillas 1999	W150	6.20	17.00	76.80	75.70	91.20	1473	143
Chan 1999	MM-500	3.11	37.34	59.65	51.25	81.80	773	114
	MM-600	3.11	37.34	59.65	50.63	80.80	873	182
	MM-700	3.11	37.34	59.65	51.25	81.80	973	180
	MM-800	3.11	37.34	59.65	50.63	80.80	1073	272
	MM-900	3.11	37.34	59.65	51.25	81.80	1173	210
	Kiverton Park-500	3.83	35.13	61.04	53.00	81.70	773	73
	Kiverton Park-600	3.83	35.13	61.04	53.65	82.70	873	68
	Kiverton Park-700	3.83	35.13	61.04	54.30	83.70	973	222
	Kiverton Park-800	3.83	35.13	61.04	54.95	84.70	1073	212
	Kiverton Park-900	3.83	35.13	61.04	55.59	85.70	1173	184
	Goldthorpe	1.66	40.27	57.97	47.01	78.70	773	50
	Goldthorpe	1.66	40.27	57.97	47.61	79.70	873	29
	Goldthorpe	1.66	40.27	57.97	48.20	80.70	973	263
	Goldthorpe	1.66	40.27	57.97	48.80	81.70	1073	215
Masnadi 2014	Sub-bituminous coal	30.50	31.30	38.30	50.22	73.10	1023	246
							1073	243
							1173	238

Continued

Biomass		Ash% db	VM% db	FC% db	C% db	c% daf	Prep. T	Ag
							K	m2/g
Suliman 2016	Douglas fir wood	0.3	82	17.7	51.30	51.30	723	333
		0.3	82	17.7	51.30	51.30	773	404
		0.3	82	17.7	51.30	51.30	823	446
		0.3	82	17.7	51.30	51.30	873	500
	Douglas fir bark	2.4	84.6	13.0	53.40	53.40	723	291
		2.4	84.6	13.0	53.40	53.40	773	318
		2.4	84.6	13.0	53.40	53.40	823	395
		2.4	84.6	13.0	53.40	53.40	873	424
	Hybrid poplar	1	81.32	17.35	50.40	50.40	723	277
		1	81.32	17.35	50.40	50.40	773	361
		1	81.32	17.35	50.40	50.40	823	382
		1	81.32	17.35	50.40	50.40	873	417
Masnadi 2014	Sawdust	0.4	87.6	12.00		50.10	1023	575
		0.4	87.6	12.00		50.10	1073	574
		0.4	87.6	12.00		50.10	1173	565
Lopez, 2013	Silver Fir	0.4	78.7	6.50		51.20	873	374
	Stone Pine	0.7	82.1	7.40		50.40	873	334
Vallejos-Burgos, 2016	Sawdust	0.4	86.9	11.90		50.20	823	290
		0.4	86.9	11.90		50.20	973	350
		0.4	86.9	11.90		50.20	1123	392
		0.4	86.9	11.90		50.20	1173	565
		0.4	86.9	11.90		50.20	1273	380
		0.4	86.9	11.90		50.20	1423	250
		0.4	86.9	11.90		50.20	1573	120
Chowdhury, 2016	Sawdust- B550	10.52	85.80	3.68	36.73	41.05	823	221
Abdul Halim	Malaysian wood char	0.91	80.12	18.97		48.19	773	333
& Swithenbank 2016		0.91	80.12	18.97		48.19	1073	390
	Rubberwood char	1.48	79.60	18.93		48.69	773	259
		1.48	79.60	18.93		48.69	1073	489

Appendix – C: Published Data on Char true and Apparent Densities of Biomass & Coal

Coal

Ref.	Coal Sample	C% daf	Char Prep. Temp	Apparent Density	True Density
			K	kg/m3	kg/m3
Smith, 1971	Bituminous caol char	95.7	1500	730	
	Bituminous caol char	94.1	1500	840	
Smith & Tyler, 1972	semi-anthracite coal	91.25	1480	1330	1790
Liming Lu 2001	Bitu coal	96.2	1473	680	
Matsuoka 2005	Berau Coal	68.4	1073	330	
	Adaro	70.6	1073	280	
	Pasir	71.7	1073	170	
	Taiheiyo	76.1	1073	400	
	Blair Athol char	78.4	1073	230	
	Shenmu	77.4	1073	370	
Nandi Walker 1964	St. Nicolas	94.0	973	1490	1730
		94.0	1073	1500	1800
		94.0	1173	1560	1860
		94.0	1273	1610	2080
	Dorrance	92.7	773	1350	1650
		92.7	873	1420	1790
		92.7	1073	1570	1850
		92.7	1173	1650	2060
	Treverton	92.0	773	1270	1630
		92.0	873	1360	1670
		92.0	973	1430	1750
		92.0	1073	1540	2050
		92.0	1173	1650	2080
Chan 1999	Markham Main	80.8	673.15	950	990
		80.8	773.15	980	1010
		80.8	873.15	1020	1070
		80.8	973.15	1070	1150
		80.8	1073.15	1180	1230
		80.8	1173.15	1330	1460
	Kiverton Park	81.7	673.15	940	980
		81.7	773.15	960	990
		81.7	873.15	980	1010
		81.7	973.15	1010	1030

Continued

		81.7	**1073.15**	**1030**	**1060**
		81.7	1173.15	1120	1190
	Goldthorp	78.7	673.15	950	1050
		78.7	773.15	970	1010
		78.7	873.15	1010	1080
		78.7	973.15	1090	1110
		78.7	1073.15	1100	1130
		78.7	1173.15	1190	1270

Biomass

Ref.	**Sample**	**C% daf**	**Char Prep. T**	**Apparent Density**	**True Density**
		K	**kg/m3**	**kg/m3**	
Sulimanne 2016	Douglas fir wood	51.30	723		2273
		51.30	773		2326
		51.30	823		2273
		51.30	873		1754
	Douglas fir bark	53.40	723		2564
		53.40	773		2778
		53.40	823		1852
		53.40	873		2326
	Hybrid poplar		723		2632
			773		2000
			823		1754
			873		1538
Guo 1998	palm oil stone	51.64	673	1440	1570
		51.64	773	1400	1600
		51.64	873	1350	1630
		51.64	973	1320	1640
		51.64	1073	1270	1670
		51.64	1173	1310	1690
Vaughn 2015	QV	51.14	1073		1640
	RP	47.97	1073		1570
	CR	52.92	1073		1590
	Aa	52.92	1073		1680
	CO	56.01	1073		1700
	CC	48.23	1073		1720
	EU	48.77	1073		1750
	VP	48.15	1073		1770
	GT	56.78	1073		1820
	PS	56.50	1073		1830
	MP	52.90	1073		1830

	LT	51.50	1073		1860
	TA	51.34	1073		1740
Pastor-Villegas et al. 2006	EnC	49.53	1173	890	
	EnHD	49.53	1173	650	
	EuHD	48.76	1173	620	
	EuHC	48.76	1173	610	
ECN	Biochar Beech wood 3518	48.06	943		2100
ECN	Biochar mixed waste 3522	45.45	943		1780
ECN	Biochar green waste 3536	47.39	673		1670
ECN	Biochar green waste 3535	47.39	873		1870
ECN	Biochar green waste 3519	47.39	943		1810
ECN	Biochar green waste 3520	47.39	1023		1800